ISSN en trámite

Geofísica Internacional

Revista Trimestral Publicada por el Instituto de Geofísica de la Universidad Nacional Autónoma de México

México
Volume 56 Number 1
January - March
2017

— Geofísica Internacional —

GEOFÍSICA INTERNACIONAL, Año 56, Vol. 56, Núm. 1, enero - marzo de 2017 es una publicación trimestral, editada por la Universidad Nacional Autónoma de México, Ciudad Universitaria, Alcaldía Coyoacán, C.P. 04150, Ciudad de México, a través del Instituto de Geofísica, Circuito de la Investigación Científica s/n, Ciudad Universitaria, Alcaldía Coyoacán, C.P. 04150, Ciudad de México, Tel. (55)56 22 41 15. URL: http://revistagi.geofisica.unam.mx, correo electrónico: revistagi@igeofisica.unam.mx. Editora responsable: Andrea Rostan Robledo. Certificado de Reserva de Derechos al uso Exclusivo del Título: 04-2022-081610251200-102, ISSN: en trámite, otorgados por el Instituto Nacional del Derecho de Autor (INDAUTOR). Responsable de la última actualización Saúl Armendáriz Sánchez, Editor Técnico. Fecha de la última modificación: 31 de diciembre 2016, Circuito de la Investigación Científica s/n, Ciudad Universitaria, Alcaldía Coyoacán, C.P. 04150, Ciudad de México.

Geofísica Internacional

Vol. 56, Núm. 1, enero-marzo de 2017

Contents

Unusual, equivocal Rayleigh-dispersion curves for simple models taking into account the special propagation conditions in the valley of Mexico City (CDMX) - Preliminary results.
Peter G. Malischewsky, Thomas Forbriger, Cinna LomnitzÂ†

7

The Mw 7.3 Papanoa, Mexico earthquake of April 18, 2014: Implications for recurrent M > 7 thrust earthquakes in western Guerrero.
Carlos Mendoza, María del Rosario Martínez López

13

Evaluation of macroseismic intensities in Mexico from recent earthquakes using Â¿Sintió un sismo? (Did you feel it?).
Juan C. Montalvo-Arrieta, Rocío L. Sosa-Ramírez, Xyoli Pérez-Campos

27

Mapping Geologic Interfaces that may alter seismic wave propagation in the Mexico City basin.
Román Álvarez

37

Tsunami deposits of September 21st 1985 in Barra de Potosí: comparison with other studies and evaluation of some geological proxies for southwestern Mexico.
Brenda Grisset Ocampo-Rios, Priyadarsi D. Roy, Ma. Consuelo Macías, M.P. Jonathan, Rufino Lozano-Santacruz

57

Estimation of source, path and site effects at MASE array stations: a comprehensive study.
Carlos Ortiz-Alemán, Maricarmen Reyes-Olvera, Arturo Iglesias-Mendoza, Mauricio Gabriel Orozco-Del-Castillo, Jorge Hernández-Gómez

71

Geofísica
Internacional

A probabilistic seismic hazard assessment of the Trans-Mexican Volcanic Belt, Mexico based on historical and instrumentally recorded seismicity. José Antonio Bayona Viveros, Gerardo Suárez Reynoso, Mario Gustavo Ordaz Schroeder

87

Frecuency-wavenumber analysis of strong ground motion in Mexico City.
Marcela Baena-Rivera, L. Eduardo Pérez-Rocha, Francisco J. Sánchez-Sesma. Marcela Baena-Rivera, L. Eduardo Pérez-Rocha, Francisco J. Sánchez-Sesma

103

High-Resolution Early Earthquake Damage Assessment System for Mexico City Based on a Single-Station.
Mario Ordaz, Eduardo Reinoso, Miguel A. Jaimes, Leonardo Alcántara, Citlali Pérez

117

Geofísica Internacional (2017) 56-1: 7-12

Original paper

Unusual, equivocal Rayleigh-dispersion curves for simple models taking into account the special propagation conditions in the valley of Mexico City (CDMX) – Preliminary results

Peter G. Malischewsky, Thomas Forbriger and Cinna Lomnitz†

Received: March 07, 2016; accepted: November 11, 2016; published on line: January 01, 2017

DOI: 10.19155/geofint.2017.056.1.1

Resumen

Contrario a lo que normalmente es asumido en sismologia, la fase-velocidad de olas Rayleigh no necesariamente es una función de valor único de frecuencia. Se demuestra esto para el primer modo más alto en modelos simples de una capa homogénea encima de un semiespacio homogéneo (LOH), los cuales, han sido utilizados en estudios anteriores en el subsuelo de la zona de Texcoco en el valle de Ciudad de México. En la estructura de una capa homogénea con fondo fijo (LFB) el fenómeno existe para valores del coeficiente de Poisson entre 0.19 y 0.5 y es más pronunciado para velocidades de P que son tres veces la velocidad de S (Coeficiente de Poisson de 0.4375). En este trabajo se demuestra este tipo de dispersión y se discuten sus posibles consecuencias fatales para los métodos habitualmente usados en sismología en el análisis de dispersión y síntesis de relaciones de dispersión.

Palabras clave: Ondas de Rayleigh, dispersión, ambigüedad, valle de CDMX.

Abstract

Other than commonly assumed in seismology, the phase velocity of Rayleigh waves not necessarily is a single-valued function of frequency. We demonstrate this for the first higher mode in simple models of a homogeneous layer on top of a homogeneous halfspace (LOH), which are used for the subsurface of the Texcoco zone in Mexico City valley in previous studies. In the structure of a homegenous layer with fixed bottom (LFB) the phenomenon exists for values of Poisson's ratio between 0.19 and 0.5 and is most pronounced for P-velocity being three times S-velocity (Poisson's ratio of 0.4375). This type of dispersion is demonstrated and a discussion of their possible fatal consequences for methods customarily used in seismology for dispersion analysis and synthesis of dispersion relations is presented.

Key words: Rayleigh waves, dispersion, ambiguity, Mexico City valley.

P. G. Malischewsky
Institute of Geosciences
Friedrich-Schiller University Jena
07749 Jena, Germany

Karlsruhe Institute of Technology
76187 Karlsruhe, Germany
*Corresponding author: p.mali@uni-jena.de

T. Forbriger
Karlsruhe Institute of Technology
76187 Karlsruhe, Germany

C. Lomnitz†
Instituto de Geofísica
Universidad Nacional Autonoma de México
Ciudad Universitaria
Delegación Coyoacán 04510
CDMX, México

Introduction

Without doubt the great 1985 Michoacán earthquake (M_w 8.1) was the most damaging in Mexico City history. This earthquake and its disastrous effects have been thoroughly and controversially analyzed and discussed during the last three decades after the tragedy. We refer to the review paper by Flores-Estrella *et al*. (2007) with an exhaustive list of references. Surface waves always play an important role in the earthquake effects for well-known physical reasons. These waves carry most of the energy from the source because the crust layers constitute an efficient waveguide. The Malischewsky's (2004) report examined the propagation conditions for surface waves in the valley of Mexico City (CDMX). One notorious characteristic is an extremely high Poisson ratio in the uppermost layers together with a very high impedance contrast between the layers and the subsoil. Investigating the so-called osculations of dispersion curves (Kausel *et al*., 2015) we have casually discovered unusual higher-mode Rayleigh waves because of the equivocal behaviour of their dispersion curves in a certain frequency range. Following Furumura and Kennett (1998) the dominant seismic phases at regional distances are usually the crustal P_g and L_g phases and the recorded L_g phase can be regarded either as a superposition of multiply reflected S waves in the crust or as a sum of a number of higher surface wave modes sampled at the free surface of the crust. So it is appropriate to have a closer look on the higher modes as well. It turns out that the conditions for the occurrence of this special behaviour, to be presented here, coincide with the natural conditions in Mexico City. This behaviour is reproduced by using very simple models. This observation agrees also with the Paul Dirac's statement that natural laws seem to be constructed following the principle "As simple as possible, as complicated as necessary".

Equivocalness of dispersion curves

Usually it is silently (to avoid saying shamefully) assumed in seismological literature that dispersion curves of Rayleigh waves are unique in the sense that *one* phase-velocity value belongs to a given frequency. However, we have observed that this is not always true. To illustrate this, let us consider the elastic model of a "Layer with Fixed Bottom" (LFB), i.e. a layer with a stress-free surface and a bottom with vanishing displacements. The secular equation for LFB is

$$\Delta_{LFB}(F,C,\nu) = -4(C^2-2)+(-C^4+4C^2-8)\cos\left(\frac{2F\pi\sqrt{C^2-1}}{C}\right)\cos\left(\frac{2F\pi\sqrt{\frac{C^2(1-2\nu)}{2(1-\nu)}-1}}{C}\right)+$$

$$\left[8-4C^2\left\{2+\frac{1-2\nu}{2(1-\nu)}\right\}+C^4\left\{1+\frac{2(1-2\nu)}{1-\nu}\right\}\right]\sin\left(\frac{2F\pi\sqrt{C^2-1}}{C}\right)\sin\left(\frac{2F\pi\sqrt{\frac{C^2(1-2\nu)}{2(1-\nu)}-1}}{C}\right)$$

$$\frac{}{\sqrt{C^2-1}\,\sqrt{\frac{C^2(1-2\nu)}{2(1-\nu)}-1}} = 0\,, \qquad (1)$$

where F and C are the dimensionless frequency and phase velocity, respectively, defined by

$$F = (h/\beta)f,\ C = c/\beta \qquad (2)$$

with f=frequency, c=phase velocity, β=shear velocity, h=layer thickness, and ν=Poisson ratio. Formula (1) implies the dispersion equation $C = C(F)$ and was rewritten from the one found by Tran (2009). The phenomenon to be described here occurs for higher modes only. We have analysed Eq. (1) with the software Mathematica and have obtained dispersion curves of the first higher mode of Rayleigh waves for different values of ν, the Poisson ratio. Figure 1 presents results for two of them.

Obviously, there is a frequency range for each ν - value, in which each frequency has two different phase velocities. By defining the distance d,

$$d = F_\infty - F_{min} \qquad (3)$$

with F_∞ = frequency value for $C = \infty$, and F_{min} = minimal frequency value of the curve, we have found a measure for the strength of

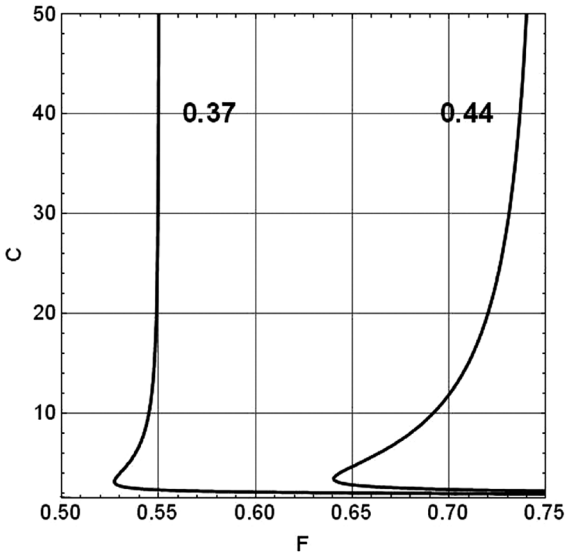

Figure 1. Rayleigh-wave dispersion curves of the first higher mode for the LFB model with ν = 0.37 and ν = 0.44, respectively

the effect under consideration. By using the ordinary formula for the group velocity it would become zero for $F = F_{min}$. This point is known in ultrasonic literature as Zero-Group Velocity (ZGV) point and is subject of voluminous considerations and discussions, which are far beyond the scope of this article. The interested reader may find a good entry into this field e. g. by Negishi (1987) or Prada *et al*. (2009), where dispersion curves of Lamb waves with a very similar shape like our curves in Figure 1 are presented. While plate-structures are known to bear rich features of dispersion, layered structures with seismic velocity monotonously increasing with depth are silently expected to show normal dispersion for all modes, commonly. Kausel (2012) provides a thorough analysis of these phenomena together with an interesting discussion of the occurrence of ZGV-points of higher modes depending on Poisson's ratio. It should be also noted that Lysmer (1970) presented a group velocity curve for a layered model with positive and negative parts in a seismological context, which anyhow gives tentatively evidence in the same direction.

Because d is not accessible analytically it was numerically calculated and depicted in Figure 2.

Apparently, the phenomenon is present in a range approximately $0.19 < \nu < 0.5$ and has its maximum at about $\nu \approx 0.4375 = 7/16$, where the P-wave velocity is the threefold of the S-wave velocity. Therefore, this special behaviour occurs in the whole range of practically important ν- values with preference of higher values.

The special feature continues to appear for the "Layer Over Halfspace" (LOH) model as well, when the impedance contrast between layer and half-space is big enough. For lower impedance contrasts the picture is more complicated and some new effects occur, which are beyond this communication. Let us demonstrate the behaviour of the first higher mode for 2 simplified models TEX1 and TEX2 of the Texcoco region from Malischewsky Auning *et al*. (2006) and Malischewsky *et al*. (2010) with slightly modified parameters. Both models differ in their shear-wave ratios between layer and half-space, which is about 0.0256 for TEX1 and 0.12 for TEX2. The parameters are given in Table 1.

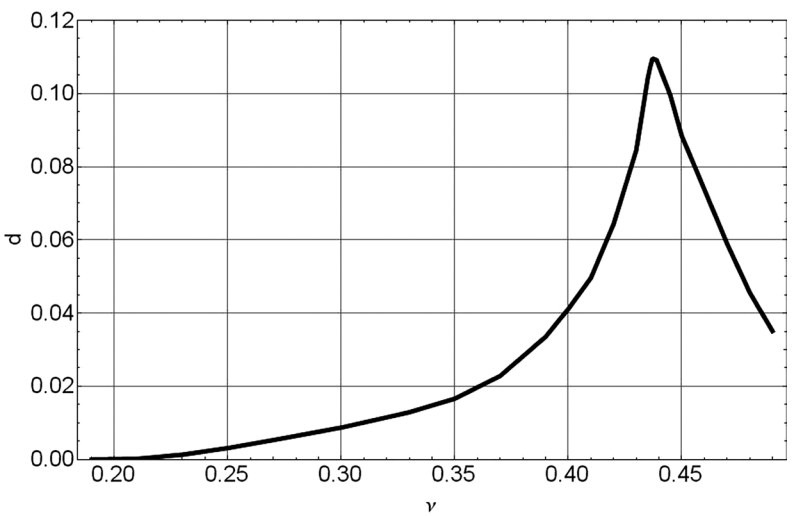

Figure 2. Dependence of d on Poisson's ratio ν.

Table 1. Parameters for the models under consideration: β = shear-wave velocity, ν = Poisson ratio, ρ = density, and h = thickness of the layer.

Model	Layer	β [m/s]	ν	ρ [g/cm^3]	h[m]
TEX1	1	59.2	0.4992	1.1	40
	2	2310	0.2498	2.6	∞
TEX1a	1	59.2	0.4375	1.1	40
	2	2310	0.2498	2.6	∞
TEX2	1	56.5	0.4375	1.1	40
	2	475	0.2498	2.6	∞

Table 1 contains also the model TEX1a, which differs from TEX1 only by a somewhat diminished ν for the layer in order to demonstrate the greater effect in this case, in agreement with Figure 2. It is very likely that some regions, even within Texcoco, have not such an extremely high Poisson ratio as the one in TEX1. The dispersion curves for the models were calculated again with Mathematica, but the secular equation for LOH is by far too voluminous to be given here. The results for all 3 models are included in Figure 3.

The described effect can be seen in a pronounced manner around $F = 0.65$ for TEX1a, but it also occurs in a not so pronounced manner around $F = 0.725$ for TEX1 and a bit weaker for TEX2 with a lower impedance contrast. Such effects appear for multilayered media too, when the impedance contrast at the bottom is high enough. The analytical results of Figure 3 were checked by using two numerical approaches. Namely, the one by Fuchs and Müller (1971), and also, by Schwab and Knopoff (1972) and a perfect coincidence was found. On the other hand, there are computer programs widely used for the calculation of dispersion curves which are simply not fit to handle the special cases described above. Thus, it is advisable in applying numerical schemes to be aware of the occuring peculiarities of dispersion curves under analysis.

Discussion

It is noticed that instead of $C = C(F)$ the inverse function $F = F(C)$ can be considered as a dispersion curve. In this case, an ambiguity will occur for fixed phase velocity with 2 different frequencies when the curve $C = C(F)$ has a local extremum, but this does not happen for the LFB and LOH models. Further, it should be noted that the occurrence of 2

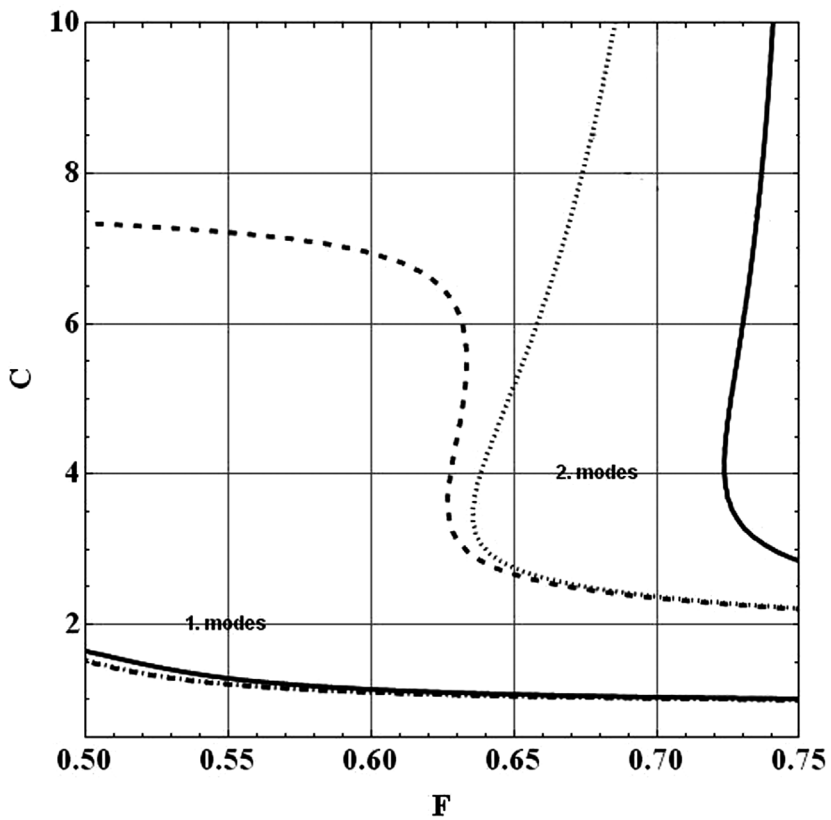

Figure 3. Dispersion curves of the 1. Fundamental, and 2. First higher modes for the models TEX1, TEX1a and TEX2 depicted with solid, dotted, and dashed lines, respectively.

different phase velocities for a fixed frequency generates beats in the wave field. A standard dispersion analysis based on phase differences will inevitably fail in such cases. This analysis approach calculates the phase difference of the seismograms Fourier coefficients at two observation locations divided by the distance between these locations. The reciprocal of this value times the angular frequency is taken as the phase velocity. In the case, an ambiguity would occur the Fourier phase becomes meaningless with respect to phase velocity in the frequency band where three roots of the secular equation exist at each frequency. For the very same reason all methods must fail with the dispersion discussed here which rely on a unique dispersion relation $k_l(\omega)$ for the wavenumber k_l of the l-th surface wave mode. This applies to the deconvolution method used by Sèbe *et al*. (2009) for the extraction of fundamental mode data as well as to phase-matched filter techniques like those presented by Herrin and Goforth (1977) or by Russel *et al*. (1988) for example. Methods of wave field transformation (Forbriger, 2003; McMechan and Yedlin, 1981) however remain applicable for the purpose of dispersion analysis.

Likewise, methods of calculating synthetic dispersion curves might get into trouble. Commonly dispersion curves are constructed by finding the roots of the secular equation starting at the cut-off frequency. Roots for the same overtone are then searched with increasing frequency near the phase velocity value for the previous (smaller) frequency. In the current case the extremum of $F(C)$ causes such algorithms to loose the dispersion curve, which first becomes stationary with frequency and then continue to decreasing frequency values.

So the influence of this special dispersion is two-fold: it produces a special wavefield, whose manifestation and influence for Mexico City has yet to be investigated in the future. On the other hand it requires care in inverting surface wave data for a correct underground model, which for its part is essential for the estimation of the seismic hazard.

The unusual cases described herein suggest care in the analysis of surface waves and may be a warning for the research community to explore these anomalous problems. In other context, the dispersion curves may seem usual but produce slowly attenuating leaky modes for a restricted set of mechanical parameters (García-Jerez and Sánchez-Sesma, 2015).

Conclusions

The special feature "unusual or equivocal dispersion curves", although hardly known in seismology, seems to be rather common for higher mode Rayleigh waves in layered models with sharp impedance contrasts between layers and half-space and sufficiently high Poisson ratios in the layers. Just these conditions are fulfilled in the valley of Mexico City and these dispersion curves influence the surface-wave field and have to be kept in mind in processing the dispersion curves for model-parameter inversion. Although this research was focused on the characteristics of Mexico City soft layers like those found in the ancient Texcoco lake zone, the results are so general and should not be disregarded as exotic, strange phenomena. Certainly, the problem requires further scrutiny.

Ackowledgements

We thank Dr. Tran Thanh Tuan from the University of Hanoi/Vietnam for a discussion about this special behaviour of dispersion curves. Prof. Francisco J Sánchez-Sesma from UNAM, Mexico made useful suggestions and Prof. Eduardo Kausel from MIT, Boston helped us with references in the field of ultrasonics and some explanations.

The support of the DFG in the framework of the project FO 506/1-1 is kindly acknowledged.

References

Flores-Estrella H., Yusim S., Lomnitz C., 2007, Seismic response of the Mexico City Basin: A review of twenty years of research. *Nat. Hazards*, 40, 357-372.

Forbriger T., 2003, Inversion of shallow-seismic wavefields: I. Wavefield transformation. *Geophys. J. Int.*, 153, 719-734.

Fuchs K., Müller G., 1971, Computation of synthetic seismograms with the reflectivity method and comparison with observations. *Geophys. J. R. astr. Soc.*, 23, 417-433.

Furumura T., Kennett B.L.N., 1998, On the nature of regional seismic phases-III. The influence of crustal heterogeneity on the wavefield for subduction earthquakes: the 1985 Michoacan and 1995 Copala, Guerrero, Mexico earthquakes. *Geophys. J. Int*., 135, 1060-1084.

García-Jerez A., Sánchez-Sesma F.J., 2015, Slowly-attenuating P-SV leaky waves in a

layered elastic halfspace. Effects on the coherences of diffuse wavefields, *Wave Motion*, 54, 43–57.

Herrin E., Goforth T., 1977, Phase-matched filters: application to the study of Rayleigh waves. *Bull. seism. Soc. Am.*, 67, 5, 1259–1275.

Kausel E., 2012, Number and location of zero-group-velocity modes. *J. Acoust. Soc. Am.*, 131, 3601-3610.

Kausel E., Malischewsky P., Barbosa J., 2015, Osculations of spectral lines in a layered medium. *Wave Motion*, 56, 22-42.

Lysmer J., 1970, Lumped mass method for Rayleigh waves, *Bull. Seism. Soc. Am.*, 60, 89-104.

Malischewsky Auning P.G., 2004, Report on the stay 08. 02. – 08. 05. 2004, UNAM, Instituto de Geofísica, Mexico, D. F.

Malischewsky Auning P.G., Lomnitz C., Wuttke F., Saragoni R., 2006, Prograde Rayleigh-wave motion in the valley of Mexico. *Geofísica Internacional*, 45, 149-162.

Malischewsky P.G., Zaslavsky Y., Gorstein M., Pinsky V., Tran T., Scherbaum F., Flores Estrella H., 2010, Some new theoretical considerations about the ellipticity of Rayleigh waves in the light of site-effect studies in Israel and Mexico. *Geofísica Internacional*, 49, 141-152.

McMechan G.A., Yedlin M.J., 1981, Analysis of dispersive waves by wave field transformation. *Geophysics*, 46, 869-874.

Negishi K., 1987, Existence of negative group velocities in Lamb waves. *Jpn. J. Appl. Phys.* 26 (1987) Suppl. 26-1, 171-173.

Prada C., Clorennec D., Murray T.W., Royer D., 2009, Influence of the anisotropy on zero-group velocity Lamb modes. *J. Acoust. Soc. Am.* 126, 620-625.

Russel D.R., Herrmann R.B., Hwang H.-J., 1988, Application of frequency variable filters to surface wave amplitude analysis. *Bull. seism. Soc. Am.*, 78, 1, 339–354.

Schwab F., Knopoff L., 1972, Fast surface wave and free mode computations. In: *Methods in Computational Physics, Seismology: Surface Waves and Earth Oscillations.* Ed. by B. A. Bolt. New York and London: Academic Press, 87-180.

Sèbe O., Forbriger T., Ritter J.R.R., 2009, The shear wave velocity underneath Bucharest city, Romania, from the analysis of Love waves*. Geophys. J. Int*., 176, 965-979.

Tran Thanh Tuan, 2009, The ellipticity (H/V-ratio) of Rayleigh surface waves, PhD dissertation, Friedrich-Schiller University Jena, Germany.

Geofísica Internacional (2017) 56-1: 13-26

Original paper

The Mw 7.3 Papanoa, Mexico earthquake of April 18, 2014: Implications for recurrent M > 7 thrust earthquakes in western Guerrero

Carlos Mendoza* and María del Rosario Martínez López

Received: March 24, 2016; accepted: November 11, 2016; published on line: January 01, 2017

DOI: 10.19155/geofint.2017.056.1.2

Resumen

Se aplica un procedimiento de inversión de falla finita para obtener un modelo de deslizamiento del sismo Mw 7.3 de Papanoa, México, del 18 de abril 2014 utilizando ondas de cuerpo telesísmicas de banda ancha. La inversión de ondas P y SH en desplazamiento identifica un modelo de ruptura caracterizado por dos fuentes principales de deslizamiento en la costa noroeste de Guerrero donde también ocurrieron varios sismos de M > 7 en 1943, 1979 y 1985. Una comparación del modelo de deslizamiento de 2014 con las rupturas observadas para los sismos de 1979 y 1985 sugiere que las zonas de alto deslizamiento no coinciden espacialmente, a pesar de la similitud en el tamaño y la ubicación de las áreas de réplicas de los tres eventos. Las zonas de mayor deslizamiento cosísmico se interpretan como asperezas en la frontera entre las placas de Cocos y Norteamérica. El empalme limitado de asperezas entre un evento y otro indica que las caracteristicas de la ruptura para sismos inversos M > 7 en la costa noroeste de Guerrero no se han repetido en los últimos 70 años. Este comportamiento sugiere que es mas probable que sismos futuros de M > 7 involucren áreas en el contacto interplaca ubicadas entre las zonas principales del fallamiento cosísmico observado recientemente. Además, las asperezas observadas y los espacios entre ellas podrían identificar lugares de fallamiento cosísmico en megasismos futuros. Los resultados tienen implicaciones importantes para el potencial sísmico y la recurrencia de sismos de subducción M > 7 además de la simulación del movimiento fuerte esperado para estos eventos.

Palabras clave: propiedades de la fuente sísmica, inversión de falla finita, distribución de asperezas, zona de subducción de México.

C. Mendoza*
Centro de Geociencias
Universidad Nacional Autónoma de México
Campus Juriquilla
Querétaro, México
*Corresponding author: mendozac@geociencias.unam.mx

M.R. Martínez López
Posgrado en Ciencias de la Tierra
Universidad Nacional Autónoma de México
Campus Juriquilla
Querétaro, México

Abstract

We apply a single-step, finite-fault waveform inversion procedure to derive a coseismic slip model for the large MW 7.3 Papanoa, Mexico earthquake of 18 April 2014 using broadband teleseismic body waves. Inversion of the P and SH ground-displacement waveforms yields a rupture model characterized by two principal sources of slip in the northwest portion of the Guerrero coast. The region is also the site of several M > 7 earthquakes in 1943, 1979 and 1985. A comparison of the 2014 slip model with ruptures observed for the 1979 and 1985 earthquakes suggests that the zones of high slip do not spatially coincide, despite similarities in the size and location of their aftershock areas. The zones of high coseismic slip are interpreted to represent asperity areas along the Cocos-North America plate boundary, and their limited spatial overlap from one event to another indicates that the rupture characteristics of recurring M > 7 thrust earthquakes in this portion of western Guerrero have not repeated in the last 70 years. The abutting nature of the asperities suggests that future large M > 7 earthquakes are likely to involve interplate patches between areas where large coseismic failure has been recently observed. Also, the observed asperities and their intervening regions may define locations where seismic failure may occur in future megathrust events. The results have important implications for the potential and recurrence of large M > 7 subduction earthquakes and the estimation of the strong ground motions expected from these events.

Key words: earthquake source properties, finite-fault inversion, asperity distribution, Mexico subduction zone.

Introduction

The Michoacán-Guerrero portion of the Mexico subduction zone has been the site of numerous large M > 7 earthquakes in the last century that have caused significant damage both inland and along the coast (Figure 1). These events generally result from shallow reverse faulting along the Cocos-North America plate boundary and include the recent Mw 7.3 Papanoa earthquake of 18 April 2014 that caused significant damage near the epicenter and minor damage in Mexico City (UNAM Seismology Group, 2015). The Papanoa earthquake is the latest of several large M > 7 subduction events in Michoacán and western Guerrero that includes the Mw 8.0 and Mw 7.5 earthquakes of 19 and 21 September 1985 (Table 1), which resulted in unprecedented damage and loss of life in Mexico City. The 2014 Papanoa earthquake occurred southeast of the 21 September 1985 event, near the epicenters of the Mw 7.4 earthquake of 14 March 1979 and the Ms 7.5 earthquake of 22 February 1943. An Ms 7.0 earthquake on 27 March 1908 had also been considered to be located within this region (e.g., Singh *et al*., 1984a). However, a review of felt and damage reports suggests that it occurred southeast of Acapulco (at 16.3°N, 98.5°W), following the large Ms 7.8 earthquake of 26 March 1908 (UNAM Seismology Group, 2015).

Aftershock areas for the 21 September 1985, the 14 March 1979, and the 22 February 1943 earthquakes appear to at least partially overlap (Figure 2), suggesting that the earthquakes may have ruptured common localized areas of the Cocos-North America plate boundary (UNAM Seismology Group, 2015). Aftershocks located by the Servicio Sismológico Nacional (SSN) in the 3 weeks following the 2014 Papanoa earthquake also extend across the aftershock areas of the 1943, 1979, and 1985 events (Figure 2). Aftershock areas of large earthquakes have generally been used to delineate the location and extent of historical seismogenic ruptures in subduction regions (e.g., Sykes, 1971; Kelleher, 1972; McCann *et al*., 1979; Lay *et al*., 1982). Such qualitative observations are useful for documenting the general earthquake history at subduction zones and evaluating the potential for large damaging events. However, they provide little detailed information on the distribution of interplate rupture during particular earthquakes or the behavior of recurring seismic events. The observed geographic overlap of aftershock areas in western Guerrero, for example, would suggest that recent coseismic rupture has been confined to the same portion of the shallow Cocos-North America plate interface, implying an average recurrence interval of ~24 years for M > 7 thrust earthquakes in the region. However, a more detailed examination of the location of primary slip areas for these events may provide valuable information on the character of large, recurrent earthquakes in the region.

In this study, we derive the coseismic fault slip for the 18 April 2014 Papanoa earthquake and compare with the locations of the rupture areas derived for the 14 March 1979 Petatlán and the 21 September 1985 Zihuatanejo earthquakes to examine the relationship

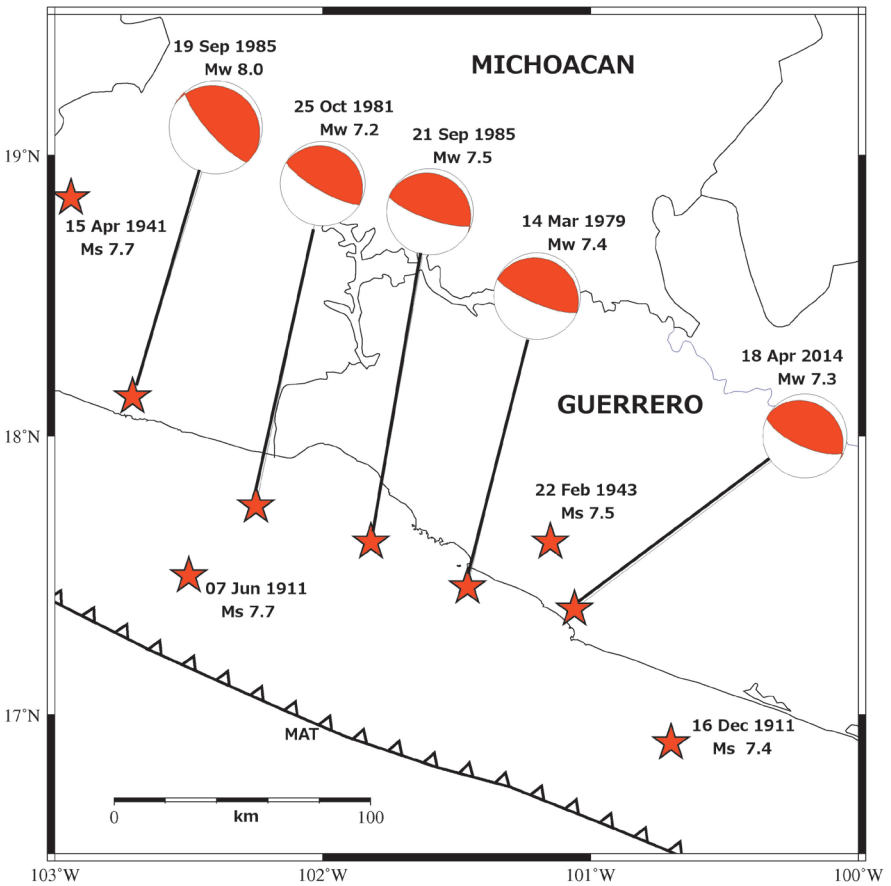

Figure 1. Epicenters (stars) of large, shallow M > 7 earthquakes in the last century along the Michoacán-Guerrero portion of the Mexico subduction zone. Source mechanisms obtained from the Global Centroid Moment Tensor Project catalog (http://www.globalcmt.org) are shown for recent events. MAT = Middle America Trench.

Table 1. M ≥ 7 thrust earthquakes in the Michoacán-Guerrero portion of the Mexico subduction zone (100ºW - 103ºW).

Date (dd-mm-yr)	Lat (º)	Lon (º)	Magnitude
07-jun-1911[0]	17.50	-102.50	7.7 Ms
16-dec-1911[1]	16.90	-100.70	7.4 Ms
15-apr-1941[2]	18.85	-102.94	7.7 Ms
22-feb-1943[2]	17.62	-101.15	7.5 Ms
14-mar-1979[3]	17.46	-101.46	7.4 Mw
25-oct-1981[4]	17.75	-102.25	7.2 Mw
19-sep-1985[5]	18.14	-102.71	8.0 Mw
21-sep-1985[5]	17.62	-101.82	7.5 Mw
18-apr-2014[6]	17.38	-101.06	7.3 Mw

Epicentral locations from: 0, Anderson *et al*. (1989); 1, Singh *et al*. 1984a; 2, Kelleher *et al*. (1973); 3, Gettrust *et al*. (1981); 4, Havskov *et al*. (1983); 5, UNAM Seismology Group (1986); 6, UNAM Seismology Group (2015).

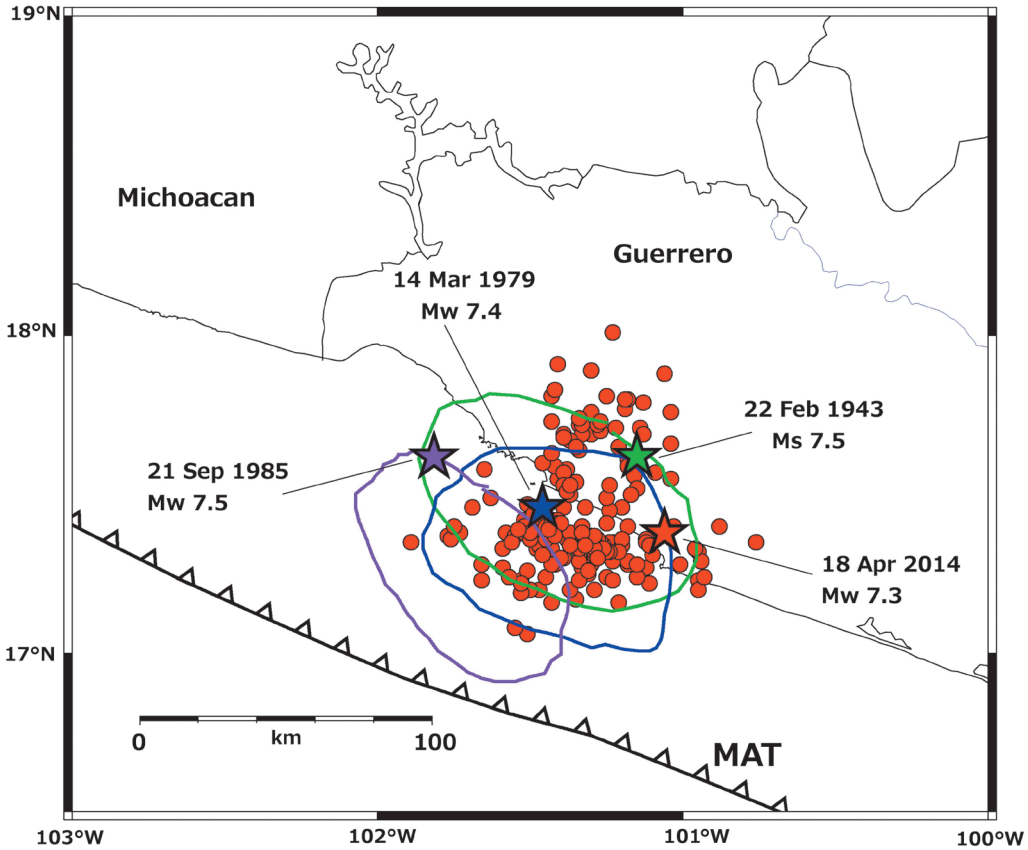

Figure 2. Epicenters (stars) and aftershock areas (ovals) of large, recent M > 7 thrust earthquakes in the Papanoa region. Aftershock areas for the September 21, 1985 (purple) and the March 14, 1979 (blue) earthquakes are from UNAM Seismology Group (1986). The aftershock area of the February 22, 1943 earthquake (green) is from Kelleher *et al*. (1973). Epicenters of Mw > 3 aftershocks (red) located by the Servicio Sismológico Nacional in the 3 weeks following the April 18, 2014 Papanoa mainshock are also shown.

between recurring slip zones along the shallow interplate boundary. We apply a finite-fault waveform inversion procedure to recover a coseismic slip model for the 2014 Papanoa earthquake using an extensive teleseismic, broadband dataset that includes 70 body-wave records. Our comparison of the 2014 Papanoa slip model with rupture areas previously observed for the 1979 Petatlán and 1985 Zihuatanejo earthquakes provides insight on the interaction of interplate asperities for recurring events along this portion of the Cocos-North America plate boundary.

Inversion method

We use the finite-fault inversion scheme developed by Hartzell and Heaton (1983), where the observed seismic waveforms are inverted to recover the coseismic slip on a fault plane of prescribed orientation placed at a specific depth in a given crustal structure. In the finite-fault formulation, the fault dimensions are chosen to encompass the rupture area expected for the known earthquake magnitude. The fault is then divided into a given number of subfaults, and a set of point sources are distributed uniformly across each subfault. Body-wave point-source responses (Green´s functions) are calculated at each recording station using a boxcar source-time function of finite duration. Generalized ray theory (Helmberger and Harkrider, 1978) is used to calculate the Green´s functions for a layered, near-source crustal structure. These include internal reflections and mode conversions, incorporating depth-phase contributions to the body waves. In this study, we use a layered structure derived from the gradient velocity model developed by Stolte *et al*. (1986) for the Michoacán-Guerrero region.

Synthetic waveforms are then constructed for each subfault at all the recording sites by

summing the point-source responses, taking into account the appropriate time delays for a rupture front propagating at a prescribed speed across the fault. The synthetic records constructed for each subfault are placed end-to-end to form the columns of a matrix A of subfault synthetics. The observed waveforms recorded at all the stations are also placed end-to-end to form a data vector b. Together, these form an overdetermined system of linear equations Ax=b where the elements of the solution vector x represent the slips required of each subfault to reproduce the observations. Multiple slip intervals are accommodated by adding columns to the A matrix constructed by successively lagging the subfault synthetics by the width of the boxcar source-time function. This results in a specified number of time windows that discretize the rise time on the fault. The inversion then recovers the slip in each subfault for each of the specified time windows, thus identifying a long rise time if required by the observations.

The inverse problem is stabilized by adding constraint equations of the form $\lambda F_n x = 0$ to the linear system,

$$\begin{bmatrix} C_d^{-1} A \\ \lambda F_1 \\ \lambda F_2 \end{bmatrix} \mathrm{x} = \begin{bmatrix} C_d^{-1} b \\ 0 \\ 0 \end{bmatrix}$$

where F_1 corresponds to the difference in slip between adjacent subfaults, and F_2 is the identity matrix. The former imposes a smooth transition of slip from subfault to subfault, and the latter reduces the length of the x vector, effectively minimizing the total seismic moment. The value of λ controls the tradeoff between applying the constraints and fitting the observations, and C_d^{-1} is a data covariance matrix that normalizes each station record to its maximum amplitude.

In the teleseismic inversion problem, errors in the epicentral location of the rupture initiation point do not affect the resulting slip model since differences in location due to these errors have a minimal effect on the teleseismic Green´s functions. That is, the solution is obtained strictly from the timing of waveform contributions following the initial P-wave arrival at each of the recording sites, and teleseismic slip models derived using the methodology can be simply moved over along the fault to coincide with an epicentral location that is believed to be more accurate. Errors in the hypocenter depth, however, are more important since different depths result in synthetic waveforms with depth-phase contributions arriving at different times following the direct P arrival. Fault-depth uncertainties can generally be reduced by performing several inversions at different hypocentral depths and selecting the solution with the lowest Euclidean Norm ||Ax - b||, which provides a direct measure of the fit to the observed waveforms.

The inversion method of Hartzell and Heaton (1983) has historically been performed by iteratively incrementing the smoothing value λ until the waveform fits become visibly degraded in an effort to identify the simplest solution that satisfies the observations. However, Mendoza and Hartzell (2013) showed that the amount of stabilization to apply can be estimated directly from the inverse problem using the relation $\lambda=90|a|_{avg}$, where $|a|_{avg}$ is the average of the absolute values of the elements of the coefficient matrix $C_d^{-1}A$. This smoothing estimate is comparable to the value obtained using the visual iterative approach, yielding a more timely calculation of the distribution of coseismic slip. In this study, we use the Mendoza and Hartzell (2013) relation to estimate the degree of smoothing to use in the inversion of the teleseismic body waveforms, recovering the rupture model in a single step.

2014 Papanoa Slip Model

We invert the broadband, teleseismic P and SH waveforms recorded for the 2014 Papanoa earthquake by the Global Seismographic Network, obtained from the Incorporated Research Institutions for Seismology (IRIS) Data Center (http://www.iris.edu). The data include 43 vertical P-wave records from stations located 25º-95º from the earthquake epicenter and 27 SH waveforms obtained by rotating the horizontal components to their source-station azimuths for recording sites located at distances of 40º-80º (Table 2). We use the epicenter computed by the UNAM Seismology Group (2015) using local P-wave arrival times and source-station azimuths. Observed P and SH records were deconvolved to ground displacement, resampled to a time step of 0.25s, and passband-filtered between 1 and 60s. The waveforms were then windowed to 70s record lengths, and an exponential taper was applied 40s after the record start time to minimize the mapping of non-source related effects onto the fault.

The fault geometry (300º strike, 23º dip, and 95º rake) is based on the source parameters derived from a W-phase analysis

Table 2. Teleseismic P and SH records used in source inversion

Station	Distance (°)	Azimuth (°)	Wave Type	Station	Distance (°)	Azimuth (°)	Wave Type
ADK	67.7	-40.5	P	SAML	45.7	122.0	P
AFI	76.4	-109.4	P	SDDR	28.3	82.1	P
BBSR	36.0	58.6	P	SDV	30.8	102.0	P
BFO	89.5	39.0	P	SFJD	59.2	20.7	P
BILL	75.0	-22.9	P, SH	SJG	33.2	83.3	P
BORG	70.1	26.7	P	SSPA	30.6	36.0	P
CMB	26.7	-35.6	P	TIXI	85.0	-14.1	P
CMLA	68.3	55.7	P	YAK	91.3	-21.4	P
COLA	56.8	-21.8	P	YSS	94.2	-38.0	P
COR	32.9	-29.8	P	ANM	63.5	-25.8	SH
EFI	78.3	154.3	P	BBB	40.8	-25.4	SH
ESK	80.3	35.1	P	BERG	52.7	-25.0	SH
FFC	37.3	-0.9	P	BESE	48.5	-23.1	SH
GRGR	38.4	92.3	P	CNP	55.5	-28.4	SH
GRTK	28.5	76.8	P	CRQ	52.6	-24.4	SH
HOPE	90.0	148.0	P	EYAK	53.6	-25.6	SH
HRV	35.5	38.9	P	GHO	55.6	-25.3	SH
KBS	77.4	10.5	P	JIS	47.7	-23.1	SH
KDAK	55.3	-30.7	P	LPAZ	46.6	134.1	SH
KEV	85.8	15.9	P	MID	53.2	-27.0	SH
KONO	85.1	28.5	P	MPG	48.9	98.5	SH
LVC	50.7	140.5	P	NIUE	76.8	-115.0	SH
LVZ	89.1	15.3	P	PEL	58.0	150.0	SH
MA2	84.0	-29.1	P	PLCA	64.4	154.7	SH
MACI	77.3	64.2	P, SH	PNL	50.5	-24.1	SH
MSVF	86.9	-109.5	P	PPTF	59.0	-123.6	SH
NNA	37.7	139.0	P	PTPK	52.7	-23.8	SH
NV31	25.8	-32.1	P	SIT	47.2	-24.8	SH
PAB	84.1	50.5	P	SKAG	48.8	-22.5	SH
PET	82.3	-36.9	P	SPB	66.3	126.2	SH
PTGA	44.3	109.7	P	SSP	52.2	-24.9	SH
RCBR	68.3	103.7	P	TAOE	46.6	-120.9	SH
RSSD	26.8	-4.8	P	TGL	52.5	-24.3	SH
SACV	73.9	79.0	P	WAT7	56.1	-24.2	SH

of the regional broadband waveforms (UNAM Seismology Group, 2015) and is consistent with a shallow, northeast-dipping thrust along the Cocos-North America plate boundary. The fault dimensions are 100 km x 100 km, and the fault is divided into 400 5 km x 5 km subfaults. The hypocenter is 40 km from the top and 30 km from southeast edge of the fault, and a boxcar of 1s duration is used to calculate the point-source Green´s functions. A rupture velocity of 2.6 km/s is used to construct the subfault synthetics, corresponding to about 70% of the average shear-wave speed in the assumed near-source crustal structure. Ten time-windows are used in the inversion, allowing up to 10s for the rise time on the fault.

We test several nucleation depths to constrain the depth of the fault. Table 3 gives estimates of the misfit between observed and predicted waveforms for several hypocentral depths, as measured by the Euclidean norm ||Ax-b|| obtained in the inversion. The best fit is obtained for a depth of 18 km, which coincides with the focal depth computed by the SSN for the earthquake (UNAM Seismology Group, 2015). The resulting slip model (Figure 3) shows two distinct sources of large slip separated by about 10 km: a 30 km x 30 km area near the hypocenter with a peak slip of 2.2 m and a second 20 km x 35 km source to the northwest with a peak slip of 1.9 m.

Table 3. Inversion results for different hypocentral depths.

Depth (km)	Euclidean Norm (||Ax-b||)
16	21.15
18	20.97
20	21.47
22	22.43
24	23.96

The waveform fits (Figure 4) correspond to an estimated seismic moment of 1.0 x 10^{27} dyne-cm (Mw 7.3). A rise time of 2-4s is estimated for both zones of maximum slip. Five 1s time windows would therefore be sufficient to recover the teleseismic source model. An inversion of the P and SH data recorded for the Papanoa earthquake using five, instead of ten, time windows yields a fault-slip distribution that is practically identical to that shown in Figure 3.

The UNAM Seismology Group (2015) obtained a similar slip model for the 2014 Papanoa earthquake from an inversion of the teleseismic body waves, the recorded surface waves, and geodetic measurements from two near-source sites. Their slip model also shows two areas of coseismic slip separated by 10 km along the fault, one near the hypocenter with a peak slip of about 2 m and a second source with a peak slip of about 1.7 m located updip and to the northwest. They obtain a seismic moment of 8.3 x 10^{26} dyne-cm from the body- and surface-wave records (UNAM Seismology Group, 2015).

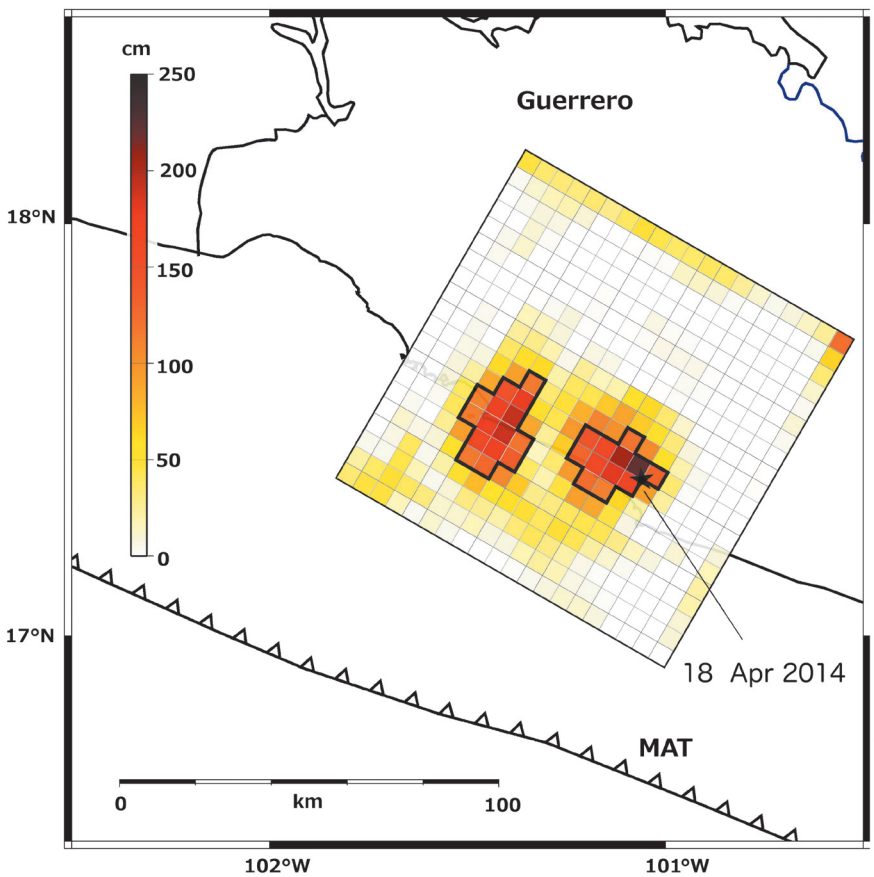

Figure 3. Coseismic slip (in cm) derived in this study for the April 18, 2014 Papanoa earthquake projected to the surface based on the location of the earthquake epicenter (star). The fault is divided into 400 5-km x 5-km subfaults and strikes at 300º with a 23º dip to the northeast. The black polygons outline subfaults with slip greater than 50 percent of the maximum slip of 2.2 m observed near the hypocenter.

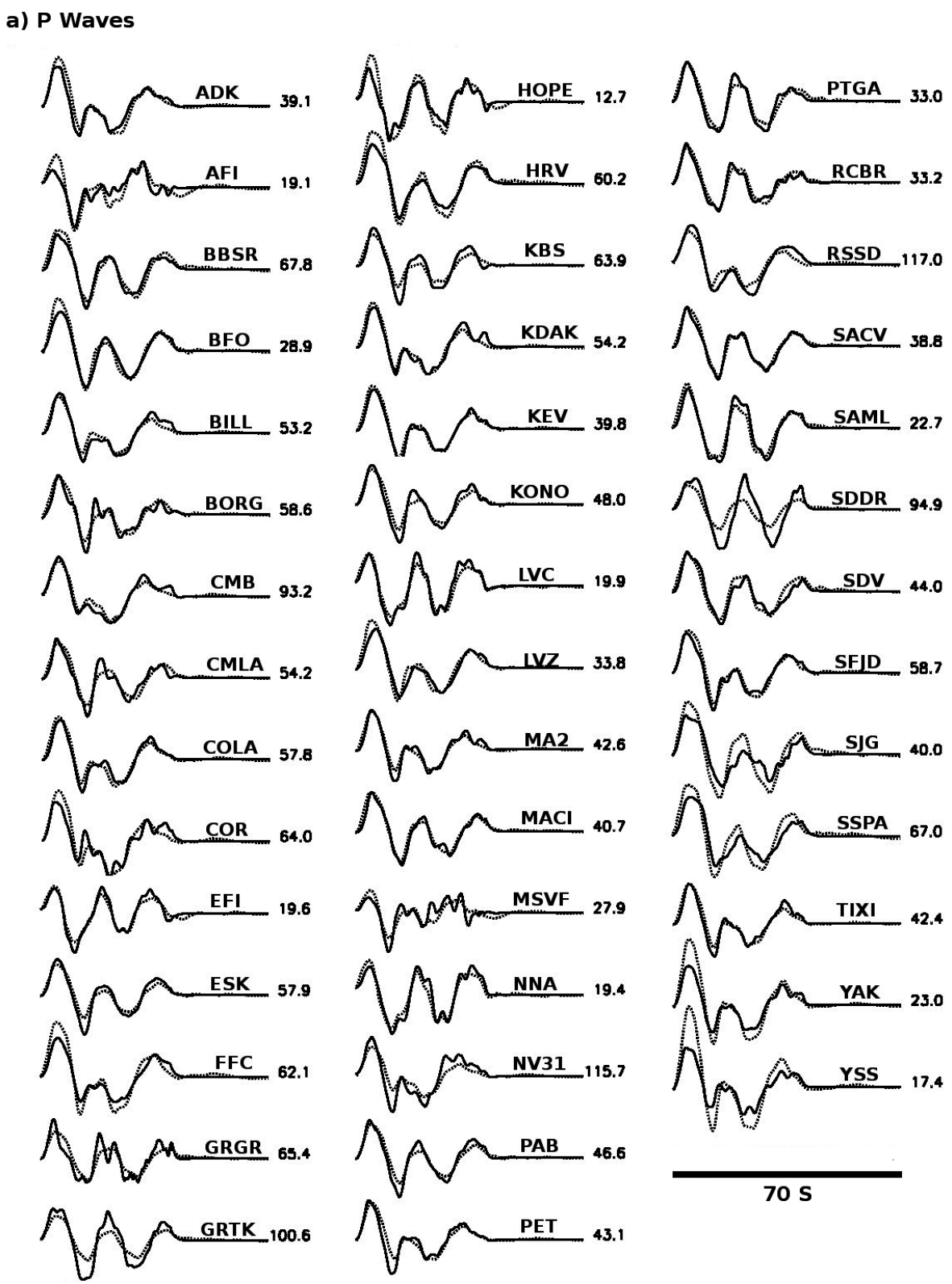

Figure 4. a) P and b) SH waveform fits between observed (solid) and theoretical (dotted) records for the 2014 Papanoa source model shown in Figure 3. Observed peak amplitudes (in microns) are shown to the right for each station. Waveform fits correspond to a seismic moment of 1.0 x 10^{27} dyne-cm.

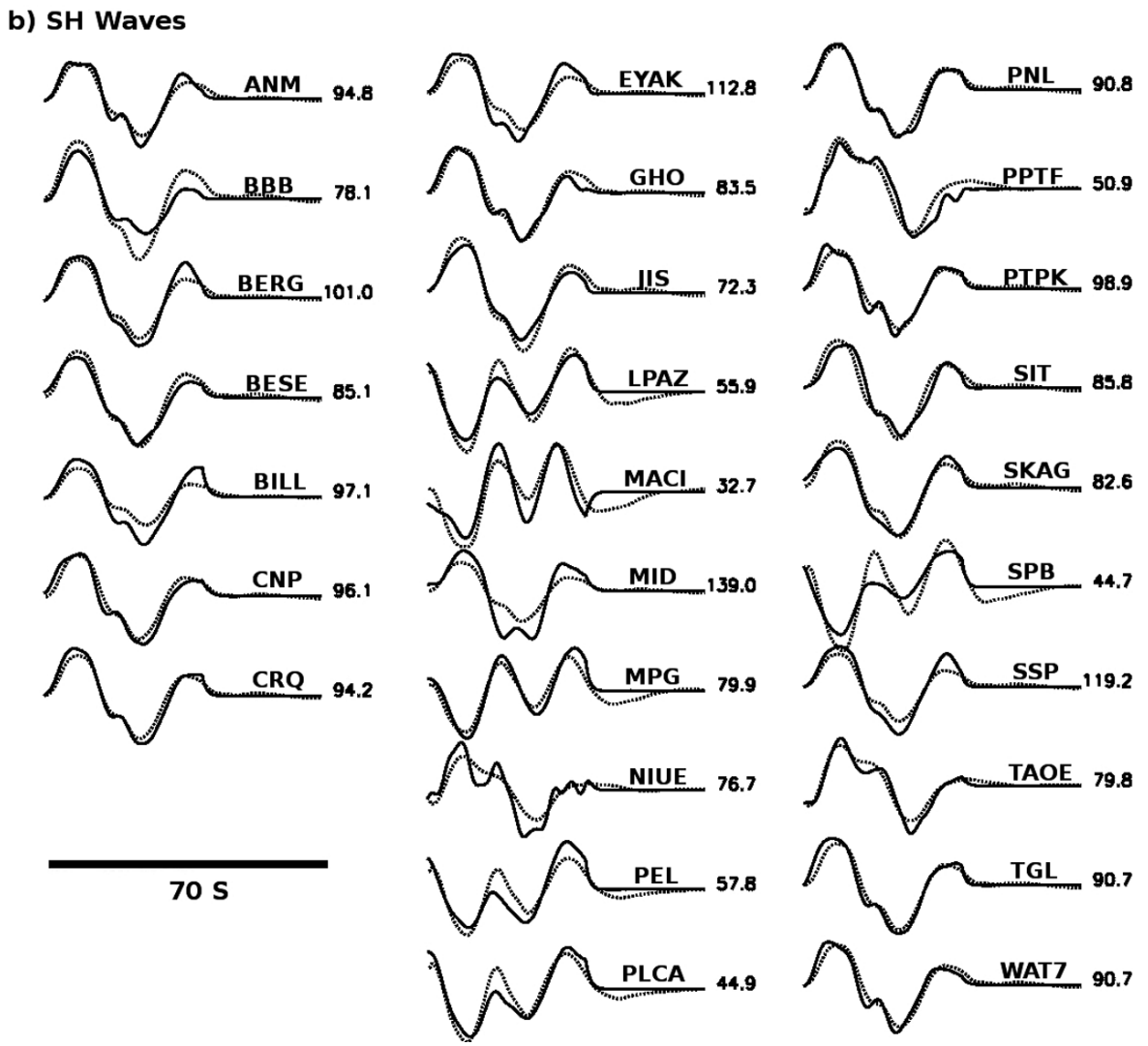

Figure 4. (Continue).

Other interplate ruptures in western Guerrero

As mentioned earlier, the 2014 Papanoa earthquake is located near the site of several M > 7 earthquakes that occurred on 22 February 1943, 14 March 1979, and 21 September 1985. The earthquake of 1943 occurred before the modern instrumental era, and there is not enough information to allow a detailed study of its rupture extent or slip distribution. Modeling of analog P waveforms recorded at European seismograph stations, however, indicate significant differences between the event and the earthquakes of 1979 and 1985 (Singh *et al*., 1984b; Singh and Mortera, 1991). Source time functions calculated for the 1943 earthquake at stations DBN (DeBilt, Holland) and STU (Stuttgart, Germany) are more complex, showing the contribution of 4 to 6 subevents (Singh and Mortera, 1991). This is in contrast to the 1979 and 1985 recordings, which indicate a simpler rupture process (Singh and Mortera, 1991).

For the March 1979 Petatlán and the September 1985 Zihuatanejo earthquakes, Mendoza (1993; 1995) derived the extended source properties using the finite-fault methodology utilized in this study, although the procedure was slightly different. For the 1979 Petatlán earthquake, Mendoza (1995) applied the multiple time-window approach using five time windows of 1s duration, allowing up to 5s for the rise time on the fault. The slip model shows a large 70 km x 70 km rupture area with a small source (70-cm peak) near the hypocenter and a larger source (1.2-m peak)

about 10 km to the southeast (Figure 5a). The source model was obtained from the inversion of 19 digital and analog teleseismic P waveforms that include long-period, broadband, and short-period records (Mendoza, 1995). For the 1985 Zihuatanejo earthquake, Mendoza (1993) used a single 1s triangular source time function to parameterize the fault, invoking a fixed rupture velocity and a short 1s rise time that may not be long enough for an event of this size.

Our goal is to conduct a consistent comparison between interplate ruptures in the region, and we analyze the teleseismic body waveforms recorded for 1985 earthquake using the multiple-time window approach to allow a comparable flexibility in the fault rise time. We inverted 13 long- and intermediate-period P waveforms and 4 intermediate-period SH records obtained from the IRIS Data Center for the event. The dataset is similar to that used by Mendoza (1993), who included 14 broadband and intermediate-period P waveforms and 5 intermediate-period SH records. In our analysis, we deconvolved the records to ground displacement and processed them in the same manner as the Papanoa data. We used a 100 x 100 km fault divided into 5 km x 5 km subfaults, keeping the same geometry (300° strike, 14° dip, 90° rake), hypocentral depth (20 km), and subfault rupture velocity (2.6 km/s) used by Mendoza (1993). We then performed the inversion using five 1s time windows to allow up to 5s for the rise time on the fault. The resulting slip model (Figure 5b) shows rupture dimensions similar to those observed by Mendoza (1993), with the majority of the slip located just southeast of the hypocenter. Our result, however, shows slip to be concentrated primarily in the downdip portion of the fault, rather than both updip and downdip of the hypocenter. A peak slip of 2.9 m is observed at a depth of about 24 km.

The slip models of the 1979 Petatlán, the 1985 Zihuatanejo, and the 2014 Papanoa earthquakes show distinct source regions where coseismic slip is concentrated along the plate interface during the rupture process. These sources are interpreted to represent asperity zones that fail coseismically, radiating the primary portion of the seismic-wave energy recorded at the far-field observation sites. The asperities are presumably surrounded by weak intervening regions of low relative slip that contribute significantly less seismic energy at the seismic stations. Together, the stronger asperities and intervening areas of low slip map the overall rupture area of the earthquake (e.g., Kanamori, 1981; Lay *et al*., 1982). In

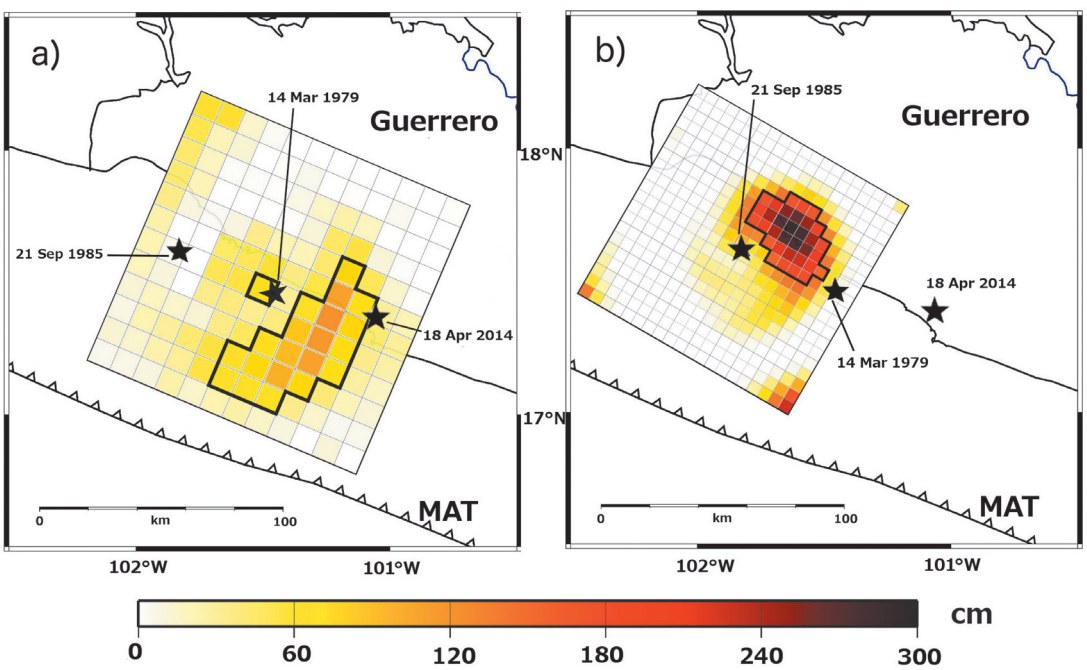

Figure 5. Distribution of coseismic slip for a) the March 14, 1979 Petatlán and (b) the September 21, 1985 Zihuatanejo earthquakes shown projected to the surface relative to the epicenter of the 2014 Papanoa earthquake. The 1979 slip model was obtained by Mendoza (1995) using 144 10-km x 10-km subfaults and has a peak slip of 1.2 m. The slip model of the 1985 Zihuatanejo earthquake was derived in this study using 400 5-km by 5-km subfaults and has a peak slip of 2.9 m. Black polygons outline subfaults with slip greater than 50 percent of the peak observed for each event.

this respect, the entire rupture area excites the longer-period seismic-wave energy that is used to characterize the seismic moment of the earthquake.

To examine the failure of these asperities and their behavior over different earthquake cycles, we compare the principal rupture areas observed for the 1979 Petatlán, the 1985 Zihuatanejo, and the 2014 Papanoa earthquakes along the northwestern portion of the Cocos-North America plate boundary. There is an appreciable overlap between the overall slip areas of the 1979 and 2014 earthquakes, making it difficult to simply overlay the slip models along the coast. We thus plot the locations of the regions of high slip observed for each event, defined by values greater than 50 percent of the maximum and constrained by the corresponding earthquake epicenters (Figure 6). The epicenter of the 1979 Petatlán earthquake was obtained by Gettrust *et al*. (1981) using local P and S arrival times. For the 1985 Zihuatanejo earthquake, the epicenter was obtained by the UNAM Seismology Group (1986) using body-wave arrival times from 12 local seismic stations. The 2014 Papanoa epicentral location was recomputed by the UNAM Seismology Group (2015) using local source-station azimuths and P arrival times. These are the most accurate epicenters available to date for all three events, and our comparison provides a direct examination of the rupture locations and asperities along the plate interface. We assume that the epicenters obtained using local data represent the rupture-nucleation points used to invert the teleseismic records. Large subduction earthquakes, however, sometimes exhibit low-amplitude, emergent beginnings that are not well recorded at teleseismic distances. Small precursors and emergent features, for example, have been previously observed for the 1979, 1985 and 2014 earthquakes (Mendoza, 1993; 1995; UNAM Seismology Group, 2015). Detailed studies of the effect of these features on the relative location of the principal coseismic slip have yet to be undertaken, although they may help define more precisely the position of large earthquake ruptures along the plate boundary.

The high-slip zones of the three events differ in size and shape and do not occupy the same position along the plate interface (Figure 6). The areas of high slip observed for the 1979 and 1985 ruptures are located at or near the edges of the regions of high slip that were observed during the 2014 Papanoa earthquake, 30-35 years later. High slip in 1979 appears to overlap the hypocentral source of 2014 ; however, we see from Figure 5a that this 2014 source is located at the lower downdip margin of the highest slip observed in 1979. The second 2014 source of high slip to the northwest is located near, but does not coincide with, the small region of high slip observed in 1979 near the Petatlán hypocenter. This second 2014 source, in fact, appears to straddle the intervening region between the highest-slip area observed in 1979 and the principal rupture area of the 1985 Zihuatanejo earthquake to the northwest. Also, aftershocks

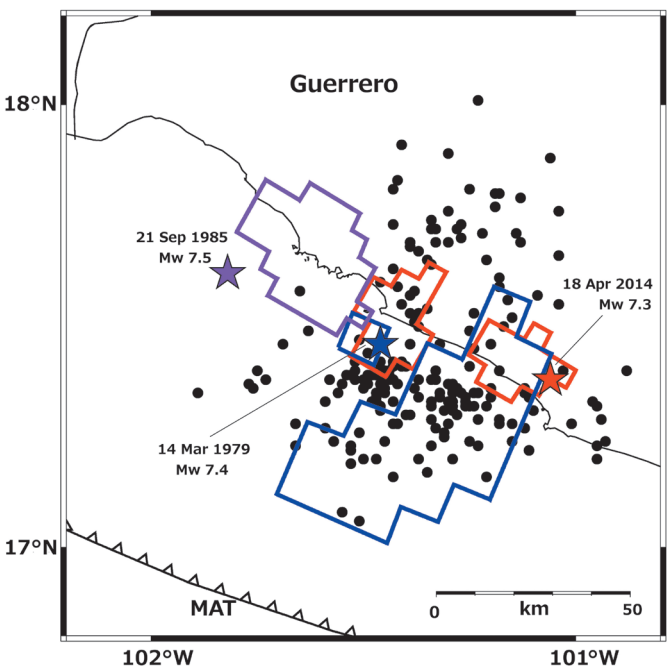

Figure 6. Regions of high slip observed for the 2014 Papanoa (red), the 1985 Zihuatanejo (purple), and the 1979 Petatlán (blue) earthquakes represented by areas of slip greater than 50 percent of the peak for each event. Also shown are the 3-week aftershocks located by the SSN following the 2014 Papanoa mainshock.

of the 2014 Papanoa earthquake occur landward and seaward of the 2014 asperities and within the rupture zone of the 1979 earthquake, showing the limitations of using aftershock distributions to study the details of recurring interplate ruptures.

The principal areas of slip for all three events thus appear to abut, rather than coincide, suggesting that different localized portions of the plate interface were responsible for the observed seismic-wave radiation. To further examine this hypothesis, we reviewed the waveforms recorded for the 1979 Petatlán and 2014 Papanoa earthquakes at common teleseismic distances. In particular, we compared the short-period, P-wave ground-velocity records observed at stations ZOBO, MAJO and KONO for the 1979 earthquake with equivalent P waveforms recorded for the 2014 event (Figure 7). The 2014 waveforms were obtained by deconvolving the instrument response from the broadband, vertical records and applying the same 0.08-5 Hz Butterworth bandpass filter used by Mendoza (1995) to filter the 1979 short-period records at ZOBO, MAJO and KONO. The P waveforms observed at the three stations within this frequency range differ dramatically for the two earthquakes, indicating distinctly different rupture characteristics.

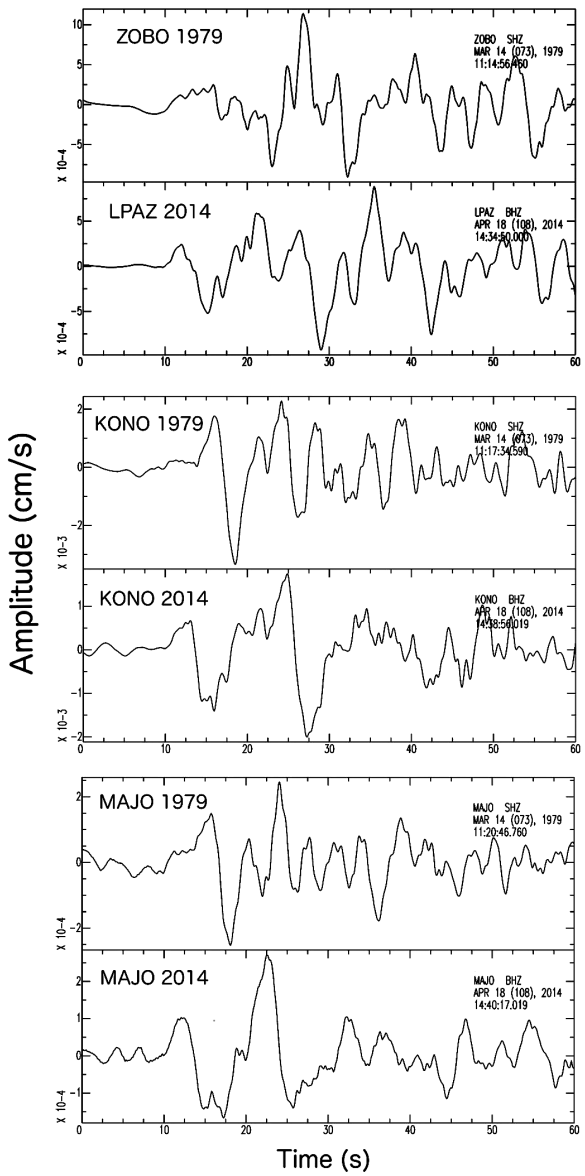

Figure 7. Comparison between the short-period, P-wave ground-velocity records observed for the 1979 Petatlan earthquake and the equivalent P waveforms recorded for the 2014 Papanoa earthquake at stations ZOBO (top frame), KONO (middle frame) and MAJO (bottom frame). The 2014 waveforms shown were obtained by removing the instrument response from the broadband, vertical records at LPAZ, KONO and MAJO and then applying the same 0.08-5 Hz Butterworth bandpass filter used on the 1979 records. The LPAZ station location is very similar to the ZOBO site.

Conclusions and discussion

We have conducted a single-step finite-fault inversion of the high-quality, digital, teleseismic broadband body waves recorded for the Mw 7.3 Papanoa, Mexico earthquake of 18 April 2014 to recover a detailed rupture model for the event. We inverted 43 P-wave and 27 SH records to derive a coseismic slip model characterized by two principal sources of similar extent (700-900 km^2 area) and slip amplitude (~2-m peak). The sources are interpreted to represent asperity areas along the shallow Cocos-North America plate boundary that contribute the primary portion of the body-wave energy recorded at the teleseismic stations. A comparison of these 2014 asperities with principal slip sources identified for two previous M > 7 thrust earthquakes indicates that the asperities of the three events do not coincide, despite the similarities and proximity in aftershock area locations.

The two previous events are the Mw 7.4 Petatlán earthquake of 14 March 1979 and the Mw 7.5 Zihuatanejo earthquake of 21 September 1985. The slip model of the 1979 Petatlán earthquake was previously obtained by Mendoza (1995) from an inversion of teleseismic P waves using a multiple time-window parameterization similar to that used to analyze the 2014 Papanoa earthquake. Mendoza (1993) also derived a slip model for the 1985 Zihuatanejo earthquake from the

teleseismic P waves, although the analysis did not allow for a variable rise time. To assure a more consistent comparison, we analyzed the digital teleseismic P and SH waves recorded for the 1985 Zihuatanejo earthquake using the same multiple time-window approach used to study the 1979 and 2014 earthquakes. The slip models of the three events allow a consistent examination of the asperity locations along this portion of the Mexico subduction zone.

The abutting nature of the principal slip zones implies that the same asperity areas did not fail from one earthquake to another. This conclusion is supported by the dissimilar character of the short-period teleseismic waveforms observed for the 1979 and 2014 earthquakes. The source time functions calculated at European stations by Singh *et al*. (1984b) and Singh and Mortera (1991) also suggest differences in the rupture process between the February 1943 earthquake and the more recent 1979 and 1985 events. Singh and Mortera (1991), for example, noted that the different results obtained for the 1943 and 1979 earthquakes could be due to differences in the rupture characteristics of the earthquakes within the same interplate area. The adjoining rather than coincident behavior of the asperity zones would be at odds with the idea that the rupture process in the Petatlán region repeats every 35 years, as might be inferred from the observed overlap in aftershock areas in 1943, 1979, and 2014. Instead, it would indicate that we have yet to observe a repeat of similar large M > 7 earthquakes along the western Guerrero portion of the Mexico subduction zone. Thus, if we additionally consider the rupture models inferred for the 25 October 1981 Mw 7.2 Playa Azul and the 19 September 1985 Mw 8.0 Michoacán earthquakes (Mendoza, 1993), we see that high-slip zones for recent M > 7 earthquakes have generally been filling in the shallow-dipping contact between the Cocos and North America plates, and the question arises as to whether these asperity zones will fail again individually in the future or as an ensemble of asperities that will produce a much larger, possibly megathrust event. In this regard, perhaps the intervening regions between asperities can serve to locate potential regions of high slip during future M > 7 earthquakes. Thus, if we can map the asperity zones for previous M > 7 earthquakes and identify intervening zones that could fail in future earthquakes, we may be able to identify the character of great megathrust events produced by a single simultaneous failure of all or many of the asperities along the plate boundary.

To the extent that the hypocenters of the 1979, 1985 and 2014 events are well-determined and the corresponding slip models well-resolved, the results have important implications for the rupture and re-rupture of interplate boundaries in subduction regions. Finite-fault studies and synthetic tests conducted to date indicate that broadband teleseismic data can be used to derive accurate coseismic slip models that are relatively insensitive to uncertainties in rupture velocity and fault rise time. The slip models are affected mostly by errors in the dip and depth of the fault due to greater inaccuracies in the computed Green´s functions (Mendoza *et al*., 2011; Mendoza and Hartzell, 2013). A more complete examination of these possible errors may provide a more quantitative assessment of the expected variations in asperity size and location along subduction margins.

Our results suggest that sequential plate-interface ruptures do not involve the failure of the same asperity zones and do not constitute characteristic earthquakes that repeat in a periodic manner from one seismic cycle to another. This may account for some of the difficulty encountered in forecasting seismic potential based on the simple tabulation of numbers of earthquakes above a certain size along subduction margins (e.g., Rong *et al*., 2003). Although there is a limited amount of seismic waveform data available for large M > 7 subduction earthquakes prior to the age of digital instrumental recording (since ~1980), it would be beneficial to study the extended source properties of these earlier events to examine the behavior of asperity regions over more than one earthquake cycle. Such detailed information on the episodic nature of asperity rupture would be of great value in the evaluation of the potential for large earthquake occurrence along subduction zones. The results would also have important implications for the simulation of ground motion from recurring thrust earthquakes along a plate boundary. Since the asperity zones are defined by areas of high slip, their size and distribution along the plate interface would have a significant impact on the radiation of the higher-frequency seismic-wave energy that controls the near-field and regional strong motions.

Acknowledgments

This paper was greatly improved by valuable comments provided by three anonymous reviewers. Support for this work was provided by DGAPA/PAPIIT Project IN104013 and by the CONACYT graduate-assistance program.

References

Anderson J.G., Singh S.K., Espíndola J.M., Yamamoto J., 1989, Seismic strain release in the Mexican subduction thrust, *Phys. Earth Planet. Int.,* 58, *307–322*.

Gettrust J., Hsu V., Helsley C.E., Herrero E., Jordan T., 1981, Patterns of local seismicity preceding the Petatlán earthquake of 14 March 1979, *Bull. Seism. Soc. Am. 71, 761-769*.

Hartzell S.H., Heaton T.H., 1983, Inversion of strong ground motion and teleseismic waveform data for the fault rupture history of the 1979 Imperial Valley, California, earthquake, *Bull. Seism. Soc. Am., 73, 1553-1583*.

Havskov J., Singh S.K., Nava E., Domínguez T., Rodríguez M., 1983, Playa Azul, Michoacán, Mexico earthquake of 25 October 1981 (Ms = 7.3), *Bull. Seism. Soc. Am. 73, 449-457*.

Helmberger D.V., Harkrider D., 1978, Modeling earthquakes with generalized ray theory, in *Modern Problems in Elastic Wave Propagation*, J. Miklowitz and J. D. Achenbach (Eds.), John Wiley and Sons, New York.

Kanamori H., 1981, The nature of seismicity patterns before major earthquakes, in *Earthquake Prediction, an International Review*, Maurice Ewing Series IV, D.W. Simpson and P.G. Richards (Eds.), American Geophysical Union, Washington D.C., 1-19.

Kelleher J.A., 1972, Rupture zones of large South American earthquakes and some predictions, *J. Geophys. Res. 77, 2087-2103*.

Kelleher J., Sykes L., Oliver J., 1973, Possible criteria for predicting earthquake locations and their application to major plate boundaries of the Pacific and the Caribbean, *J. Geophys. Res. 78, 2547-2585*.

Lay T., Kanamori H., Ruff L., 1982, The asperity model and the nature of large subduction zone earthquakes, *Earth. Pred. Res. 1, 3-71*.

McCann W.R., Nishenko S.P., Sykes L.R., Kraus J., 1979, Seismic gaps and plate tectonics: Seismic potential for major boundaries, *Pageoph 117, 1087-1147*.

Mendoza C., 1993, Coseismic slip of two large Mexican earthquakes from teleseismic body waveforms: Implications for asperity interaction in the Michoacán plate boundary segment: *J. Geophys. Res. 98, 8197- 8210*.

Mendoza C., 1995, Finite-fault analysis of the 1979 March 14 Petatlán, Mexico, earthquake using teleseismic P waveforms, *Geophys. J. Int. 121, 675-683*.

Mendoza C., Hartzell S., 2013, Finite-fault source inversion using teleseismic P waves: Simple parameterization and rapid analysis, *Bull. Seism. Soc. Am. 103, 834-844*.

Rong Y., Jackson D.D., Kagan Y.Y., 2003, Seismic gaps and earthquakes, *J. Geophys. Res. 108(B10), 2471, doi:10.1029/2002JB002334.*

Singh S.K., Rodríguez M., Espíndola J.M., 1984a, A catalog of shallow earthquakes of Mexico from 1900 to 1981, *Bull. Seism. Soc. Am. 74, 267–279*.

Singh S.K., Domínguez T., Castro R., Rodríguez M., 1984b, P waveform of large, shallow earthquakes along the Mexican subduction zone, *Bull. Seism. Soc. Am. 74, 2135–2156*.

Singh S.K., Mortera F., 1991, Source time functions of large Mexican subduction earthquakes, morphology of the Benioff zone, age of the plate, and their tectonic implications, *J. Geophys. Res. 96, 21,487–21,502*.

Stolte C., McNally K.C., González-Ruiz J., Simila G.W., Reyes A., Rebollar C., Munguia L., Mendoza L., 1986, Fine structure of a post-failure Wadati-Benioff zone, *Geophys. Res. Lett., 13, 577-580.*

Sykes L.R., 1971, Aftershock zones of great earthquakes, seismicity gaps, and earthquake prediction for Alaska and the Aleutians, *J. Geophys. Res. 76, 8021-8041*.

UNAM Seismology Group, 1986, The September 1985 Michoacán earthquakes: Aftershock distribution and history of rupture, *Geophys. Res. Lett. 13, 573-576*.

UNAM Seismology Group, 2015, Papanoa, Mexico earthquake of 18 April 2014 (M_W 7.3), *Geof. Int. 54-4, 363-386*.

Geofísica Internacional (2017) 56-1: 27-36

Original paper

Evaluation of macroseismic intensities in Mexico from recent earthquakes using *¿Sintió un sismo? (Did you feel it?)*

Juan C. Montalvo-Arrieta*, Rocío L. Sosa-Ramírez and Xyoli Pérez-Campos

Received: March 30, 2016; accepted: October 17, 2016; published on line: January 01, 2017

DOI: 10.19155/geofint.2017.056.1.3

Resumen

Las investigaciones macrosísmicas utilizando datos recolectados a partir de encuestas en línea han adquirido un gran auge en los últimos años. Su fácil acceso y bajo costo permiten realizar evaluaciones de la severidad del sismo a partir de los efectos observados por la población. Además es posible generar curvas de atenuación para una región en particular, visualizar el estado de las construcciones y los posibles efectos de sitio. En regiones donde no se tiene una buena cobertura de redes sísmicas, las intensidades macrosísmicas han demostrado ser un gran sustituto de datos instrumentales. En este trabajo se presentan mapas de intensidades macrosísmicas para cuatro sismos en distintos puntos del país. Los datos se obtuvieron de la base de datos del programa ¿Sintió un sismo?, una encuesta en línea implementada en el 2014. Encontramos que la atenuación es menor en zonas consideradas tectónicamente estables que en regiones activas.

Palabras clave: Mapas de distribución de intensidades, curvas de atenuación de la intensidad, intensidad comunitaria de internet, sacudida del terreno, efectos de sitio.

Abstract

Macroseismic investigations with data collected through online surveys has acquired relevance in recent years. Its easy access and low cost allow assessments of the severity of an earthquake from its effects as observed by the population. Furthermore, it is possible to generate attenuation curves for a particular region, visualize the condition of the buildings from a zip code-averaged distribution map, and estimate possible site effects. In regions without a good coverage of seismic networks, macroseismic intensities have proved to be a substitute for instrumental data. In this paper intensity maps for four earthquakes in different regions of Mexico are presented, based on data from the database of *¿Sintió un sismo?* program, an online survey implemented in 2014. Less attenuation was found in areas considered tectonically stable than in those considered as active regions.

Key words: Intensity distributions maps, attenuation intensity curves, community internet intensity, ground shaking, site effects.

J. C. Montalvo-Arrieta*
Facultad de Ciencias de la Tierra
Universidad Autónoma de Nuevo León
Ex-Hacienda de Guadalupe km 8.
Carr. Linares – Cerro Prieto 67700
Linares, N.L., México
Corresponding author: jmontalvoa87@gmail.com

R. L. Sosa-Ramírez
Facultad de Ciencias de la Tierra
Universidad Autónoma de Nuevo León
Ex-Hacienda de Guadalupe km 8.
Carr. Linares – Cerro Prieto 67700
Linares, N.L., México

X. Pérez-Campos
Departamento de Sismología
Instituto de Geofísica
Universidad Nacional Autónoma de México
Ciudad Universitaria
Delegación Coyoacán 04510
CDMX, México

Introduction

An evaluation of ground shaking through macroseismic intensities of four recent earthquakes in Mexico is presented. The intensity data were obtained through the web questionnaire *¿Sintió un sismo?* (last access March 2016), available in Spanish at http://eventos.uanl.mx/sismologia/ which is based on the "Did you feel it?" program (DYFI; Wald *et al*., 1999). The interest in earthquake intensity data is fomented by: (a) the use of internet as a tool to collect very rapidly large amounts of macroseismic data; (b) the recent development of new algorithms to analyze intensity data; and (c) the need to obtain the source parameters of historical earthquakes to improve our understanding of vulnerability, seismic hazard and seismic risk (e. g., Singh *et al*., 1996; Suter *et al*., 1996; Bakun and Wentworth, 1997; Zobin and Ventura-Ramírez, 1998; Suter, 2001; Atkinson and Wald, 2007; Wald *et al*., 2011; Hough, 2012; Hough, 2013; Suter, 2015).

¿Sintió un sismo?, is a web questionnaire that was initially implemented in northeastern Mexico as a tool for the evaluation of ground shaking in a region with few seismological observatories, such as the State of Nuevo León (Montalvo-Arrieta *et al*., 2015). However, after its implementation on the web, several reports of users located in several regions of Mexico were also received. As a result, a link to *¿Sintió un sismo?* was implemented by the Servicio Sismologico Nacional (SSN) on their web page (http://www.ssn.unam.mx), so that internet users could report their experiences and observations for any earthquake felt in Mexico. The macroseismic intensity data collected by *¿Sintió un sismo?* provides information about ground shaking by giving a quick indication of the extent and nature of shaking effects through the generation of intensity distributions maps. These maps are based on citizen input, and allow data collection at rates and quantities not available before. Additionally, it is possible to integrate the macroseismic intensities with instrumental strong-motion recordings to evaluate the ground-motion attenuation relations and seismic site effects.

Macroseismic Intensity Data

Macroseismic intensity data of four earthquakes felt by the population, from different regions in Mexico, was analyzed (Table 1). Events 1 and 2 are crustal earthquakes in northeastern Mexico, whereas events 3 and 4 are located in the subduction zone between the Cocos and North America plates. For event 4, we compare our results to those generated by DYFI. Unfortunately, for the other events this comparison was not possible due to a low response from the population, either for our survey (event 3) or DYFI (events 1 and 2). The attenuation of macroseismic intensity curves obtained by *¿Sintió un sismo?*, are compared only with the regression curves obtained by Atkinson and Wald (2007) to DYFI. Hough (2013, 2014) shows that the comparison of historical intensity distributions with those determined using the DYFI system reveals a qualitative difference between them due to the historical intensity distributions, suggesting more widespread damage and other effects revealed by spatially DYFI data.

2 March, 2014, (M4.3) earthquake (Event 1)

On March 2, 2014, at 16:30:16 UTC (11:30:16 local time), a M_c4.3 earthquake was felt in the central portion of the state of Nuevo León (Figure 1). This event is part of the

Table 1. Source Parameters of the Studied Earthquakes.

Reference	Date DD.MM.YYYY	Latitude (km)	Longitude	Depth	*M*
1*	02.03.2014	25.52°	-99.59°	5	4.3
2*	31.05.2015	25.25°	-101.15°	20	4.0
3*	23.11.2015	16.86°	-98.94°	10	5.6
4*	17.12.2015	15.76°	-93.70°	90	6.6
4§	17.12.2015	15.8009°	-93.6294°	85	6.6

Source: *Servicio Sismológico Nacional (SSN). §National Earthquake Information Center. U. S. Geological Survey (USGS).

October, 2013, to March, 2014, ($1.9 \leq M_c \leq 4.5$) seismic sequence in the region. Some of these events resulted in the first internet earthquake intensity reports in northeastern Mexico. Houses damaged were reported in some communities near the epicentral area and in the Monterrey Metropolitan Area (MMA), located approximately 90 km northwest of the epicentral zone, where strong ground shaking was described by the population. Montalvo-Arrieta *et al*. (2015) analyzed intensities from this earthquake; they reported a total of 144 received web questionnaires, 137 of them from the MMA. The descriptions by citizens in the epicentral area correspond to the highest community internet intensity (CII) values, V-VI. In the MMA and other localities of the state, CII values were II–V (Figure 1). The number of responses to the individual questionnaires with respect to time is shown in Figure 2. It is clear that the response of the people took some time, since, as mentioned, this was one of the first attempts to collect information through an online questionnaire.

The averaged MMI values were fit using the standard functional form for the intensity-attenuation relation:

$$MMI = a - br - c\log_{10}(r) \qquad (1)$$

where *a*, *b*, and *c* are constants determined by a least-squares fit to the observations and *r* is the epicentral distance (Hauksson *et al*., 2008; Hough, 2012).

Figure 3 shows the comparison of the attenuation of the macroseismic intensity reported for this earthquake with the logarithmic regression model (which is based on the maximum likelihood method of Joyner and Boore, 1993 obtained by Atkinson and Wald (2007) using the database of DYFI for Central and Eastern United States (CEUS), representing a stable continental region, and California (CA) characterizing the ground-motion attenuation to the west of CEUS. The latter region has a higher attenuation than CEUS (Nutli, 1973; Gupta and Nutli, 1976). Kanter (1994) included

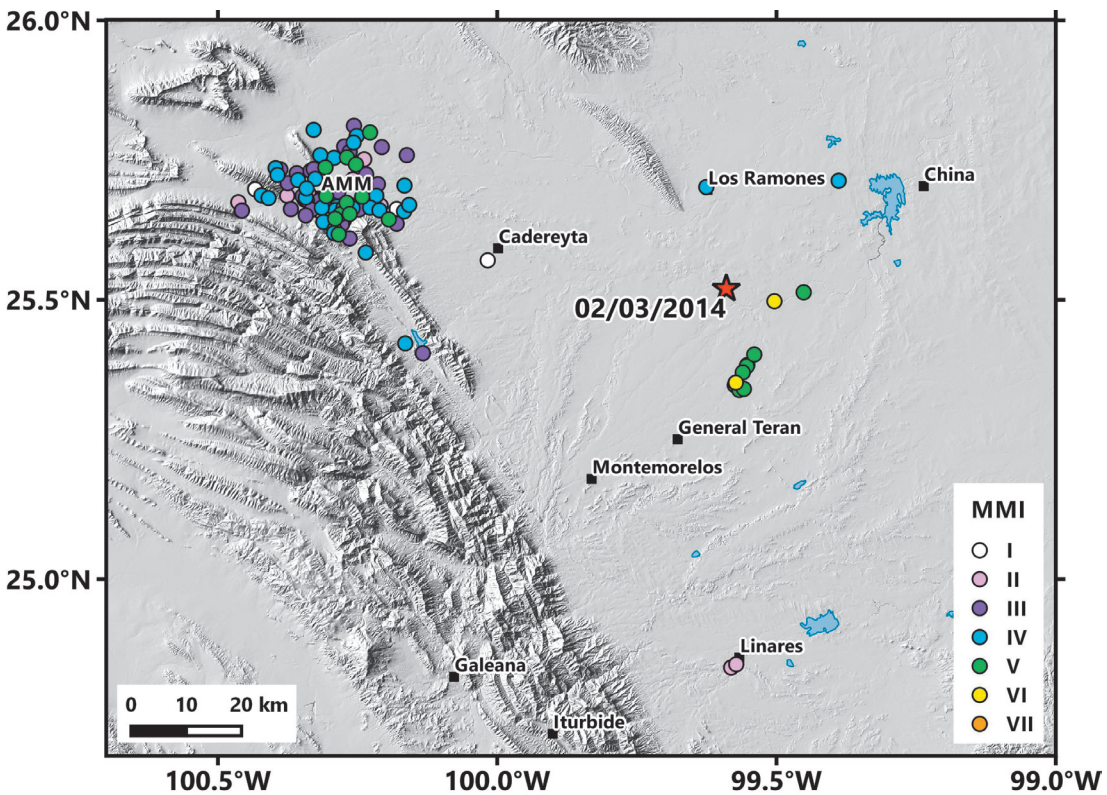

Figure 1. Community Internet Intensity (CII) map showing the distribution of intensities and felt area for the March 2, 2014, earthquake. 144 individual responses from 90 ZIP code areas were received. The red star represents the epicenter.

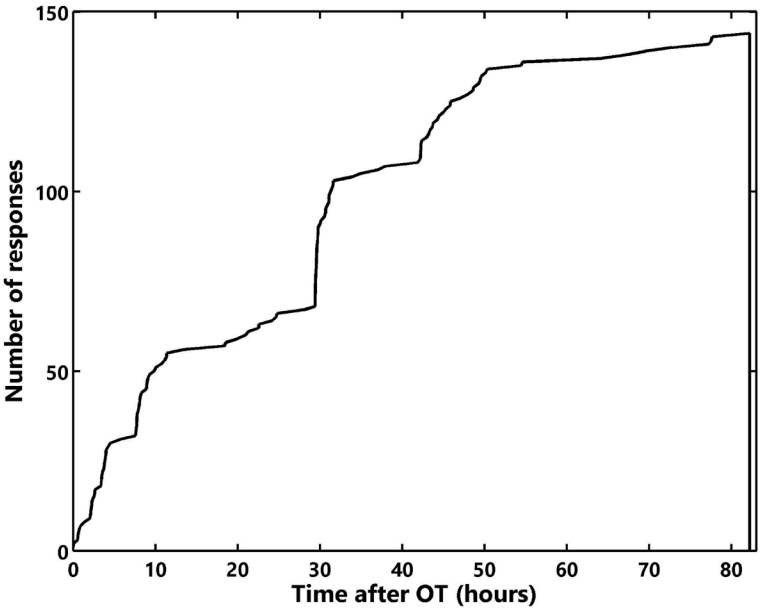

Figure 2. Number of individual questionnaire responses versus time for the March 2, 2014, event. Over 145 entries were received. The earthquake occurred at 11:30:16 local time. The last questionnaire was received 82 hours after the origin time (OT).

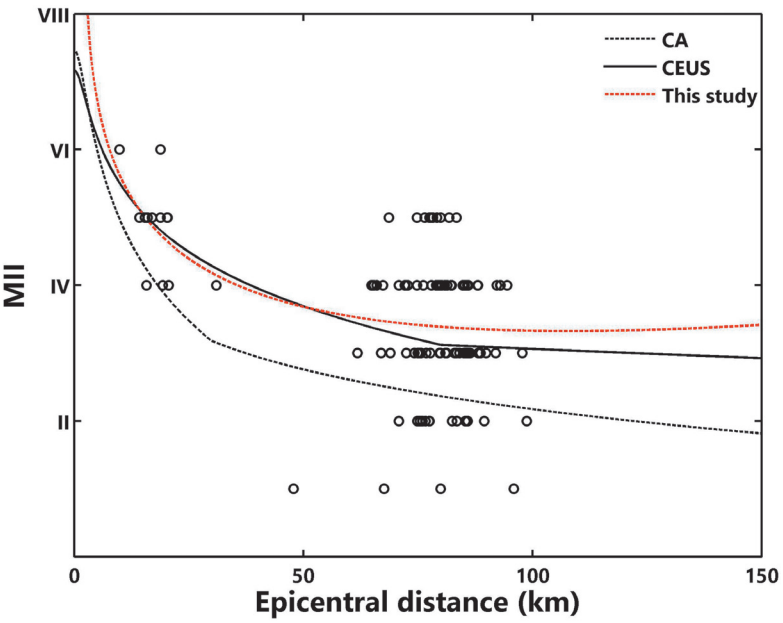

Figure 3. Intensity versus epicentral distance showing the Atkinson and Wald (2007) attenuation models, as well as equation (1) in red for the March 2, 2014, event. Note that the intensity reports show a similar behavior as compared with CEUS model.

the central portion of the state of Nuevo León in the southern limit of CEUS. It is notable the similitude between the intensity-attenuation curve for this event (equation 1) and the attenuation curve proposed by Atkinson and Wald (2007) for CEUS. The attenuation of the seismic intensity reported for event 1 may have a similar behavior to that for the stable continental region of U.S.A.

31 May, 2015, (M_c4.0) earthquake (Event 2)

The epicenter of the Saltillo earthquake of May 31, 2015, (M_c4.0) was located 26 km to southwest of Saltillo city. It occurred at 23:34:17 (local time). Due to its origin time, the earthquake was widely felt in Saltillo and Ramos Arizpe, Coahuila, in northeastern Mexico. Information about this event was extensively spread through social networks, and caused a big concern among the population in the region. Near the epicentral area the population density is scarce so,questionnaires were only received from the two mentioned cities. More than 250 users responded to *¿Sintió un sismo?,* allowing an evaluation of the macroseismic intensities for this earthquake.

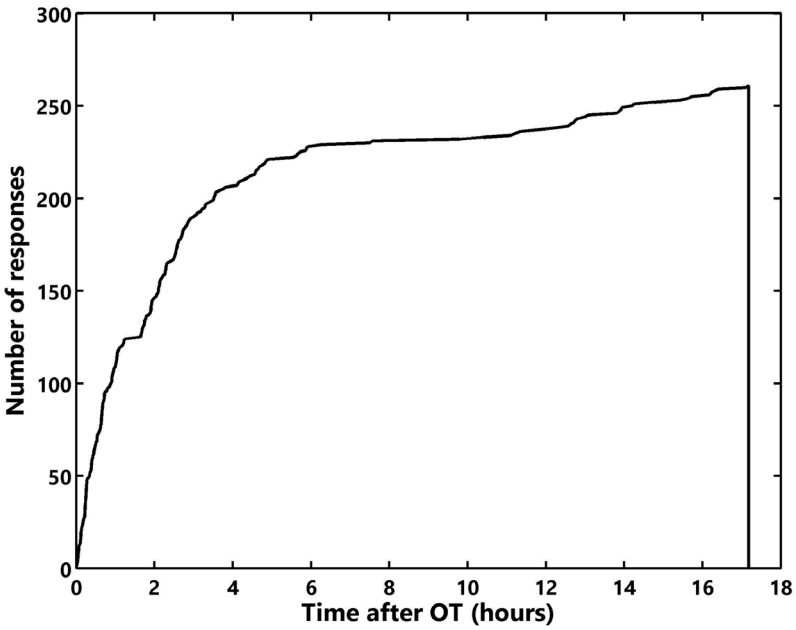

Figure 4. Number of individual questionnaire responses versus time for the May 31, 2015, event. A total of 261 surveys were received. The earthquake occurred at 23:34:17 local time. The last questionnaire was received 17 hours after the origin time (OT).

Responses were received during the first 17 hours after the event. In the first 30 minutes we received 50 questionnaires and 150 during the first two hours. Figure 4 shows the impressive rate of responses and feedback from users for the Saltillo earthquake. This is very noticeable in a region with no recently felt earthquakes. In this case the data quality and quantity depend on the population density and internet access (Mak and Schorlemmer, 2016), but not necessarily on earthquake awareness or overall hazard of the region (Wald *et al*., 2011). This behavior is similar in the MMA for the March 2, 2014, earthquake. As responses are received from a community, their ZIP code area is color-coded according to the computed CII. The map is then updated as we receive more surveys. Figure 5a shows the intensity map for the first 30 minutes after receiving the first questionnaire. Figure 5b depicts the final CII map 17 hours after the origin time. These maps also show that individual communities can change intensity (color) as data from more respondents are processed, and a new consensus is reached. This can be seen in the intensity data of Figures 5a and 5b. Therefore for multiple observations in a community, the intensity value reflects the average effects of shaking reported by that community. Additionally, according to Wald *et al*. (1999), with sufficiently distributed responses it has been shown that even small-scale variations in intensity can be recovered.

Figure 5b shows the final CII map for the Saltillo earthquake, the intensity values vary from II to V. Additionally, the distribution of intensity data shows a northeast trend. The propagation of energy could be affected by the structural orientation of main faults and lineaments in this portion of Mexico, in agreement with the explanation by Horton and Williams (2012) and Hough (2012) for the Mineral Virginia earthquake of 2011. These authors mentioned that axial distribution of intensities can be caused by anisotropic propagation resulting from local tectonics. In Mexico, the same conclusion was reached by Aguilera (1888) for the intensity distribution of the 1887 Sonora earthquake (see Suter, 2006).

23 November, 2015, (M5.6) earthquake (Event 3)

This event was located 48 km East of San Marcos, Guerrero (SSN, 2015), and originated at Cocos-North American subduction zone. This event was felt in Mexico City and some localities of central Mexico. Figure 6a shows the CII map obtained for central Mexico. We received 22 questionnaires in a lapse time of 15 hours (Figure 7), all of them from Mexico City.

Figure 6b shows the CII map for Mexico City, superimposed to the geotectonic zones defined by Marsal and Mazari (1959) as: (1) the hill zone, formed by volcanic tuffs and lava flows; (2) the lake-bed zone, formed by clays with thicknesses varying from 10 to 130 m; and (3) the transition zone, composed of alluvial sandy and silt layers, with scattered clay layers. In Mexico City the CII varied from I to III, in the lake-bed zone the MMI values were III.

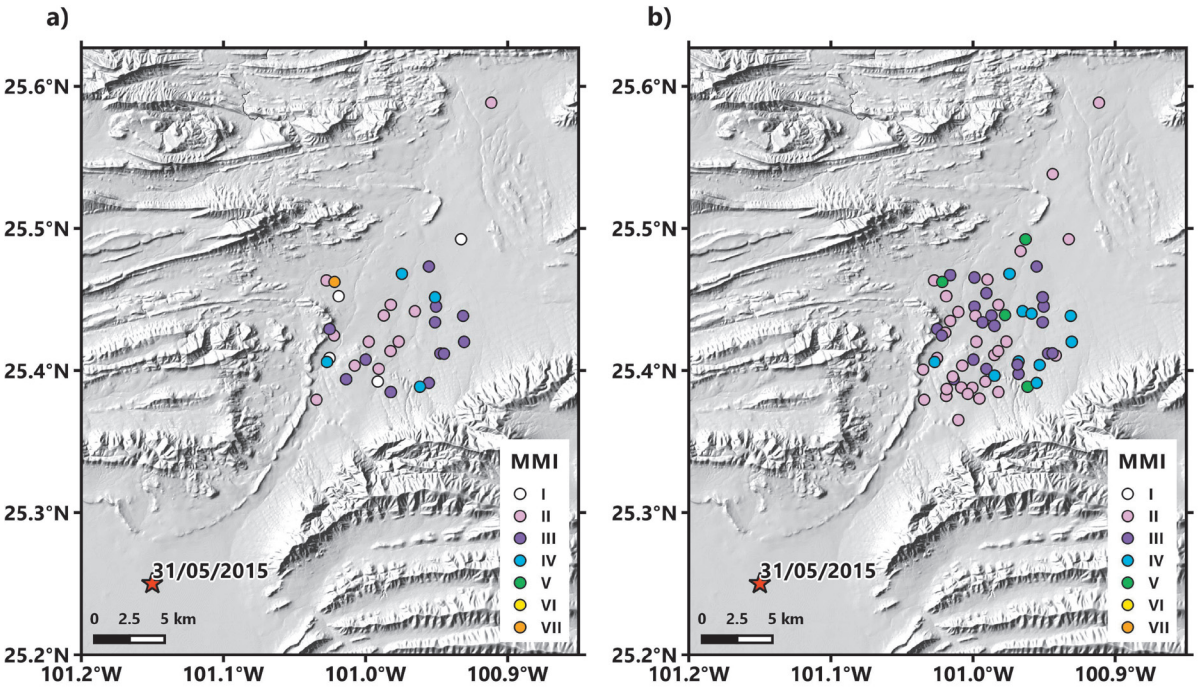

Figure 5. Community Internet Intensity (CII) map showing the distribution intensities and felt area for the May 31, 2015, earthquake after (a) 30 minutes from the origin time, and (b) after 17 hours of the origin time. 261 individual responses from 73 ZIP code areas were received. The red star represents the epicenter.

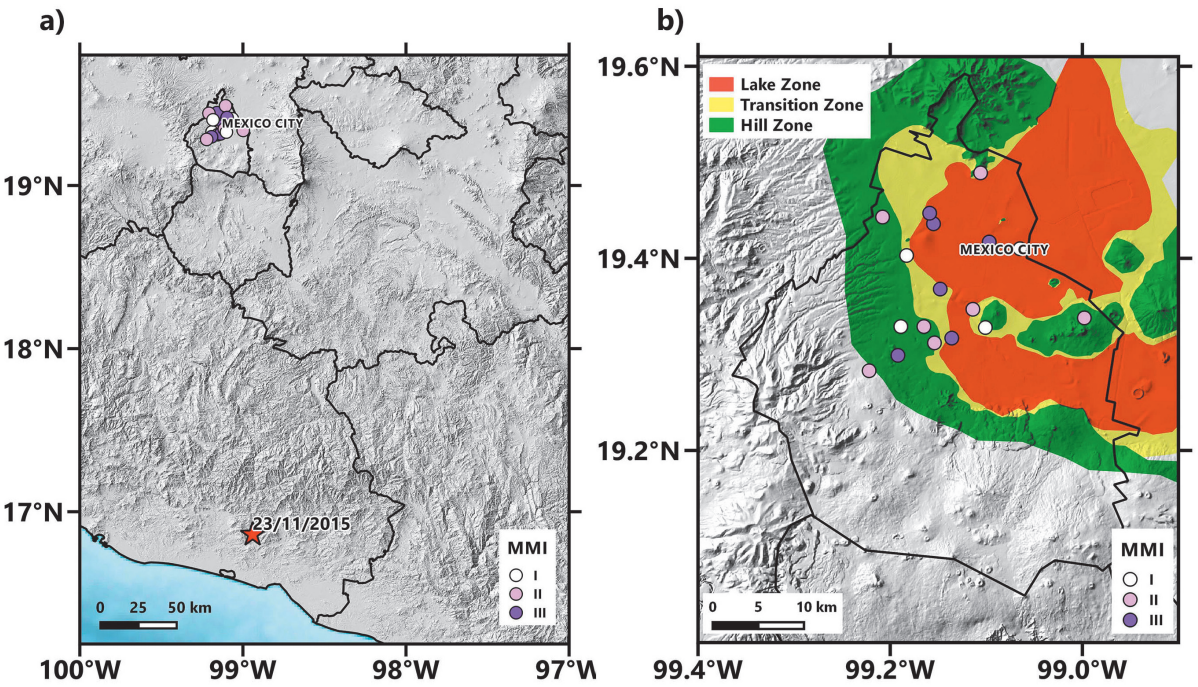

Figure 6. (a) Community Internet Intensity (CII) map showing the distribution intensities and felt area for the November 23, 2015, earthquake. 22 individual responses from 19 ZIP code areas, all of them from Mexico City, were received. The red star represents the epicenter. (b) Comparison of geotectonic zones from the Valley of Mexico (Marsal and Mazari, 1959; Flores-Estrella *et al*., 2007) and CII values.

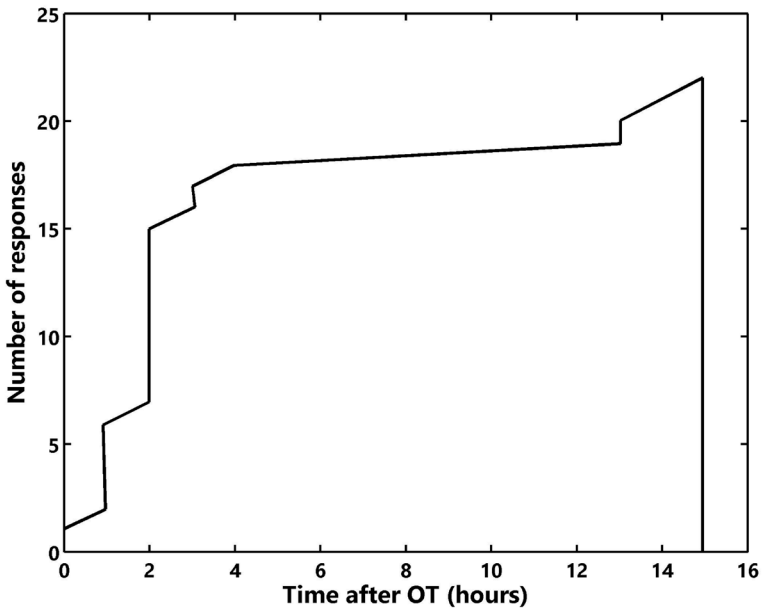

Figure 7. Individual questionnaire responses versus time for the November 23, 2015, event. Over 20 entries were received. The last one was received 15 hours after the origin time (OT). The earthquake occurred at 14:41:20 local time.

17 December, 2015, (M6.6) earthquake (Event 4)

Event 4 occurred in the subduction zone between Cocos and North American plates, at 90 km depth according to the SSN (Table 1). The epicenter was located near the city of Tonalá in the state of Chiapas (Figure 8). The earthquake was widely felt in southeastern Mexico and some places in Belize and Guatemala (SSN, USGS). During this event we probed the capabilities of *¿Sintió un simo?* in terms of the response of web users located in cities of several states of Mexico. Figure 8 shows the CII map. CII data are mainly focused in the Chiapas and Tabasco states. In the state of Chiapas, including the capital city Tuxtla Gutierrez, the intensities had values between IV - VI. Near the epicentral area the CII reported was IV. The CII reports from Tabasco state come from cities located in the basin of the Grijalva River, such as Villahermosa. This basin is characterized by thick soil deposits from the Quaternary, that amplify the ground motions. Other CII data were from Oaxaca, Veracruz and Estado de México states.

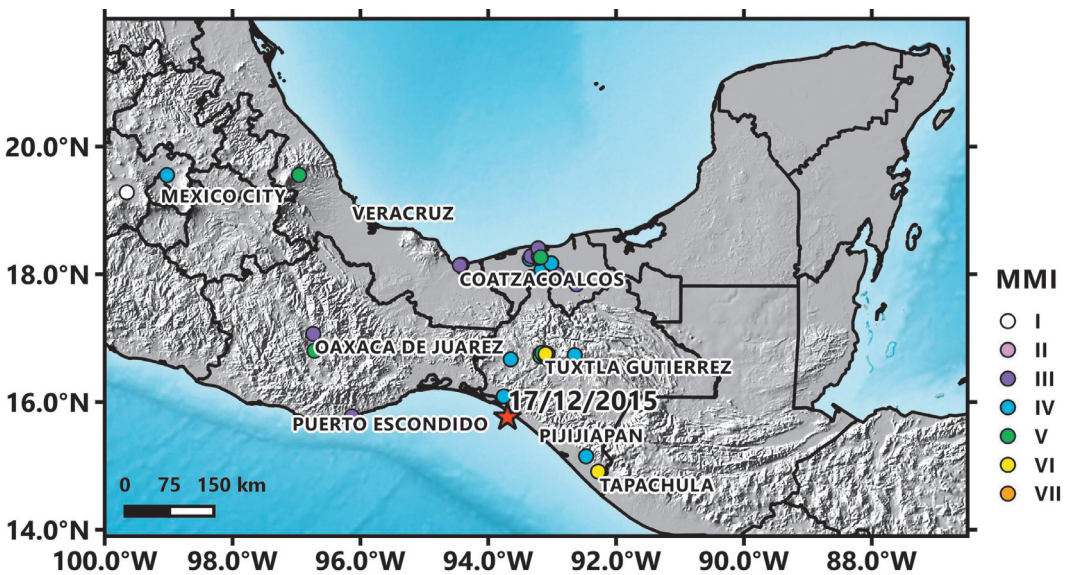

Figure 8. Community Internet Intensity (CII) map showing the distribution intensities and felt area for the December 17, 2015, earthquake. 51 individual responses from 41 ZIP code areas were received. The red star represents the epicenter.

The CII map generated in this study (Figure 9a) was compared with the DYFI intensity map (Figure 9b). In contrast to Figure 8, these maps report the CII averaged by city, similar as DYFI procedures for intensity maps outside U.S.A. DYFI received 122 CII reports from Belize, Guatemala and Mexico, 48 of them were from Mexico. DYFI and *¿Sintió un sismo?*, received reports of almost the same Mexican states; however, DYFI received only one survey from the state of Tabasco, while *¿Sintió un sismo?*, 30. Figure 10 depicts the response time for DYFI and *¿Sintió un sismo?*, DYFI includes the reports from Belize, Guatemala and Mexico. The DYFI intensity map for Mexico shows CII values that vary from III to IV, whereas for *¿Sintió un sismo?,* CII reports vary from III to VI. The differences in CII data could be related to the larger number of surveys received by *¿Sintió un sismo?*

Figure 11 shows the intensity attenuation obtained by DYFI and *¿Sintió un sismo?* (equation (1)) compared with CEUS and CA models. In both curves, the attenuation intensity is correlated with an active province. The intensity attenuation curve of DYFI includes all reports received from Belize, Guatemala and Mexico.

Discusion and Conclusions

In this study we presented the first CII maps for Mexico from *¿Sintió un sismo?*, which is a web questionnaire where citizens report their experiences and observations for any felt earthquake, just by answering a simple multiple-choice questionnaire. Based on the information obtained with our web questionnaire, we have documented the intensity maps of the March 2, 2014, (*M*4.3),

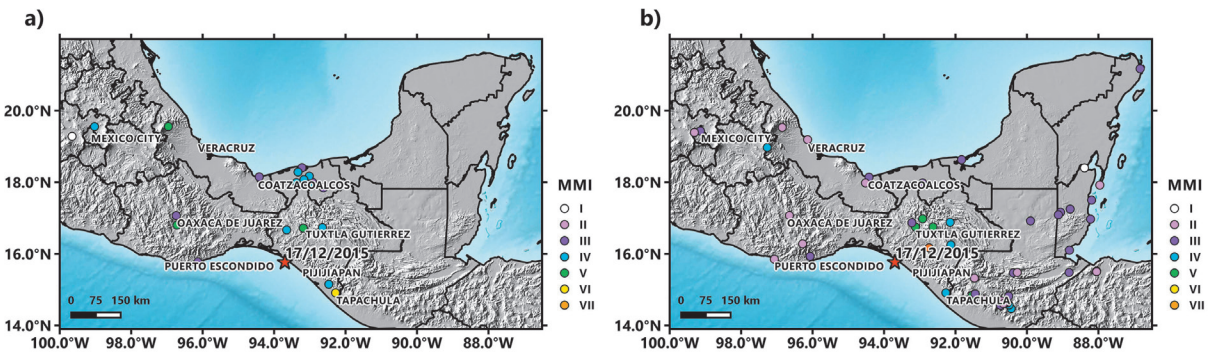

Figure 9. Comparison of felt area for (a) this paper results of the December 17, 2015, earthquake averaged by city, and (b) the DYFI results.

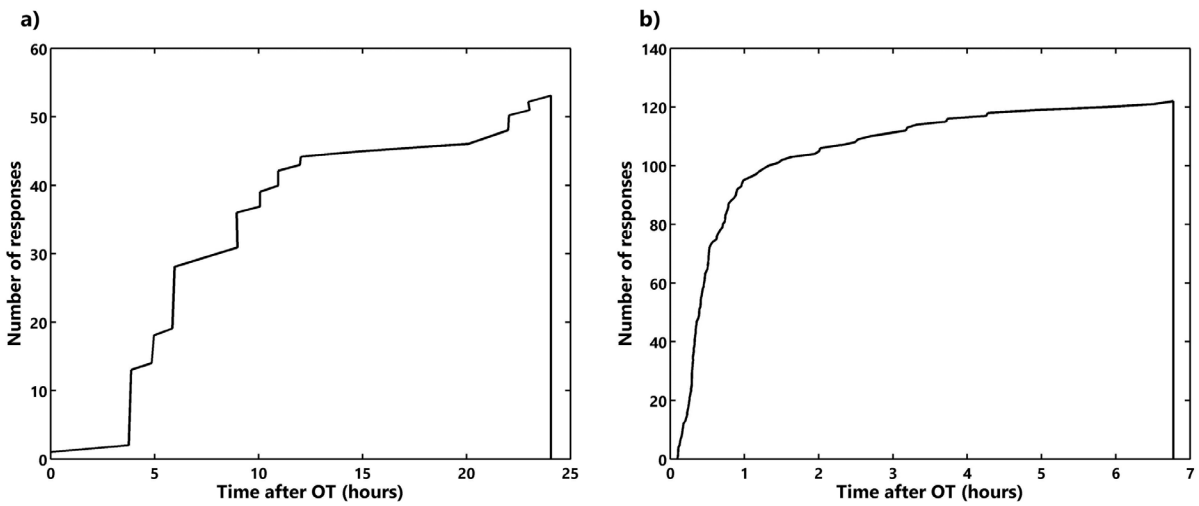

Figure 10. Comparison of individual questionnaire responses versus origin time (OT) for (a) this paper results of the December 17, 2015, earthquake, and (b) the DYFI results.

May 31, 2015, (*M*4.0), November 23, 2015, (*M*5.6), and December 17, 2015, (*M*6.6) earthquakes that were originated in different seismotectonic settings of Mexico reflected in the obtained CII maps.

Although *¿Sintió un sismo?* was launched in 2014 as a web questionnaire to assess the ground shaking in northeastern Mexico, it was until 2015 that it started being used throughout the country. The number of questionnaires is expected to increase over time, in order to improve the evaluation of effects caused by earthquakes across the country. In addition, in the future we can: (a) test the correlation between the macroseismic intensities obtained by *¿Sintió un sismo?*, and the instrumental ground-motion recordings such as peak ground acceleration and peak ground velocity to create Shake Maps (Wald *et al*., 1999a, b; Wald *et al*., 2005), (b) to obtain an empirical regression to determine the dependence of MMI on M and the distance from the fault, for the seismotectonic provinces in Mexico.

Acknowledgments

The authors are grateful to the anonymous reviewer whose critical comments on the manuscript helped to improve it. Thanks to Dirección General de Informática, Universidad Autónoma de Nuevo León, for their support. To INEGI and GTOPO30 whose data of the Digital Elevation Model was used in this paper. To Consejo Nacional de Ciencia y Tecnología (CONACYT) for the scholarship to the MSc student Rocío L. Sosa-Ramírez. We thank to the SSN for keeping the questionnaire available on its home page.

References

Atkinson G., Wald D., 2007, "Did you feel it?" Intensity data: A surprisingly good measure of earthquake ground motion. *Seismol. Res. Lett., 78*, 362–368.

Bakun W.H., Wentworth C.M., 1997, Estimating earthquake location and magnitude from seismic intensity data. *Bull. Seismol. Soc. Am.*, *87*, 1502–1521.

Flores-Estrella H., Yussim S., Lomnitz C., 2007, Seismic response of the Mexico City Basin: A review of twenty years of research. *Nat Hazards* 40, 357–372, doi: 10.1007/s11069-006-0034-6.

Gupta I.N., Nuttli O.W., 1976, Spatial attenuation of intensities for central U.S. earthquakes, *Bull. Seismol. Soc. Am.* 66, 743–751.

Hauksson E., Felzer K., Given D., Giveon M., Hough S.E., Hutton K., Kanamori H., Sevilgen V., Yong A., Wei S., 2008, Preliminary report on the 29 July 2008 Mw5.4 Chino Hills, eastern Los Angeles Basin, California, earthquake sequence, *Seismol. Res. Lett.* 79, 855–866.

Horton J.W., Williams R.A., 2012, The 2011 Virginia earthquake: What are scientists learning? *Eos Trans. AGU*. *93*, 317–324.

Hough S.E., 2012, Initial assessment of the intensity distribution of the 2011 Mw 5.8 Mineral, Virginia, earthquake. *Seismol. Res. Lett.*, *83*, 649–657.

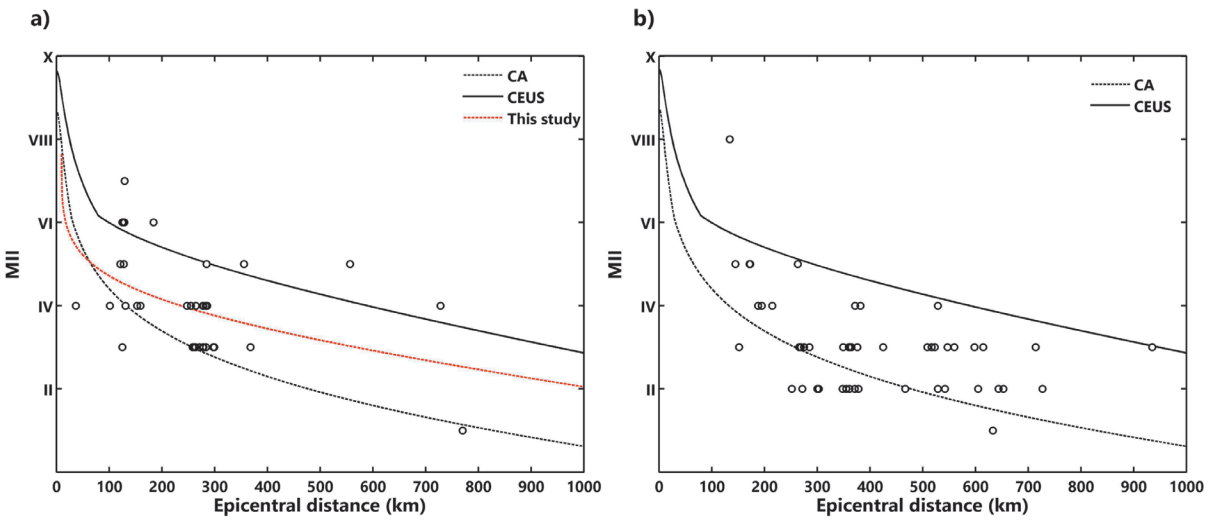

Figure 11. Comparison of intensity-distance attenuation for (a) this paper results of the December 17 , 2015, earthquake, and (b) the DYFI results. Dotted red line is the fit using equation (1).

Hough S.E., 2013, Spatial Variability of "Did You Feel It?" Intensity Data: Insights into Sampling Biases in Historical Earthquake Intensity Distributions. *Bull. Seismol. Soc. Am.*, *103*, 2767–2781, doi: 10.1785/0120120285.

Hough S.E., 2014, Earthquake intensity ditributions: a new view. *Bull. Earthquake Eng*., 12, 135-155, doi: 10.1007/s10518-013-9573-x.

Joyner W.B., Boore D. M., 1993, Methods for regression analysis of strong-motion data. *Bull. Seismol. Soc. Am.*, *83*, 469–487.

Kanter L.R., 1994, Tectonic interpretation of stable continental crust, in The Earthquakes of Stable Continental Regions: Assessment of Large Earthquake Potential, chapter 2, pp. 2-1– 2-98, edited by J. F. Schneider, EPRI Rpt. TR-102261, *Electric Power Res. Inst*., Palo Alto, CA.

Marsal R.J., Mazari M., 1959, El subsuelo de la Ciudad de México, Facultad de Ingeniería, Universidad Nacional Autónoma de México, México, p. 501.

Mak S., Schorlemmer D., 2016, What makes people respond to "did you feel it"?. *Seismol. Res. Lett.*, *87*, 119–131, doi: 10.1785/0220150056

Montalvo-Arrieta J.C., Sosa-Ramírez R.L., Paz-Martínez E.G., 2015, Relationship between MMI data and ground shaking in the State of Nuevo León, northeastern Mexico. *Seismol. Res. Lett.*, *86*, 1489 – 1495, doi: 10.1785/0220140206.

Nuttli O.W., 1973, Seismic wave attenuation and magnitude relations for eastern North America, *J. Geophys. Res*. 78, 876-885.

Singh S.K., Ordaz M., Pérez-Rocha L.E., 1996, The great Mexican earthquake of 19 June 1858: Expected ground motions and damage in Mexico City from a similar future event. *Bull. Seismol. Soc. Am.*, *86*, 1655-1666.

Suter M., Carrillo-Martínez M., Quintero-Legorreta O., 1996, Macroseismic study of shallow earthquakes in the central and eastern parts of the Trans-Mexican volcanic belt, Mexico. *Bull. Seismol. Soc. Am.*, *86*, 1952-1963.

Suter M., 2001, The historical seismicity of northeastern Sonora and northwestern Chihuahua, Mexico (28–32° N, 106–111° W). *J. South Am. Earth Sci.*14, 521–532.

Suter M., 2006, Contemporary Studies of the 3 May 1887 Mw 7.5 Sonora, Mexico (Basin and Range Province) Earthquake. *Seismological Research Letters*, 77, 134 – 147. doi:10.1785/gssrl.77.2.134

Suter M., 2015, The A.D. 1567 Mw 7.2 Ameca, Jalisco, earthquake (Western Trans-Mexican Volcanic Belt): Surface rupture parameters, seismogeological effects, and macroseismic intensities from historical sources. *Bull. Seismol. Soc. Am.*, *105*, 646-656.

Wald D.J., Quitoriano V., Heaton T.H., Kanamori H., 1999a, Relationship between Peak Ground Acceleration, Peak Ground Velocity, and Modified Mercalli Intensity in California. *Earthquake Spectra*, v. 15, 3, p. 557-564.

Wald D.J., Quitoriano V., Heaton T.H., Kanamori H., Scrivner C.W., Worden B.C., 1999b, TriNet "ShakeMaps": Rapid generation of peak ground-motion and intensity maps for earthquakes in southern California. *Earthquake Spectra*, 15, 537-556.

Wald D., Quitoriano V., Dengler L., Dewey J., 1999, Utilization of the Internet for rapid community intensity maps. *Seismol. Res. Lett.*, *70*, 680–697.

Wald D.J., Worden B.C., Quitoriano V., Pankow K.L., 2005, ShakeMap manual: technical manual, user's guide, and software guide. U.S. Geological Survey, 132 p.

Wald D.J., Quitoriano V., Worden C.B., Hopper M., Dewey J.W., 2011, USGS "Did You Feel It?" internet-based macroseismic intensity maps. *Ann. Geophys.*, *54*, 688–709.

Zobin V.M., Ventura-Ramírez J.F., 1998, The macroseismic field generated by the Mw 8.0 Jalisco, Mexico, earthquake of 9 October 1995. *Bull. Seismol. Soc. Am.*, *88*, 703-711.

Geofísica Internacional (2017) 56-1: 37-56

Original paper

Mapping Geologic Interfaces that may alter seismic wave propagation in the Mexico City basin

Román Álvarez

Received: March 30, 2016; accepted: November 11, 2016; published on line: January 01, 2017

DOI: 10.19155/geofint.2017.056.1.4

Resumen

En el temblor del 19 de septiembre de 1985 la ciudad de México se dañó de forma extensa. Aunque toda la ciudad sufrió diversos grados de destrucción, la región de daño máximo estuvo restringida a una zona densamente poblada al oeste del aeropuerto internacional, donde aún en la actualidad se encuentran capas de sedimentos saturados de agua. Otras regiones en la ciudad, también con sedimentos saturados, no experimentaron daños tan amplios. Entre los diversos mecanismos propuestos para explicar tal grado de destrucción se propuso uno que involucra la interacción de ondas sísmicas incidentes y reflejadas sobre, o cerca de, la superficie saturada. La existencia y localización de superficies reflejantes en la cuenca de México es por lo tanto de importancia básica. En este trabajo se propone que las estructuras geológicas de alta densidad dentro de la cuenca pueden constituir esas superficies reflejantes. Se efectúa un modelaje de gravedad 2-D dentro de la cuenca entre la Sierra del Tepeyac (N) y Xochimilco (S); algunas líneas intersectan y modelan estructuras volcánicas en esta región. Una inversión 3-D del campo gravimétrico muestra que la Sierra del Tepeyac-Peñón de Los Baños es una estructura densa potencialmente capaz de reflejar ondas sísmicas hacia el oeste, mientras que la Sierra de Santa Catarina las reflejaría preferencialmente hacia el sur. Las regiones de alta densidad se definen y mapean en el espacio 3-D. Estos resultados apoyan la posibilidad de tener fuertes interacciones entre ondas sísmicas viajando en direcciones opuestas en regiones seleccionadas de la cuenca de México. El mecanismo de reflexión obviamente será proporcional a la magnitud de la perturbación sísmica que lo origina.

Palabras clave: Sismo del 19 de septiembre de 1985, sismo de la Ciudad de México, refexión de ondas sísmicas, inversión gravimétrica 3-D, eventos sísmicos de gran magnitud.

R. Álvarez
Instituto de Investigaciones
en Matemáticas Aplicadas y en Sistemas
Universidad Nacional Autónoma de México
Ciudad Universitaria
Delegación Coyoacán 04510
CDMX, México
Corresponding author: roman.alvarez@iimas.unam.mx; ralva@prodigy.net.mx

Abstract

Mexico City experienced a large amount of damage during the September 19, 1985, earthquake. Although the whole city experienced different destruction degrees the region of maximum damage was constrained to a densely populated area west from the international airport, where water saturated sediments are still abundant. Other regions within the city, also with saturated sediments, did not experience a similar destruction. Among the mechanisms proposed to explain such large amount of destruction, one was proposed involving the interaction of incoming and reflected seismic waves in, or close to, the saturated surface. The existence and location of seismic wave reflecting surfaces within the basin of Mexico is thus of basic importance. It is herein proposed that high-density geologic structures within the basin may constitute those reflecting surfaces. 2-D gravity modeling is performed across the basin between Sierra del Tepeyac(N) and Xochimilco (S); some lines intersect and model volcanic structures in this region. A 3-D inversion of the gravity field shows that Sierra del Tepeyac-Peñón de Los Baños is a dense structure potentially capable of reflecting seismic waves towards the west, while Sierra de Santa Catarina would preferentially reflect them towards the south. The high-density regions are defined and mapped in 3-D space. These findings support the possibility of strong interactions between seismic waves travelling in opposite directions in selected regions of the Mexico basin. The reflection mechanism will obviously be proportional to the magnitude of the originating seismic disturbance.

Key words: September 19, 1985 earthquake, Mexico City earthquake, seismic wave reflection, 3-D gravity inversion, large-magnitude seismic events.

Introduction

Mexico City is mostly affected by seismic events occurring in the subduction zone of the Cocos plate in Michoacán, Guerrero and Oaxaca states. The hypocenter of the September 19, 1985, occurred at Michoacán coast at (17.6 N y 102.5 W) with a magnitude M_w of 8.1 (IGF-IIN, 1985), at a depth of 15 km (USGS, 1985) and inflicted an enormous damage in the city. Cities within 150 km from Mexico City and at similar distances to the Middle America Trench (MAT) have never been so strongly affected by large magnitude seismic events. Puebla and Toluca, neighboring, populated state capitals, did not report the type of damage experienced by the nation's capital in the above and other strong earthquakes. This indicates that Mexico City possesses certain characteristics that are peculiar of its geographic location that seem to enhance seismic events. One peculiarity of the Mexico basin is indeed the existence of an ancestral lake that filled the basin in which Mexico City has been expanding since the XIVth century. Although this lake has been progressively fragmented and desiccated there still remain many areas with saturated sediments. Building in these areas has traditionally required particular civil engineering expertise. Bribiesca (1960) presented various stages of the lake evolution, illustrating how the lake's surface has changed over time. Although surface water has evaporated or drained out of the basin, subsurface water still saturate many portions of the upper clay formations. Based on surface geology three regions of different geological characteristics have been traditionally defined (Marsal and Mazari, 1969) for the Mexico City area: hills, transition, and lake deposits. This classification corresponds to geologic formations not deeper than 300 m. A description of the deeper characteristics of the basin is still missing. This work aims at describing them at depths reaching 3 km in the region encompassing the length of the basin in the E-W direction and from Sierra del Tepeyac to Xochimilco in the N-S direction.

Geologic description

The basin of Mexico contains numerous volcanic edifices in and around its limits. Their ages range from Mid Tertiary to Pliocene and Pleistocene. Mid Tertiary deposits are found in Sierra del Tepeyac and the Xochitepec range SW of the basin, and outcrops are present at the footsteps of the ranges E and W of the basin. In the Pliocene, Sierra del Tepeyac flows were reactivated ejecting considerable amounts of dacitic and rhyolitic lavas. In the Upper Pliocene the north drainage of the basin was blocked by flows of basaltic andesite. Erosion of the ranges confining the basin produced alluvial fans that filled the canyons until the Lower Pleistocene (Marsal and Mazari, 1969). A new episode of volcanic activity started in the Pleistocene following SW to NE fractures in the crust covering the region with layers of basalt and pumice. Several volcanic structures belong to this episode (Chiconautla, Chimalhuacán and Cerro de la Estrella). Discharge of the basin was towards the south at this time, until the basin's drainage was blocked again by the emplacement of Sierra Chichinautzin in the Upper Quaternary, and a lake developed in its interior. As previously mentioned, this ancestral lake was subsequently fragmented into several lakes within the basin. The lake corresponding to the location of Mexico City has been drained and embanked since colonization by the Aztecs. Initially embankments or "Calzadas" were built on the lake, subsequently expanding, reaching a point in the last stages such that only water channels persisted as water bodies. Eventually, even those channels were filled out; however, the underlying formations remained saturated. The only remaining channels in the region are those found in the southern Xochimilco Lake.

An objective of this study is revealing the basement topography of Mexico City's basin. Basement here means the boundary between higher-density formations and sediments. Some of the models to be described ahead show a peculiar pattern for the density distribution in the basin. They show higher densities towards the surface in many locations underlain by low-density materials. One would expect the reverse distribution; a tentative explanation for this phenomenon is that profuse distribution of dense volcanic materials, such as volcanoes and lava flows, have been emplaced on top of the calcareous formations and sedimentary fill throughout the basin. A case in point is that of Ciudad Universitaria where basaltic rocks of ~20m-thickness overlie low-density tuffs and volcanic breccias extending down to 1580 m depth (CENAPRED, 1996). Since lakes and lake deposits are also present in the surface, surface patterns may be observed between the two media in which higher density materials alternate with the lower-density layers. Empirical relations between seismic wave speed and density have been developed (Gardner *et al*., 1974; Brocher, 2005); generally, low densities correspond to low velocities and high densities to high velocities.

Seismic wave interactions

The intensity of September 19, 1985, earthquake in Mexico City exhibited the inadequacy of

the seismological one-dimensional theory to explain the observed motion in the bed lake zone (Sánchez-Sesma *et al*., 1988; Bard *et al*., 1988); these authors highlighted the importance of lateral terrain irregularities to properly describe the observed phenomena. They showed that 2-D models yielded better reproductions of recorded events. These models confine to a vertical plane the extent of the affected media; the confining medium has a propagation velocity several fold that of the sediments involved (e.g. from V_S =2000 to V_S =500 m/s, respectively). According to the empirical relation (Brocher, 2005) between V_S and density ϱ, the change in velocity would imply density changes from 1.90 to 2.32 (g/cm^3). This underlines the importance of knowing: i) the geometry of the region involved and, ii) the propagation velocities or the densities of the materials involved, in order to obtain an adequate description of the seismic interactions in a given region. In principle, a 3-D treatment would yield the most realistic description of the actual problem.

Another problem observed in the saturated sediments is an unusually long coda compared with the corresponding one in the hill zone (Singh and Ordaz, 1993); this long coda usually has demolishing effects in the constructions built in that region. Different models have been proposed to explain the long-coda effect; they were summarized by Chávez-García (1991), that discarded 2-D models in favor of models involving lateral resonance of P waves. In the latter type of problems, establishing the boundary conditions is of outmost importance in order to get the adequate response. The surface boundary conditions may be defined by the surface contact between sediments and igneous formations; however, in order to define the equivalent boundaries at depth, exploration wells, geophysical surveys, and models must be done to properly locate the interfaces.

Among the destruction mechanisms reported to operate during the 1985 earthquake one was proposed that involves the interaction of surface waves (Álvarez, 1986a). This mechanism requires two waves travelling in opposite directions, crossing each other at or near the surface, inducing constructive amplitude interactions in some places. The analyses of teleseismic records and local vertical displacements in the 1985 devastating earthquake in Mexico City led Sánchez-Sesma *et al*. (1988) to establish that, in order to explain the induced damage and the observed ground motions, simultaneous consideration must be given to source, path and site conditions. In the mechanism described by Álvarez (1986a) the incoming wave is generated at the hypocenter, arrives in the Mexico basin, is reflected at an interface, travelling in the opposite direction and interacting with the incoming wave train. The site conditions referred to above are thus directly connected with the site at which reflection occurs. The way Álvarez (1986a) reported recorded damage (damage fronts) includes not only collapsed buildings, but small but significant damage to pavement, sidewalks, pipelines, and graveyard monuments not higher than 1 m, whose continuity could be traced from one block to the next. The damage fronts are closely perpendicular to the direction of the incoming wave train; some are concave in this direction whilst others are concave in the opposite direction, and still another set shows no concavity. Destruction observed in many other sites could not be associated with any of the damage fronts and appear as isolated points.

The question arises of which are the reflecting surfaces, where are they located, and what is its orientation with respect to the incoming waves. In the present work it is supposed that the reflecting surfaces in Mexico City's basin are the interfaces between the low-density and the high-density materials, making 3-D density mapping in the basin of Mexico a key in establishing boundary conditions to wave propagation within the basin. In a general way it can be stated that these are the interfaces between sedimentary and igneous formations. The largest effects of reflected waves with the incoming wave train are expected to occur with surfaces oriented almost perpendicular to the incoming waves, in such a way as to create reflected waves travelling in the oppo-site direction. This appears to be in line with Campillo *et al*. (1988) observation that plane wave response at small angles of incidence properly reproduces the most significant characteristics of Mexico's basin seismic response.

Gravimetric study

Previous gravimetric reports of the Mexico basin (Marsal and Mazari, 1969; Álvarez, 1986b, 1988, 1990) were based on the contoured Bouguer anomaly map published in the former reference (Figure 4). That survey was performed with station separations of 500 m and at longer intervals in regions as the Texcoco Lake (Marsal and Mazari, 1969) using two Houston Technical Laboratories gravimeters. Unfortunately the station locations are not specified in the map, only the contoured values are plotted. However,

station density is reported as 0.9 stations/km^2. Closure errors are reported as less than 0.2 mGals. Latitude, Bouguer, and topographic corrections were performed. Interpretation of the Bouguer anomaly map is restricted to a few comments; no modeling of these data was reported by Marsal and Mazari, (1969); the first gravimetric models of these data apparently were those reported by Álvarez (1986b). The gravimetric map allowed Marsal and Mazari (1969) the definition of four main secondary basins: Mexico City, Texcoco, Teotihuacan, and Chalco.

A more recent gravimetric survey on the gravimetry of the basin (CENAPRED, 1996) reports a station density of 0.7 stations/km^2 covering the most centric portion of Mexico City with 556 stations distributed in a square 26 (E-W) x 26 (N-S) km. The report locates the SW vertex of the square at 19-12.6216°N and 99-18.8490°W; however, in the Bouguer anomaly map of the report no geographic or UTM coordinates appear, only the distances in meters in the X and Y directions. When one tries to superpose this map with the topographic, geologic, or Bouguer anomaly map reported by Marsal and Mazari, (1969) it cannot be properly fit by means of linear adjustments. If the north part of the map (e.g. Sierra de Guadalupe) gets a good fit, the southern portion (e.g. Xochimilco-Chalco) is displaced from its correct location. This type of registration problem is common when trying to match maps with different projections. Additionally, in this gravimetric survey they used a Bouguer reduction density of 2.40 g/cm^3, probably to enhance the influence of the sediments in the basin, contrasting with the more commonly used value of 2.67 g/cm^3. Although the registration and the reduction density discrepancies can be solved for this set of measurements, this task is beyond the scope of the present study.

Consequently the former Bouguer anomaly map will be used in this study. Notwithstanding, the modeled area has been increased several fold. 1957 observation points are used now versus 225 previously used to define the anomaly (Álvarez, 1988) in a 15 (E-W) by 20 (N-S) km area. Also, new 3-D inversion techniques are introduced. The Bouguer anomaly map is shown in Figure 2a. It extends from Sierra de Las Cruces (W) to Texcoco (E) and from San Juan Teotihuacan (N) to Xochimilco (S). This map shows a gravity gradient decreasing from N to S across de basin, which allows the region to be divided in three anomaly areas, with the largest values to the north and the smallest values to the south; the corresponding range of amplitude variation is of approximately 24 mGals. Farther S from Xochimilco, Sierra del Chichinautzin rises abruptly and so does its corresponding Bouguer anomaly. A similar boundary is found on the western portion of the map between Sierra de Las Cruces and the old Mexico lake region. Figure 2b shows the Bouguer anomaly contours superposed to a reference map in which various locations can be identified.

Within the region of lowest anomaly values to the S and W of the map one can identify three apparently interconnected anomaly areas; they will be designated as Centro, Xotepingo, and Xochimilco. The Texcoco lake region occupies the central-eastern portion of the map. It also corresponds to a negative Bouguer anomaly; however, it does not reach as low values as the former three anomalies. The distribution of those three anomalies leads Álvarez (1988) to propose the existence of a buried canyon connecting those areas; he called it Cañón de México.

Previous models

Marsal and Mazari (1969) made reference to the unpublished report of the geophysical contractor that performed the gravimetric measurements (Figure 1). Assuming an Earth's crust with only two components for the main strata with densities of 1.8 and 2.6 g/cm^3, the former corresponding to alluvial and lacustrine deposits, and the latter to igneous masses, they reached the conclusion that the maximum depression in the basin reaches about 1000 m. However, they didn't point at the location, or locations, where this occurs, recommending additional seismic exploration and borings in order to make more precise determinations.

The model of Álvarez (1988) appears to be the only previous attempt in describing the basement structure in the western portion of Mexico basin in a quantitative fashion. Using the same data reported above, sampled in a mesh of 225 points, complemented with a bicubic-spline interpolation (González-Casanova and Álvarez, 1985), it develops a gravity mesh that was subsequently used to perform 3-D forward modeling of the gravimetric field observed. The final model consists of a dozen right-rectangular prisms that represent basement outcrops (three prisms) and buried structures with a distribution of densities of 2.75 g/cm^3 for the denser materials and sediment layers in the 2.27-2.52 g/cm^3 range. The prism distribution is N-S extending from Sierra del Tepeyac to Cerro de la Estrella. Towards the W the prisms descend *en échelon* in 200-m

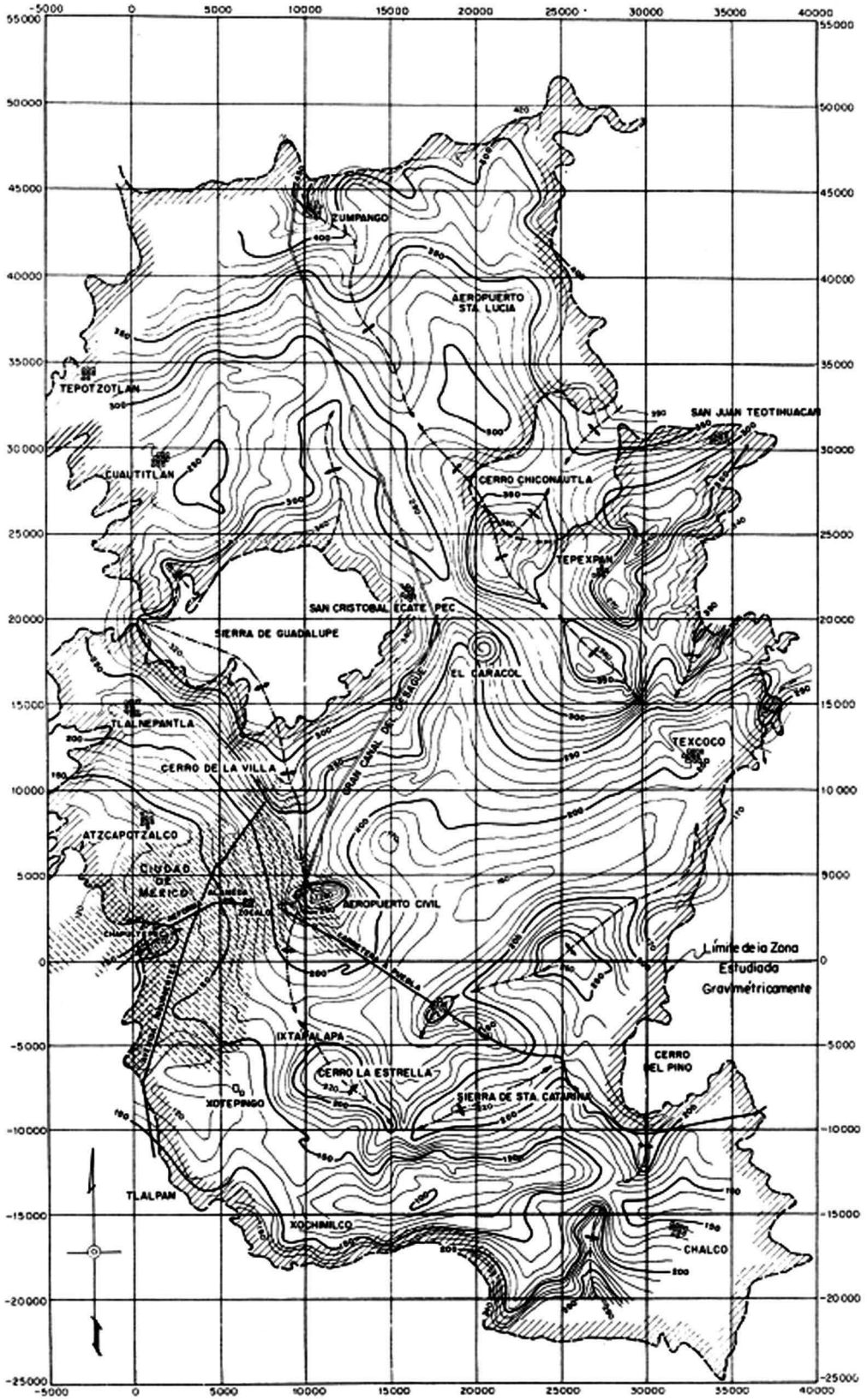

Figure 1. The gravimetric map reported by Marsal and Mazari, (1969). Contour values divided by 10 are mGals. Rectangular coordinates are in meters.

steps reaching a depth of 1000 m. This model corresponds to the area in which the largest damage was recorded in the September 19, 1985, earthquake in Mexico City.

Gravity inversion

Various new approaches to 3-D potential field inversion are now available (e.g., Camacho *et al*. 2002; Montesinos *et al*. 2003), which appeared after the forward model reported by Álvarez (1986b) for a portion of the basin of Mexico. They are being applied more frequently to the modeling of volcanic edifices, including their magma chambers (Represas *et al*., 2012; Álvarez and Yutsis 2015). In the present case the inversion method described by Macleod and Ellis (2013) was used, based in turn in the theoretical considerations of Ellis *et al*. (2012). A 3-D mesh is built under a selected surface area in which a grid of magnetic or gravity values is defined. In the present case the selected surface area is delimited by the polygon in Figure 2a. Each volume element (voxel) of the mesh is assigned a density or a magnetic susceptibility value, depending on the type of inversion performed. Next, the contribution to the total field of each voxel is calculated at an observation point in the surface. The total contribution of the set of voxels is compared to the corresponding measured value on the surface. The process is repeated for each observation point in the surface until the difference between the calculated and measured values is less than a predetermined value. In the present case this value was chosen to be 5 percent of the standard deviation. Thus the grid generated by the inversion process does not differ from the measured grid more than 5 percent of the standard deviation. In the present inversions grid dimensions within the polygon are 43 x 37 x 8 cells of X=1.0, Y=1.0, and Z= 0.5 km respectively. Padding cells are added where appropriate, to fulfill computation requirements.

Modeling is performed on the gravimetric field only, since aeromagnetic data over this region are missing (NAMAG, 2002). 3-D inversion of the gravity field yielded the density distribution in Figure 3a, showing the inverted volume clipped along L4 and the full (unclipped) density range. Darker colors correspond to higher densities and lower ones to lower densities. Notice the presence of a narrow SW-NE surface alignment of higher density materials (volcanic) across practically all the inverted region; it apparently corresponds to the volcanic activity that started in the Pleistocene following SW-NE fractures. Figure 3b shows the inverted volume clipped along azimuth 53° following the above surface alignment; the highest density shown in the vertical section corresponds to the roots of Cerro de la Estrella. Both figures exhibit low-density materials (blue tones) in the deeper layers; these may correspond to Lower Cretaceous limestones that exist in this region below elevations ~1000 m (SGM, 2002), or to mixtures of sedimentary and igneous formations whose densities are averaged in the voxel volumes of 1 x 1 x 0.5 km.

The density distribution can now be analyzed selecting density ranges of interest. In Figures 4a through 4f results are presented in various density ranges. The inversion results in the region enclosed by the black polygon in Figure 2a will be analyzed by means of a density clipping process. This way one can select density ranges of interest and see their 3-D distributions under the basin. Figure 4a shows a 3-D rendering of the density volumes in the 2.70-2.78 g/cm^3 density range under the basin; all other density values are suppressed. This density range corresponds to the highest densities in the inverted distribution, including the higher density materials outcropping in various places: basalts and dacites. The topography (Ryan *et al*., 2009) is included for reference purposes. Notably, on the western side of the basin there is a lack of these materials while the eastern side is heavily populated with them. In terms of seismic waves travelling W to E this implies intersecting a density interface where these waves can be reflected back to the west. As mentioned above, Álvarez (1988) proposed the existence of a canyon in this region, which by now should be filled out with clastic and sedimentary materials.

The distribution of materials within the intermediate density range (2.68-2.74 g/cm^3), shows they are intermixed with the higher density materials in the east side (Figure 4b). Materials of intermediate densities begin to populate the west side of the inverted volume.

Intermixed with the above materials there are regions in the next density range (2.57-2.70 g/cm^3) as shown in Figure 4c. Towards the west the region corresponding to the canyon proposed by Álvarez (1988), found empty in the high-density range, now appears as an isolated volume. This may represent the canyon filled up with sediments.

In Figure 4d, a perpendicular view, an attempt is made for mapping the regions with lowest densities (2.57-2.63 g/cm^3) that should correspond with the water saturated sediments. The correlation of these regions with the presently known saturated zones is quite satisfactory.

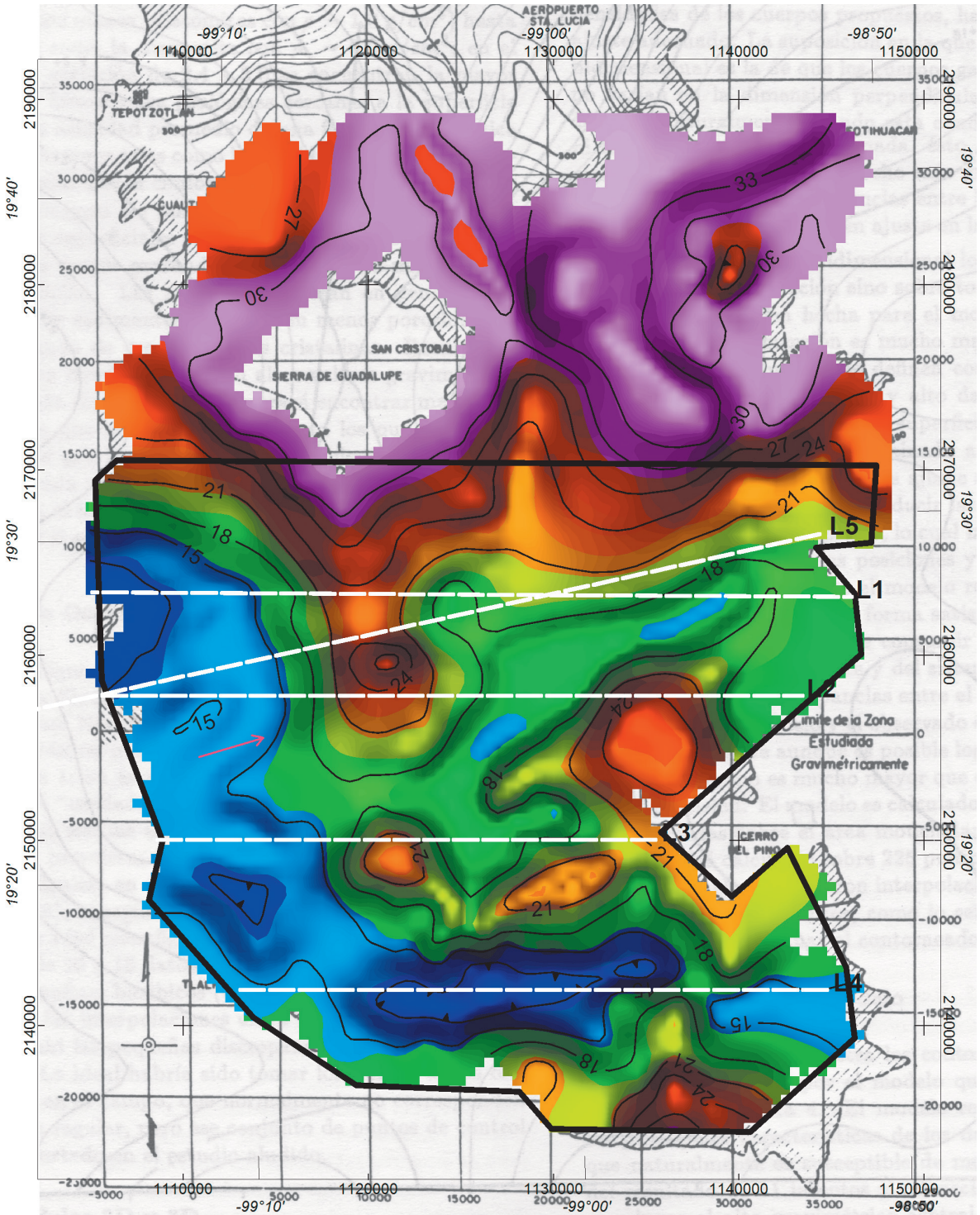

Figure 2a. Gravimetric map resampled and contoured from that in Figure 1. Contour values are in mGals. Coordinates are geographic and UTM. The reference polygon (black) for the 3-D inversion is included, as well as five dashed lines (L1 to L5) indicating the location of the gravity models discussed in the text.

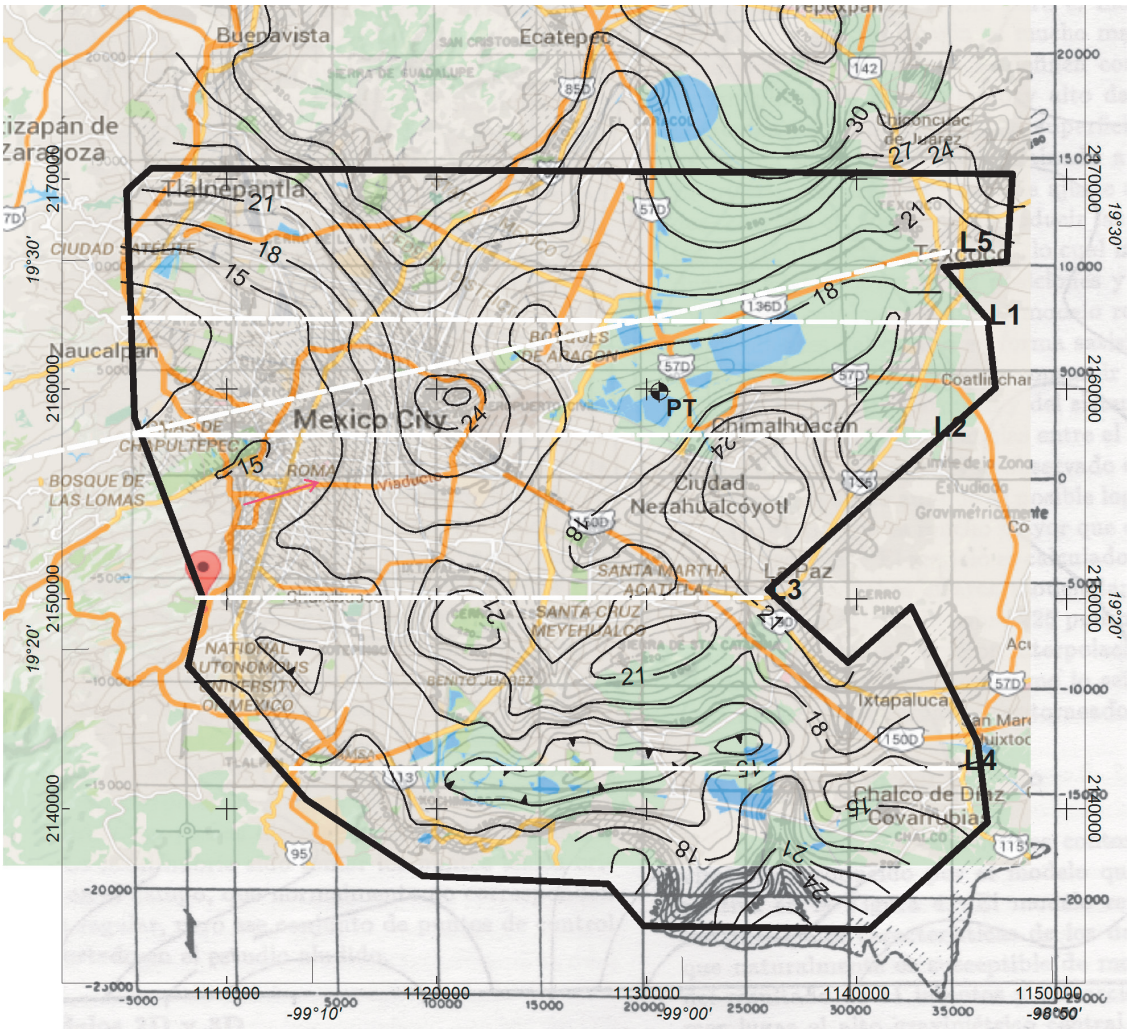

Figure 2b. The contours of the Bouguer anomaly are superposed to a reference map in which various locations in the study area can be identified. The reference polygon and L1 to L5 are the same as in Figure 2a. PT approximate location of Pozo Texcoco (Marsal and Graue, 1969) that penetrated 2065 m.

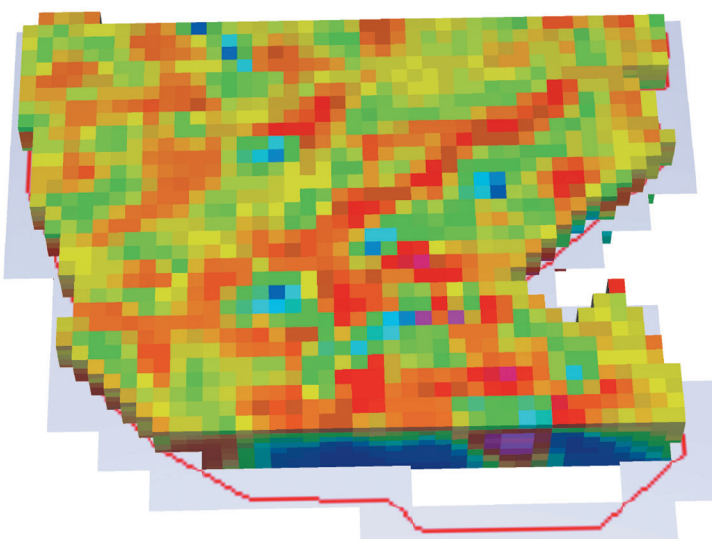

Figure 3a. 3-D density distribution obtained from the inversion of the gravity field in Figure 2a. The polygon defining the inverted region is shown in red. The full density range is shown (2.55-2.78 g/cm3). The distribution is clipped along the Y-axis coinciding with L4 Xochimilco-Chalco (see Figure 8). Towards the center, notice the high-density SW-NE (red) alignment crossing the region almost completely. The depth range is -2750<z<2620 m.

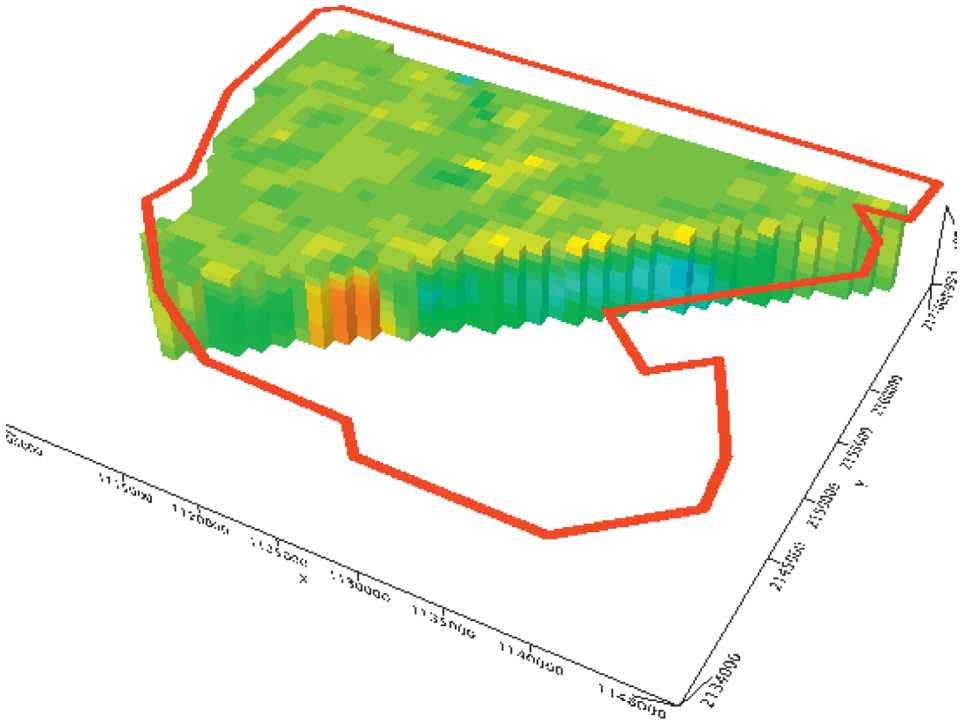

Figure 3b. 3-D density distribution obtained from the inversion of the gravity field in Figure 2a clipped along azimuth 53°, along the high-density alignment mentioned in Figure 3a. The full density range is displayed. This view shows a low-density region under Texcoco Lake overlain by the shallow, higher-density materials that form the surface alignment. The depth range is the same as in Figure 3a. Coordinates are UTM.

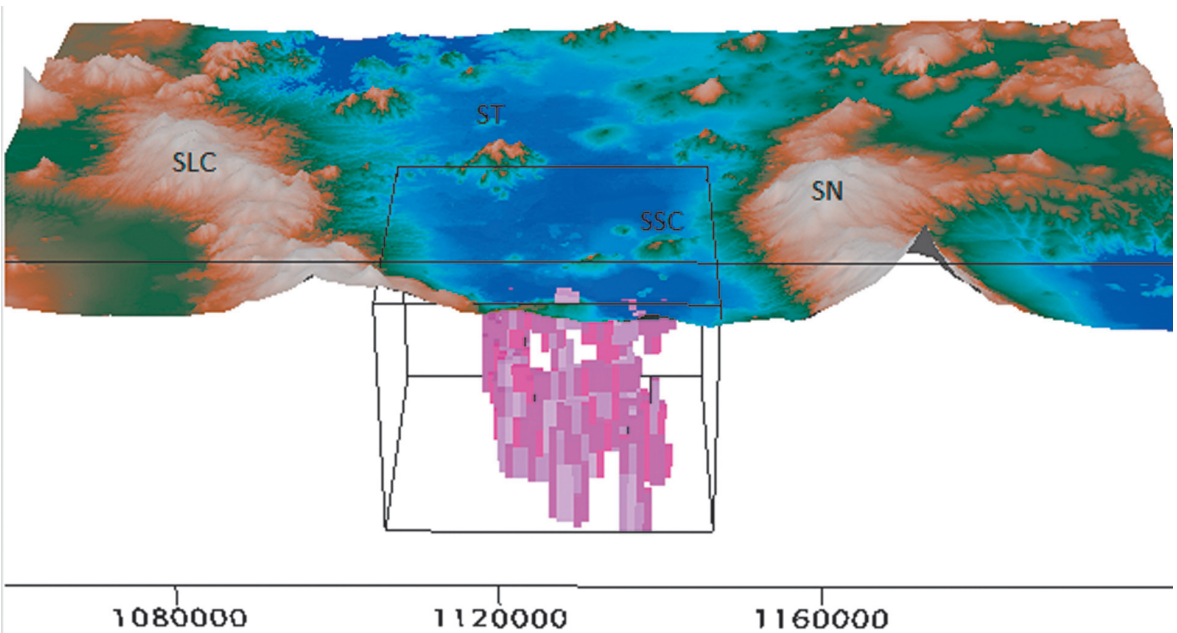

Figure 4a. 3-D rendering of the basin of Mexico showing the inverted region in the reference box, displaying the density distribution in the 2.70-2.78 g/cm3 range. The west portion is devoid of these density materials. Vertical exaggeration of 10 gives the rendering an elongated appearance. Topography from Ryan et al. (2009). SLC Sierra de Las Cruces, ST Sierra del Tepeyac, SSC Sierra de Santa Catarina, SN Sierra Nevada.

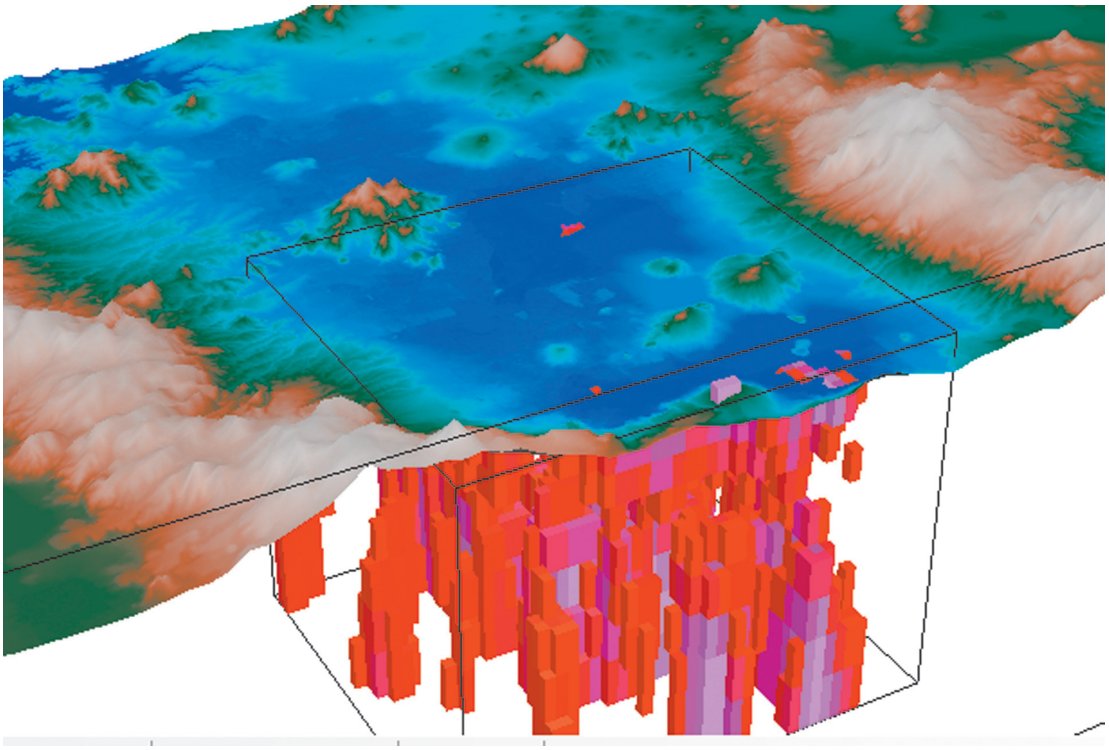

Figure 4b. 3-D display of the density distribution in the 2.68-2.74g/cm3 range view from the SW. Magenta represents the lowest values. Vertical exaggeration is 10. Owing to their size, a few voxels pierce the surface of the digital elevation model.

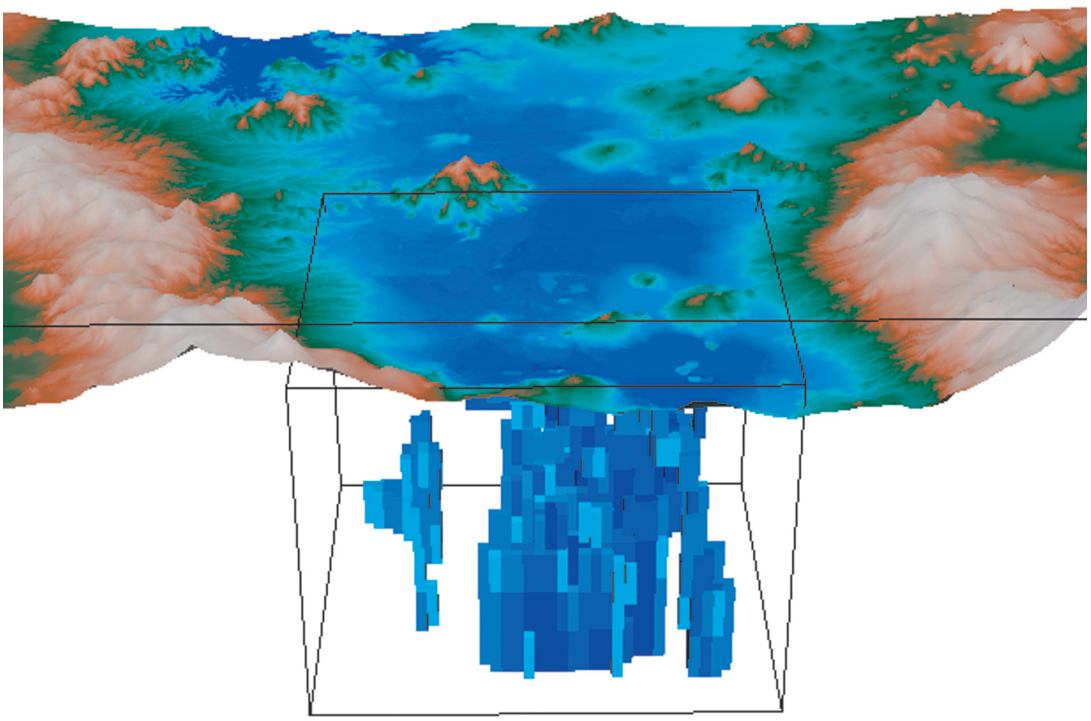

Figure 4c. 3-D display of the density distribution in the 2.57-2.70 g/cm3 range. Darker blue corresponds to the lowest densities; notice how on the eastern side they extend to the deepest layers. In the west side appear layers of materials filling out the region previously devoid of high-density materials. Vertical exaggeration is 10.

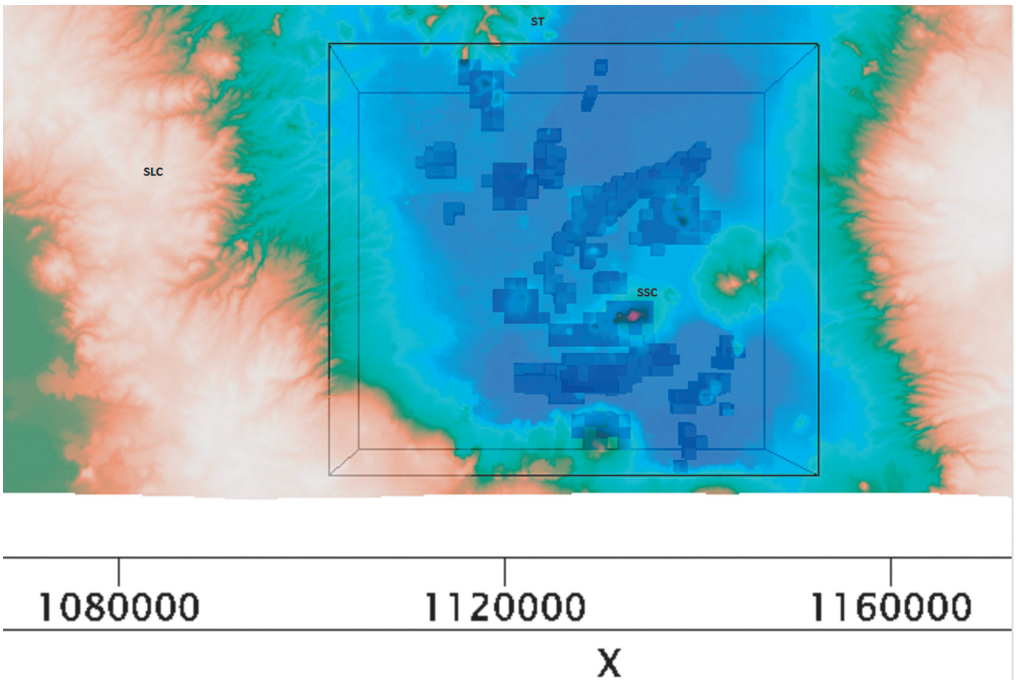

Figure 4d. The density distribution in the lowest range (2.57-2.63 g/cm3) is shown in a vertical view. Notice the coincidence between this voxel distribution and the presently mapped regions of saturated lacustrine regions in the basin.

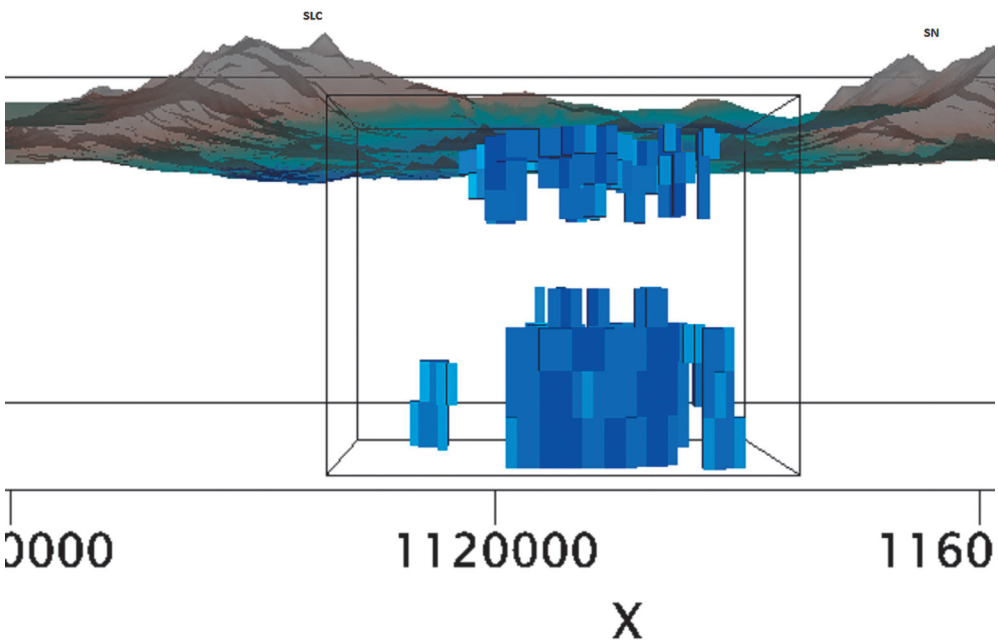

Figure 4e. This is the same density distribution as that of Figure 4d, the only change is the orientation of the 3-D view, which is now from the south. It shows two voxel distributions separated by a gap. The upper distribution corresponds to the saturated sediments distribution while the lower one corresponds to a mix of igneous and sedimentary materials.

The view in Figure 4d no7d is changed to view from the south in Figure 4e, which shows that the same density distribution is vertically divided into an upper and a lower cluster, which could not be appreciated in the previous view. The former corresponds to the surface saturated sediments, while the latter is tentatively assigned to Cretaceous limestone formations.

A cross-section along the Xochimilco-Chalco region is derived from the inversion, and presented in Figure 4f; it is simply a different way of showing the inversion results, where the blocky voxel appearance has been substituted by an interpolation. It shows high-density materials overlying a low-density distribution. Here we can readily appreciate the link between higher densities and volcanic materials, since at the center we have a volcanic structure (Volcán Xico) and under it a high-density distribution. At about half the depth shown there is a sharp interface separating the high-density region from the lower density distribution, probably corresponding to Cretaceous limestone. The 2-D modeling presented below will complement this result.

2-D gravity models

The area analyzed includes all the southern portion of the basin, from Sierra del Tepeyac to the Xochimilco-Chalco region. Five 2-D models are constructed across the basin. Four W-E lines are shown in Figure 2a labeled L1 through L4, and one diagonal (SW-NE) labeled L5. Notice they are contained within the extent of the 3-D inverted area; they are calculated with the Talwani *et al*., (1959) algorithm. In the 2-D model, formations above the densest one (basement) consist of layers of lesser densities. Density layers with D=2.55 g/cm^3 appear to correspond to lava flows and other volcanic materials, while those with D=2.45 g/cm^3 correspond to clastic Quaternary fill and lake deposits.

L1 runs from Atzcapotzalco to Texcoco (Figure 5). At x= 14 km a positive Bouguer anomaly reflects the presence of the south extension of Sierra del Tepeyac which is buried by sediments. The 2.8 g/cm^3 density region shows a steep angle to the west; this density interface is proposed to be a reflector of seismic waves arriving from the west-southwest. In the eastern portion another volcanic region is intercepted at x= 39 km that apparently corresponds to an underground extension of Chimalhuache volcano edifice. The 18 mGal contour in Figure 2a shows a SW-NE elongation around this volcanic structure suggesting that the original intrusion has such an orientation; the NE portion of L1 intercepts this anomaly at that location.

L2 runs from Bosques in the hills area to Texcoco in the eastern portion of the basin (Figure 6). The west end of this line matches the model of L5, as it should, since both start approximately in the same region, the 2.55 g/cm^3 formation surface in the hills area in both models. Some layers in the 2.70<D<2.75

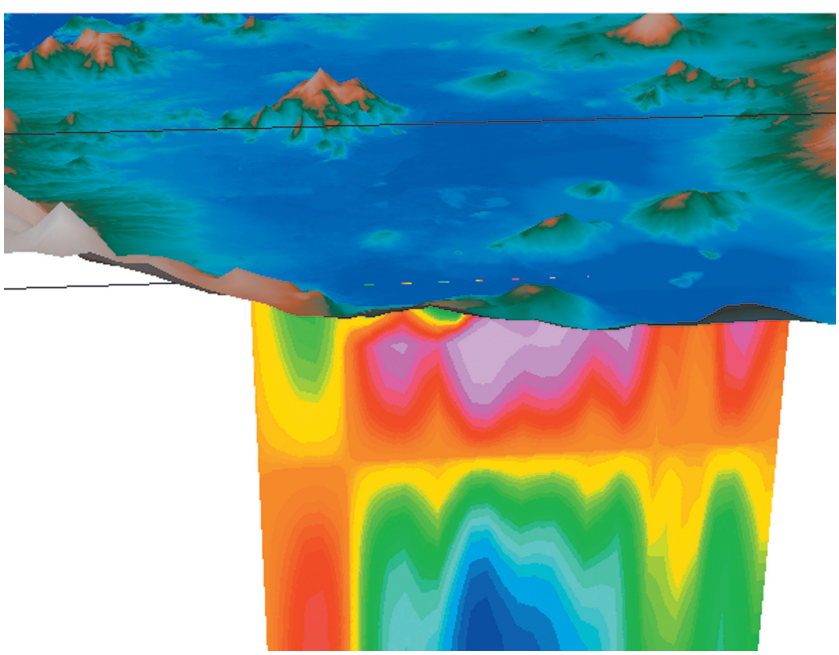

Figure 4f. Cross-section along L4 derived from the 3-D inversion. Vertical exaggeration is 10. The blocky appearance in Figures 3a and 3b are substituted by a smooth interpolation. High densities are associated with surface volcanic structures. Deeper low-density regions appear to correspond to limestone formations.

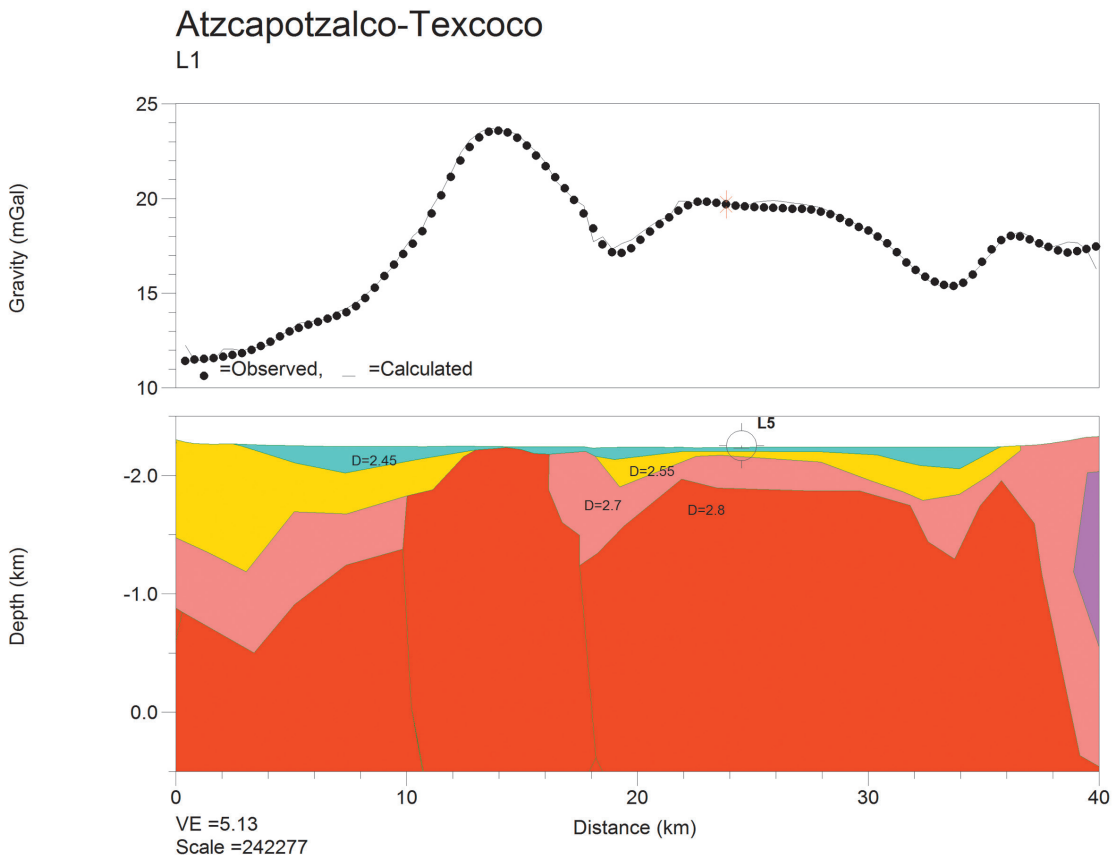

Figure 5. 2-D gravity model along L1 to a depth of 500 meters below sea level (mbsl). W is to the left and E to the right. Position marked L5 shows the intersection with that line. The eastern section apparently corresponds with an extension of the anomaly corresponding to Chimalhuache volcano (see Figure 6).

g/cm^3 density range are interpreted as Cretaceous limestones, although the actual nature of these layers cannot be confirmed with this gravity model alone. At x=29 km the line intersects an isolated, dome-type structure above an otherwise flat region. The 2-D model reflects the underground geometry of this formation as a volcanic chimney mapped as andesite (SGM, 2002) corresponding to the monogenetic Chimalhuache volcano. A similar dense structure approach the surface at x= 14 km; it corresponds to the same volcanic formation as Sierra del Tepeyac and Peñón de los Baños.

The structure at x=14 km is close to the surface but does not outcrop; however, it outcrops 5 km south of that position, close to the International Airport, at Peñón de los Baños location. Incidentally, this name makes reference to the presence of Temazcales or baths of thermal waters that were used since the Aztec times with medicinal purposes. The presence of these hot springs is intimately linked to recent volcanic activity, confirming its volcanic origin. A geological cross-section inferred across two neighboring exploration wells was reported (Marsal and Mazari, 1969; Álvarez, 1988) in which the interface between sedimentary/clastic-andesite/basalt reaches 120 m below the surface in that region, providing an additional validation of this model. One well intersected andesites from 220 m to its bottom at 1250 m, and the second well intersected basalts from 500 m to its bottom at 1350 m depth.

Pozo Texcoco (Marsal and Graue, 1969) penetrated 2,065 m (Figure 2b). The stratigraphic column shows conglomerates, breccias, sandstones, sandy-clays, clays, lacustrine limestone, anhydrite, igneous rocks, sandy tuffs, tuffs, ashes and clayey tuffs. The presence of 13 interspersed igneous

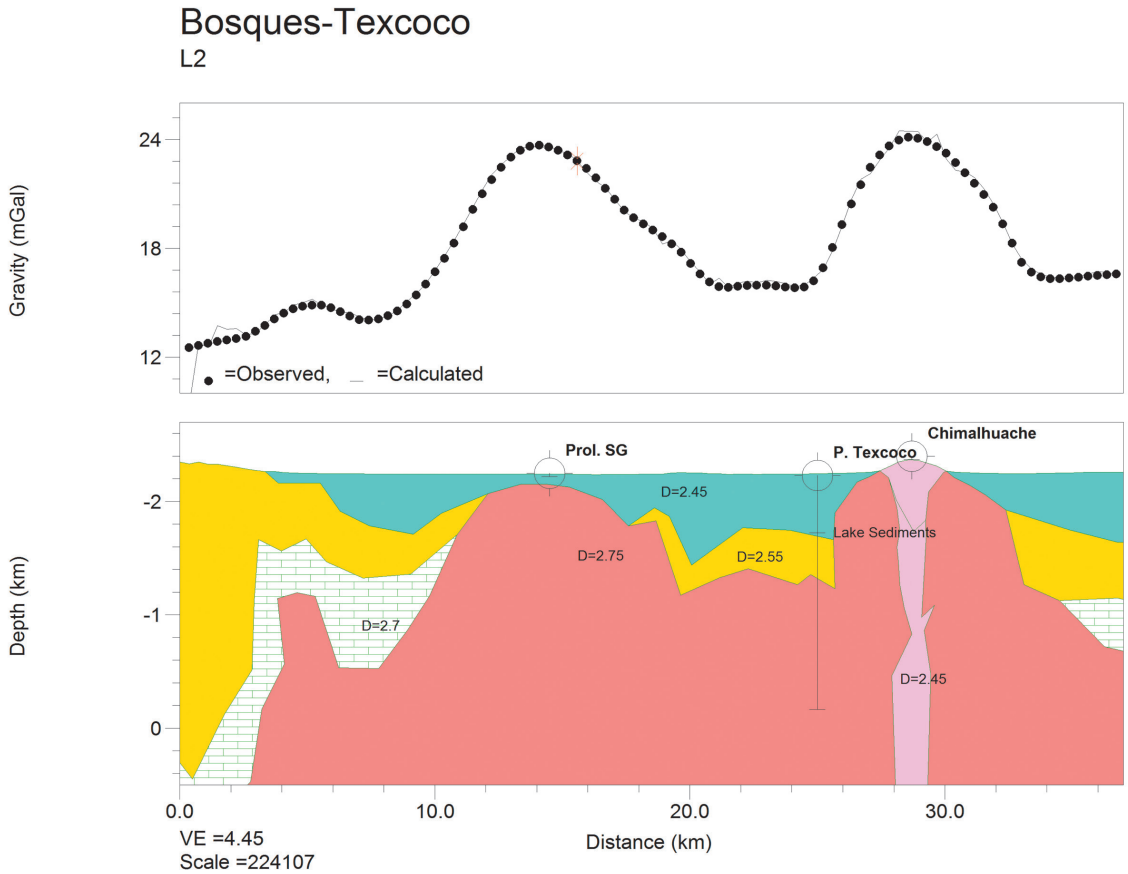

Figure 6. 2-D gravity model along L2 to a depth of 500 mbsl. Topography reflects the hills region to the W and the presence of Chimalhuache volcanic structure at x=29 km whose chimney is neatly defined in the model. The body at x=14 km approaching the surface corresponds to the underground extension of Sierra de Guadalupe (Prol. SG). Pozo Texcoco reached 2065 m depth.

flows of thicknesses varying from 3.5 to 108 m at depths from 600 to 2000 m denotes great volcanic activity in the Tertiary. In the 3-D inversion the varying densities of these materials are averaged in each voxel of 1 x 1 x 0.5 km dimensions; consequently they may only reflect rough density patterns at their corresponding positions.

L3 runs from Xotepingo to La Caldera in the east (Figure 7). Topography along the line is rather flat except where it intersects two volcanic structures. At x=12 km the volcanic structure intersected corresponds to Cerro de la Estrella, and at x=25 km the volcanic structure appears to be connected with La Caldera volcanic edifice; two volcanic conduits are modeled at those places. A graben-type structure at x=21.5 km, near La Caldera, appears to be presently filled up with volcanoclastic materials. Although aligned with the Sierra del Tepeyac-Peñón de Los Baños structure, Cerro de La Estrella does not belong to it; further ahead (Figure 10a) it will become apparent that they are geologic formations independent of each other, emplaced at different times in the Mexico basin.

L4 runs W-E from the Tlalpan region to Chalco (Figure 8). The whole region is located within the largest negative Bouguer anomaly and the whole region was covered by a lake until a few decades ago. Actually, that was one of the individual lakes left after the ancestral lake fragmentation. At x=1.8 and x=24.7 km two structures are intercepted in the 2-D model. The former shows only a slight surface deformation and the latter correspond to Xico volcano, which is located 2 km to the north and projected onto L4. The 2-D model and the associated cross-section from the 3-D inversion (Figure 4d) show a remarkable region of low densities towards the center of the line, 15 km in width, starting at a depth of ~1 km

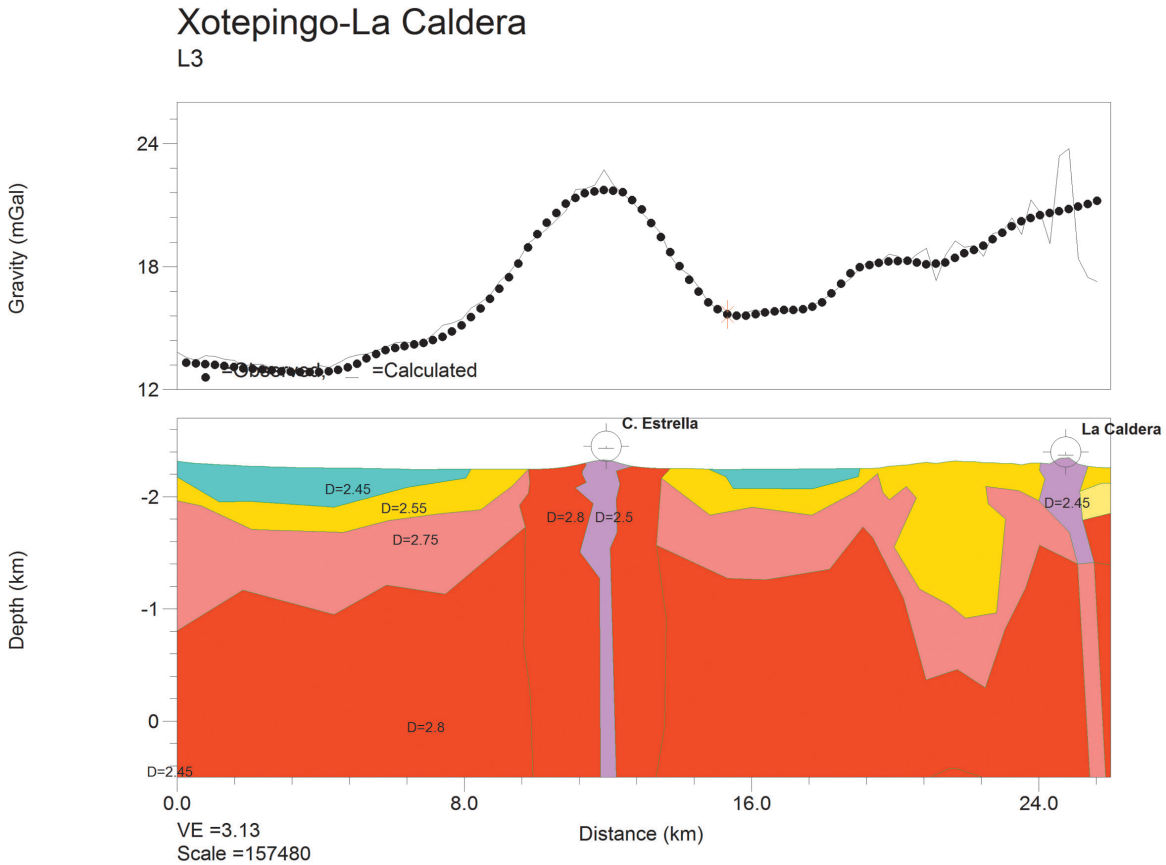

Figure 7. 2-D gravity model along L3 to a depth of 500 mbsl. W is to the left and E to the right.Two volcanic structures are intersected: Cerro de La Estrella at x=12 km and La Caldera at x=25 km. The model admits two volcanic chimneys at those places.

and continuing below sea level, and in the case of the cross-section high-density materials associated with volcanic flows overlie the low-density region. The 2-D model, however, shows low-density materials at the top. This discrepancy will be discussed below.

As reported above, in the Pleistocene the basin contained deep canyons that drained toward the south, prior to the Upper Quaternary emplacement of Sierra del Chichinautzin. It is plausible that the low-density anomaly under discussion corresponds to Creatceous limestone. The presence of higher density materials on top of the sediments can be explained as the result of younger volcanic materials such as lava flows and intrusions populating that region. The limestones would be located between 9<x<16 km with the deepest portion between 12 and 14 km. At x=27 km another low-density region appears at depths below ~1 km. It is possible that this may also correspond to limestones. In a geological cross-section of Sierra del Chichinautzin (SGM, 2002) limestones are present at depths ~1500 m below the surface; this formation also outcrops in neighboring Morelos State.

The model reveals a volcanic chimney that corresponds to Xico volcano located at x=24.5 km that actually fed the volcano. In fact this observation exemplifies how intrusions in this area deposit higher-density materials in the surface, as detected in the inversion process. The cross-section also shows the presence of the volcanic conduit at this position in the form of a thin, medium-density region.

The surface density distributions of the 2-D model and the cross-section from the 3-D model show discrepancies, particularly regarding the uppermost layers. The 2-D model shows low-density materials associated with the water saturated layers, while the inverted cross-section shows high-density materials in those layers. The difference arises in the modeling

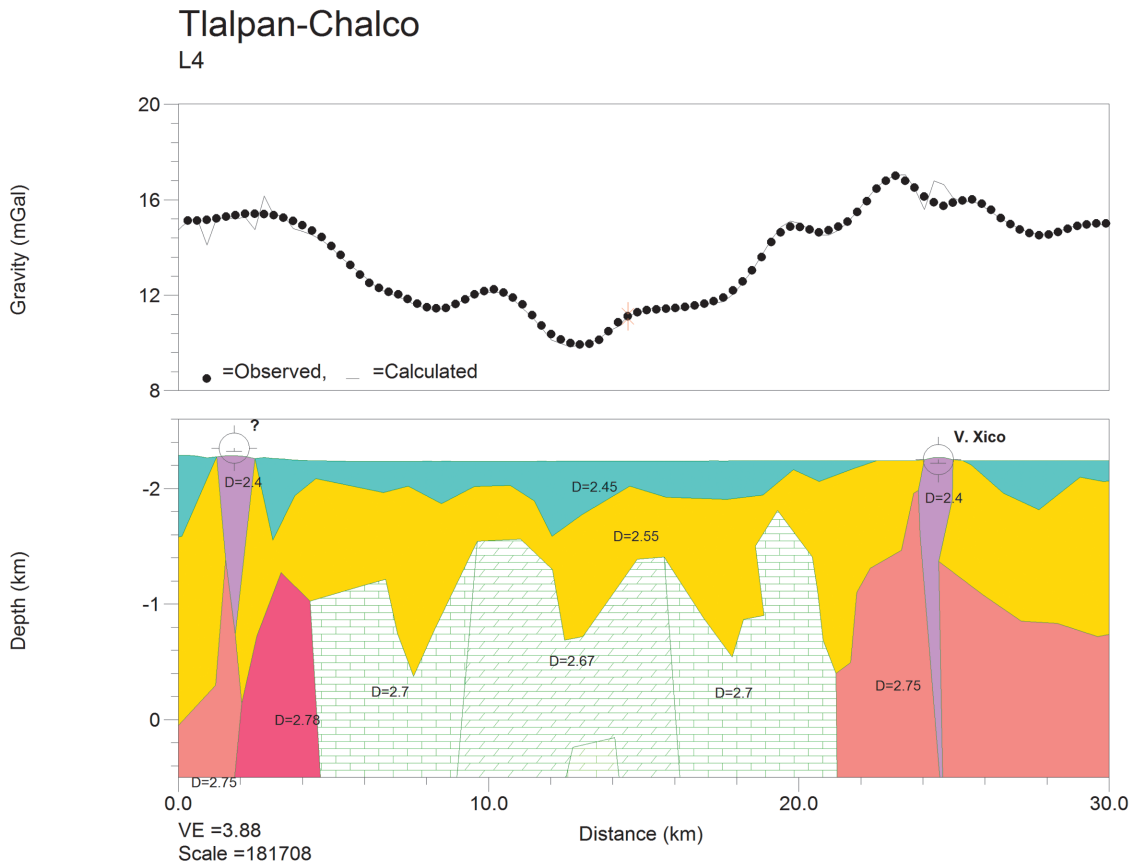

Figure 8. 2-D gravity model along L4 to a depth of 500 mbsl. W is to the left and E to the right.The region of low densities toward the center probably corresponds to Cretaceous limestone, mapped under nearby Sierra del Chichinautzin at similar depths (SGM, 2002).

procedure. In the case of the inversion the uppermost layer is defined by voxels of 1 x 1 x 0.5 km in which the densities of the various geologic formations are necessarily averaged. It is apparent that in such volumes the densities of the volcanic materials prevail over those of the sedimentary layers. In the 2-D direct models the averaging process does not exist, although there the assumption is made that the formations extend to infinity in the Y-direction. In spite of these modeling differences there are remarkable coincidences between the results of both procedures, which tend to strengthen the validity of the models, particularly regarding the presence of volcanic structures.

In order to sample the Texcoco Lake region a diagonal line (L5) runs SW to NE (Figure 9); it starts at approximately the same location as L2 (here named Chapultepec), ending north of L1. It also intersects a dense formation (D=2.8 g/cm^3) between 16<x<23 km, interpreted as the underground extension of Sierra del Tepeyac. The Bouguer anomaly of this formation, in a rather flat terrain, reveals the presence of a dense body at that position. The boundaries of this body to the west and east are almost vertical walls; it was probably intruded in the same time span corresponding to the formation of Sierra del Tepeyac. Comparing the western portion of this model with that of L2 one finds neat similarities. The region of Texcoco Lake is located on the eastern half. Under the surface, the model shows the third layer with a density of 2.75 g/cm^3 that may represent a mixture of limestone, igneous formations and sedimentary fill.

Discussion

The aim of this study was to try to define regions within the basin of Mexico that may be reflecting surfaces to incoming seismic waves. After reaching such surfaces, an incoming seismic wave would be reflected and refracted.

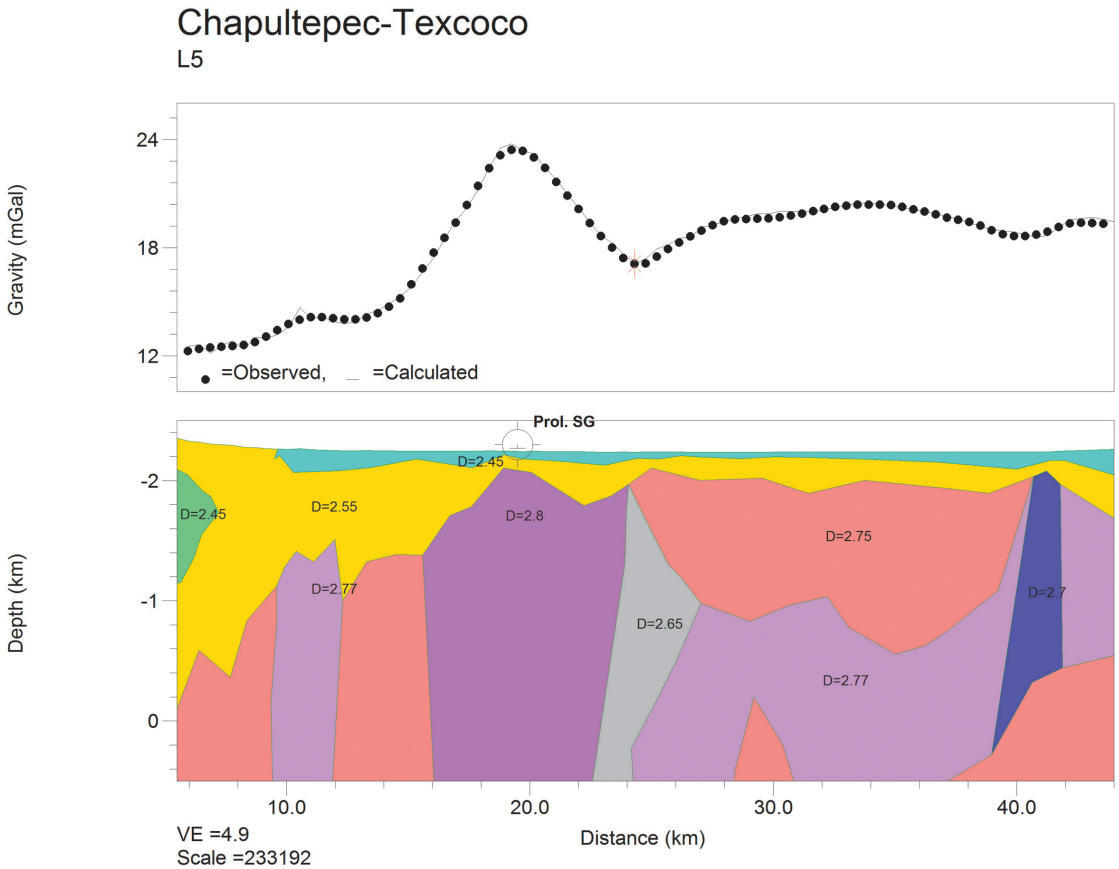

Figure 9. 2-D gravity model along L5 to a depth of 500 mbsl. The topography is rather flat except to the west, in the hills region. The mark at x=19 km shows the center of the Sierra de Guadalupe extension (Prol. SG). The Texcoco Lake region is located between 24<x<40 km, where the third layer has a density of 2.75 g/cm3; this layer may represent a limestone formation.

The possibility of having reflected waves in this region opens the possibility of interaction of these waves with incoming ones. As previously noted, a model of interaction between such waves was proposed (Álvarez, 1986a) that affects the surface saturated layers in such a way as to produce strong, local, vertical motions of the ground, affecting distances of only a few meters, capable of deflecting, and in some cases breaking, tram rails in the vertical direction. It is of the outmost importance to bear in mind the great wavelength difference between these interactions and those of the seismic travelling waves; the former involves meters while the latter involves kilometers.

Using seismic reflection techniques Marsal and Graue (1969) report seismic wave propagation velocities in the Texcoco Lake area starting with a surface layer of 30 m thickness and 600 m/s velocity. From that depth to ~350 m they found a 1700 m/s layer that ends at "Refractor A" interface, followed by a layer of 2900 m/s ending at another "Refractor B" interface at 1000 m depth. The deepest region showed a 4500 m/s velocity down to the maximum depth of the well (2065 m). The propagation velocity increasing with depth in the formations sampled by the well, appear to be due only to compaction and, consequently, with density increments with depth. Velocities in dense, igneous masses should reach ~6000 m/s. Interaction of arriving and reflected waves should occur in the surface of the low-velocity surface layer, in order to induce the observed damage (Álvarez, 1986a).

Seismic wave reflection may occur at surfaces where there is a density contrast between the geological formations involved (i.e, where a change in propagation velocity occurs). Figure 10a shows a vertical view of the surface in the basin of Mexico where density has a value of 2.70 g/cm^3. This surface

encloses the volumes in which density is higher than the above value, as can be seen in the south portion of the figure, where two red spots of higher density pierce the surface. Notice that surfaces along the N-S direction will preferentially reflect seismic waves arriving from the W, such as Sierra del Tepeyac, while those along the W-E direction, such as Sierra de Santa Catarina, will preferentially reflect waves from the S. Naturally, reflection phenomena will depend on the magnitude of the earthquake; the higher the magnitude the larger the amplitude of the reflected waves and the larger their effects on the surface.

Figure 10b shows a horizontal view of the same surface, seen from the SW; that is, from the approximate direction of the incoming seismic waves of the September 19, 1985, earthquake. Arriving waves from the hypocenter may have encountered these surfaces, experiencing reflections on them. To the NW, two bodies represent Sierra del Tepeyac formation, separated by what appears to be a gorge covered by sediments. This figure shows a gap between the lower and upper distribution of denser bodies. The upper distribution corresponds to young volcanic edifices and flows covering the basin, while the lower one corresponds to intrusive of older ages associated with the larger surface edifices such as Sierra del Tepeyac and Sierra de Santa Catarina. What appears as a gap in this figure is actually filled with sedimentary materials of lower densities. A similar gap was found in Figure 4e.

Conclusions

The previous model of the deeper geologic formations in the Mexico basin has been extended to include the E-W limits of the basin from Sierra de Las Cruces to Sierra Nevada and from N to S from Sierra del Tepeyac to Sierra del Chichinautzin. The presence of young, dense, bodies on, or close, to the

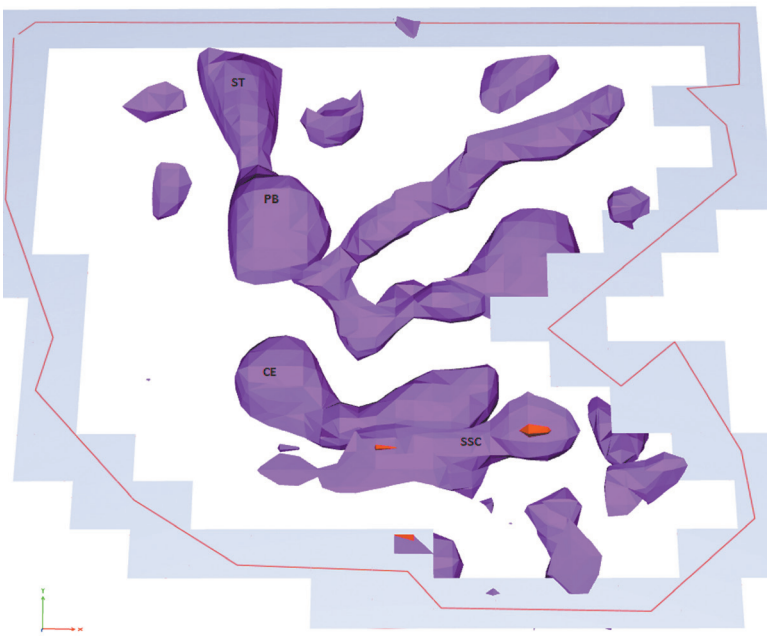

Figure 10a. Plan view of the iso-surface representing the region where the density has a value of 2.70 g/cm3 in the studied area of the basin of Mexico. This is obtained from the density distribution of the inverted gravity field. The polygon shows the inverted region, as in previous figures. In the south portion, corresponding to Sierra de Santa Catarina (SSC), two red spots pierce the surface, corresponding to higher-density formations enclosed by this surface. ST Sierra del Tepeyac, PB Peñón de Los Baños, CE Cerro de La Estrella.

Figure 10b. Horizontal view of the surface depicted in Figure 10a from the SW; the dark lines correspond to the representation of the polygon under this projection. A gap devoid of high-density regions is observed between the upper and lower distributions. ST Sierra del Tepeyac, PB Peñón de Los Baños, SSC Sierra de Santa Catarina.

surface was modeled and explained as recent volcanic edifices, usually of the monogenetic type, as well as their flows. The boundaries of the higher-density formations have been defined to depths of ~1 km below sea level suggesting that they are potential reflectors of seismic waves. The former model of Álvarez (1986b) that proposed the continuity of dense formations between Sierra del Tepeyac to Cerro de La Estrella is now modified, establishing such continuity only up to Peñón de Los Baños since a surface discontinuity is now shown to exist between Peñón de Los Baños and Cerro de La Estrella.

Depending on the orientation of these boundaries they will preferentially reflect seismic waves that are perpendicular to their orientation. It is concluded that waves arriving from the W-SW (e.g., the Michoacán subduction region) will be preferentially reflected by the structure associated with Sierra del Tepeyac-Peñón de Los Baños, and that seismic waves originating S of the basin (e.g., the Guerrero-Oaxaca subduction region) will be reflected by Sierra de Santa Catarina, given its E-W extension. Sánchez-Sesma *et al*., (1988) made a similar observation suggesting that the latter region could be particularly vulnerable to seismic events originating in southern Mexico.

In Mexico City the region of maximum damage in the September 19, 1985, earthquake was located W of Sierra del Tepeyac-Peñón de Los Baños (e.g., Álvarez, 1986a, 1990), a region in which saturated sediments and reflecting surfaces coexist, in agreement with the observations made above. The Xochimilco area to the south sustained a comparatively small damage, in spite of being a region where saturated sediments coexist with some of the lakes, but where reflecting surfaces perpendicular to the incoming seismic waves are small or missing.

In order to further test these hypotheses seismic models should be constructed considering the orientation of the incoming seismic waves and the location of the potentially reflecting boundaries described in here.

Acknowledgements

The valuable suggestions of an anonymous reviewer greatly contributed to the improvement of the manuscript. The present models are based on modeling experiences developed through projects PAPIIT IN111110, IN100912, and IN102614 from Universidad Nacional Autónoma de México, whose support is acknowledged.

References

Álvarez R., 1986a, Local surface deformations in the September 19, 1985 earthquake in Mexico City. *Comunicaciones Técnicas, Serie Naranja*, No. 412, 13p, IIMAS-UNAM, México DF. http://biblat.unam.mx/es/revista/comunicaciones-tecnicas-serie-naranja-investigaciones-instituto-de-investigaciones-en-matematicas-aplicadas-y-en-sistemas-unam

Álvarez R., 1986b, Gravimetric definition of underground formations in Mexico City: Relevance for seismic risk. *Comunicaciones Técnicas, Serie Naranja*, 443, 5p, IIMAS-UNAM, México DF. http://biblat.unam.mx/es/revista/comunicaciones-tecnicas-serie-naranja-investigaciones-instituto-de-investigaciones-en-matematicas-aplicadas-y-en-sistemas-unam

Álvarez R., 1988, Configuración profunda del valle de México: Un estudio gravimétrico. *Simp. Generación, Propagación y Efectos de Temblores,* Soc. Mex. Fís., Soc. Mex. Mecánica de Suelos, U. Geof. Mex. y Soc. Mex. Ing. Sísmica, 19-31.

Álvarez R., 1990, Structure of the basin of Mexico City and its relation to destruction in the earthquake of 1985, In *Geotechnical and Environmental Geophysics*, Ed. S. H. Ward, vol. III, 263-280, Soc. Explor. Geophysicists, Tulsa.

Álvarez R., Yutsis V., 2015, Southward migration of magmatic activity in the Colima Volcanic Complex, Mexico: An ongoing process. *International Journal of Geosciences*, 2015, 6, 1077-1099. http://www.scirp.org/journal/ijg http://dx.doi.org/10.4236/ijg.2015.69085

Bard P-Y, Campillo M., Chavez-Garcia F.J., Sanchez-Sesma F.J., 1988, A theoretical investigation of large and small-scale amplification in the Mexico City Valley. The Mexico Earthquake of September 19,1985, Earthquake Spectra 4, 609–635

Bribiesca C., J.L., 1960, Hidrología histórica del Valle de México. *Ing. Hidráulica en México*, Jul.-Ago.-Sep., 43-59.

Brocher T.M., 2005, Empirical relations between elastic wave speeds and density in the Earth's crust. *Bulletin of the Seismological Society of America*, 95, no. 6, p2081-2092. doi: 10.1785/0120050077

Camacho A.G, Montesinos E.G., Vieira R. 2002, A 3-D gravity inversion tool based on exploration of model possibilities. *Comput. Geosci*. 28, 191-204, doi: 10.1016/S0098-3004(01)00039-5.

Campillo M., Bard P-Y, Nicollin E., Sánchez-Sesma F., 1988, The Mexico earthquake of September 19, 1985-The incident wavefield in Mexico City during the great Michoacán earthquake and its interaction with the deep basin. *Earthquake Spectra*, 4, No. 3, 591-608.

CENAPRED, 1996, Estudios del subsuelo en el Valle de México. Centro Nacional de Prevención de Desastres, Cuaderno de Investigación 34, 91 p. México, DF.

Chávez-García F.J., 1991, Diffraction et amplification des ondes sismiques dans le bassin de Mexico. Ph.D. thesis, Université de J. Fourier de Grenoble, 331 p.

Ellis R.G., de Wet B., Macleod I.N., 2012, Inversion of magnetic data for remnant and induced sources, Australian Society of Exploration Geophysicists, Extended Abstracts 2012, 1-4. Melbourne, Australia.

Gardner G.H.F., Gardner L.W., Gregory A.R., 1974, Formation velocity and density - The diagnostic basics for stratigraphic traps. *Geophysics*, 39, no. 6, p770-780.

González-Casanova P., Álvarez R., 1985, Splines in Geophysics. *Geophysics*, 50, 2831-2848.

IGF-IIN, 1985, El Sismo del 19 de Septiembre de 1985. Informe y Evaluación preliminar. Elaborado por el Instituto de Geofísica con la colaboración del Instituto de Ingeniería, Universidad Nacional Autónoma de México. 25 de septiembre de 1985. http://www2.ssn.unam.mx:8080/website/jsp/Sismo85/sismo85_inf.htm

Macleod I.N., Ellis R.G., 2013, Magnetic vector inversion, a simple approach to the challenge of varying direction of rock magnetization, Australian Society of Exploration Geophysicists, Extended Abstracts 2013, 1-4, Melbourne, Australia.

Marsal R.J., Mazari M., 1969, The subsoil of Mexico City, Fac. Ingeniería, UNAM, 2a. ed. México.

Marsal R.J., Graue R., 1969, El subsuelo del Lago de Texcoco, En *El Hundimiento en la Ciudad de México y Proyecto Texcoco*, vol. N. Carrillo. Sec. Hacienda y Crédito Público. 167-202. México.

Montesinos F.G., Camacho A.G., Nunes J.C., Oliveira C.S., Vieira R., 2003, A 3-D gravity model for a volcanic cráter in Terceira Island (Azores). *Geophys. J. Inter.* 154, 393-406.

NAMAG, 2002, North American Magnetic Anomaly Group. Magnetic Anomaly Map of North America. US Department of the Interior and US Geological Survey.

Represas P., Catalao J., Montesinos F.G., Madeira J., Mata J., Antunes C., Moreira M., 2012, Constraints on the structure of Maio Island (Cape Verde) by a three-dimensional gravity model: imaging partially exhumed magma chambers. *Geophys. J. Int.* (2012), 190, 931-940. doi:10.1111/j.1365-246.2012.05536.x

Ryan W.B.F., *et al*., 2009, Global multi-resolution topography synthesis, *Geochemical Geophysical Geosystems,* 10, Q03014, doi:10.1029/2008GC002332.

Sánchez-Sesma F., Chávez-Pérez S., Suárez M., Bravo M.A., Pérez-Rocha L.E., 1988, The Mexico earthquake of September 19, 1985-On the seismic response of the valley of Mexico. *Earthquake Spectra*, 4, 569-589.

SGM, 2002, Carta Geológico-Minera Ciudad de México E14-2. Servicio Geológico Mexicano.

Singh SK, Ordaz M., 1993, On the origin of the long coda observed in the lake-bed strong-motion records of Mexico City. *Bull Seism. Soc. Am.* 84, 1298–1306

Talwani M., Worzel J.L., Landisman M., 1959, Rapid computation for two-dimensional bodies with applications for the Mendocino submarine fracture zone*. J. Geophys. Res.*, 64, 49-59.

USGS, 1985. «Shakemap atlas Magnitude 8.0 Michoacán, Mexico, 1985 September 13:17:47 UTC»

Geofísica Internacional (2017) 56-1: 57-69

Original paper

Tsunami deposits of September 21st 1985 in Barra de Potosí: comparison with other studies and evaluation of some geological proxies for southwestern Mexico

Brenda Grisset Ocampo-Rios, Priyadarsi D. Roy*, Ma. Consuelo Macías, M.P. Jonathan and Rufino Lozano-Santacruz

Received: April 01, 2016; accepted: October 26, 2016; published on line: January 01, 2017

DOI: 10.19155/geofint.2017.056.1.4

Resumen

Los habitantes del pueblo de Barra de Potosí en el suroeste de México fueron testigos de la inundación por olas después del sismo de 7.5 Mw del 21 de septiembre de 1985 hasta una distancia de ~ 500 m desde la costa. Se identificaron los sedimentos depositados por la ola de tsunami cerca del estero del Potosí y se compararon la sedimentología, mineralogía y composición química de dichos depósitos con los sedimentos que representan los entornos de pre-tsunami y los depositados en la zona cercana no afectada. Los sedimentos asociados al tsunami se caracterizaron como arenas finas (tamaño medio: 2.13-2.47 Φ), de bien a moderadamente bien ordenados (desviación estándar: 0.4-0.7 Φ). Contienen mayores cantidades tanto de fracciones finas como de gruesas (sesgo de negativo a positivo) y tienen una distribución que va de leptocúrtica a extremadamente leptocúrtica. Las características sedimentológicas de los depósitos de tsunami y los del pre-tsunami son similares. La abundancia y la asociación de los minerales pesados son también comparables en ambos depósitos. Sin embargo, los depósitos de tsunami tienen contenidos más bajos de Br y Fe_2O_3 y contenidos más altos de SiO_2 y TiO_2 comparados con los depósitos de pre-tsunami. La comparación con los depósitos ocurridos en la región durante los tsunamis del 14 de marzo de 1979, del 21 de septiembre de 1985 y del 11 de marzo de 2011, no arrojó ninguna firma característica. A excepción de la estratigrafía (i.e. base erosiva), no se observó alguna otra característica geológica que pudiera ser útil para la identificación de paleo-tsunamis en la región.

Palabras clave: Tsunami, sedimento, mineralogía, Geoquímica, 21 de septiembre de 1985, Barra de Potosí, México.

Abstract

Residents of Barra de Potosí village in southwestern Mexico witnessed inundation by waves up to a distance of ~500 m from the shore after the Mw 7.5 earthquake on September 21st, 1985. Sediments deposited by the tsunami wave were identified near El Potosí estuary and their geological characteristics (sedimentology, mineralogy and chemical composition) were compared with pre-tsunami sediments and deposits from the nearby-unaffected area. Tsunami sediments were characterized by well and moderately well sorted (standard deviation: 0.4-0.7 Φ) fine sand (mean size: 2.13-2.47 Φ) and contain higher amounts of both finer and coarser fractions (negative to positive skewed) and had leptokurtic to extremely leptokurtic distribution. Sedimentological characteristics of tsunami and pre-tsunami deposits were similar. Abundance and association of heavy minerals were also comparable both in tsunami and pre-tsunami deposits. However, lower amounts of Br and Fe_2O_3 and higher SiO_2 and TiO_2 differentiate tsunami deposits from the pre-tsunami sediments. Comparison with sediments deposited during the tsunamis of March 14th, 1979, September 21st, 1985, and March 11th, 2011, in the region did not yield any characteristic signature. Except for stratigraphy (i.e., erosive base), no other geological characteristic was useful for identifying paleo-tsunami in the region.

Key words: Tsunami, sediment, mineralogy, Geochemistry, September 21st, 1985, Barra de Potosí, Mexico.

B. Grisset Ocampo-Rios
Posgrado en Ciencias de la Tierra
Universidad Nacional Autónoma de México
Ciudad Universitaria
Delegación Coyoacán 04510
CDMX, México

Priyadarsi D. Roy*
Ma. Consuelo Macias
Rufino Lozano-Santacruz

Instituto de Geología
Universidad Nacional Autónoma de México
Ciudad Universitaria
Delegación Coyoacán 04510
CDMX, México
*Corresponding author: roy@geologia.unam.mx

M.P. Jonathan
Centro Interdisciplinario de Investigaciones
y Estudios sobre Medio Ambiente y Desarrollo
Instituto Politecnico Nacional
Calle 30 de Junio de 1520
Barro la Laguna Ticomán
Delegación Gustavo A. Madero 07340
CDMX, México

Introduction

Most of the tsunamis are caused by earthquakes with magnitude >6.5 and are associated with reverse fault in an oceanic plate. In general, the tsunamigenic earthquakes are characterized by epicenters at <60 km depth (Bryant, 2008). The southwestern coast of Mexico has been affected by local as well as distal tsunamis linked to large earthquakes originated in the Cocos and Pacific plates. Tectonic activity in the Pacific coast of Central America and South America constitutes an additional source (Farreras *et al*., 2007). Subduction of the Cocos plate underneath the North American plate at a rate of ~5.3-5.8 cm/year (DeMets *et al*., 1994) causes the local tsunamis. Data provided by Singh and Suaréz (1986) suggest that the tsunamigenic earthquakes had a recurrence interval of ~34-38 years in the state of Oaxaca, ~32-56 years in the state of Guerrero and ~74 years in the state of Michoacán. In the last three centuries, the Pacific coast of Mexico witnessed at least 56 tsunamis (Sánchez and Farreras, 1993). Besides the relatively frequent <1 m high waves, the tsunami of November 16th, 1925, generated waves up to 10 m high in Zihuatanejo (Guerrero) (Borrero *et al*., 1997).

Tsunami waves generally leave sediments deposited along the coastal regions. Some of them are buried and preserve evidence of paleo-tsunami in the geological records. They also help to reconstruct recurrence interval of past tsunamis and extend the relatively short or non-existent historical records to the geological past. The observation of modern tsunami deposits provides clues to recognize paleo-tsunami events occurred over the last thousands of years. A tsunami deposit is usually identified by sedimentary context, i.e. larger grain size than the surrounding sediments indicating high-energy depositional conditions and spatial distribution. Depending upon the availability of sediments in the source region, the deposits can vary from fine sand to gravel. Tsunami sands overly peat and mud in coastal marsh stratigraphy (Atwater, 1987). Preservation of rooted plant material beneath the sand deposit indicates deposition of sand occurred after the subsidence (Atwater and Yamaguchi, 1991). Hutchinson *et al*. (1997, 2000) observed that the tsunami deposits in lakes usually consist of a bed of coarser sand layer between two organic rich finer mud layers. Sometimes the tsunami deposits are massive and may contain multiple fining upward sequences, e.g., the Cascadian margin (Benson *et al*., 1997). Tsunami deposits in Peru consists of multiple sand layers, rip-up clasts near the base of sand layers, erosional base, a mud layer between two sand layers, mud cap and normal grading (Jaffe *et al*., 2003). Apart from the sediment texture and structure, chemical composition (higher Br, Sr, and Na), abundance of heavy minerals and microfossils were used as proxies to distinguish the tsunami deposits (Goff *et al*., 2010, 2011; Morton *et al*., 2007; Roy *et al*., 2012; Ramírez-Herrera *et al*., 2012). However, chemical dissolution and diagenesis in sedimentary deposits of tropical regions reduce the possibility of persevering these proxies in geological records (Goff *et al*., 2011).

In this study, we present texture, mineralogy and chemical composition of sediments deposited by waves associated with the tsunami of September 21st, 1985, in Barra de Potosí village in southwestern Mexico. Calculation of hydraulic roughness of the terrain of inundation through estimation of the Manning's number evaluates both the instrumental and eyewitness records of maximum wave height and inundation limit. We also compared results of this study with geological characteristics of sediments deposited by tsunamis of March 14th, 1979, and September 21st, 1985, in Zihuatanejo area (Ramírez-Herrera *et al*., 2012) and tsunami of March 11th, 2011, in several locations along the southwestern coast of Mexico (Roy *et al*., 2012).

Earthquake and tsunami of September 21st, 1985.

Tsunamigenic earthquake of Mw 7.5 had its epicenter located at 17.6 km depth at the southeast ruptured region of Zihuatanejo with ~33 km length and ~66 km width (Mendoza, 1993). However, Corona-Esquivel *et al*. (1988) did not observe any uplifted segment near Zihuatanejo but noticed raised segments along the coast of Michoacan state (west and northwest of Guerrero state). The gauges of mareographic station at Acapulco registered tsunami waves with maximum height of 1.2 m and mean speed of 709 km/h (Sanchez-Devora and Farreras-Sanz, 1993). The National Geophysical Data Centre of NOAA reports 1.2 m high waves in the Pacific Ocean and up to 2 run-ups. Recently, Ramírez-Herrera *et al*. (2012) reported that tsunami waves inundated the entire village of Barra de Potosí and identified the associated sand layer near Zihuatanejo (Figure 1).

The village of Barra de Potosí is located at a distance of ~25 km southeast of Zihuatanejo and at ~180 km northwest of Acapulco (Figure 1). El Potosí estuary is located at its southern limit and it is separated from the Pacific Ocean

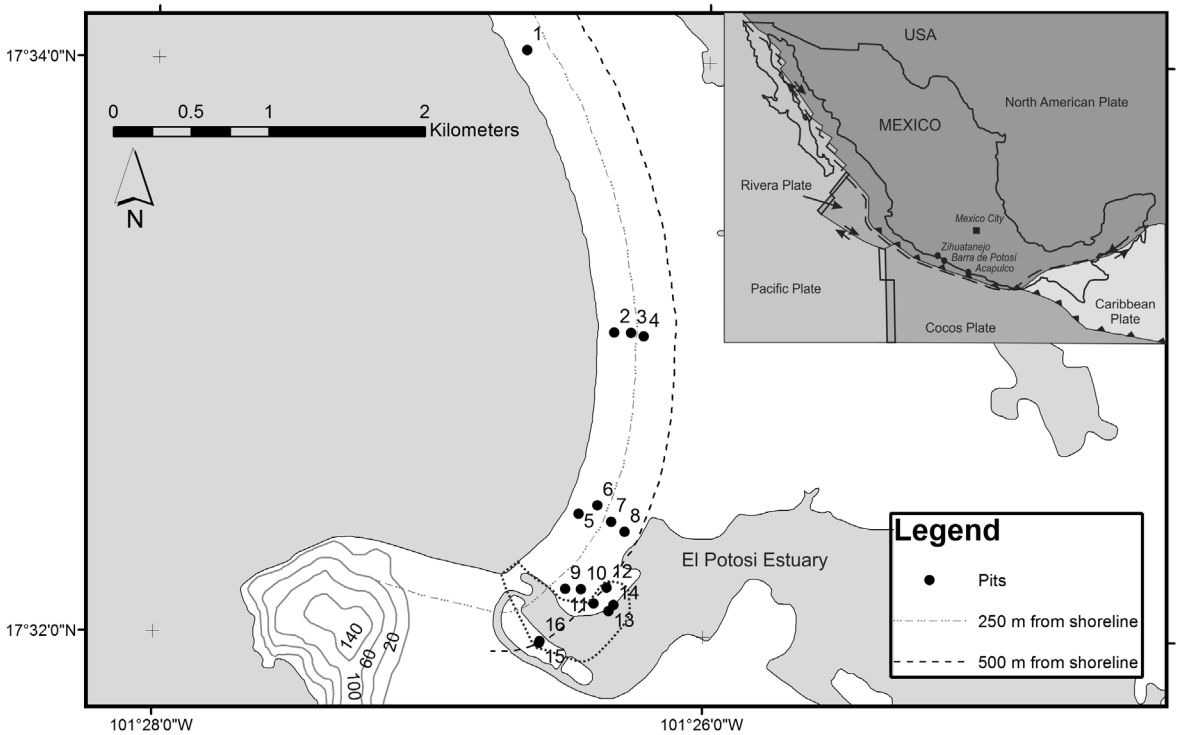

Figure 1. Tectonic setting of southwestern Mexico and location of Barra de Potosí village. Sixteen different pits/trenches are distributed at El Potosí estuary margins and in farmlands away from it. Sites of pits located in estuary margins (11, 12, 13, 14, 15 and 16) were inundated by the September 21st, 1985, tsunami waves and the reconstructed inundated area is shown in a dotted line.

by a shallow spit barrier. It is connected to the open sea during the intervals of high tide. During both the field works (April, 2010 and February, 2011), we interviewed the residents with ages between 46 and 64 years. Apart the variable wave height (~2.5 to 10 m), all the eyewitnesses agreed that tsunami waves inundated up to a distance of ~500 m from the shore and transported fishing boats from the shore into the estuary. The sites located away from the El Potosí estuary (i.e., farmlands) were unaffected by inundation and there was no loss of human life in this village.

Material and methods

A total of 16 pits and trenches up to a maximum depth of 1.2 m were dug both parallel and perpendicular to the shore. Ten of them (1, 2, 3, 4, 5, 6, 7, 8, 9 and 10) are located away from the estuary and six (11, 12, 13, 14, 15 and 16) were dug in the margin of El Potosí estuary (Figure 1). The pits/trenches dug in the estuary margin were shallow, as the ground water did not permit to dig deeper. We observed sediments deposited by the tsunami in these 6 different pits/trenches. A total of 12 samples representing tsunami deposits (6 samples by avoiding superficial layer of pedogenesis) and sediments deposited in an environment prior to the tsunami (6 pre-tsunami samples) were collected. Additionally, 4 different samples from 4 out of 10 different pits located away from the estuary were collected. Sedimentological and geochemical analyses were carried out in all the samples and mineralogical analysis was done only in 4 different samples. Sedimentological and mineralogical analyses were performed after oven drying the samples at ~40°C and sieving through 230, 120, 60 and 40 meshes. For the sedimentological analysis, we calculated mean grain size, standard deviation, skewness and kurtosis (Wentworth, 1922).

Mafic and heavy minerals were identified in two tsunami and two pre-tsunami samples collected from pits 12 and 15. Samples were separated in terms of medium sand (1.25-2 Φ), fine sand (2-3 Φ) and very fine sand (3-4 Φ). In each fraction, heavy and mafic minerals with density >2.8 g/cm^3 and lighter minerals with density <2.8 g/cm^3 were separated. Minerals with density >2.8 g/cm^3 were counted in each fraction under an optical stereoscopic microscope Leica Mz APO after preparing resin based polished sections and expressed as %. For the concentrations of 10 major element

oxides (SiO_2, TiO_2, Al_2O_3, Fe_2O_3, MnO, CaO, MgO, Na_2O, K_2O, P_2O_5) and Bromine (Br), all the oven dried samples were ground and homogenized in an agate mortar and measured in a Siemens SRS 3000 X-ray fluorescence (XRF) spectrometer.

Results

Stratigraphy

Pits (1, 2, 3, 4, 5, 6, 7, 8, 9 and 10) located away from the estuary had similar stratigraphy and consist of homogeneous massive sand and occasional heavy mineral layers (Figure 2). Most of the pits lack any primary structure (i.e., lamination) and some have a ~10-15 cm thick heavy mineral layer (e.g., at ~95-105 cm depth of pit 1). We did not observe any sedimentary unit with characteristics of tsunami deposits and consider that sediments of all these pits belong to the unaffected area.

Pits located in the estuary margins (11, 12, 13, 14, 15 and 16) comprise of three distinct sedimentary units (Figure 3). The basal unit has organic rich dark gray sand and it is overlain by oxidized massive yellow sand with a transitional contact. The uppermost unit has massive gray sand with remnants of roots, plants and shell fragments. This unit has variable thickness (~15 cm in pit 15 to 70 cm in pit 13) and is characterized by an erosive base with respect to the underlying unit. Based on the stratigraphy, we interpret the uppermost massive sand unit with an erosive base as tsunami sediments and the underlying oxidized massive sand unit as pre-tsunami sediments.

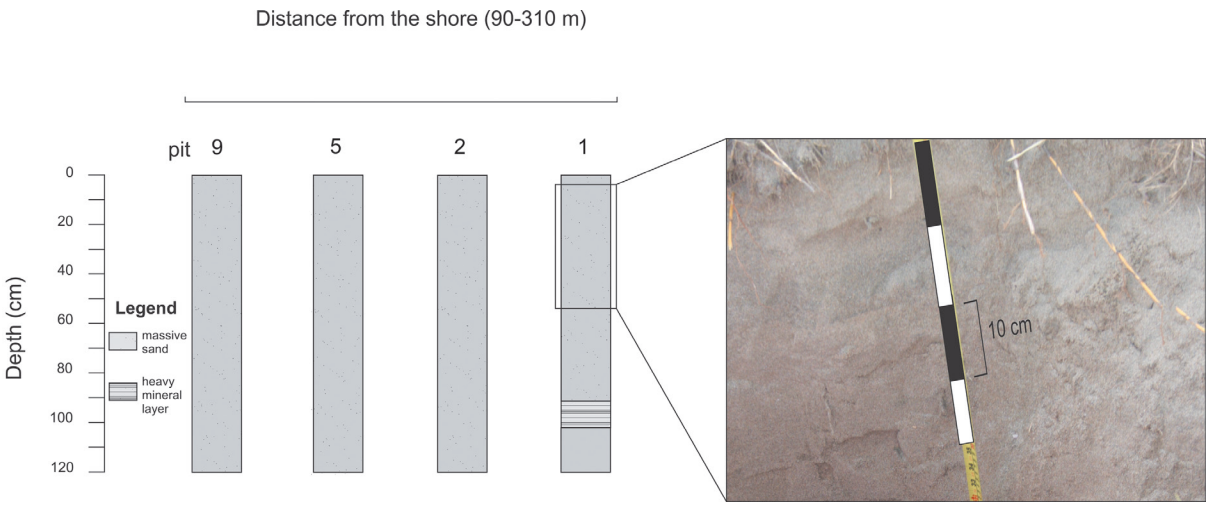

Figure 2. Stratigraphy of pits/trenches of sites located away from the estuary, Barra de Potosi, southwestern Mexico.

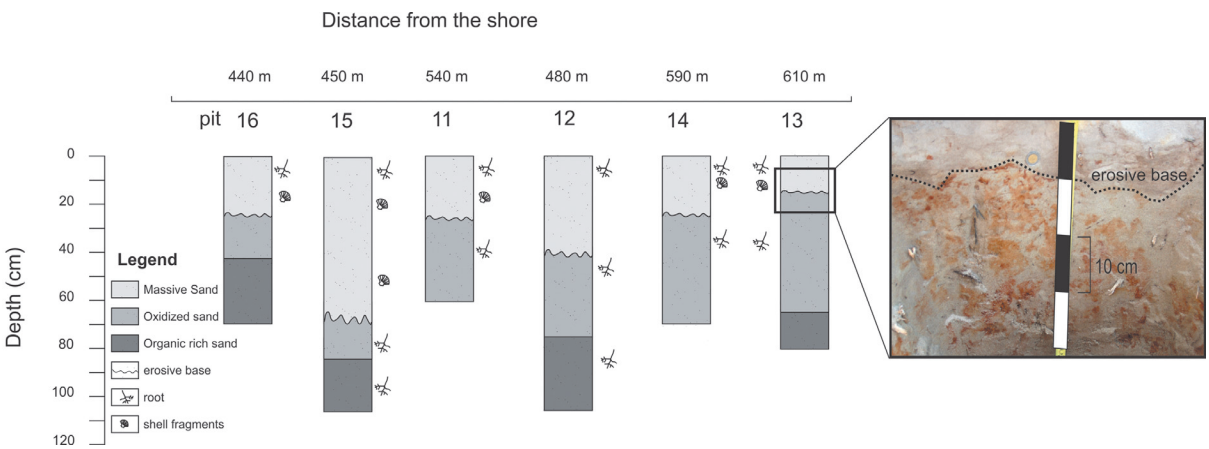

Figure 3. Stratigraphy of pits/trenches of sites located near the margins of El Potosí estuary, Barra de Potosi, southwestern Mexico.

Sediment texture

Table 1 and Figure 4 present texture of tsunami and pre-tsunami sediments and sedimentary deposits in the unaffected area.

Tsunami sediments: Mean grain size varies between 2.13 and 2.47 Φ and standard deviation ranges between 0.4-0.7 Φ. Kurtosis ranges between 1.31 and 3.83 and skewness varies between -0.25 and 0.43. Sedimentological parameters suggest that tsunami sediments are well to moderately well sorted, fine sand with leptokurtic to extremely leptokurtic distribution and highly variable skewness. Sample with negative skewness has coarser fractions and samples with positive skewness contain higher amounts of finer silt and clay.

Pre-tsunami sediments: Texture of pre-tsunami sediments is similar to the tsunami sediments (Figure 4). Pre-tsunami sediments

Table 1. Texture of sediments deposited by tsunami waves of September 21st, 1985, pre-tsunami sediments and sediments deposited in unaffected area in the village of Barra de Potosí, southwestern Mexico (see Figure 1 for pit locations).

	Pit	Mean grain size (ø)	Standard deviation (ø)	Skewness	Kurtosis	Synthesis
Tsunami	15	2.13	0.4	-0.25	1.31	Fine sand, well to moderately well sorted, variable skewed (negative to positive) and leptokurtic to extremely leptokurtic
	11	2.33	0.5	0.09	1.64	
	12	2.47	0.4	0.25	1.48	
	14	2.30	0.7	0.43	3.83	
	13	2.40	0.4	0.43	2.05	
Pre-tsunami	15	2.30	0.4	0.00	1.64	Fine sand, well to moderately well sorted, symmetrical to positively skewed and leptokurtic to extremely leptokurtic
	11	2.27	0.7	-0.08	2.19	
	12	2.57	0.5	0.20	1.64	
	14	2.47	0.5	0.56	2.25	
	13	2.33	0.5	0.11	1.64	
Unaffected	9	2.47	0.5	-0.01	1.06	Fine sand, well sorted, symmetrically distributed and mesokurtic to leptokurtic
	5	2.48	0.5	-0.09	1.00	
	2	2.07	0.5	-0.11	1.15	
	1	2.10	0.4	0.00	1.31	

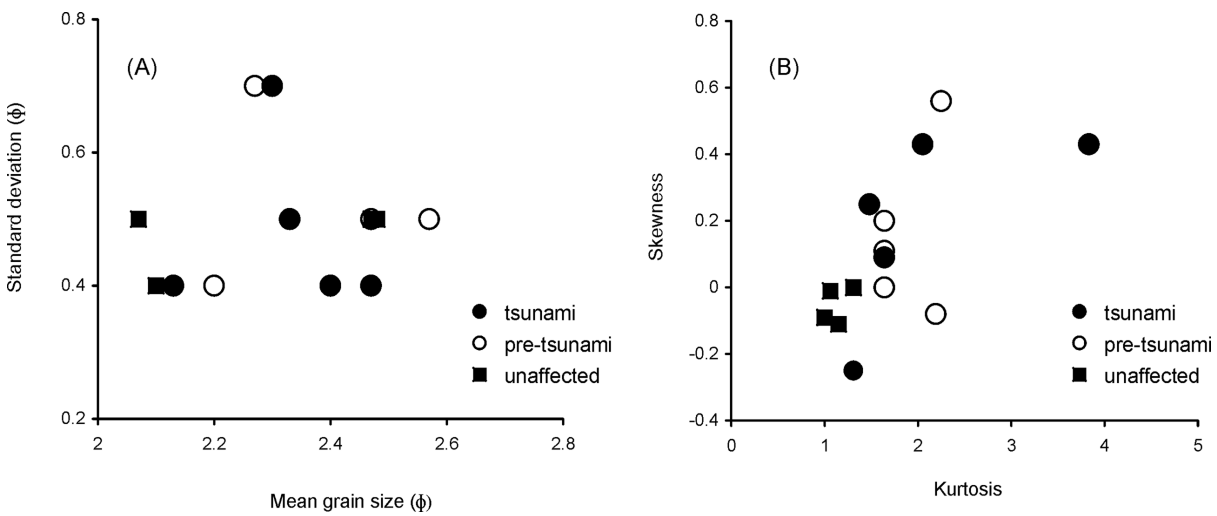

Figure 4. Distributions of (A) mean grain size vs. standard deviation and (B) kurtosis vs. skewness in sediments deposited by tsunami waves of September 21st, 1985, pre-tsunami sediments and sediments deposited in unaffected area in the village of Barra de Potosi, southwestern Mexico.

are also well to moderately well sorted (standard deviation: 0.4-0.7 Φ) fine sand (mean grain size: 2.27-2.57 Φ). Kurtosis (1.64-2.25) suggests leptokurtic to extremely leptokurtic distribution. Skewness ranges between symmetrical (-0.08) and positively skewed (0.56) and it suggests higher fractions of fine sand in some samples and more abundance of silt and clay in others.

Unaffected area: Sediments deposited in unaffected area are well sorted (standard deviation: 0.4-0.5 Φ), and fine sand (mean grain size: 2.10-2.50 Φ). All of them have mesokurtic to leptokurtic (kurtosis: 1.0-1.3) and symmetrical distribution (skewness: -0.11-0). Both of the parameters suggests that these sediments are better sorted compared to tsunami and pre-tsunami sediments and have higher fraction of fine sand (Figure 4).

Geochemistry

Table 2 presents chemical composition of tsunami and pre-tsunami sediments and sedimentary deposits in the unaffected area.

Tsunami sediments: Sediments have 69.90-74.72% of SiO_2, 0.68-1.26% of TiO_2, 11.62-13.44% of Al_2O_3, 2.48-3.80% of Fe_2O_3, 0.06-0.11% of MnO, 0.87-1.27% of CaO, 2.76-3.60% of MgO, 2.50-3.12% of Na_2O, 2.44-2.70% of K_2O, 0.03-0.08% of P_2O_5 and 5-40 ppm of Br.

Pre-tsunami sediments: In general, pre-tsunami sediments have less SiO_2 and TiO_2 and more Fe_2O_3 and Br compared to tsunami sediments (Figure 5). Contents of MnO, CaO, K_2O and P_2O_5 are comparable both in tsunami and pre-tsunami sediments. Pre-tsunami sediments have 69.08-72.72% of SiO_2, 0.45-1.17% of TiO_2, 11.35-13.04% of Al_2O_3, 3.51-4.73% of Fe_2O_3, 0.05-0.10% of MnO, 0.86-1.25% of CaO, 2.60-3.59% of MgO, 2.57-3.32% of Na2O, 2.41-2.71% of K_2O, 0.04-0.12% of P_2O_5 and 40-75 ppm of Br.

Unaffected area: Sediments deposited in unaffected area have more variable SiO_2, TiO_2, Fe_2O_3, MnO and Br compared to the tsunami and pre-tsunami sediments. However, concentrations of MgO, Na_2O, K_2O and P_2O_5 are homogeneous compared to both tsunami and pre-tsunami sediments. These sediments have 66.52-74.48% of SiO_2, 0.38-1.83% of TiO_2, 10.99-12.06% of Al_2O_3, 2.98-7.85% of Fe_2O_3, 0.05-0.16% of MnO, 0.97-1.57% of CaO, 3.05-3.84% of MgO, 2.25-2.56% of Na_2O, 2.15-2.29% of K_2O, 0.05-0.07% of P_2O_5 and 13-95 ppm of Br.

Table 2. Chemical compositions (oxides in % and Br in ppm) of sediments deposited by the tsunami waves of September 21st, 1985, pre-tsunami sediments and sediments deposited in unaffected area in the village of Barra de Potosí, southwestern Mexico (see Figure 1 for pit locations).

	Pit	SiO_2	TiO_2	Al_2O_3	Fe_2O_3	MnO	CaO	MgO	Na_2O	K_2O	P_2O_5	Br
Tsunami	15	69.90	0.68	13.44	3.80	0.06	1.27	2.93	3.12	2.70	0.06	40
	11	70.38	1.26	11.64	3.53	0.11	0.91	3.47	3.12	2.56	0.04	12
	12	74.72	0.58	11.62	2.48	0.06	0.95	2.76	2.86	2.64	0.03	20
	14	72.82	0.87	12.08	3.43	0.09	0.87	3.45	2.67	2.49	0.04	10
	13	71.80	0.77	11.84	3.79	0.07	0.93	3.60	2.50	2.44	0.08	5
Pre-tsunami	15	69.08	0.45	13.04	3.60	0.05	1.25	2.87	3.32	2.71	0.07	75
	11	69.95	1.17	11.35	4.39	0.10	0.86	3.59	2.88	2.48	0.04	44
	12	71.66	0.55	11.84	4.15	0.06	1.05	2.60	2.93	2.62	0.04	55
	14	72.72	0.69	11.99	3.51	0.07	0.87	3.08	2.66	2.59	0.04	40
	13	70.12	0.86	12.01	4.73	0.07	1.02	3.45	2.57	2.41	0.12	40
Unaffected	9	72.27	0.64	12.06	4.19	0.06	0.97	3.28	2.56	2.29	0.05	13
	5	66.52	1.83	11.79	7.85	0.16	1.57	3.84	2.25	2.20	0.07	95
	2	71.24	0.94	11.75	5.20	0.10	1.52	3.51	2.38	2.15	0.07	45
	1	74.48	0.38	10.99	2.98	0.05	1.25	3.05	2.44	2.28	0.06	50

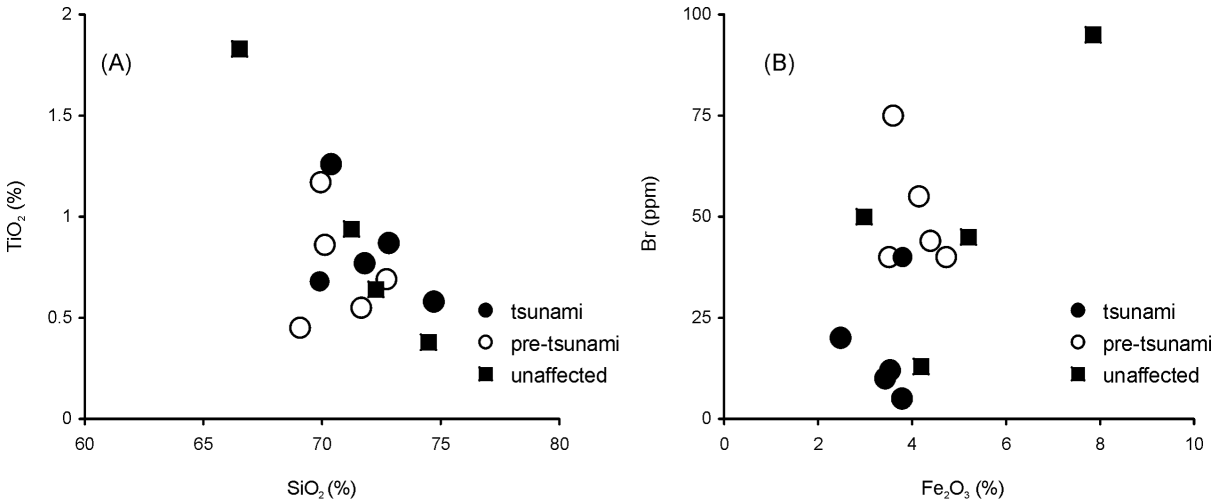

Figure 5. Concentrations of (A) SiO_2 (%) vs. TiO_2 (%) and (B) Fe_2O_3 (%) vs. Br (ppm) in sediments deposited by tsunami waves of September 21st, 1985, pre-tsunami sediments and sediments deposited in unaffected area in the village of Barra de Potosi, southwestern Mexico.

Mineralogy

Minerals with density <2.8 g/cm^3 comprise quartz, feldspars, clay minerals and carbonates. The assemblage of minerals with density >2.8 g/cm^3 consists of amphibole, pyroxene, epidote, lithic fragments, biotite, chlorite, garnet, zircon, sphene, rutile, apatite, sillimanite, tourmaline and chlorite. Both the tsunami and pre-tsunami sediments have similar associations and comparable abundances of mafic and heavy minerals with density >2.8 g/cm^3 (Figure 6).

Tsunami sediments: Very fine sand fraction (24-26.5%) has relatively more mafic and heavy minerals compared to other fractions (medium sand: 3-7% and fine sand: 8-14%). Both the analyzed tsunami samples (pits 12 and 15) have similar assemblage of mafic and heavy minerals. Amphibole (20-45%), epidote (10-35%) and lithic fragments (10-25%) are more abundant compared to pyroxene (5-15%) and garnet (<5-40%). Zircon, sphene, rutile, apatite, sillimanite, tourmaline and chlorite are present in traces (<5%). Biotite is present as an abundant mineral (10-25%) in one of the samples (pit 15), whereas it is absent in other (pit 12). Similarly, abundances of amphibole, epidote and pyroxene are more in fine and very fine sand. Garnet is present in higher concentrations in the medium sand fraction.

Pre-tsunami sediments: In one of the samples (pit 12), abundance of mafic and heavy minerals is higher in very fine sand fraction (24.5%) compared to the rest (3-9%). Another sample (pit 15) has more mafic and heavy minerals both in very fine sand (30%) and medium sand (24.5%) fractions compared to fine sand (11%). Abundances of amphibole (15-40%), epidote (5-45%), pyroxene (<5-25%) and lithic fragments (<5-65%) are variable. Garnet, zircon, sphene, rutile, apatite, sillimanite, tourmaline and chlorite are present either as traces (<5%) or absent. Biotite is abundant (15-25%) in one sample and it is absent in another. Abundances of amphibole and pyroxene are higher in very fine sand. Lithic fragments are present in higher concentrations in the medium sand fraction.

Discussion

Limit of inundation and hydraulic roughness

Record of the National Geophysical Data Center reported maximum tsunami height of 1.2 m both in Acapulco and Zihuatanejo during the tsunami of September 21st, 1985, (http://www.ngdc.noaa.gov/nndc/struts/form?t=101650&s=167&d=166). It also documented inundation of 200 m inland at Zihuatanejo. However, the eyewitnesses claim that the minimum wave height was 2.5 m and the waves swept a distance of 500 m inland at Barra de Potosí. Similar to the eyewitness records, the sedimentary unit representing tsunami was observed at a distance of ~600 m inland near El Potosí estuary (Figure 1). We evaluate wave heights reported by instrumental record and eyewitness by using empirical formula for calculating the inland flooding limit (Xfl) of a tsunami (Hills and Mader, 1997; Figure 7):

$$Xfl = Ht^{1.33}\, \mathbf{n}^{-2} k$$

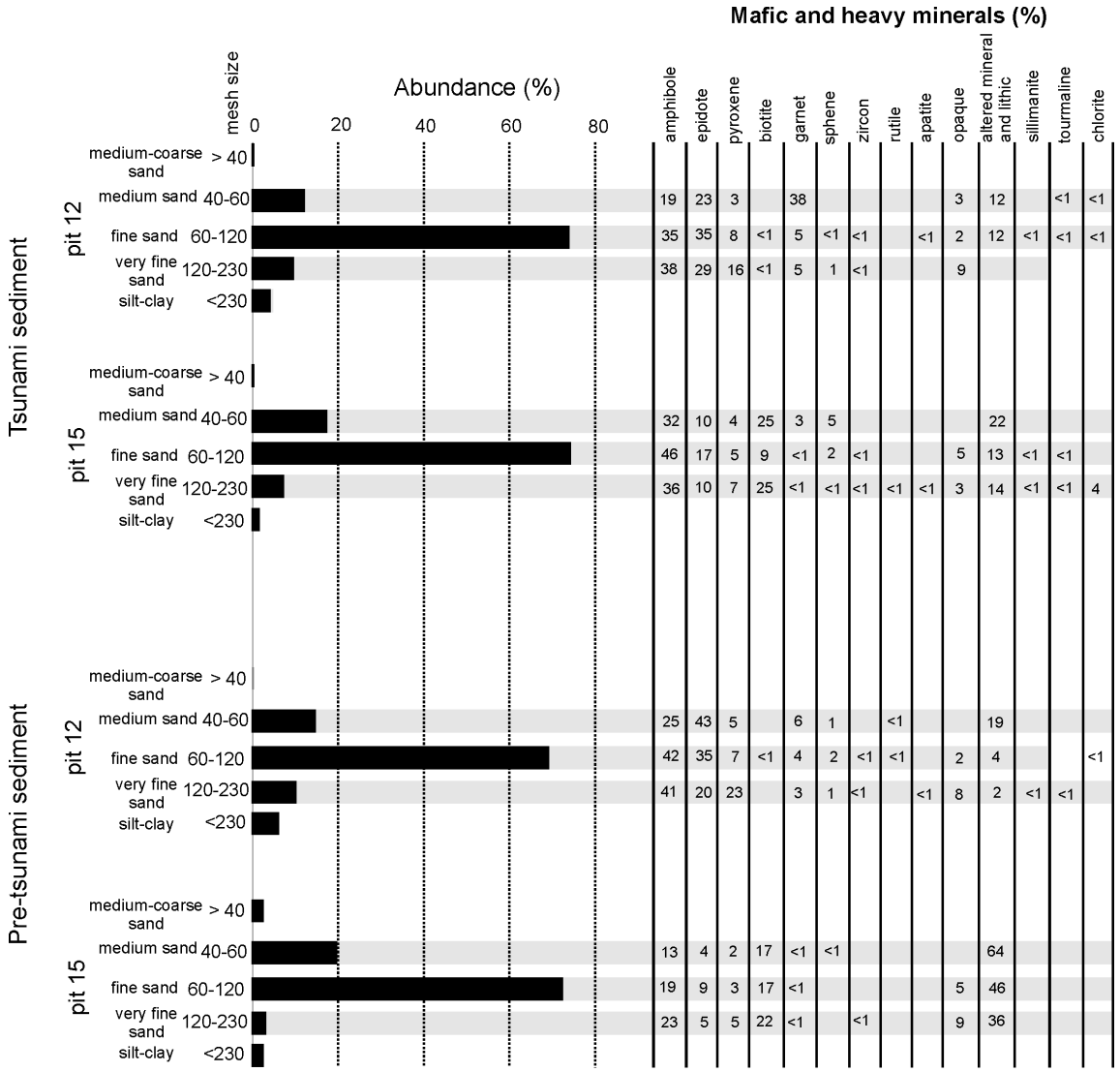

Figure 6. Mafic and heavy minerals identified in tsunami and pre-tsunami sediments collected from pits 12 and 15 in the village of Barra de Potosi, southwestern Mexico.

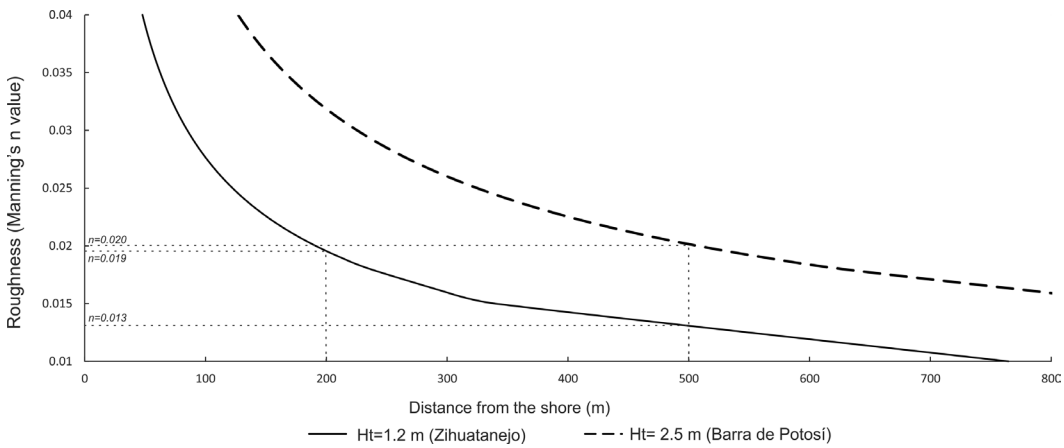

Figure 7. Calculation of Manning's number indicating hydraulic roughness of the terrain affected by tsunami using instrumental (1.2 m) and eyewitness (~2.5 m) records of wave heights. The reconstructed inundated area is shown in dotted line in Figure 1.

Where Ht is tsunami height at coastline, n is Manning's number and k=0.06 (a constant for tsunamis). Manning's number is a coefficient expression of the micro-topography and sinuosity of the surface. It represents hydraulic roughness of the terrain that causes resistance to the water flow by creating retarding force (Chow, 2009). Arcement and Schneider (1989) estimated approximate values of Manning coefficient for different terrain typology and suggest that roughness of any terrain varies over time. Both river flood models and shallow water tsunami inundation models have incorporated the importance of varying roughness values for different land use types (Bricker *et al*., 2015).

A hydraulic roughness of ~0.02 was calculated to achieve an inundation limit of 200 m with a wave height of 1.2 m at Zihuatanejo (Figure 7). Roughness calculated for Barra de Potosí is also similar with a wave height of 2.5 m and an inundation limit of ~500 m. A Manning's number of 0.02 represents farmland (Kotani *et al*., 1998) and lagoons have relatively lower hydraulic roughness (0.01-0.015; Arcement and Schneider, 1989). Similarly, rocky coasts, mangroves and forest have much higher roughness (> 0.047; Arcement and Schneider, 1989). However, both the eyewitness and stratigraphy of pits suggest that inundation of Barra de Potosí occurred from the open sea into the estuary (shown in a dotted line in Figure 1). Farmland located away from the estuary and parallel to the shore were not affected. Recalculation with an inundation limit of ~500 m and tsunami wave height of 1.2 m yield a Manning's number of ~0.013 and this value is comparable for lagoons. We consider that eyewitness inundation limit is close to the real maximum inundation limit but it overestimates the wave height.

Geological characteristics of tsunami sediments and comparison

Tsunami deposit at Barra de Potosí is located in margins of the El Potosí estuary and it is characterized by massive well to moderately well sorted fine sand with an erosive base (Table 1, Figure 3). Sediments have variable skewness and leptokurtic to extremely leptokurtic distribution. They also contain shell fragments and remnants of roots and plants. Compared to sediments deposited in the unaffected area (well sorted fine sand), tsunami deposits are poorly sorted. However, the pre-tsunami deposits have sedimentological characteristics almost similar to tsunami deposits. They are characterized by well to moderately well sorted and leptokurtic to extremely leptokurtic oxidized fine sand but lack of shell fragments. Except for SiO_2, TiO_2, Fe_2O_3 and Br, both tsunami and pre-tsunami deposits have similar chemical composition (Table 2). Tsunami deposits have higher concentrations of SiO_2 and TiO_2, whereas pre-tsunami deposits have more Fe_2O_3 and Br (Figure 5).

Both the tsunami and pre-tsunami sediments have similar association and abundances of both mafic and heavy minerals (Figure 6). We did not observe higher abundance of any of the heavy minerals only in tsunami deposits compared to the pre-tsunami deposits. Higher abundance of garnet observed in medium sand fraction of tsunami deposit in one pit was not observed in tsunami deposit of the other nearby pit. Similar association of the mafic and heavy minerals (amphibole, epidote, pyroxene, biotite, garnet, sphene, zircon, rutile, apatite, sillimanite and chlorite) suggests that the tsunami as well as pre-tsunami deposits were reworked sediments sourced from similar provenances. Fluvial activity in the southwestern Mexico transports sediments into the coast and continental shelf by eroding the basement rocks (i.e., Xolapa and Guerrero complexes; Pérez-Gutiérez *et al*., 2009; Martini *et al*., 2010) and wave actions rework them from continental shelf or coast into the coastal lagoons during both tsunami and non-tsunami events.

Sedimentological and geochemical characteristics of tsunami and pre-tsunami deposits of the Barra de Potosí are compared with previously reported tsunami and pre-tsunami deposits from the southwestern Mexico in order to observe similarities and identify geological characteristics that might be useful to identify paleo-tsunamis in the region (Table 3). Ramírez-Herrera *et al*. (2012) reported sedimentological and chemical composition of deposits by the tsunamis of March 14th, 1979, and September 21st, 1985, by studying samples in a pit near Zihuatanejo. Similarly, Roy *et al*. (2012) analyzed grain size, mineralogy and geochemistry of sediments by collecting samples immediately after the March 11th, 2011, Japan tsunami in seven different sites along the southwestern coast of Mexico. We converted concentrations of main elements of Ramírez-Herrera *et al*. (2012) into oxides for comparison and observed anomalous values. In XRF analysis, concentrations of all the oxides together with loss on ignition should add up to 100%. Total concentrations of all main element oxides of Ramírez-Herrera *et al*. (2012) show much higher values (Table 3). As Ramírez-Herrera *et al*. (2012) overestimated Al_2O_3, Fe_2O_3 and K_2O by 2 to 4 fold compared

Table 3. Comparison between average chemical composition of sediments (n = number of samples) deposited during tsunamis of March 14th, 1979 (Zihuatanejo; Ramírez-Herrera *et al*., 2012) and September 21st, 1985 (Barra de potosi; this study, Zihuatanejo; Ramírez-Herrera *et al*., 2012) and March 11th, 2011 (along the coast of southwestern Mexico; Roy *et al*., 2012).

	March 14th, 1979 (Ramírez-Herrera et al., 2011)		September 21st, 1985 (Ramírez-Herrera *et al*., 2011)		September 21st, 1985 (this study)		March 11th, 2011 (Roy *et al*., 2012)	
	Tsunami n=1	Pre-tsunami n=3	Tsunami n=2	Pre-tsunami n=3	Tsunami n=5	Pre-tsunami n=5	Tsunami n=7	Pre-tsunami n=7
Major element oxides (%)								
SiO_2	68.52	63.74	75.37	66.31	71.92	70.71	73.60	80.00
TiO_2	0.72	0.78	0.78	0.89	0.83	0.74	0.80	0.76
Al_2O_3	41.67	50.25	42.42	51.89	12.12	12.05	7.86	7.87
Fe_2O_3	14.70	16.27	13.08	16.49	3.41	4.08	5.09	4.44
MnO	0.08	0.10	0.09	0.11	0.08	0.07	0.07	0.07
CaO	2.56	2.17	2.61	2.27	0.99	1.01	1.82	1.89
MgO	2.52	2.41	2.35	2.58	3.24	3.12	1.37	1.39
Na_2O	-	-	-	-	2.85	2.87	5.20	1.70
K_2O	5.18	4.39	6.00	4.57	2.57	2.56	1.61	1.36
P_2O_5	1.24	1.07	1.35	1.07	0.05	0.06	0.08	1.10
Trace element (ppm)								
Br	-	-	-	-	17.4	50.8	77	9
Sr	214	148	214	171	-	-	-	-
Ba	260	215	356	235	-	-	-	-
Zr	99	62	130	66	-	-	-	-
Sediment texture	very fine sand	clay+ silt	very fine sand	clay+silt	fine sand	fine sand	coarse- medium sand	fine sand

to the average continental crust (e.g., Taylor and McLennan, 1985), we consider that their elemental concentrations do not represent correct chemical composition of the tsunami sediments. However, we used their data in order to document the relative enrichment/depletion in tsunami and pre-tsunami sediments.

All the tsunami deposits have relatively coarser sediments than those deposited in an environment previous to the high-energy events. Even though both tsunami (2.13-2.47 Φ) and pre-tsunami (2.27-2.57 Φ) deposits of Barra de Potosí are fine sand, there is slight difference in gran size. Tsunami sediments from the Zihuatanejo and Barra de Potosí are enriched in SiO_2 and depleted in Fe_2O_3 compared to the pre-tsunami sediments. However, average values of sediments deposited along the southwestern coast during the March 11th, 2011, tsunami are depleted in SiO_2 and enriched in Fe_2O_3 compared to pre-tsunami sediments. Tsunami deposits have more TiO_2 at Barra de Potosí and less TiO_2 at Zihuatanejo compared to pre-tsunami deposits. Compared to pre-tsunami deposits, tsunami deposits along the southwestern coast have more Na_2O and Br, whereas sediments from Barra de Potosí have lower Br. Both Na and Br are soluble elements and reflect influence of the seawater through precipitation of salts (e.g., Peters *et al*., 2001). The difference between tsunami sediments of both studies might be due to the fact that samples of the March 11th, 2011, tsunami were collected immediately after the event, whereas samples of the September 21st, 1985, tsunami were collected after two decades. Interaction of tsunami sediments with rainwater might have washed away the salts and associated soluble elements. Ramírez-Herrera *et al*. (2012) reported higher concentrations of Ca, Sr and Ba in tsunami deposits of Zihuatanejo. However, some of the sediments deposited prior to both their tsunami events have either higher or equivalent concentrations of these elements. During the comparison, we did not

observe any other geological characteristics that might be useful for identifying paleo-tsunamis in the region except for the grain size (i.e., coarser sediment) and stratigraphy (i.e., erosive base).

Conclusion

Sedimentological, mineralogical and geochemical characteristics of deposits associated with the tsunami of September 21st, 1985, were analyzed and compared with geological characteristics of both pre-tsunami deposits and sediments deposited in unaffected areas of Barra de Potosí village in southwestern Mexico. Both the tsunami and pre-tsunami sediments have similar sedimentological and mineralogical characteristics. Compared to pre-tsunami sediments, we observe higher concentrations of SiO_2 and TiO_2 in tsunami sediments. More specifically;

I. Tsunami deposits are massive well to moderately well sorted fine sand with shell fragments and contain remnants of plants and roots. They have leptokurtic to extremely leptokurtic distribution and are characterized by variable skewness.

II. Pre-tsunami deposits are also massive well to moderately well sorted sand but they are oxidized and lack of shell fragments. These sediments are also leptokurtic to extremely leptokurtic in nature.

III. Both the tsunami and pre-tsunami sediments have similar association and variable abundances of mafic and heavy minerals comprising amphibole, epidote, pyroxene, biotite, garnet, sphene, zircon, rutile, apatite, sillimanite and chlorite.

IV. Compared to the pre-tsunami deposits, tsunami deposits have more SiO_2 and TiO_2. Pre-tsunami deposits in general have higher concentrations of Fe_2O_3 and Br.

V. A comparison with other studies of tsunami deposits in the region suggests that sediments associated with at least 3 different tsunamis (i.e., March 14th, 1979, September 21st, 1985, and March 11th, 2011) have different geochemical characteristics. Except for stratigraphy (i.e., erosive base), we did not observe any other geological characteristic useful for identifying paleo-tsunamis in the region.

VI. Absence of any characteristic mineralogical and geochemical signature for sediments associated with tsunami deposits in the southwestern Mexico suggests that both tsunami and non-tsunami sediments have similar provenances. However, higher concentration of some oxides might represent higher abundance of some minerals associated with higher energy events.

Acknowledgements

Data presented in this paper were financed by the bilateral project between Mexico and India (Conacyt B330.163). Revised version of the manuscript was developed during the sabbatical of Priyadarsi D. Roy at Ecosur (Chetumal) with a scholarship from DGAPA-UNAM. Brenda G. Ocampo-Ríos received a postgraduate scholarship from Conacyt. Dr. Jose Luis Sánchez Zavala and M. en C. Jesús David Quiroz Jiménez helped in fieldwork. Comments and suggestions from the editor and anonymous reviewers are thankfully acknowledged.

References

Arcement G.J., Schneider V.R., 1989, Guide for selecting Manning's roughness coefficients for natural channels and flood plains, U.S. *Geol. Surv. Water Supply Pap*., 2339, 1-38.

Atwater B.F., Yamaguchi D.K., 1991, Sudden, probably coseismic submergence of Holocene trees and grass in coastal Washington state. *Geology*, 19, 706–709.

Atwater B.F., 1987, Evidence for great Holocene earthquakes along the outer coast of Washington State. *Science*, 236, 942-944.

Benson B.E., Grimm K.A., Clague J.J., 1997, Tsunami Deposits beneath Tidal Marshes on Northwestern Vancouver Island, British Columbia. *Quaternary Research*, 48, 192-204.

Borrero J., Ortiz M., Titov V., Synolakis C., 1997, Field survey of Mexican tsunami produces new data, unusual photos. *EOS*, 78, 85-88.

Bricker J.D., Gibson S., Takagi H., Imamura F., 2015, On the Need for Larger Manning's Roughness Coefficients in Depth-Integrated Tsunami Inundation Models. *Coastal Engineering Journal*, 57, 1550005.

Bryant E., 2008, Tsunami The Underrated Hazard. Springer in association with Paxis Publishing, Chichester, 330pp.

Chow V.T., 2009, Open-Channel Hydraulics. McGraw-Hill, New York, 680pp.

Corona-Esquivel R., Ortega-Gutiérrez F., Martínez-Reyes J., Centeno-García E., 1988, Evidencias de levantamiento tectónico asociado con el sismo del 19 de septiembre de 1985, en la región de Caleta de Campos, Estado de Michoacán. *Revista Mexicana de Ciencias Geológicas*, 7, 106-111.

DeMets C., Gordon R.G., Argus D.F., Stein S., 1994, Effect of recent revisions to the geomagnetic reversal time scale on estimates of current plate motions. *Geophysical Research Letters*, 21, 1944-8007.

Sánchez-Devora A.J., Farreras-Sanz S.F., 1993, Catalog of tsunamis on the western coast of Mexico. World data center A for Solid Earth Geophysics Publication, SE-50, National Oceanic and Atmospheric Administration, Geophysical Data Center, Boulder, 79 pp.

Farreras S., Ortiz M., González J., 2007, Steps Towards the Implementation of a Tsunami Detection, Warning, Mitigation and Preparedness Program for Southwestern Coastal Areas of Mexico. *Pure and Applied Geophysics*, 164, 605-616

Goff J., Chagué-Goff C., Dominey-Howes D., McAdoo B., Cronin S., Bonté-Grapetin M., Nichol S., Horrocks M., Cisternas M., Lamarche G., Pelletier B., Jaffe B., Dudley W., 2011, Palaeotsunamis in the Pacific. *Earth-Science Reviews*, 107,141–146.

Goff J., Pearce S., Nichol S.L., Chague-Goff C., Horrock M., Strotz L., 2010, Multi-proxy records of regionally-sourced tsunamis, New Zealand. *Geomorphology*, 118, 369-382.

Hills J.G., Mader C.L., 1997, Tsunami produced by the impacts of small asteroids. Annals of the New York Academy of Sciences, 822, 381-394.

Hutchinson I., Clague J., Mathewes R.W., 1997, Reconstructing the Tsunami Record on an Emerging Coast: A Case Study of Kanim Lake, Vancouver Island, British Columbia, Canada. *Journal of Coastal Research*, 13, 545-553.

Hutchinson I., Guilbault J.-P., Clague J.J., Bobrowsky P.T., 2000, Tsunamis and tectonic deformation at the northern Cascadia margin: a 3000 year record from Deserted Lake, Vancouver Island, British Columbia, Canada. *The Holocene*, 10, 429–439.

Jaffe B., Gelfenbaum G., Rubin D., Peters R., Anima R., Swensson M., Olcese D., Bernales L., Gómez J., Riega P., 2003, Tsunami deposits: Identification and interpretation of tsunami deposits from the June 23, 2001 Perú tsunami. Proceedings of the International Conference on Coastal Sediments, 13.

Kotani M., Imamura F., Shuto N., 1998, Tsunami run-up simulation and damage estimation by using GIS. *Proc. Of Coastal Eng*., 42, 356-360.

Martini M., Ferrari L., López-Martínez M., Valencia V., 2010, Stratigraphic redefinition of the Zihuatanejo area, southwestern Mexico, *Revista Mexicana de Ciencias Geológicas*, 27, 412-430.

Mendoza C., 1993, Coseismic slip of two large Mexican earthquakes from teleseismicbody waveforms: Implications for asperity interaction in the Michoacan plateboundary segment. *J. Geophysical Research*, 98, 8197-8210.

Morton R.A., Gelfenbaum G., Jaffe B.E., 2007, Physical criteria for distinguishing sandy tsunami and storm deposits using modern examples. *Sedimentary Geology*, 200, 184-207.

Pérez-Gutiérrez R., Solari L.A., Gómez-Tuena A., Martens U., 2009, Mesozoic geologic evolution of the Xolapa migmatitic complex north of Acapulco, southern Mexico: implications for paleogeographic reconstructions. *Revista Mexicana de Ciencias Geológicas*, 26, 201-221.

Peters B., Jaffe B.E., Peterson C., Gelfenbaum G., Kelsey H., 2001, An overview of tsunami deposits along the Cascadian Margin. Proceedings of the International Tsunami Symposium, 479-490.

Ramírez-Herrera M.T., Lagos M., Hutchinson I., Kostoglodov V., Machain M.L., Caballero M., Goguitchaichvili A., Aguilar B., Chague-Goff C., Goff J. Ruiz-Fernandez A.C., Ortiz M., Nava H., Bautista F, López G.I., Quintana P. 2012, Extreme wave deposits on the Pacific coast of Mexico: tsunamis or storms? — A multi-proxy approach. *Geomorphology*, 139, 360–371.

Roy P.D., Jonathan M.P., Macías M.C., Sánchez J.L., Lozano R., Srinivasalu S., 2012, Geological characteristics of 2011 Japan tsunami sediments deposited along the coast of Southwestern Mexico. *Chemie Der Erde — Geochemistry*, 72, 91–95.

Singh S.K., Suárez G., 1986, Review of the Seismicity of Mexico with Emphasis on the September 1985, Michoacan Earthquakes. Ciudad de México. Instituto de Geofísica, UNAM.

Taylor S.R., McLennan S.M., 1985, The continental crust: its composition and evolution. Blackwell, Oxford, 312 pp.

Wentworth C.K., 1922, A scale of grade and class terms for clastic sediments: *Journal of Geology*, 30, 377-392.

Geofísica Internacional (2017) 56-1: 71-85

Original paper

Estimation of source, path and site effects at MASE array stations: a comprehensive study

Carlos Ortiz-Alemán, Maricarmen Reyes-Olvera, Arturo Iglesias-Mendoza, Mauricio Gabriel Orozco-Del-Castillo and Jorge Hernández-Gómez

Received: April 01, 2016; accepted: November 11, 2016; published on line: January 01, 2017
DOI: 10.19155/geofint.2017.056.1.6

Resumen

En este trabajo se presenta una técnica de inversión parametrizada de los efectos de la fuente y el trayecto, basada en el empleo de métodos de optimización global. Se aplica esta técnica a los datos de velocidad correspondientes a varios eventos sísmicos registrados entre agosto de 2005 y abril de 2007 en México, por la red sísmica regional MASE (Meso American Subduction Experiment) así como por otras estaciones pertenecientes a la red permanente del Servicio Sismológico Nacional (SSN). Los parámetros de la fuente, el trayecto y el efecto de sitio, correspondientes a los espectros de amplitud para ondas S de 219 registros sísmicos de velocidad (162 pertenecientes a la red MASE y 57 a la red SSN), fueron estimados por medio de este esquema de inversión generalizada. Los parámetros invertidos simultáneamente a partir de los registros de 55 estaciones muestran un acuerdo significativo entre los espectros observados y calculados, lo cual apoya la confiabilidad de tales estimaciones. Se empleó la técnica de Nakamura para calcular una estimación inicial para la inversión generalizada. Se establecieron comparaciones entre la técnica de Nakamura y la inversión parametrizada de los efectos de la fuente y el trayecto, utilizando el método de simulated annealing. Finalmente, se calculó una nueva relación de atenuación dependiente de la frecuencia para el área de estudio, empleando un esquema de inversión basado en algoritmos genéticos.

Palabras clave: Efectos de sitio, inversion, fuente, trayecto, atenuación, peligro sísmico.

Abstract

A parameterized source and path effects inversion method based on the use of global optimization techniques is presented. We applied this method on velocity data from various seismic events collected between August, 2005 and April, 2007 in Mexico by the regional MesoAmerican Subduction Experiment (MASE) seismic network and other stations from the permanent Mexican Seismological Survey Network (SSN). The source, path and site parameters corresponding to the S wave amplitude spectra of 219 velocity seismic records (162 from MASE and 57 from SSN) were estimated by means of a generalized inversion approach. The simultaneously inverted parameters from the records of 55 stations shows a significant agreement between the observed and calculated spectra, which supports their realiability. Nakamura's method was used to compute an initial guess for the generalized inversion. Comparisons between Nakamura's technique and parameterized source and path effects inversion by using simulated annealing method were also established. Finally, a frecuency dependent attenuation relationship for the study area was computed by using a genetic algorithm inversion approach.

Key words: Site-effects, inversion, source, path, attenuation, seismic hazard.

C. Ortiz-Alemán
M. Reyes-Olvera
M.G. Orozco-Del-Castillo
J.J. Hernández-Gómez
Instituto Mexicano del Petroleo
Eje Central Lázaro Cárdenas
152 San Bartolo Atepehuacan
Delegación Gustavo A. Madero
CDMX, México
*Corresponding author: mgorozco@imp.mx

A. Iglesias-Mendoza
Instituto de Geofísica
Universidad Nacional Autónoma de México
Ciudad Universitaria
Delegación Coyoacán 04510
CDMX, México

J.J. Hernández-Gómez
Centro de Desarrollo Aeroespacial
Instituto Politécnico Nacional
Belisario Domínguez 22, Col. Centro
Delegación Cuauhtémoc, 06010
CDMX, México

Introduction

Seismic hazard in Mexico is mainly related to the subduction zone in the Pacific Ocean coast. Significant effort has been devoted to understand plate motion in this complex geological region and the characterization of its dynamic behavior (Pérez-Campos, 2008). However, estimation of ground motion variations due to local site conditions is of great engineering interest, with an important contribution to studies of seismic hazard, where the main purpose is to reduce human and economic losses that ground motions may lead to civil structures (Kramer, 1996).

In order to estimate local site-response contribution to the recorded seismic ground motion, it is necessary to remove the source and path effects. Several source and path effects inversion methods have been developed (Field and Jacob, 1995), each involving assumptions in order to constrain source and/or path effect estimations. Most of these methods include a site response term, but their main goal is the enhancement of source and path effects (Field and Jacob, 1995). In this work, the interest is focused on an accurate estimation of the site response at southern Mexico by using high quality seismic records from a temporal and permanent very broad band array, but also in source and path effects to a minor degree.

In this paper a generalized-inversion scheme to estimate local site response effects was used (Field and Jacob, 1995), where shear-wave amplitude spectra is represented by a parameterized source and path effects model and a frequency dependent site response term for each site. Estimating the local site response using this non-reference site dependent technique involves solving a strongly nonlinear multiparameter problem. Solutions to this parameterized inversion scheme were introduced by using two global optimization methods, also called heuristic methods: genetic algorithms (GAs) and simulated annealing (SA). This methods allow to explore a wider range of non-linear potential solutions, as compared to other conventional linear methods (Rodriguez-Zúñiga *et al*., 1997; Ortiz-Alemán *et al*., 2004).

An inversion problem solution by using heuristic techniques, such as GAs or SA, requires setting parameters of initial models, including upper and lower bounds to their feasible values. In the case of the source-effect term, parameter values and their bounds were taken from the scalar seismic moment as reported at Global Centroid-Moment-Tensor (CMT) and SSN catalogues. For the path effect term, the theoretical arrival time of the S-wave and the attenuation function for earthquakes traveling from the coast towards the continental region (García *et al*., 2009), were considered. An initial local site response term was set by using the non-reference site dependent technique proposed by Lermo and Chávez-García (1993), which is a variation of the spectral ratio method. Initially proposed by Nakamura (1989) to analyze Rayleigh waves from microtremor records, this technique consists in taking spectral ratios between horizontal and vertical components of the ground motion records. Field and Jacob (1995) compared various site response estimation techniques, including this one, finding the basic assumption of local geology as being relatively transparent to the motion observed on the vertical component supported by the revealed frequency dependence of site response. Although they pointed out that investigations based only on the vertical component may underestimate the local site response at sedimentary sites.

Finally, the source, path and site parameters corresponding to the S wave amplitude spectra of 219 velocity seismic records (162 from MASE and 57 from SSN) were estimated by means of the previously described generalized inversion approach. The simultaneously inverted parameters from the records of 55 stations showed a significant agreement between the observed and calculated spectra, which supports the reliability of such estimates. A comparision between local site response terms estimated through both techniques, H/V ratios and the global inversion approach, as introduced in this work, is discussed at the conclusions section.

Data acquisition and processing

Two different seismic networks provided the velocity records used in this work. The first one was the temporary network deployed as part of the MASE project. In the first stage of this project, one hundred broadband seismometers were located in a profile across the south-center of Mexico (Figure 1), from December 2004 to July 2007. The second seismic network was the permanent Mexican SSN, formed by an array of 23 seismic stations covering the whole country.

Original data sets consisted in 68 seismic events, with at least one recording in any of the 123 stations from the total array (100-MASE and 23-SSN). We carefully selected seismic records, discarding those with undesirable (less than 2) signal-to-noise ratios.

We selected broadband seismograms from six earthquakes (four subduction and two inslab events) which were simultaneously recorded by both seismic networks from August, 2005 to April, 2007 in southern Mexico. The magnitudes of these events range from 5.0 to 5.6 Mw and their focal depths from 10 to 80 km. Also, we constrained the analysis to a sub-array of only 55 stations (41 from MASE and 14 from SSN). Figure 1 shows epicenter locations of these intermediate depth earthquakes, numbered from 1 to 6 (stars), and locations of the 55 broadband stations (triangles for SSN and squares for MASE). Table 1 contains the main features of the six events depicted in Figure 1.

Selected records were properly corrected by removing the mean and linear trends, and avoiding any other filtering. For all the records, the theoretical arrival time of the S-wave was picked in the horizontal component. Using these theoretical picks, for each one of the three components, we selected a window including the intense part of the ground motion (20s). These windows were Fourier-transformed by an FFT routine using 2048 samples, and then smoothed by 1/3 octave-band filter.

An initial site response for each station was estimated by computing the spectral ratio technique with a single station (Lermo and

Table 1. Main features of the intermediate-depth seismic events considered in this work. 1,4,5, and 6 correspond to subduction events and 2 and 3 to inslab earthquakes.

EVENT #	DATE (yy/mm/dd)	LAT °N	LAT °W	H [km]	CMT Mw	*Mo* [Nm]	SSN Mw	*Mo* [Nm]
1	05/08/14	15.994	-98.400	15.3	5.4	1.560E+17	5.2	6.11E+16
2	05/09/24	18.052	-96.989	80.5	5.0	3.700E+16	5.1	4.51E+16
3	06/08/11	18.446	-101.284	50.9			5.2	7.89E+16
4	06/08/19	16.013	-97.499	11.1	5.6	2.780E+17	5.3	1.09E+17
5	07/03/30	15.874	-99.061	16.1	5.3	9.900E+16	5.1	4.32E+16
6	07/04/13	17.137	-100.303	35.5	5.3	1.260E+17	5.3	1.00E+17

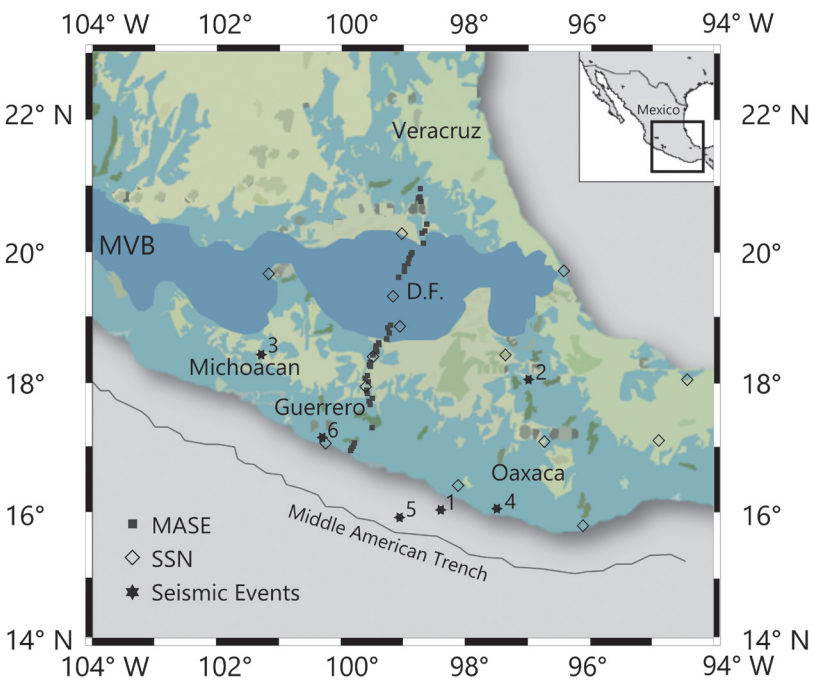

Figure 1. Geographic location of the 55 seismic stations (14 SSN – 41 MASE), and epicentral location of the six seismic events considered in this study.

Chávez-García, 1993), that involves dividing horizontal to vertical components of the velocity records, as shown in equation (1). In the case when some seismic station recorded more than one seismic event, site response was computed as the average of the spectral ratios from all recorded events,

$$H/V=\sqrt{\frac{EW^2+NS^2}{2Z^2}}, \qquad (1)$$

where *H* and *V* are the horizontal and vertical components, respectively. And *EW*, *NS*, and *Z* are the east-west, north-south and vertical components, respectively.

Spectral decay analysis

As mentioned above, a window including the intense part of the seismic motion and beginning at the shear-wave arrival was employed for signal spectra estimation. Fourier amplitudes were computed for both vertical and horizontal components from the records. In Figures 2 and 3, spectra were plotted for 8 frequency values at 0.1, 0.5, 1, 2, 4, 6, 8, and 10 Hz, respectively, as a function of epicentral distances to the MASE array stations. Continuous black line is the expected attenuation curve by just considering geometrical spreading with a (1/r) law.

As can be noticed in Figures 2 and 3, spectral amplitudes do not match the expected attenuation with distance (1/r). In such figures, it is possible to clearly observe two regions with different amplitude behaviours. First, in the region from r = 200 to approximately 400 km, we observe a consistent amplification of amplitudes in all propagated frequencies, above the geometrical spreading; this is due to the presence of the Trans Mexican Volcanic Belt (TMVB) (see Figure 1), where the strata consist mainly in volcanic rock. Farther from r = 400 km to the north, a greater attenuation than 1/r, particularly for higher than 2 Hz frequencies, was found. This might be due to the complexity in the response at each site of the MASE array, maybe as a result of the trade-off between large scale amplification patterns (Ordaz and Singh, 1992), and the particular attenuation features at each site.

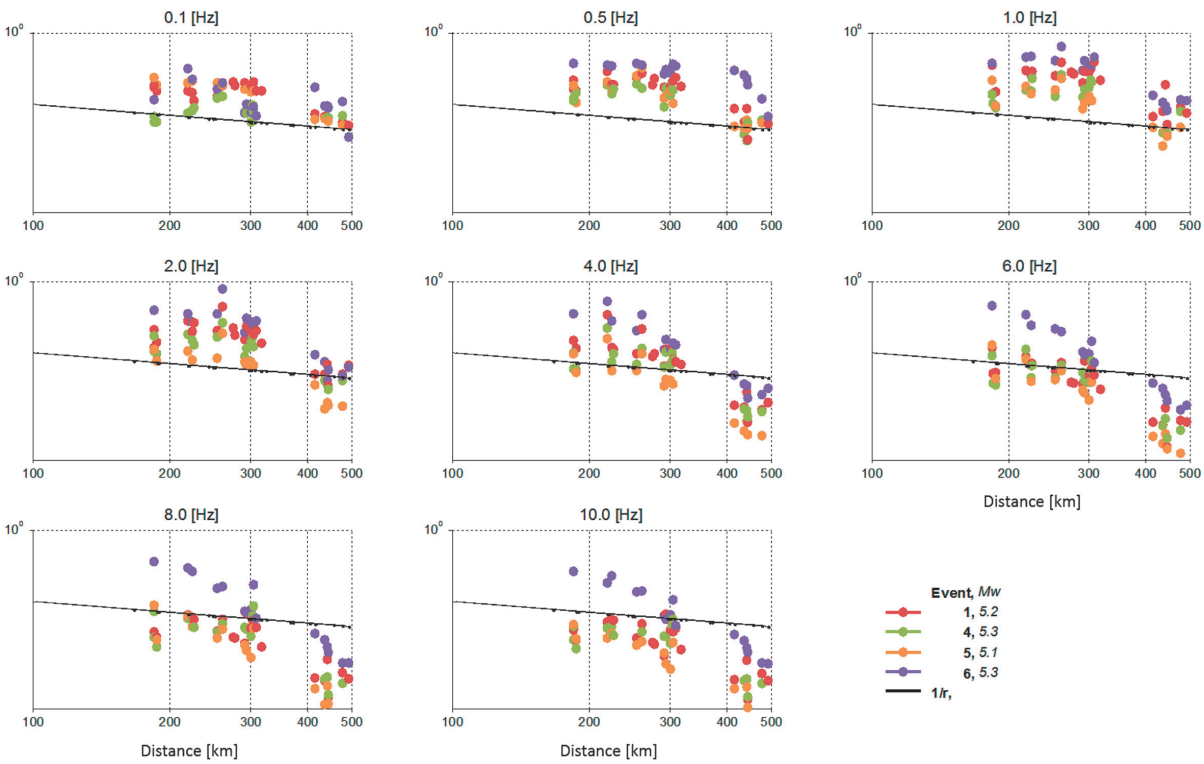

Figure 2. Spectral amplitude [cm] as a function of epicentral distance. Eight frequency values in the range from (0.1 – 10 [Hz]) were plotted for each one of the MASE array seismic stations. The continuous black line represents the expected trend for geometric attenuation. Subduction events labelled as 1,4,5,and 6 (see Figure 1), with similar seismic propagation paths towards the MASE array were depicted.

In Figure 2, amplitudes corresponding to events 1, 4, 5 and 6 were plotted against epicentral distance. In these events, seismic waves traveled perpendicular to the coast towards the MASE array. Events numbered as 1 and 5 have similar epicenter locations, and they show similar amplitude decay behavior with distance for all frequency windows. Amplitudes from seimic event 6 exhibit a similar behavior relative to the other three events (1, 4 and 5) up to 4[Hz], but from 6 to 10 [Hz] amplitudes are higher.

In Figure 3, amplitudes for events 2 and 3 are plotted versus distance. Both events propagate almost perpendicular to the MASE array. Event 3 was located to the north and event 2 to the south of the MASE array. Both events show similar spectral decay with distance following the expected trend 1/r.

Parameterized source- and path-effects inversion scheme

Many seismological studies consider a site-response term primarily to remove this effect, in order to enhance source and/or path effect estimates. In this work the main interest was the site response estimates themselves. For this last reason, a parameterized source and path effects inversion scheme were used.

Following the formulation from Field and Jacob (1995), for a network of I sites over which J events were recorded, amplitude spectrum of the j-th event recorded at the i-th site, $A_{ij}(f)$, can be written as

$$A_{ij}(f) = E_j(f)P_{ij}(f)S_i(f), \qquad (2)$$

where $E_j(f)$ represents a source term, $P_{ij}(f)$ a path term and $S_i(f)$ a site effect term.

In this work the spectral method from Brune (1970) was used, as a quantitative evaluation tool for source parameters. Using Brune's model, source parameters can be inferred from the low frequency spectral level, Ω_0, and the corner frequency, f_c, measured from a source radiation pattern and Q factor corrected

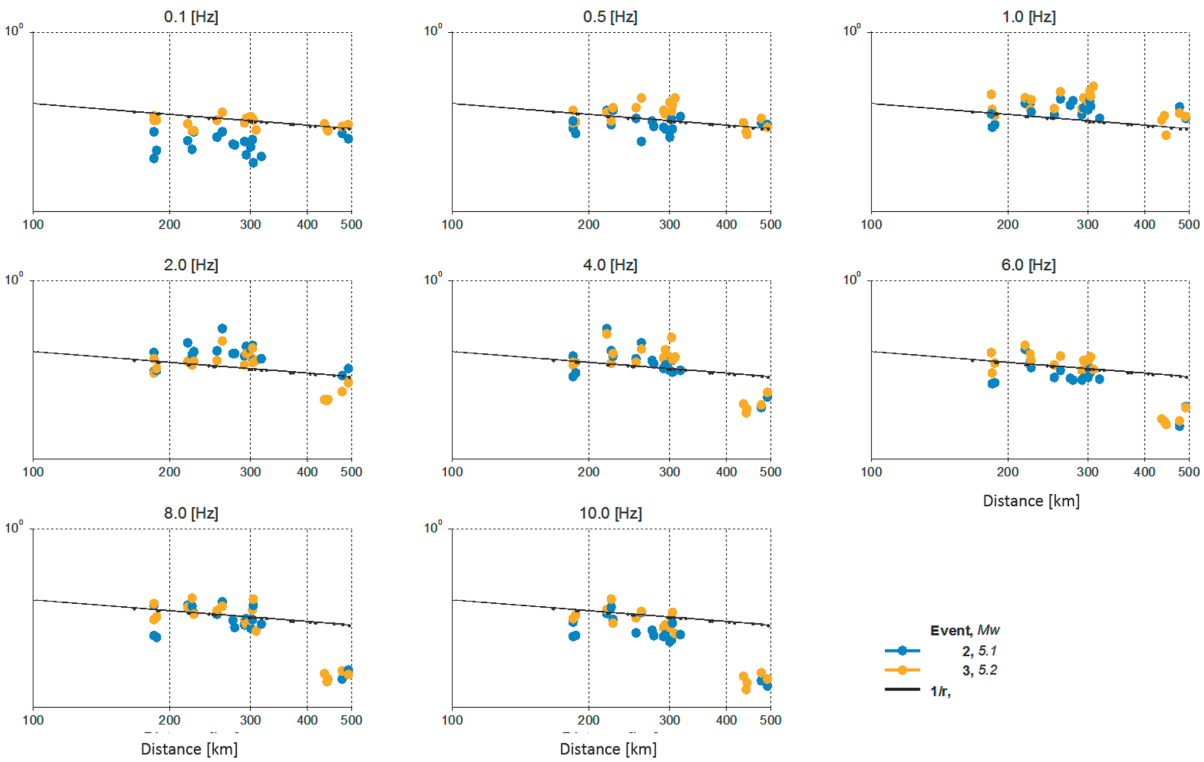

Figure 3. Spectral amplitude [cm] as a function of epicentral distance. Eight frequency values in the range from (0.1 – 10 [Hz]) were plotted for each one of the MASE array seismic stations. The continuous black line represents the expected trend for geometric attenuation. Inslab events labelled as 2 and 3 (see Figure 1), with similar seismic propagation paths towards the MASE array were depicted.

spectrum. In most seismological studies, spectra are corrected by some estimation of Q, and low frequency spectral levels and corner frequencies are obtained by visual inspection of the observed spectra. When using such kind of approach, uncertainties in Q, f_c and Ω_0 estimations can be large, leading to large uncertainties in source parameters. Here a quantitative approach to source, path and site effects inversion based on the use of a simulated annealing algorithm were introduced.

Following Boatwright *et al.* (1991), the source term in the frequency domain is expressed as

$$E_j(f) = \frac{2\pi f \quad _{0j}}{1+\left(f / f_{cj}\right)^{4} \quad ^{1/2}} \qquad (3)$$

Equation (3) is Boatwright's (1978) approximation for the Brune (1970) far-field shear-wave spectrum.

It is important to recall the relation between Ω_0 and M_0:

$$M_0 = \frac{4\pi\rho c r \quad _0}{U \quad _\theta}$$

where ρ is the density, c the wave speed, r the distance from the source, and $U_{\varphi\theta}$ the term on the radiation pattern. Generally, the focal mechanism corresponding to the radiation pattern $U_{\varphi\theta}$ is unknown; nevertheless, the seismic scalar momentum, M_0, can be estimated by replacing $U_{\varphi\theta}$ with a mean radiation term with a value of 0.52 for the P-wave and of 0.63 for the S-wave (Shearer, 2009).

Assuming path effects to be similar for all array sites, except for a geometrical spreading term of the form

$$r_{ij} = \begin{array}{ll} R & ;R < R_x \\ \sqrt{RR_x} & ;R \geq R_x \end{array}, \qquad (4)$$

where R_x was taken as 100 km for this study, the path effect term is modeled as

$$p_{ij}\left(f\right) = \frac{1}{r_{ij}} e^{-\pi f\left(t_i{}^{*}+T_{ij}/Q(f)\right)}, \qquad (5)$$

where $1/r_{ij}$ is the geometrical spreading factor described in equation (4), T_{ij} is the travel time of S waves, $Q(f)$ is a frequency-dependent quality factor, taken as $Q(f) = 211f^{0.46}$as proposed by García *et al*. (2009), and t_i^* is a local attenuation term.

In such a way, $2J$ source parameters (Ω_0 and f_0 for each event), I local attenuation parameters (t_i^*), and I frequency dependent terms corresponding to the site response, were considered. In this case, observed spectra involved N discrete frequencies, then the model contains $2J + I\ (N+1)$ parameters to invert.

Site response estimation using simulated annealing

An initial parameterized model was proposed. Source effect parameters, Ω_0 and f_c, for each event j, were estimated by using the scalar seismic moment, M_0, reported in the Harvard CMT Catalogue and SSN database. Initially, $fc_j \propto M_0{}^{-1/3}$ and $\Omega_0 \propto fM_0$; nevertheless, the following relations where used:

Table 2. Scalar seismic moment, M_0, for the six events also listed and described in Table 1. Information was taken from the Seismic Seismologic Network (SSN) and the Global CMT catalogues. Values for fc and Ω_0 were computed from M_0.

#	CMT			SSN		
EVENT	M_0 [N·m]	f_{cj} [Hz]	Ω0	M_0 [N·m]	f_{cj} [Hz]	Ω_0
1	1.560E+17	0.400	15.600	6.111E+16	0.547	6.111
2	3.700E+16	0.647	3.700	4.515E+16	0.605	4.515
3				7.890E+16	0.502	7.890
4	2.780E+17	0.330	27.800	1.098E+17	0.450	10.980
5	9.900E+16	0.466	9.900	4.324E+16	0.614	4.324
6	1.260E+17	0.430	12.600	1.008E+17	0.463	10.080

$$fc_j \propto \left(\frac{M_0}{1x10^{16}}\right)^{-1/3} \quad \text{and} \quad {}_{0j} \propto \frac{M_0}{1x10^{16}}.$$

Parameter values are listed in Table 2. Both estimations were considered as lower and upper limits in the inversion scheme, while average values were set as initial parameter values.

In order to set initial values of path effect parameters, the relationship between local attenuation and frequency dependent quality factor, as described in equation (6), was considered,

$$t_i \propto Q^{-1}. \tag{6}$$

Local attenuation t_i^*, also characterizes the attenuation of body waves, and might be estimated using the travel time of S waves as well as the quality factor Q (Shearer, 2009).

García *et al*. (2009) proposed two attenuation functions $Q(f)$ for the S-wave group, considering trajectories along the coast and towards the continent, and therefore values of $Q^{-1}(f)$, for both types of seismic stations, coastal and inland. Values of $Q^{-1}(f)\pm1\Sigma.\mathrm{D}.$ of the final models for the coastal and inland subsets for a frequency range form 1 to 10 Hz are showed in Figure 4. We considered the maximum and minimum value of $Q^{-1}(f)$ as upper and lower limits, respectively, for the path parameters.

An initial guess for the site response term was considered from results of horizontal to vertical spectral ratios, described in previous sections. Once the initial model has been set, the inversion process followed the flow chart depicted in Figure 5, which considers an inversion approach based on the SA method.

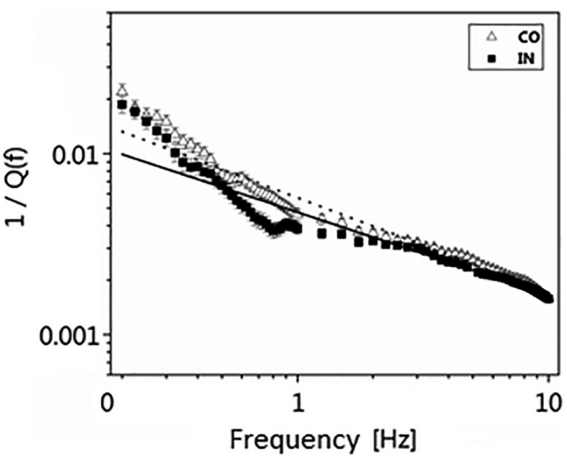

Figure 4. Estimated values of Q^{-1} for coastal (triangles) and continental seismic paths (squares). The dashed line indicates the attenuation function $Q(f)$ for coastal paths and the continuous line the continental paths, after García *et al.* (2009).

A well documented issue in this class of inverse problems is the non-uniqueness of the solution. In this case, an observed spectra can be matched to a similar approximation order by a pair of small f_c and t_i^* values, or by large values of the same parameters. Nevertheless, in the case of site response estimation this trade-off is advantageous to some extent. A very precise estimation of the real values of f_c and t_i^* is not necessary because both of them have a minor influence on the site response term. Uncertainties associated to these trade-off can be reduced if several records are simultaneously inverted. In addition, the initial model as proposed in this work constrains source parameters by including all available *a priori* information, then the trade-off effects between f_c and t^*, previously pointed out, may be reduced to some significant extent.

Three types of inversion were performed in order to include all possible combinations between the number of stations, I, and events, J. Data were fitted by means of equation (2), considering the parameterized expressions for source- and path-effects, by minimizing the function in equation (7),

$$e = \left[\sum_{j=1}^{J}\sum_{n=1}^{N}\left(A_{ij}\left(f_n\right) - Ae_{ij}\left(f_n\right)\right)^2\right]^{1/2} \tag{7}$$

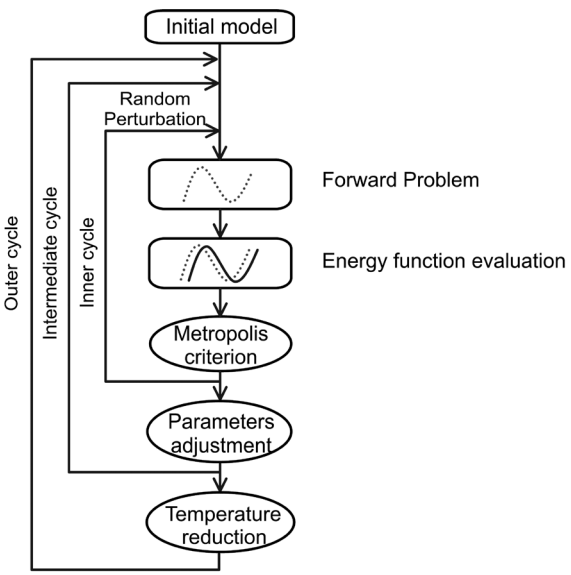

Figure 5. Schematic drawing illustrating the method of simulated annealing as used in this study (after Ortiz-Alemán *et al*., 2004).

where $A_{ij}(f_n)$ and $Ae_{ij}(f_n)$ are the observed and estimated amplitudes for spectrum i, respectively, at the frequency f_n ; N is the number of spectra samples that were simultaneously inverted and J is the total number of records that were used.

Attenuation function estimation

Another inversion was performed considering source and local site-response parameters estimated in the generalized-inversion scheme including all stations and events (55 stations and 6 events) in order to estimate a new attenuation function for trajectories towards the continent.

Only path-effect parameters were assumed as unknown, while source effect parameters and local site response values were directly fixed from the solution previously achieved by using SA. The local attenuation term values, t_i^*, and their limits remained similar to the generalized inversion scheme. For the attenuation function of the form $Q(f) = af^{\,b}$, values of the parameters a and b and their limits were taken from other two attenuation studies, Ordaz and Singh (1992) and García *et al*. (2009), that are routinely used for estimation of regional attenuation at southern Mexico. Attenuation parameters, a and b, were then inverted, which allowed to accomplish a new attenuation function, $Q(f) = 224f^{0.55}$. This new function can deal with any kind of seismic events (inslab or subduction earthquakes) and their corresponding seismic propagation paths along the coast or towards the inner continental zone. This effect is notably shown in Figure 4, where intraslab and interplate events are depicted; notwithstanding that continental models present a higher attenuation than coastal ones, the differences are not considerable, being able to be adjusted by the linear function herein provided.

Notable differences in attenuation along the coast and towards the continent have been reported by García *et al*. (2009). This study suggests that seismic waves travelling inland suffer considerably less attenuation than those propagating along the coast.

For comparison purposes, error functions as in equation (7), for each seismic station were computed by using the attenuation function proposed by García *et al*. (2009) and the one obtained in this study. Results are depicted in Figure 6, and it can be observed that along the profile across the south-center of Mexico (MASE array) and also in the case of permanent stations of the SSN, errors are lower in general by using the attenuation function from this work, which is also valid for all propagation paths and any kind of seismic event, as mentioned before. In Table 4 the main similarities and differences bertween datasets used by García *et al*. (2009) and by this work are listed, for the computation of a frequency dependent attenuation function. This table allows to appreciate the robustness of the present frequency-dependent attenuation function, due to the fact that the database of stations and records used here is of comparable size relative to the one used by García *et al*. (2009).

Table 3. Local atenuation, t^*, corner frequency, fc, and objective function e, from inversions A, B and C, for the seismic stations of the MASE array (HUIT, JIUT, PSIQ and SATA) and SSN seismic network (CUIG, MOIG, PLIG and TPIG).

ST.	A			B			C		
	t^*	fc	e	t^*	fc	e	t^*	fc	e
CUIG	0.0149	0.5807	0.4466	0.0400	0.7033	0.1696	0.0372	0.4505	0.4077
MOIG	0.0400	0.4942	0.2270	0.0400	0.7033	0.1190	0.0376	0.4505	0.2000
PLIG	0.0010	0.4786	0.1131	0.0400	0.7033	0.0422	0.0354	0.4505	0.2944
TPIG	0.0400	0.4757	0.1006	0.0092	0.7363	0.0542	0.0344	0.3668	0.5322
HUIT	0.0132	0.7603	0.0881	0.0375	0.8156	0.0186	0.0046	0.6918	0.2642
JIUT	0.0302	0.5875	0.0954	0.0397	0.7033	0.0516	0.0397	0.4505	0.2865
PSIQ	0.0010	0.4295	0.0114	0.0400	0.7033	0.0380	0.0398	0.4505	0.0858
SATA	0.0021	0.6788	0.0346	0.0248	0.8156	0.0026	0.0013	0.6918	0.2297

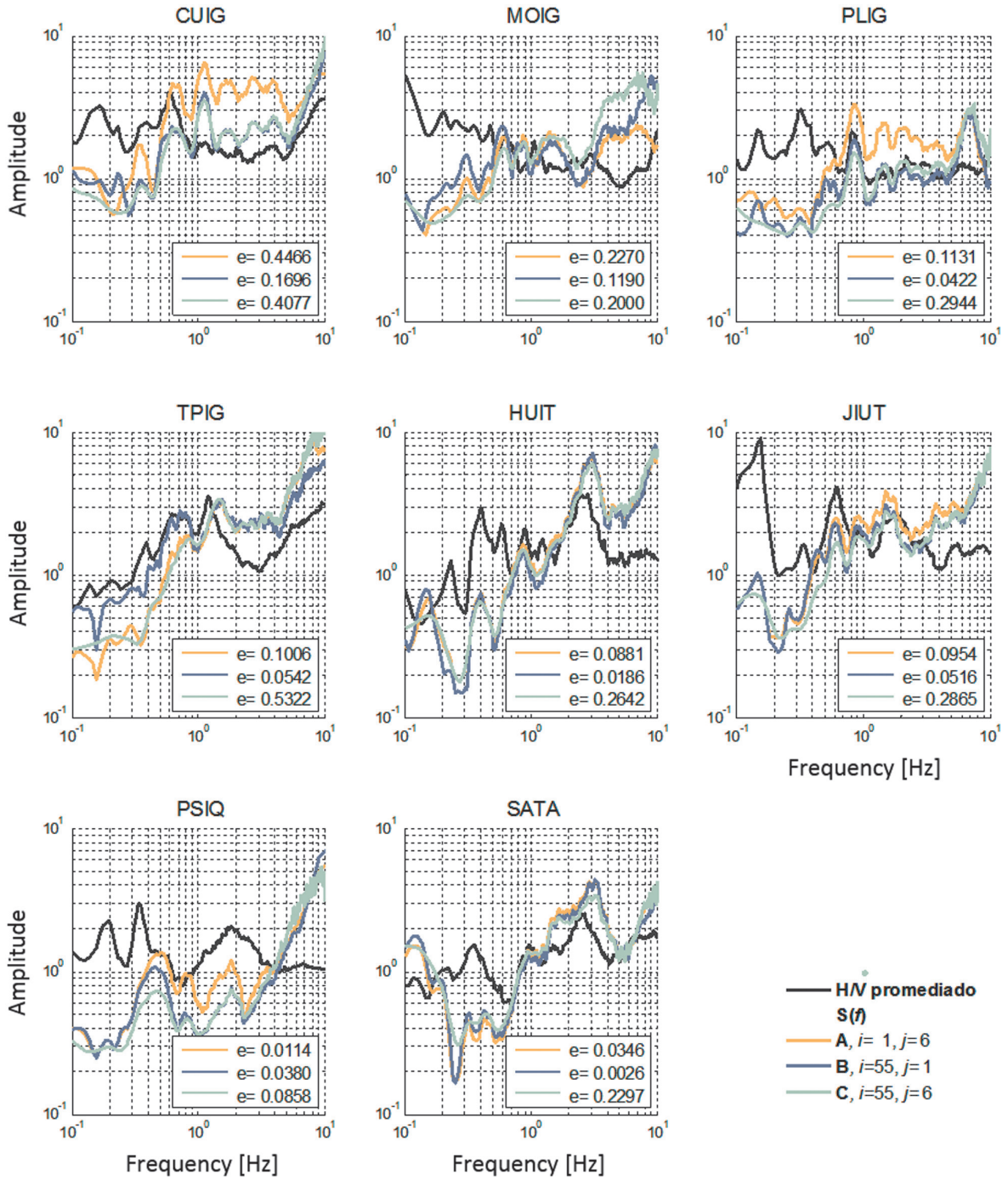

Figure 6. Objective function value, e, computed for the attenuation function. In the upper part, stations of MASE array were located considering their distance relative to the coast, being QUEM the nearest and CHIO the farest station. In the lower part, SSN network stations in alphabetical order.

Table 4. Comparison between datasets from García *et al*., (2009) and this work, for the computation of frequency dependent atenuation function, $Q(f)$.

Atenuation Function	García *et al*. (2009)	This work
Number of records	469	219
Type of records	Velocity and acceleration	Velocity
Number of stations	56	55
Magnitude of events, Mw	5.0≤Mw≤8.0	5.0≤Mw ≤5.6
Depth of events, H, [km]	10≤H≤30	10≤H≤80
Distance from seismic source to stations, r, [km]	20≤r≤400	50≤r≤500

Results and conclusions

In this paper a parameterizd stochastic global inversion method using of local seismic response was introduced, which also allows to estimate parameters of source and path effects. The technique of horizontal to vertical (H/V) spectral ratio is used to obtain an initial model for the inversion scheme. This type of initial solution approaches qualitatively local seismic response particularly in the case of hard rock sites. However in the case of sedimentary sites, certainty of estimates for site response from H/V spectral ratio is significantly conditioned by the impedance contrast between sedimentary and basement units, as well as by the three dimensional geometry of the sedimentary basin. H/V spectral ratio in the presence of a low impedance contrast presented is not suitable to use as pointed out by Luzón *et al*. (2001) and Sánchez-Sesma *et al*. (2011).

Parameterized nonlinear global inversion allowed us to obtain robust estimates of local site response, by simultaneously inverting the whole set of observed seismic records. Parameters were estimated in a frequency range of 0 - 10 [Hz] for each of the seismic stations (41 - MASE and 14 -SSN). Estimates of corner frequency and low frequency spectrum level for the six seismic events were obtained. Local atenuation values and a regional attenuation function were also introduced.

Uncertainty inherent to the non-uniqueness on the solution was restricted by incorporating *a priori* information about seismic source, path and site parameters. The kind of parameterization used in this work to estimate such seismic effects was quite appropriate as sensitivities from all estimated parameters show significant contributions on the shape of synthetic spectra computed by the forward problem calculation. Observed spectra from stations of MASE array (CUIG, PLIG, HUIT, JIUT, PSIQ and SATA) were fitted to a similar degree when compared to spectra from stations that were located far and even at opposite ends (MOIG, TPIG), as shown in Figure 7.

Three different inversions of site response were computed. In study case A, the seismic response for each one of the 55 seismic stations was separately inverted and all six seismic events were simultaneously considered. In case B, the seismic response was inverted by considering each one of the six seismic events and the whole set of 55 seismic stations simultaneously. In case C, the site response at 55 seismic stations was inverted and seismic records for six events were considered. Results are summarized in Table 3, where estimated source and path effect parameters are listed for a set of MASE and SSN seismic stations.

In Figure 8, site response estimations at some selected seismic stations from MASE and SSN seismic networks were plotted. For comparison purposes H/V average site effects for the same set of stations are also included. Three different inversion efforts (A, B, and C) are include in the same Figure 8.

In order to account for a possible trade-off between source and path effects, affecting the site effect estimations, in Figure 9 a comparison is made for the estimated source spectra for seismic event listed as 6 in Table 1. One station (CEME) near the seismic epicentral location was used for the inversion of source spectra. In order to establish the approximation quality, in Figure 9 the observed and estimated global seismic spectra (considering source, path and site effects) is are shown. At the top of Figure 9, the estimated source term for each seismic station is plotted. The effects of attenuation

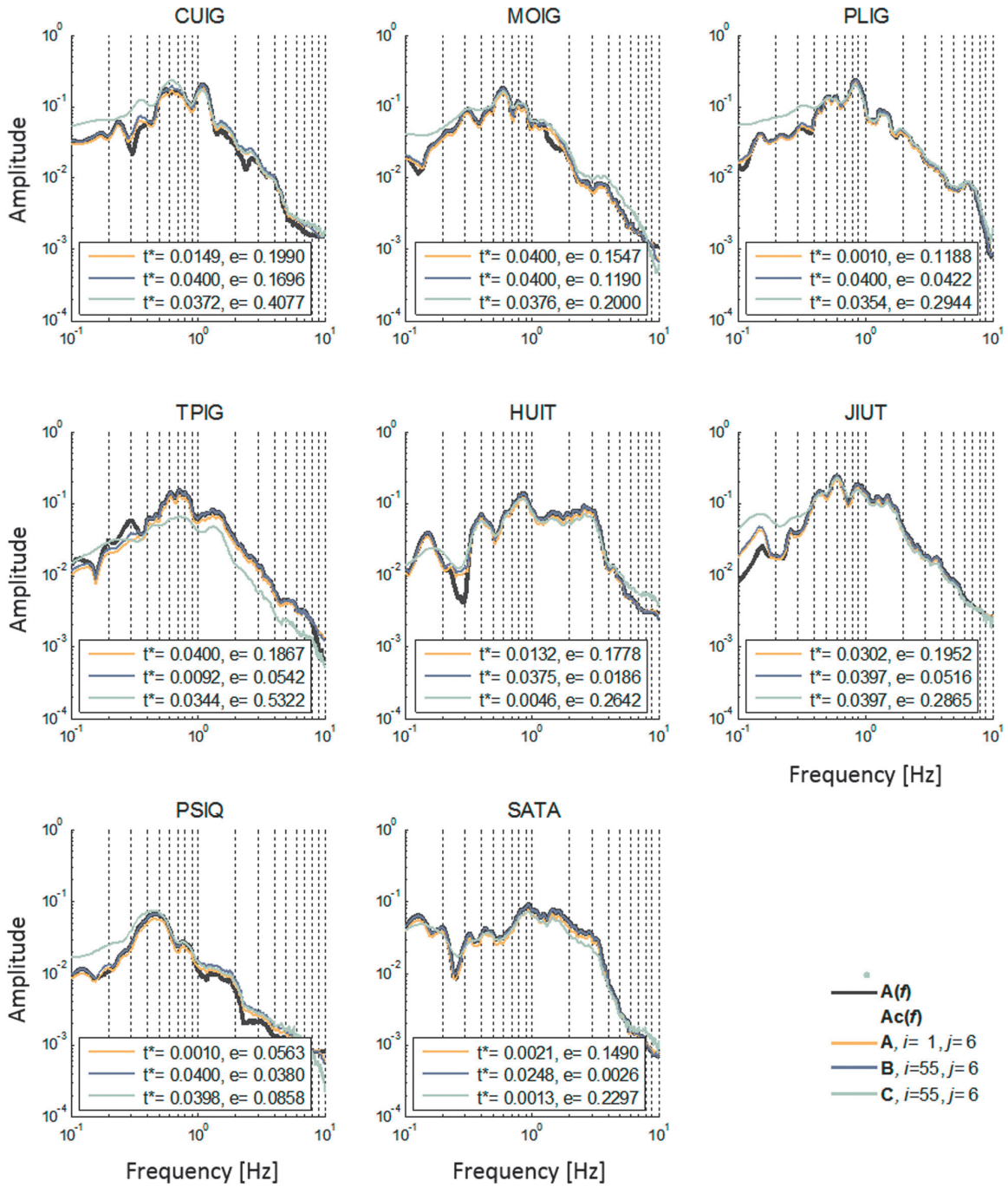

Figure 7. Observed, $A(f)$, and synthetic spectra, $Ac(f)$, computed by using estimated parameters from inversions A, B and C, for some stations of the MASE array (HUIT, JIUT, PSIQ, and SATA) and SSN network (CUIG, MOIG, PLIG and TPIG). In each case, local atenuation, t^*, and objective function value, e, are indicated.

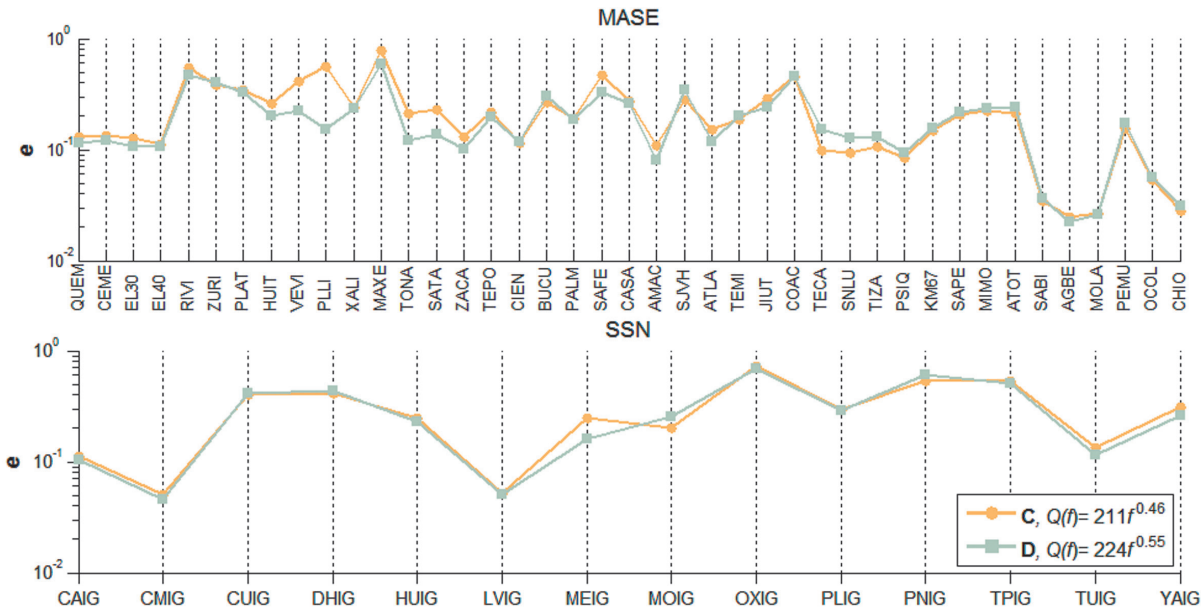

Figure 8. Estimated site response, S(f), for seismic stations of the MASE array (HUIT, JIUT, PSIQ and SATA) and SSN network (CUIG, MOIG, PLIG and TPIG), as compared to the site effect computed by average H/V ratios. In each case, the objective function value, e, is indicated.

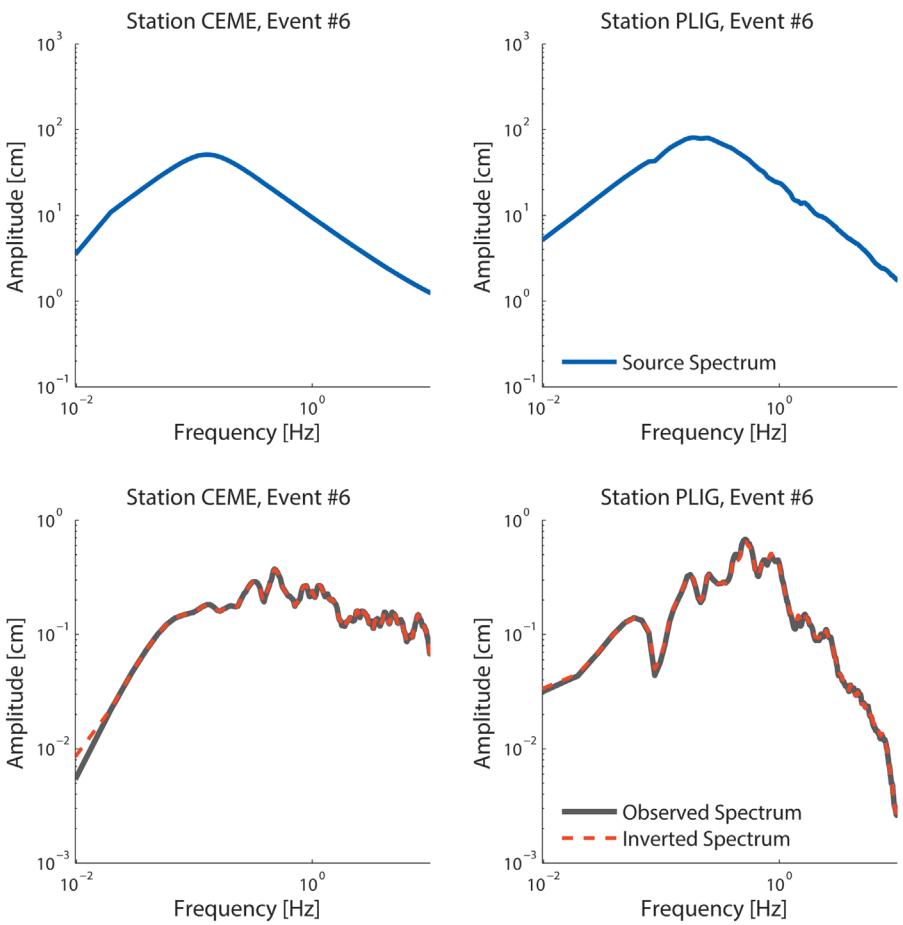

Figure 9. Estimated and observed seismic spectra for CEME and PLIG stations of the MASE array. In the upper part, the inverted source term for event 6, listed in Table 1 is included. Estimated global seismic spectra account for source, path and site effects. Attenuation with distance is less significant at CEME in comparison to PLIG, as expected, and source effect is more distinguishable at CEME station.
The synthetic spectra closely resemble the observed spectra.

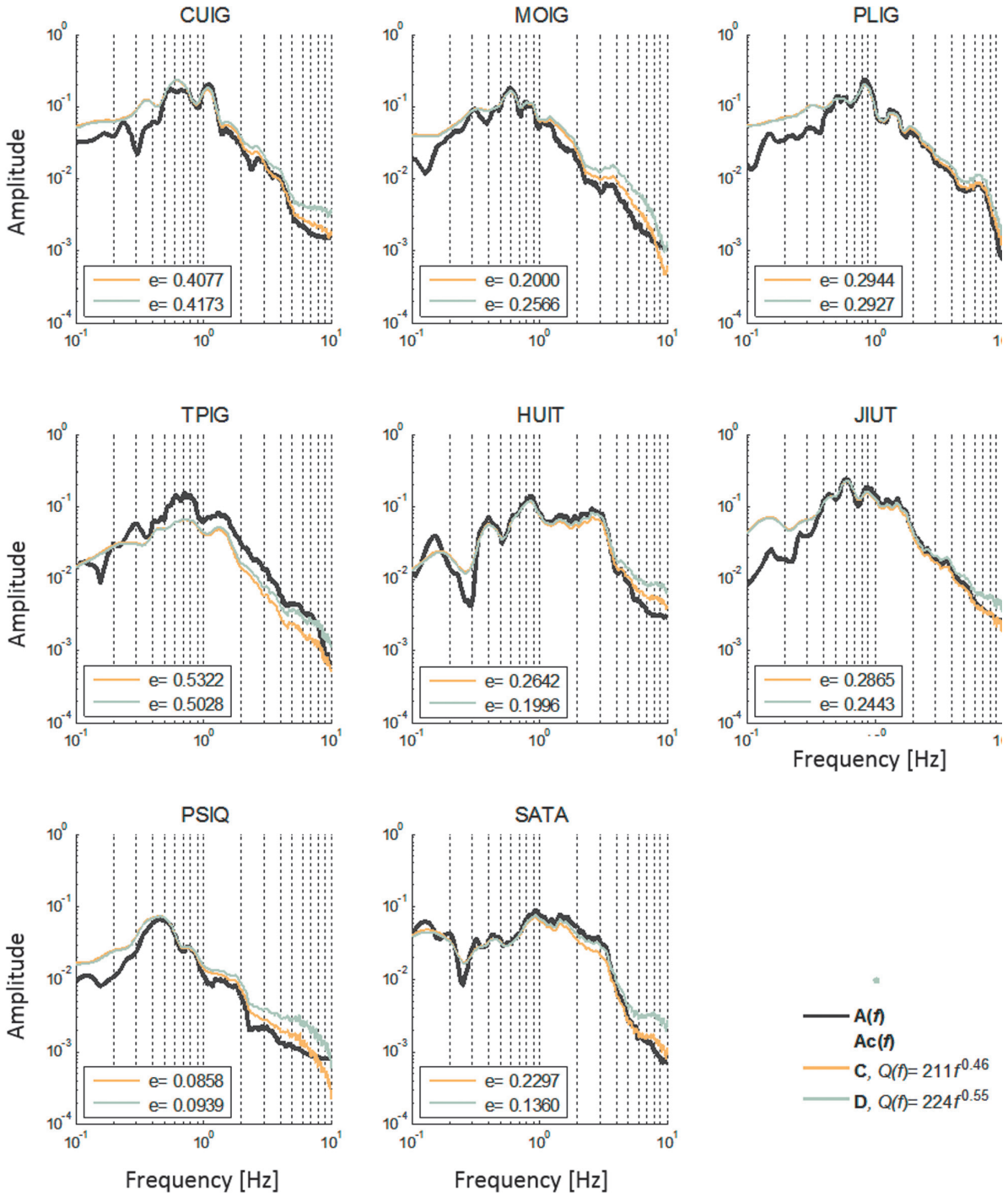

Figure 10. Observed and synthetic spectra, $A(f)$ and $Ac(f)$, computed by using the attenuation function from García *et al*. (2009), labeled as C, and attenuation function as derived in this work, labeled as D, for stations from the MASE array (HUIT, JIUT, PSIQ and SATA) and SSN network (CUIG, MOIG, PLIG and TPIG). In each case, value of objective function, e,is indicated.

with distance and local amplification can be considered as less significant at station CEME. In this same figure, source effect can be more clearly distinguishable in this station which is closer to the epicenter. A good agreement between the estimated source and the global spectra was found, on one hand, and the observed spectra on the other.

In Figure 6, the objective function value, computed for the attenuation function was plotted. Attenuation function by García *et al*. (2009) is considered in case C. Another inversion case study (D) was then computed, by optimizing coefficients a and b of a general frequency dependent attenuation function of the form $Q(f)=af^{b}$.

In Figure 10, observed and synthetic spectra, $A(f)$ and $Ac(f)$ were included, computed by using the attenuation function from García *et al*. (2009), labeled as C, and the attenuation function as derived in this work, labeled as D, for stations from the MASE array (HUIT, JIUT, PSIQ and SATA) and SSN network (CUIG, MOIG, PLIG and TPIG).

It is important to recall that pioneering work on the spectral amplification at the hill zone around Mexico City was done by Ordaz and Singh, (1992). They made evident a systematic spectral amplification in the frequency range of $f = 0.2 - 2.0$ Hz. The results herein obtained confirm that geological conditions represented by the TMVB, specially in the case of subduction events, constitute a region of relative spectral amplification in the frequency range of $f = 0.5 - 4.0$ Hz. For epicentral distances larger than 400 km (in the north side of the MASE array, beyond the TMVB) there exists a strong spectral decay in seismic energy for the frequency range of $f = 4.0 - 10.0$ Hz. Nonlinear inversion of source, path and site effects from the MASE experiment dataset probed to be an alternative tool to derive meaningful information on relative seismic amplification or attenuation in south-central Mexico.

Data and resources

Two different seismic networks provided the velocity records used in this work. The first one was the temporary network deployed as part of the MASE project. In the first stage of this project, one hundred broadband seismometers were located in a profile across the south-center of Mexico (Figure 1), from December, 2004, to July, 2007. The second seismic network was the permanent Mexican SSN, formed by an array of 23 seismic stations.

Seismic data from the MASE temporal seismic network and from the permanent SSN network were provided by the Insitute of Geophysics of the National University of Mexico (UNAM). Seismic modeling and data inversion were carried out at the Mexican Institute of Petroleum.

Acknowledgments

Authors thank the National Seismological Service from the National Autonomous University of Mexico for providing seismic data for this study. This research was partially supported by CONACyT under project 128376, as well as by projects SIP 20160105 and SIP 20160576, IPN.

References

Boatwright J., 1978, Detailed spectral analysis of two small New York State earthquakes. *Bulletin of the Seismological Society of America*, 68, 1117-1131.

Boatwright J., Fletcher J.B., Fumal T.E., 1991, A general inversion scheme for source, site, and propagation characteristics using multiply recorded sets of moderate-sized earthquakes. *Bulletin of the Seismological Society of America*, 81, 1754-1782.

Brune J., 1970, Tectonic Stress and the Spectra of Seismic Shear Waves from Earthquakes. *Journal of Geophysical Research*, 75, 4997-5009.

Field E., Jacob K., 1995, A Comparison And Test Of Various Site-Response Estimation Techniques, Including Three That Are Not Reference-Site Dependent. *Bulletin of the Seismological Society of America*, 85, 1127-1143.

García D., Krishna-Singh S., Herraiz M., Ordaz M., Pacheco J., Cruz-Jiménez H., 2009, Influence of Subduction Zone Structure on Coastal and Inland Attenuation in México. *Geophysical Journal International*, 179, 215-230.

Kramer S., 1996, Geotechnical Earthquake Engineering. Prentice Hall, University of Washington, US.

Lermo J., Chávez-García F., 1993, Site Effect Evaluation Using Spectral Ratios With Only One Station. *Bulletin of the Seismological Society of America*, 83, 1574-1594.

Luzón F., Al-Yuncha Z., Sánchez-Sesma F.J., Ortiz-Alemán C., 2001, A Numerical Experiment on the Horizontal to Vertical Spectral Ratio in Flat Sedimentary Basins. *Pure and Applied Geophysics*, 158, 2451-2461.

Nakamura Y., 1989, A Method for Dynamic Characteristics Estimation of Subsurface using Microtremor on the Ground Surface, *Quarterly Report of RTRI*, 30:1, 25-33.

Ordaz M., Singh S.K., 1992, Source Spectra and Spectral Attenuation of Seismic Waves from Mexican Earthquakes, and Evidence of Amplification in the Hill Zone of Mexico City. *Bull Seism Soc. Am.*, 82, 24-43.

Ortiz-Alemán C., Martin R., Gamio J., 2004, Reconstruction of Permitivity Images from Capacitance Tomography Data by Using Very Fast Simulated Annealing. *Measurement Science and Technology*, 15, 1380-1390.

Pérez-Campos X., 2008, MASE: Undergraduate Research and Outreach as Part of a Large Project. *Seismological Research Letters*, 79, 232-236.

Rodríguez-Zuñiga J.L, Ortiz-Alemán C., Padilla G., 1997, Application of Genetic Algorithms to Constrain Shallow Elastic Parameters Using *In Situ* Ground Inclination Measurements. *Soil Dynamics and Earthquake Engineering,* 16, 223- 234.

Sánchez-Sesma F., Rodríguez M., Iturrarán-Viveros U., Luzón F., Campillo M., Margerin L., García-Jerez A., Suarez M., Santoyo M.A., Rodríguez-Castellanos A., 2011, A Theory for Microtremor H/V Spectral Ratio: Application for a Layered Medium. *Geophysical Journal International,* 186, 221-225.

Shearer P., 2009, Introduction to Seismology, Cambridge University Press. San Diego, California.

Geofísica Internacional (2017) 56-1: 87-101

Original paper

A probabilistic seismic hazard assessment of the Trans-Mexican Volcanic Belt, Mexico based on historical and instrumentally recorded seismicity

José Antonio Bayona Viveros, Gerardo Suárez Reynoso and Mario Gustavo Ordaz Schroeder

Received: May 05, 2016; accepted: November 28, 2016; published on line: January 01, 2017
DOI: 10.19155/geofint.2017.056.1.7

Resumen

La Faja Volcánica Transmexicana (FVTM) es una cadena volcánica activa que se deforma por una red de fallas extensionales intra-arco. Aunque varios sismos corticales con magnitud>7 se han originado en la FVTM desde el siglo XVI, la sismicidad de fondo de esta estructura geológica es muy baja y la región es considerada, tradicionalmente, como de peligro sísmico bajo. En este estudio, presentamos un modelo probabilístico actualizado de la FVTM. El catálogo de sismicidad empleado incluye cuarenta y tres sismos registrados histórica e instrumentalmente desde 1858 hasta 2014; 5 de los cuales, son eventos de magnitud considerable ocurridos en la FVTM a lo largo del siglo XIX. Debido a la falta de una muestra estadísticamente representativa, proponemos, de manera cualititativa, que dicho catálogo es completo para magnitudes M≥4 desde 1964 y, para magnitudes M≥6; desde 1858. De igual modo, introducimos tres diferentes relaciones de magnitud-frecuencia entre eventos. La primera, es una relación convencional Gutenberg-Richter que ajusta la distribución de sismos registrados de manera instrumental. Las dos restantes, son aproximaciones semiparamétricas que integran datos históricos e instrumentados para determinar tasas de sismicidad en la región. Nuestro modelo preferido (modelo de sismicidad B) ajusta la distribución de datos históricos e instrumentados de manera independiente y fusiona ambos ajustes en una sola curva. Por otro lado, presentamos un mapa de peligro uniforme (USH) de la FVTM para un periodo de retorno de 500 años que se obtiene considerando tres fuentes sísmicas principales: 1) Sismos de subducción con fallamiento inverso originados en la Trinchera Mesoamericana (MAT); sismos de profundidad intermedia generados dentro de la subyacente Placa de Cocos y 3) sismos de naturaleza cortical localizados en la FVTM. De acuerdo con el modelo de sismicidad B, el periodo promedio de recurrencia de sismos M≥7 en la FVTM es, aproximadamente, 150 años. En contraste, el periodo de recurrencia calculado usando exclusivamente datos instrumentados es de 12,000 años. Los resultados de este modelo de sismicidad, que considera datos históricos e instrumentales, parecen coincidir con los periodos de retorno de sismos prehistóricos estimados para pequeños segmentos del sistema de fallas de la FVTM reportados en diversos estudios paleosismológicos. Al comparar los resultados de nuestro modelo de sismicidad predilecto, los valores de PGA obtenidos a partir de datos de sismicidad instrumentada son entre 18 y 56% menores que aquéllos predichos por el modelo de sismicidad que también considera el catálogo de sismicidad histórica.

Palabras clave: Faja Volcánica Transmexicana, catálogo de sismicidad histórica e instrumentada, modelo de sismicidad semiparamétrico, peligro sísmico.

J. Bayona
G. Suárez
Instituto de Geofísica
Universidad Nacional Autónoma de México
Ciudad Universitaria
Delegación Coyoacán 04510
CDMX, México
*Corresponding author: gersua@yahoo.com

M. Ordaz
Instituto de Ingeniería
Universidad Nacional Autónoma de México
Ciudad Universitaria
Delegación Coyoacán 04510
CDMX, México

J. Bayona
Institute of Earth and Environmental Sciences
University of Potsdam

Helmholtz-Zentrum Potsdam Deutsches
GeoForschungsZentrum

Abstract

The Trans-Mexican Volcanic Belt (TMVB) is an active volcanic chain being deformed by an intra-arc extensional fault network. Although several crustal earthquakes with magnitude>7 have originated in the TMVB since the 16th century, the background seismicity of this geological structure is very low and the region is usually considered of low seismic hazard. In this study, we present an updated probabilistic seismic hazard model of the TMVB. The seismicity catalog used here includes forty-three historically and instrumentally recorded earthquakes, from 1858 to 2014; five of these are large earthquakes that occurred in the TMVB during the XIXth century. Due to the lack of a statically representative sample, we propose, in a qualitative manner, the seismicity catalog is complete for M≥4 since 1964 and for M≥6 since 1858. Moreover, we introduce three different earthquake frequency-magnitude relations. The first one is a conventional Gutenberg Richter fit of the distribution of the instrumentally recorded earthquakes data. The other two are non-conventional, semi-parametric approaches that integrate the historical and the instrumental data to determine seismicity rates in the region. Our preferred model (seismicity model B) fits separately the instrumental and the historical data and merge the two fits into one curve. A uniform seismic hazard (USH) of the TMVB for a return period of 500 years was calculated considering three major sources of earthquakes: 1) Subduction thrust-faulting events in the Middle American Trench (MAT); 2) Earthquakes within the subducted Cocos plate and, 3) Shallow crustal earthquakes in the TMVB. According to the seismicity model B, the average recurrence time of a M≥7 earthquake on the TMVB is approximately 150 years. In contrast, the recurrence time estimated from the instrumental catalog is 12,000 years. The results of this seismicity model, which is based on historical and instrumental data, agrees also with the return periods of prehistoric earthquakes, estimated for short segments of the fault system in the TMVB in paleoseismological studies. When comparing the results of our preferred seismicity model, the PGA estimated using only the instrumental seismicity are 18 to 56% smaller than those predicted by the model using the historical catalog.

Key words: Trans-Mexican Volcanic Belt, historical and instrumental seismicity catalog, semi-parametric seismicity model, seismic hazard.

Introduction

We present a seismic hazard assessment of the TMVB that takes into account the seismic activity observed in the region from 1858 to 2014. Although this region in central Mexico is not as seismically active as some other parts of the country, such as the Pacific coast or the Gulf of California, there is evidence of major historical crustal earthquakes (M>7) occurring on the TMVB in the last 500 years (García-Acosta and Suárez; 1996; Suárez and Caballero-Jiménez; 2012). As in the case of many other continental faults, the crustal faults in the TMVB responsible for these large earthquakes apparently lie dormant for several thousand years.

Although relatively infrequent, the occurrence of these shallow, crustal events in the vicinity of densely populated areas poses an important seismic hazard to the more heavily populated area of Mexico. The larger cities in the country, such as Mexico City, Guadalajara, Morelia and Jalapa lie on the TMVB. According to the latest census of the National Institute of Statistics and Geography in 2010 (http://www.inegi.org.mx/est/contenidos/proyectos/ccpv/), more than 43 million people (approximately 40% of the population in Mexico) live in cities and towns located on this geological province. The observations of the past 500 years indicate that crustal earthquakes of large magnitude occur throughout the TMVB, regardless of the dearth of small magnitude seismicity.

Traditionally, the seismic hazard studies conducted for cities on the TMVB are based only on the instrumental seismicity catalog. However, the background seismicity is very low and, at first glance, this suggests that the seismic hazard is moderate. The Federal Power Commission (CFE) publishes a manual for the design of civil works against earthquakes, which has become a national standard. CFE classifies the TMVB as a region of moderate hazard (https://www.scribd.com/doc/52197523/CFE-Sismo-08). Nevertheless, the 1912 Acambay and the 1920 Jalapa earthquakes, together with historical reports of macroseismic data, suggest that although these crustal earthquakes have long recurrence periods, they may be of relatively large magnitudes and take place in close vicinity to major cities and towns. The purpose of this paper is to integrate the large historical earthquakes of the XIXth century in order to estimate the seismic hazard in the TMVB. Our results indicate that the

hazard estimate including the historical data is much larger than previously estimated from instrumental data.

Tectonic overview of the TMVB

The TMVB is a volcanic arc that spans Central Mexico from the Pacific coast to the Gulf of Mexico. It has a variable width that oscillates between 80 and 230 km (Figure 1). Pardo and Suárez (1993; 1995) showed that the oblique orientation of the TMVB relative to the subduction zone is due to the geometry and to the lateral changes in dip of the subducted Cocos plate beneath central Mexico (Suárez *et al*., 1990). Pardo and Suárez (1993; 1995) speculated that to the north of the region where the seismic activity within the subducted slab ceases, the subducted Cocos plate bends sharply downwards. Recent results of the tomographic inversion of teleseismic waves observed by the dense network of temporary seismic stations of the MesoAmerican Subduction Experiment (*MASE*), Pérez-Campos *et al*. (2008) suggests that in central Mexico, the subducted Cocos plate dips at an angle of 75º into the mantle, reaching a depth of 120 km beneath the TMVB.

The TMVB is affected mostly by extensional tectonics (*e.g.*, Ferrari *et al*., 2012; Suter *et al*., 1995). Suter *et al*. (1992; 2001) attribute the extensional regime in the Morelia–Acambay fault system, in the central part of the TMVB, to isostatically compensated surface loads in response to the high elevation of the volcanic belt. Ferrari *et al*. (2012), based on the heat flow measurements of Ziagos *et al*. (1985), suggest that the origin of this extension is related to the hot and low-density mantle (~950 to 1000° C) that underlies the Moho beneath the TMVB. This buoyant thermal effect presumably promotes the uplift and subsequent extensional deformation of the volcanic arc.

This extensional regime is characterized by seismically active, east west oriented normal faults throughout the volcanic belt. Most of these faults exhibit pronounced scarps that are clearly mapped on the surface for distances as long as 50 km (Figure 2). Many of these faults

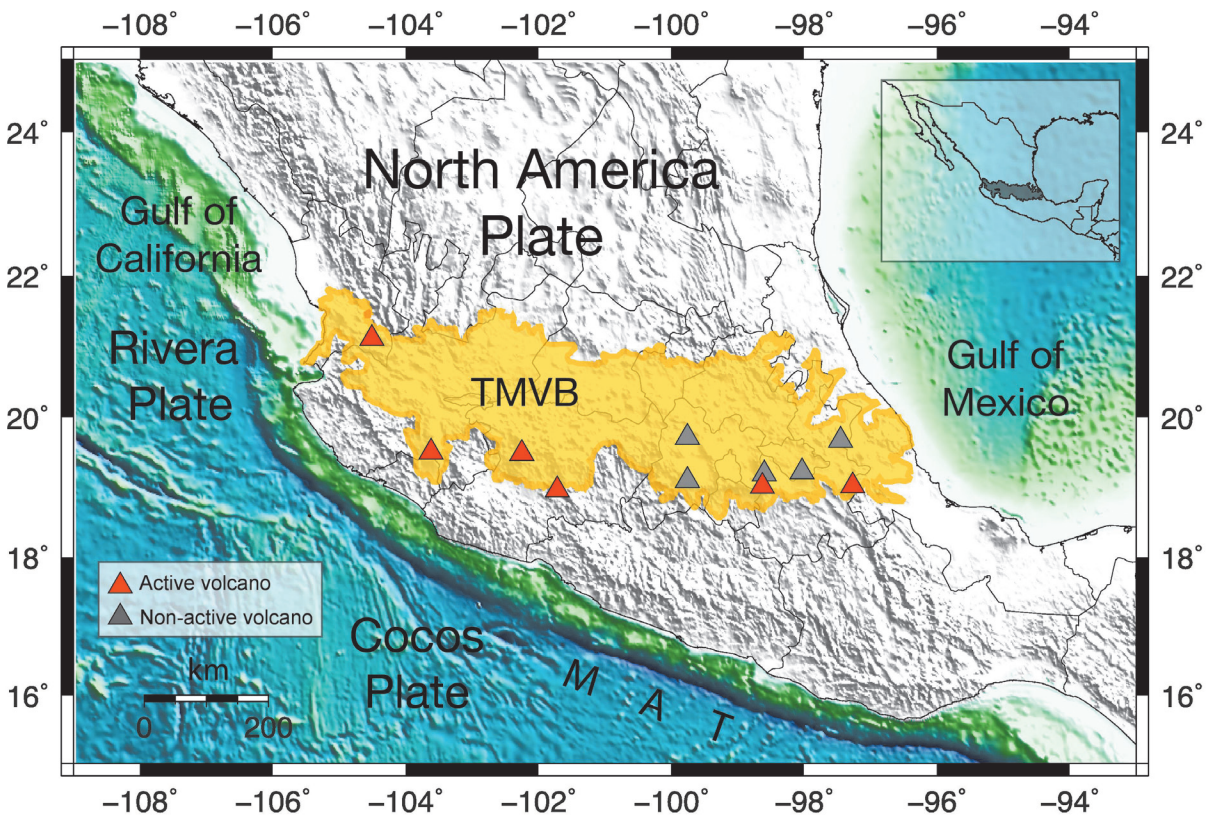

Figure 1. Extent of the TMVB reported by Ferrari *et al*. (2012).

are geologically active and cut alluvium and Quaternary scoria volcanoes, indicating recent deformation. Suter *et al*. (1992) estimate an average rate slip rate of 2 mm/yr. on these extensional faults. The Quaternary vertical slip rates of these faults have a mean of 0.07 mm/yr and the bulk extension rate of the TMVB is estimated to be 0.2 ± 0.05 mm/yr (Suter *et al.* 2001).

Some of these geologically active faults like the Acambay-Tixmadejé, the Venta de Bravo faults, and the faults bounding the Chapala graben, are located just a few kilometers away from densely populated cities, such as Mexico City, Guadalajara, Puebla or Morelia. Although many of these extensional crustal faults are clearly mapped on the surface, in some cases they are blind and show no surface expression. In the region of the 1920 earthquake, for example, there are no clearly identified faults mapped on the surface.

Historical and instrumental seismicity in the TMVB

During the past 100 years, two large crustal earthquakes in the TMVB have been recorded instrumentally. On November 19, 1912, an earthquake (M_w 6.9) took place near the city of Acambay rupturing one of the faults bounding the Acambay graben, about 80 km from Mexico City (Figure 3). This earthquake caused large destruction in the town of Acambay and in neighboring towns and villages (Urbina and Camacho, 1913) and caused moderate damage in Mexico City (Suter, 2015). A few years later, on January 4, 1920, an earthquake M_w *6.4* took place on the eastern part of the TMVB (Figure 3). According to Suárez (1992), this event is one of the more deadly earthquake ever recorded in Mexico, just after the large 1985 Michoacán earthquake (M_w 8.1). More than 1,500 fatalities were estimated. Most of them drowned or buried under the debris flows caused by the landslides on the steep cliffs bounding the course of the Pescados river (Comisiones del Instituto Geológico Mexicano, 1922). The most recent moderate-sized earthquake in the TMVB took place on February 22, 1979. The Maravatio earthquake (m_b 5.3) occurred near the western end of the Acambay fault and caused only slight damage (Astiz, 1980).

The recurrence period of some segments of these crustal faults were estimated on the basis of paleoseismological studies in the vicinity of the Acambay graben. Langridge *et al.* (2000) conducted a study on the fault trace of the 1912 Acambay earthquake. Their results show the presence of three previous ruptures with an approximate recurrence time of 3,600 years. Similar paleo seismological studies conducted on the neighboring faults, on the

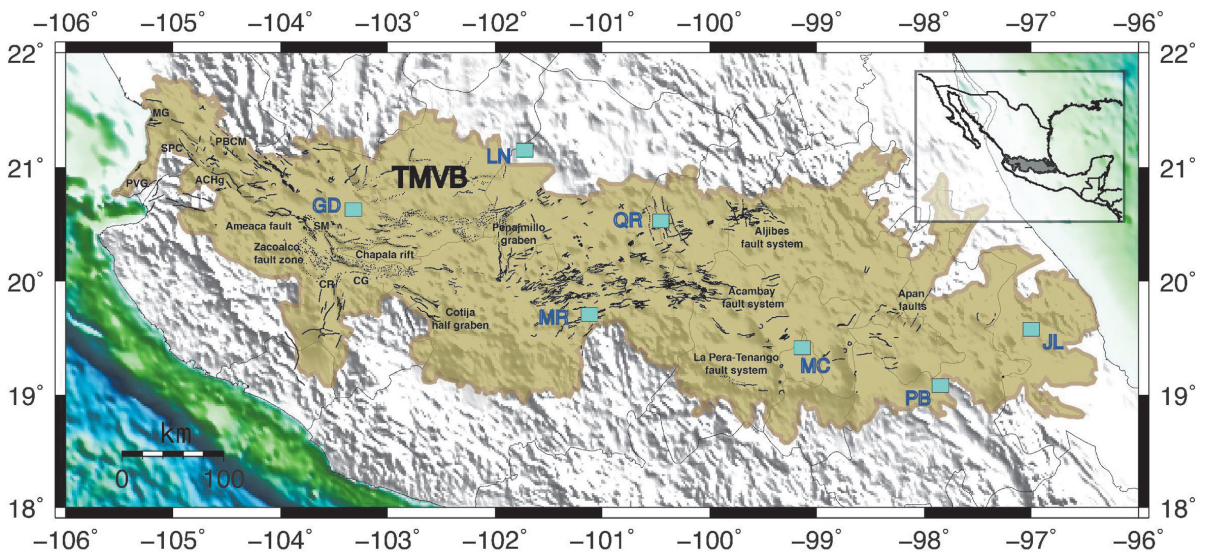

Figure 2. Distribution of the faults with Quaternary activity mapped on the TMVB. PVG represents the Puerto Vallarta graben; MG Mecatán Graben; SPC the San Pedro-Ceboruco Graben; ACH the Amatlán de Cañas Half-graben; PBCM the Plan de Barrancas-Cinco Minas Graben; SM the San Marco fault; CR the Colima Rift; CG the Citlala Graben. The major cities are abbreviated as: GD: Guadalajara; LN: León; MR: Morelia; QR: Querétaro; MC: Mexico City; PB: Puebla; and JL: Jalapa.

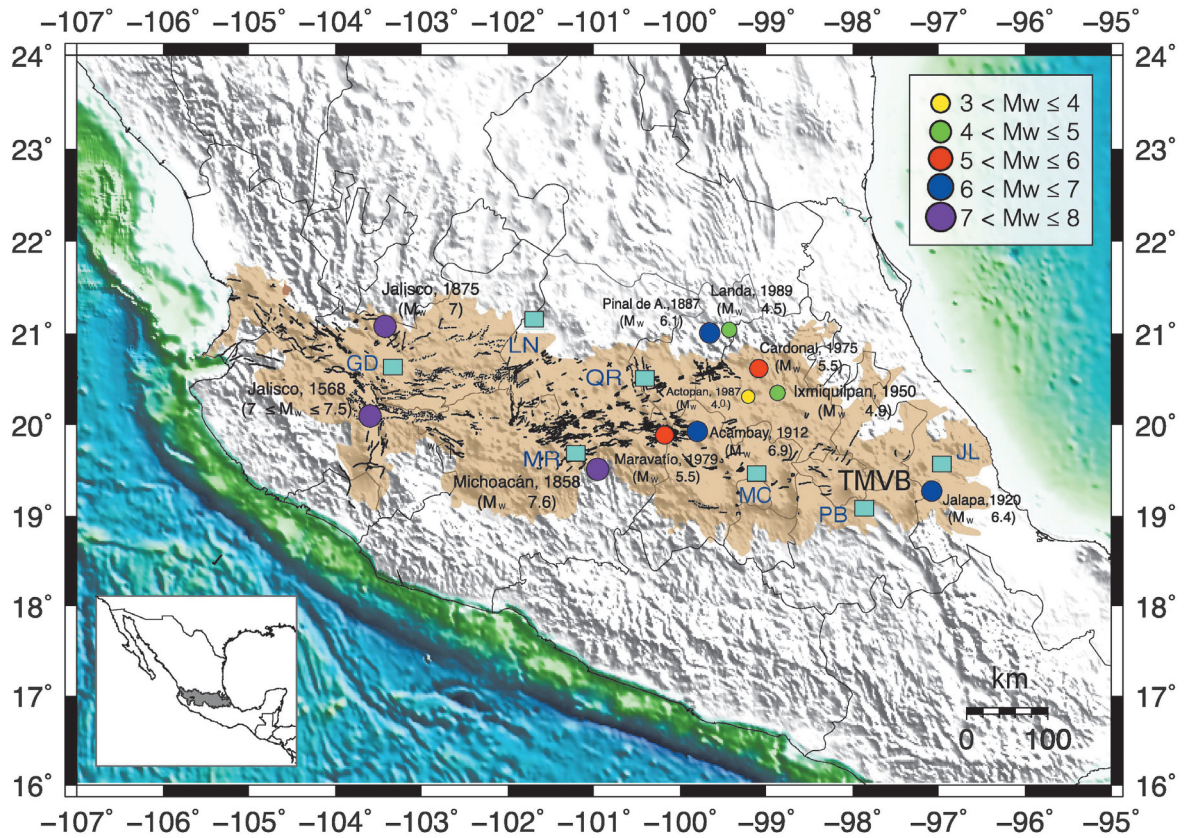

Figure 3. Spatial and temporal distribution of the more important historical and instrumental seismicity within the TMVB since the XVIth century.

southern boundary of the Acambay graben, indicate rupture intervals ranging from 600 to 10,000 years, depending on whether each fault breaks as a single unit or in separate segments (Langridge *et al*., 2013; Ortuño *et al*., 2015). Thus, based on the paleo seismological data, a significant earthquake may be expected in this region of central Mexico every 300 to 600 years (Zúñiga *et al*., 2012).

Prior to the instrumental period, several large earthquakes have been identified as crustal events in the TMVB, based on the damage and felt reports. The earliest reference is the December 27, 1568, earthquake (Figure 3). Fortunately, for an earthquake that occurred so early in the written historical record of Mexico, there are detailed descriptions of the damage and of the substantial and extended ground deformation caused by this earthquake (Suárez *et al*., 1994). Practically all of the newly built Franciscan churches in this area, located to the southwest of the city of Guadalajara, were destroyed. Based on the area of large seismic intensity, Suárez *et al*., (1994) suggest a magnitude of M_w 7.0. Later, Suter (2015) suggested a magnitude M_w 7.2 for this earthquake interpreting the ground rupture reported by historical sources as evidence of the fault trace. There are contradictions in the historical reports regarding the year of this earthquake. Suter (2015) suggests that this earthquake actually took place in 1567 and not in 1568.

Based on the inversion scheme of seismic intensity data proposed by Bakun and Wentworth (1997), Suárez and Caballero-Jiménez (2012) and Suárez *et al*. (2016) determined the approximate epicentral location and the magnitude of three large earthquakes in the TMVB that occurred during the XIXth century. The Santa Juliana earthquake on June 19, 1858, (*M* 7.6), the San Cristobal event of February 11, 1875, (*M* 7.0) and the Pinal de Amoles earthquake of November 26, 1887, (*M* 6.1) have numerous and detailed historical reports (García Acosta and Suárez, 1996).

The number and quality of the macroseismic data available was sufficient to allow for a quantitative determination of the source parameters using the inversion scheme of the observed Modified Mercalli Intensities (MMI) as a function of distance (Figure 3). Singh *et al*. (1996) interpreted the Santa Juliana earthquake as an in-slab event. Suárez and Caballero-Jiménez (2012) and Suárez *et al*. (2016) provide evidence that this event is a crustal event.

Probabilistic seismic hazard assessment

The seismic hazard analysis presented here was developed following the methodology proposed by Cornell (1968) and Esteva (1968). To this end, we compiled a robust seismicity catalog identifying the location of the seismic sources of interest that allows us to compute the mean recurrence periods of earthquakes in the region, as a function of magnitude. The seismic hazard estimations were obtained using the computer program *CRISIS 2015*, an updated version of *CRISIS 2007* (Ordaz *et al*., 2007; *https://ecapra.org/crisis-2007*).

Seismicity catalog and its level of completeness

The seismicity catalog used was based on an exhaustive search of the seismic databases. Thus the data were culled from the catalogs of the International Seismological Centre (*ISC*), the U.S. Geological Survey (*USGS*), the Global Centroid Moment Tensor Catalog (*CMT*), and of the Servicio Sismológico Nacional (*SSN*) were consulted. Duplications and aftershocks were avoided.

A total of 567 historical and instrumental earthquakes were initially selected. A maximum depth cutoff of 33 km was defined to guarantee that the earthquakes occurred in the crust (Figure 4). Due to the fact that only moderate and large earthquakes contribute to large ground accelerations, only $M \geq 4$ earthquakes were taken into account in this study. Furthermore, due to the dearth of seismic stations in the region, events $M<4$ are poorly located and there is a great uncertainty in their focal depth. In fact, many of the small earthquakes presumed to be in the TMVB crust are probably deeper, in-slab events within the subducted Cocos plate (green circles on Figure 4).

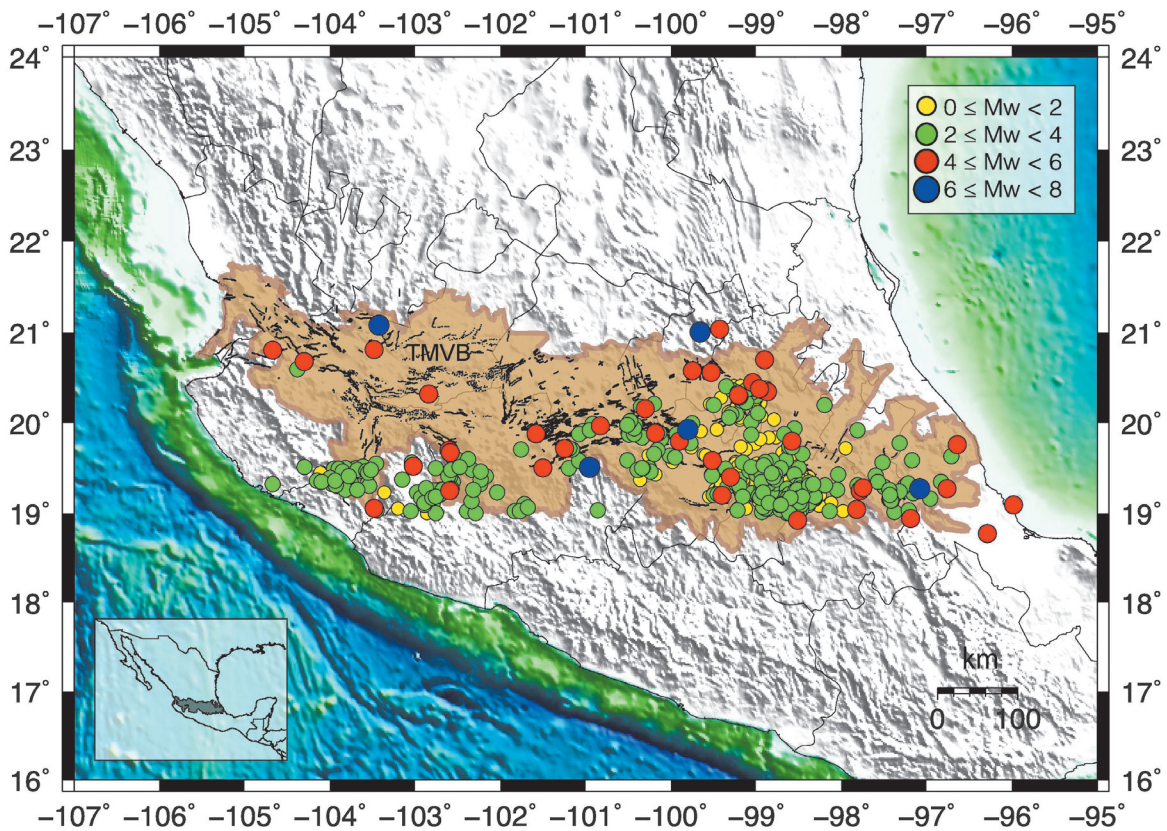

Figure 4. Epicentral locations of earthquakes observed on the TMVB sfromince 1858 to 2012. These events represent the selected seismic catalog that constitutes the basis of the seismic hazard analysis presented here.

A selected dataset of 43 events satisfied the selection criteria and constitute the basis of this analysis. The construction and operation of modern seismic networks, such as the national network of the *SSN* and the Worldwide Standard Seismic Network (*WWSSN*) substantially improved the detection capability of small earthquakes. Since 1964 the number of located small earthquakes has increased dramatically. Zuñiga *et al*. (2016) propose that the seismicity catalog of Mexico is complete for events approximately $m_b > 3.6$ since 1964. This observation is based on a completeness analysis of the Mexican catalog. The temporal changes and threshold levels observed in the Mexican seismicity catalog are similar to the variations observed worldwide (*e.g.,* Zúñiga and Wyss 1995; Zúñiga *et al*. 2005; Michael 2014). In a conservative manner, we consider here that the seismicity catalog of the TMVB is complete for $M \geq 4$ since 1964.

On the other hand, the population on the TMVB has been relatively dense since the XIXth century. As the historical catalog demonstrates, it is very likely that the damage and effects of moderate sized earthquakes would have been reported in the historical accounts. Thus we qualitatively suggest that the catalog is complete for earthquakes $M \geq 6$ since the second part of the XIXth century.

Seismic source characterization

Seismic faults on the TMVB are mapped throughout this geological province (Figures 2 and 3). Although some faults indicate recent deformation, there is insufficient geological information to state categorically that all mapped faults have been active in the Quaternary. On the other hand, it is important to point out that large crustal earthquakes have taken place in regions of the TMVB where there are no surface mapped faults. The apparent absence of faults in regions where important earthquakes have occurred may be due to insufficient mapping or to the fact that some faults are blind and do not necessarily outcrop at the surface. The more relevant example of earthquakes occurring where there are no geologically mapped faults is the 1920 Jalapa earthquake (M_w 6.4).

Considering that large historical and instrumental earthquakes are almost homogeneously distributed in the TMVB (Figures 2 and 3), we assume here that seismically capable crustal faults in the TMVB are also homogeneously distributed. This assumption means that the probability to expect an earthquake higher than a certain magnitude (in this case M_{max} 7.6 ± 0.3, the maximum magnitude earthquake observed in the region) is the same for every location of the TMVB (Suárez and Caballero-Jiménez, 2012; Suárez *et al*., 2016). Admittedly, this assumption may lead to overestimate the peak ground accelerations expected in the zone, as there is not enough evidence to confirm that all of these faults exist or remain active in the Quaternary. Thus we consider this assumption of uniformly distributed seismic hazard of the TMVB, as the more conservative assessment that can be made on the basis of the existing information.

Seismicity models

The more frequently used statistical model to represent the rate of occurrence of earthquakes is the Gutenberg-Richter relation. This relation establishes that the number of earthquakes is a function of the magnitude. This frequency magnitude relation is expressed as:

$$log_{10} N = a - bM \quad (1)$$

This relation between magnitude M and the logarithm of the number of earthquakes N is parameterized by the intercept of a and the slope b of the linear fit (Ishimoto and Ida, 1939; Gutenberg and Richter, 1944). A more conservative expression of earthquake occurrence is obtained by associating a maximum magnitude, $M_{max,}$ to the distribution (Aki, 1965). The modified seismicity model is expressed as:

$$\lambda(M) = \lambda_c \, (e^{-\beta M} - e^{-\beta Mmax})/(e^{-\beta Mc} - e^{-\beta Mmax}) \quad (2)$$

where, $\lambda_c = N/A$ is the exceedance rate of the minimum magnitude earthquake (M_c) in the catalog. $\beta = 1/(\mathrm{M_p}\text{-}\mathrm{M_c}) = b\ ln(10)$. N is the number of earthquakes with magnitudes $M \geq M_c$, the parameter A is the duration of the seismicity catalog and $\mathrm{M_p}$ is the average magnitude of all the events (Aki, 1965).

Three seismicity models were constructed based on the compiled seismicity catalog. The first one, Model A, is a traditional parametric model following the modified Gutenberg-Richter relation and using only the instrumental catalog (green curve on Figure 5). The exceedance rate for a cut-off magnitude λ_c and the β value were computed using the maximum likelihood method proposed by Aki (1965). The resulting seismicity parameters for this model are λ_c = 3.333 and β = 0.750. These values are similar to those reported by Ordaz *et al*., (2012), which are the current values used to quantify the seismic hazard of the TMVB.

Two other non-parametric models are proposed that integrate the historical and the instrumental seismic data (Figure 5). The seismicity Model B (blue line on Figure 5) represents an effort to describe the seismic activity of the TMVB in a semi-parametric manner, using both the instrumental and the historical earthquakes of the catalog. In this approach, two different Gutenberg-Richter distributions are estimated: one of the curves corresponds to the instrumental data and the other to the historical seismicity. Thus considering the assumption that the seismicity catalog is complete for magnitudes $M \geq 4$ since 1964 and for $M \geq 6$ since 1858, we estimate one Gutenberg-Richter linear function for earthquakes $4 \leq M < 6$ earthquakes, and a separate one for earthquakes $M \geq 6$ events. As we have not observed any earthquake M≥6 on the TVMB since 1964, we propose to fuse both fits into one curve by adding the exceedance rate of instrumental earthquakes to historical events with M>6. The resulting seismic parameters are: $\lambda_c = 0.033$ and $\beta = 1.282$

Finally, a third model (Model C and red curve on Figure 5) results from fusing the exceedance rates obtained from the fit of instrumental data ($4 \leq M < 6$) with the exceedance rates of M≥6 earthquakes observed from the catalog. This model represents the upper bound of peak ground accelerations PGA that would be expected in this geological province. The mean recurrence times of earthquakes of a certain magnitude that may occur anywhere in the TMVB, according to the three seismicity models, are shown on Figure 6. Notice that for earthquakes $M_w > 5.5$, the recurrence time between Model A, using only instrumental data, is substantially shorter than for the two other models, which include historical data.

Seismic hazard estimations of the TMVVB

We propose that model B is a conservative estimation of the seismicity in the TMVB. Using this model, we estimate the seismic hazard of the TMVB and a uniform seismic hazard (USH) map of the central portion of Mexico. In

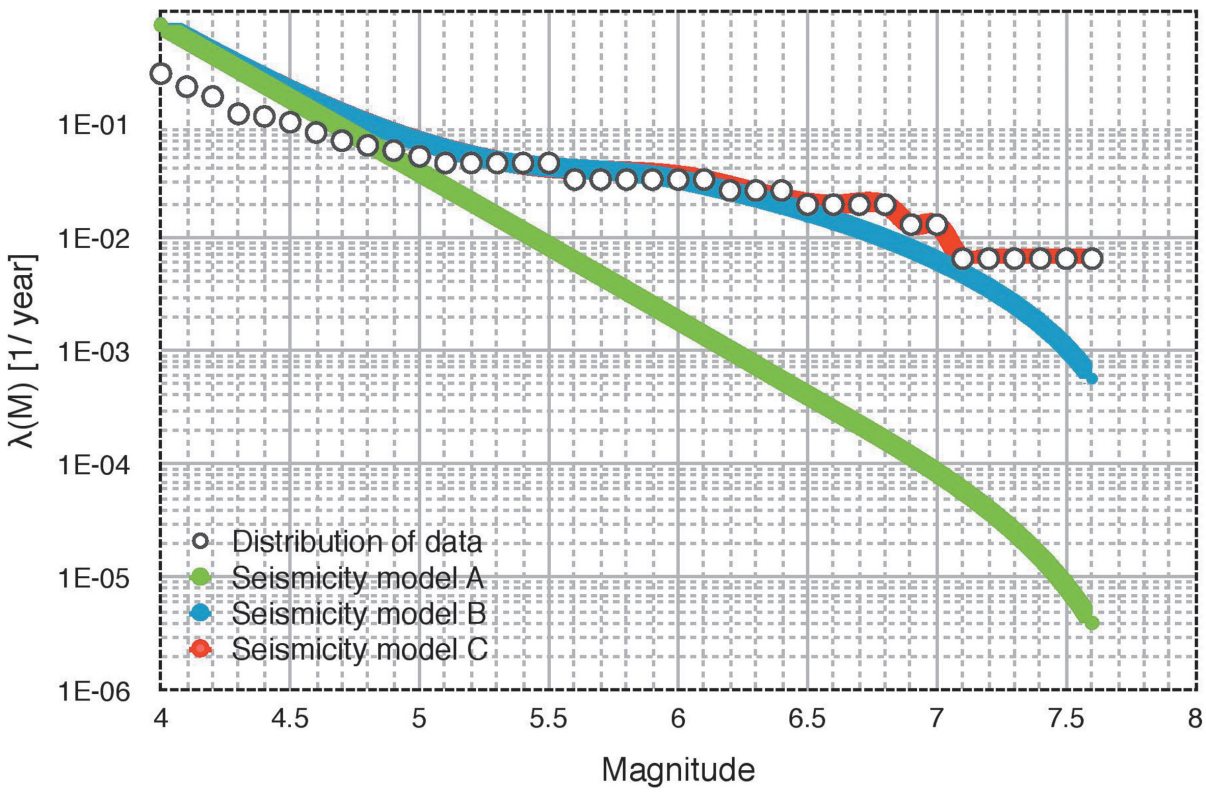

Figure 5. The exceedance rates of earthquakes expected in the TMVB are shown as a function of magnitude. Model A (red curve) is obtained from the fit of instrumental data according to a conventional Gutenberg-Richter distribution and the maximum likelihood method. Model B (blue curve) results from merging the historical and instrumental data. This semi parametric approach appears to be a conservative description of the exceedance rates of earthquakes observed in the TMVB since the 16th century. Finally, seismicity Model C (green curve) is obrtained by fusing the exceedance rates reproduced by the fit of instrumental data ($4 \leq M < 6$) with the exceedance rates of earthquakes $M > 6$ observed from the seismic catalogs.

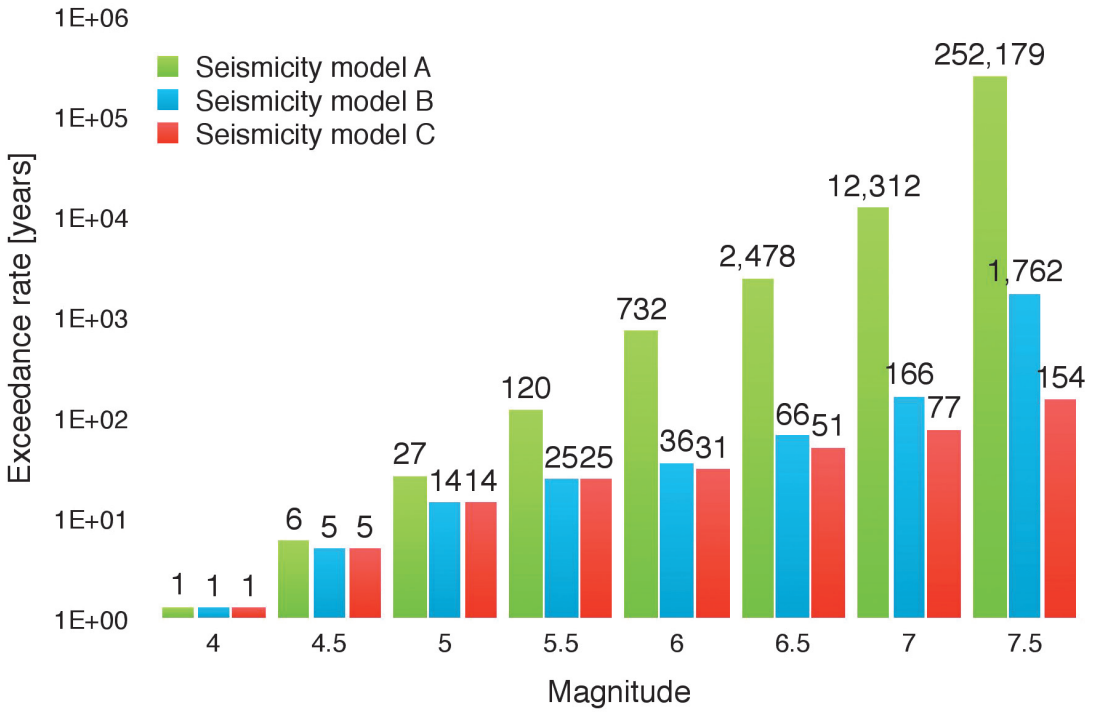

Figure 6. Mean return periods of crustal earthquakes expected on the TMVB as a function of magnitude. These estimations are computed using the three different seismicity models discussed. For earthquakes M>5.5, the results from the traditional model that uses only instrumental data (green bars) begin to differ significantly with the results predicted by the semi parametric models (bars in blue and red), which also consider historical seismicity.

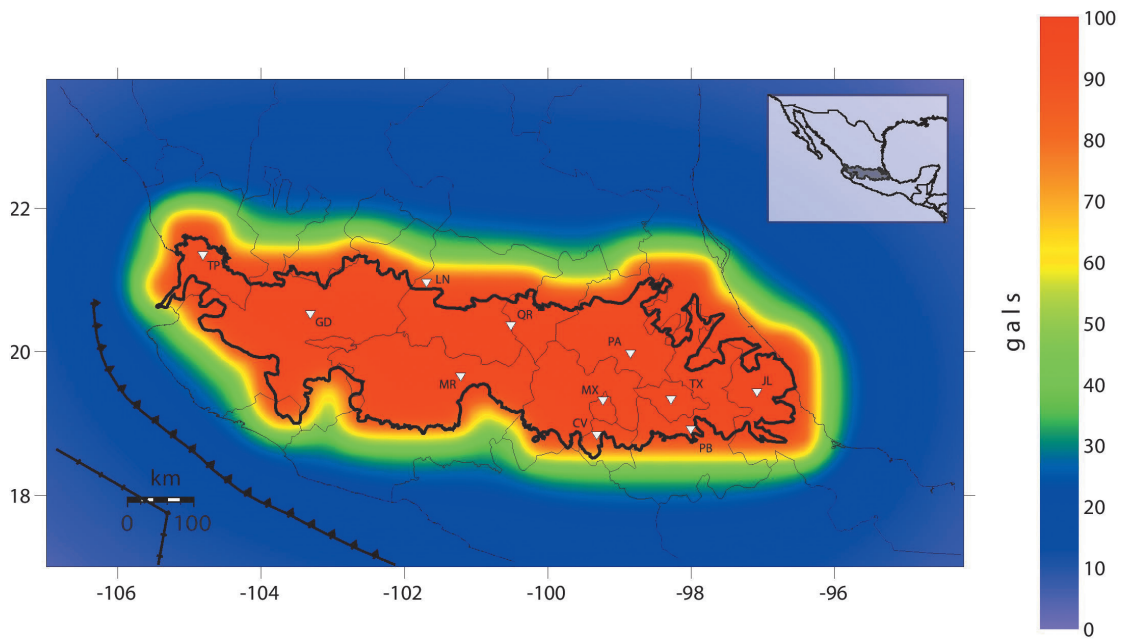

Figure 7. Seismic hazard map of the TMVB for a return period of 500 years. Peak ground accelerations are estimated thinking the TMVB as a whole and assuming the semi-parametric seismicity model B as the preferred model describing seismicity rates in the volcanic arc. Such estimations might represent upper boundaries of PGA, however, they seem to fit the few observations available to date.

order to estimate the USH of the TMVB, three types of earthquake sources are considered: 1) shallow crustal seismicity occurring on the TMVB; 2) in-slab earthquakes occurring within the subducted Cocos plate and; 3) subduction zone earthquakes along the Middle American Trench (MAT).

Attenuation models

Due to the lack of strong motion records of crustal earthquakes in the TMVB, it was necessary to use Ground Motion Prediction Equations (GMPE) from other regions of the world with similar geological characteristics. We use the ground motion prediction equations reported by Abrahamson *et al*., (2014), which describe the attenuation of the spectral response values in the horizontal and vertical components, for crustal earthquakes in tectonically active regions.

In the case of in-slab earthquakes, the parameters reported by Ordaz *et al*., (2012) and the GMPE's proposed by García *et al*., (2005) were utilized. On the other hand, the seismicity rate in the Middle American Trench was determined using a traditional Gutenberg-Richter distribution. This was obtained compiling information of 288 thrust earthquakes reported in the Global Centroid Moment Tensor (CMT) database (Dziewonsky *et al*., 1981). Earthquakes from this catalog were selected from January 1st, 1976 to December 31, 2014, within the geographic coordinates 15ºN ≥ latitude ≤ 24ºN latitudes and 106ºW ≤ longitude ≥ 92º W. All the events have magnitudes Mw ≥ 4.7 and focal depths of less than 40 km. In this case, the GMPE's estimated by Arroyo and Ordaz, (2010). for subduction zone earthquakes were utilized.

In computing ground motion expected for the return periods of 100, 500, 2500 and 10,000 years, we assumed a Poisson model to describe the probabilities of an earthquake occurrence. In other words, the seismicity rates on each seismic source are time-independent. The resulting seismicity parameters for the various seismic sources are summarized on Table 1.

Discussion of results and conclusions

In this study, we propose that a non-traditional, semi-parametric seismicity model, which incorporates instrumental and historical data, represents better the seismicity of the TMVB and is better suited to assess the seismic hazard. For example, according to the seismicity Model B, the

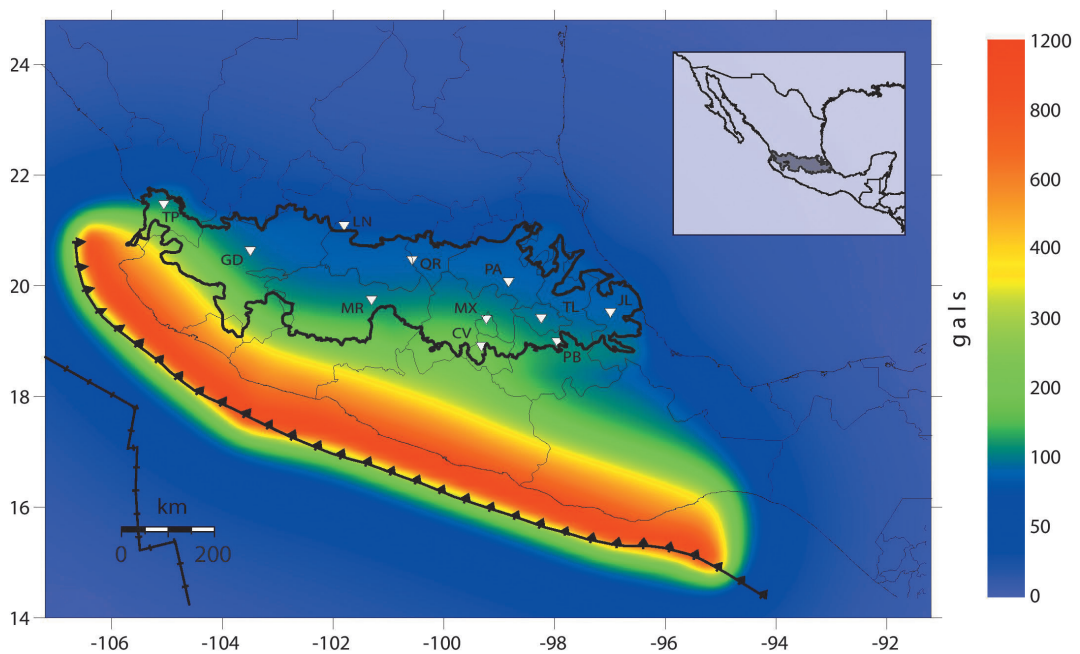

Figure 8. Uniform hazard map of central Mexico for a return period of 500 years. This model is built considering subduction thrust-faulting earthquakes occurring in the Middle American Trench, normal-faulting events within the subducted Cocos plate and shallow crustal earthquakes in the TMVB. The seismicity parameters used to create this model are reported in Table 1.

Table 1. Seismicity parameters used in this study to assess the seismic hazard of the TMVB.

Type of faulting	λ	β	$\delta\beta$	M_{max}	M_c	GMPE
Crustal instrumental earthquakes	0.750	3.333	0.17	7.6	4.0	Abrahamson *et al*., (2014)
Crustal historical earthquakes	0.033	1.282	0.45	7.6	6.0	Abrahamson *et al*., (2014)
In-slab earthquakes (Central Mexico)	9.063	2.590	0.04	8.1	4.0	García *et al*., (2005)
In-slab earthquakes (Western Mexico)	6.452	2.078	0.04	8.1	4.0	García *et al*., (2005)
Subduction Earthquakes	7.385	1.235	0.06	8.1	4.7	Arroyo *et al*., (2010)

average recurrence time of a $M \geq 7$ earthquake on the TMVB is approximately 150 years. In contrast, the mean recurrence time estimated only on the instrumental catalog (Model A) is 12,000 years. The historical earthquake record of the past 160 years indicates that two earthquakes $M \geq 7$ have taken place on the TMVB. The mean recurrence time predicted by Model B of earthquakes $M \geq 6.5$ is of 66 years. The seismicity catalog shows that there are four events in this magnitude range in the last 160 years. Again, this is in good agreement with the predictions made by Model B and clearly shows that using only instrumental data, recurrence times of moderate and large earthquakes in the TMVB are considerably underestimated.

If we also consider the data available from paleo seismological studies, a similar picture emerges (Table 2). Studies performed in segments of crustal faults located on the TMVB indicate that the mean return periods of large earthquakes ($M_w > 7.0$) are in the order of 3,600 to 12,500 years (Table 2). The return period predicted by instrumental data is 2,600 years. However, it should be stressed that the return periods estimated from paleo seismological studies refer only to short segments of the fault system in the TMVB. Clearly, considering the whole system of crustal faults observed in the TMVB, the return period predicted by Model A would be an underestimation.

Due to the epistemic uncertainties stemming from the limited data available, it was necessary to generate scenarios representing upper and lower bounds of the seismic hazard in the region. These models estimate PGA's on hard soil of the TMVB for the more densely populated locations located on this geological province based on the uniform seismic hazard assessment presented above (Tables 3 and 4).

It is worth to compare the results obtained here for the more important cities on the TMVB with the values of PGA proposed by Ordaz (2004) for a return period of 500 years (Table 5). The PGA values estimated by Ordaz (2004) are almost identical to those estimated from Model A in this study. This is not surprising, considering

Table 2. Paleoseismological studies carried out in segments of crustal faults located on the TMVB.

Reference	Fault segment	Average observation window	Number of Earthquakes	Mean Return Period (yrs)	Magnitude M_w
Langridge *et al*., (2000)	Acambay	~ 11,570	3	3,600	6.9
Langridge *et al*., (2013)	Pastores	~ 35,000	3	(10,000 - 15,000)	7.0
Suñe-Pujol *et al*., (2014)	Temascalcingo	~ 27,000	3	9,000	6.4
Ortuño *et al*., (2015)	Pastores (west segment)	~ 4,000	5	(1,000 - 2,600)	Variable rupture

Table 3. Peak ground accelerations estimated for basin fill of the TMVB according to three different models describing its seismicity rate.

Return period	Seismicity model A	Seismicity model B	Seismicity model C
100 years	14 gals	28 gals	35 gals
500 years	41 gals	102 gals	133 gals
2,500 years	98 gals	260 gals	347 gals
10,000 years	181 gals	481 gals	623 gals

Table 4. Uniform seismic hazard estimations expected in Mexico City, Guadalajara, Morelia and Jalapa, according to three seismicity models of the TMVB, for different return periods.

Mexico City (19º 26' N, 99º 8' W)

Return period	Seismicity model A	Seismicity model B	Seismicity model C
100 years	45 gals	63 gals	70 gals
500 years	130 gals	164 gals	190 gals
2,500 years	271 gals	348 gals	411 gals
10,000 years	425 gals	570 gals	698 gals

Guadalajara (20º 40' N, 103º 21' W)

Return period	Seismicity model A	Seismicity model B	Seismicity model C
100 years	38 gals	49 gals	63 gals
500 years	91 gals	134 gals	166 gals
2,500 years	182 gals	299 gals	374 gals
10,000 years	303 gals	500 gals	668 gals

Morelia (19º 46' 06'' N, 101º 11' 22'' W)

Return period	Seismicity model A	Seismicity model B	Seismicity model C
100 years	45 gals	59 gals	66 gals
500 years	112 gals	149 gals	176 gals
2,500 years	221 gals	319 gals	386 gals
10,000 years	353 gals	523 gals	674 gals

Jalapa (19º 32' 24'' N, 96º 55' 59'' W)

Return period	Seismicity model A	Seismicity model B	Seismicity model C
100 years	27 gals	34 gals	38 gals
500 years	65 gals	109 gals	136 gals
2,500 years	141 gals	275 gals	355 gals
10,000 years	241 gals	484 gals	656 gals

Table 5. Comparison of the peak ground accelerations expected in Mexico City, Guadalajara, Morelia and Jalapa, for a return period of 500 years, according to Ordaz (2004) and this article.

Seismicity Model	Mexico City	Guadalajara	Morelia	Jalapa
Ordaz (2004)	~ 125 gals	~ 75 gals	~ 100 gals	~ 90 gals
This study, model A	130 gals	91 gals	112 gals	65 gals
This study, model B	164 gals	134 gals	149 gals	109 gals
This study, model C	190 gals	166 gals	176 gals	136 gals

that both use a very similar instrumental catalog. However, when comparing with the results of Model B, the PGA's estimated using only the instrumental seismicity are 18 to 56% smaller than those predicted in the model using the historical catalog. The largest differences are in the cities of Morelia and Guadalajara, due to the proximity of large historical earthquakes (Table 5).

In conclusion, our results suggest strongly that the estimations of PGA's may be severely underestimated using the limited instrumental catalog. Important differences exist in the uniform seismic hazard estimations with the incorporation of historical seismicity into the seismicity catalog. The seismic hazard determined with the use of the historical data, albeit only available for a short period, agree better with the seismic record and with the paleo seismological observations available. Clearly, this is a first approach to the important issue of estimating seismic hazard in this highly populated region of Mexico. It is evident that as more seismic, geological and geodetic data become available, hazard estimates should be improved. In particular, future work should consider including the local site response of the larger cities on the TMVB, particularly in Mexico City, in order for these results to be incorporated in the building codes of central Mexico.

Acknowledgements

The authors thank A. Husker, L. Ferrari and M. A Jaimes, for their comments and suggestions. The authors particularly thank R. Zúñiga for his support in the compilation of a complete catalog of the TMVB. The seismicity catalog used in this manuscript is available on request from the authors. One of us GS acknowledges grant (082821) from the Mexican National Council of Science and Technology (CONACyT). The support provided by the Instituto de Geofísica, UNAM is also acknowledged. The manuscript was greatly improved by the valuable comments made by two anonymous reviewers.

References

Abrahamson N.A., Silva W.J., Kamai R., 2014, Summary of the ASK14 ground motion relation for active crustal regions. *Earthquake Spectra*, 30, 3, pp. 1025-1055.

Aki K., 1965, 17, Maximum likelihood estimate of b in the formula logN= a-bM and its confidence limits.

Arroyo D., Ordaz M., 2010, Multivariate Bayesian regression analysis applied to ground-motion prediction equations, Part 2: Numerical example with actual data. *Bulletin of the Seismological Society of America*, 100, 4, 1568-1577.

Astiz L.M., 1980, Sismicidad en Acambay, Estado de México. El temblor del 22 de febrero de 1979. *Professional thesis, Mexico City,* Universidad Nacional Autónoma de México, Facultad de Ingeniería.

Bakun W.U., Wentworth C.M., 1997, Estimating earthquake location and magnitude from seismic intensity data. *Bulletin of the Seismological Society of America*, 87, 6, 1502-1521.

Comisiones del Instituto Geológico de México, 1922, Memoria relativa al terremoto mexicano del 3 de enero de 1920: Instituto Geológico de México, Boletín 38, 106 p, *http:/bcct.unam.mx/bogeolpdf/geo38/.*

Cornell C.A., 1968, Engineering seismic risk analysis. *Bulletin of the Seismological Society of America*, 58, 5, 1583-1606.

Dziewonski A.M., Chou T.A., Woodhouse J.H., 1981, Determination of earthquake source parameters from waveform data for studies of global and regional seismicity, *J. Geophys. Res*., 86, 2825-2852, doi:10.1029/JB086iB04p02825.

Esteva L., 1968, *Bases para la formulación de decisiones de diseño sísmico*. Instituto de Ingeniería, Universidad Nacional Autónoma de México.

Ferrari L., Orozco-Esquivel T., Manea V., Manea M., 2012, The dynamic history of the Trans-Mexican Volcanic Belt and the Mexico subduction zone. *Tectonophysics*, 522, 122-149.

García-Acosta V., Suárez G., 1996, Los sismos en la historia de México, tomo I. *Universidad Nacional Autónoma de México/Centro de Investigaciones y Estudios Superiores en Antropología Social/Fondo de Cultura Económica*, 719.

García D., Singh S.K., Herráiz M., Ordaz M., Pacheco J.F., 2005, Inslab earthquakes of central Mexico: peak ground-motion parameters and response spectra. *Bulletin of the Seismological Society of America*, 95, 6, 2272-2282.

Gutenberg R., Richter C., 1944, Frequency of earthquakes in California, *Bulletin of the Seismological Society of America*, 34, pp. 185-188.

Ishimoto M., Ida K., 1939, Observations sur les seisms enregitres par le microseismograph construit dernierement, *Bull. Earthqu. Res. Int.*, 17, 443-478.

Langridge R.M., Weldon R.J., Moya J.C., Suárez G., 2000, Paleoseismology of the 1912 Acambay earthquake and the Acambay-Tixmadejé fault, Trans-Mexican volcanic belt. *Journal of Geophysical Research: Solid Earth*, 105,B2, 3019-3037.

Langridge R.M., Persaud M., Zúñiga F.R., Díaz G.D.J.A., Pérez P.V., Lacan P., 2013, Preliminary paleoseismic results from the Pastores fault and its role in the seismic hazard of the Acambay graben, Trans-Mexican Volcanic Belt, Mexico. *Revista Mexicana de Ciencias Geológicas*, 30, 3, 463-481.

Michael A., 2014, How Complete is the ISC-GEM Global Earthquake Catalog?, *Bull. of the Seism. Soc. Am.,* 104, 1829–1837, doi: 10.1785/0120130227

Ordaz M., 2004, Mapa de peligro sísmico de México con fines de calificación de equipo eléctrico, Instituto de Ingeniería, UNAM, Mexico.

Ordaz M., Aguilar A., Arboleda J., 2007, Program for Computing Seismic Hazard: CRISIS 2007 v1.1, Instituto de Ingeniería, UNAM, México.

Ordaz M., Arroyo D., Singh S.K., Suárez G., 2012, Estudios para la reevaluación del riesgo sísmico para el sitio de la Central Nucleoeléctrica Laguna Verde (CNLV), Instituto de Ingeniería, UNAM, México.

Ortuño M., Zuñiga F.R., Aguirre-Diaz G.J., Carreon-Freyre D., Cerca M., Roverato M., 2015, Holocene paleo-earthquakes recorded at the transfer of two major faults: The Pastores and Venta de Bravo faults (Trans Mexican Volcanic Belt), *Geosphere*, 11, 2, 160-184.

Pardo M., Suárez G., 1993, Steep subduction geometry of the Rivera plate beneath the Jalisco block in western Mexico. *Geophysical Research Letters*, 20, 21, 2391-2394.

Pardo M., Suárez G., 1995, Shape of the subducted Rivera and Cocos plates in southern Mexico: Seismic and tectonic implications. *Journal of Geophysical Research: Solid Earth (1978–2012)*, 100, B7, 12357-12373.

Pérez-Campos X., Kim Y., Husker A., Davis P.M., Clayton R.W., Iglesias A., Gurnis M., 2008, Horizontal subduction and truncation of the Cocos Plate beneath central Mexico. *Geophysical Research Letters*, 35, 18.

Singh S.K., Ordaz M., Pérez-Rocha L.E., 1996, The great Mexican earthquake of 19 June 1858: Expected ground motions and damage in Mexico City from a similar future event. *Bulletin of the Seismological Society of America*, 86, 6, pp.1655-1666.

Suárez G., Monfret T., Wittlinger G., David C., 1990, Geometry of subduction and depth of the seismogenic zone in the Guerrero gap, Mexico. *Nature*, 345, 6273, 336-338.

Suárez G., 1992, El sismo de Jalapa del 3 de Enero de 1920. *Rev. Mex. Ing. Sísm*, 42, 3-15.

Suárez G., García-Acosta V., Gaulon R., 1994, Active crustal deformation in the Jalisco block, Mexico: evidence for a great historical earthquake in the 16th century. *Tectonophysics*, *234,* 1, 117-127.

Suárez G., Caballero-Jiménez G.V., 2012, Quantitative Evaluation of Historical Earthquakes on the Mexican Volcanic Belt, *3rd INQUA-IGPC-567, International Workshop*

on Active Tectonics, Paleoseismology and Archaeseismology, Morelia, Mexico.

Suárez G., Caballero-Jiménez G.V., Novelo-Casanova D.A., Chico C., Ruíz D., 2016, Active Crustal Deformation in the Trans Mexican Volcanic Belt as Evidenced by Earthquakes During the last 450 Years, *J. Geophys. Res.,* Submitted.

Sunye-Puchol I., Lacan P., Ortuño M., Villamor P., Audin L., Zúñiga F.R., Lawton T.F., 2015, La falla San Mateo: nuevas evidencias paleosismológicas de fallamiento activo en el graben de Acambay, México, *Revista Mexicana de Ciencias Geológicas*, 32, 3, 361-376.

Suter M., Quintero O., Johnson C.A., 1992, Active faults and state of stress in the central part of the Trans-Mexican Volcanic Belt, Mexico 1. The Venta de Bravo Fault. *Journal of Geophysical Research: Solid Earth (1978–2012)*, 97, B8, 11983-11993.

Suter M., Quintero-Legorreta O., López-Martínez M., Aguirre-Díaz G., Farrar E., 1995, The Acambay graben: active intraarc extension in the Trans-Mexican volcanic belt, Mexico. *Tectonics*, 14, 6, 1245-1262.

Suter M., Carrillo-Martínez M., Quintero-Legorreta O., 1996, Macroseismic study of shallow earthquakes in the central and eastern parts of the trans-Mexican volcanic belt, Mexico. *Bulletin of the Seismological Society of America*, 86, 6, 1952-1963.

Suter M., Martínez M.L., Legorreta O.Q., Martínez M.C., 2001, Quaternary intra-arc extension in the central Trans-Mexican volcanic belt. *Geological Society of America Bulletin*, 113*,* 6, 693-703.

Suter M., 2015, The AD 1567 Mw 7.2 Ameca, Jalisco, Earthquake (Western Trans-Mexican Volcanic Belt): Surface Rupture Parameters, Seismogeological Effects, and Macroseismic Intensities from Historical Sources. Bulletin of the Seismological Society of America, 105, 2A, pp.646-656.

Urbina F., Camacho H., 1913, La zona megaséismica Acambay-Tixmadejé, Estado de México, conmovida el 19 de noviembre de 1912, Instituto Geológico de México, Boletín, 32, 125p.

Ziagos J.P., Blackwell D.D., Mooser F., 1985, Heat flow in southern Mexico and the thermal effects of subduction. *Journal of Geophysical Research: Solid Earth*, 90, B7, 5410-5420.

Zúñiga F.R., Wyss M., 1995, Inadvertent changes in magnitude reported in earthquake catalogs: Influence on b-value estimates, *Bull. Seismol. Soc. Am.*, 85, 1858-1866.

Zúñiga F.R., Pacheco J.F., Guzmán-Speziale M., Aguirre-Dıaz G.J., Espındola V.H., Nava E., 2003, The Sanfandila earthquake sequence of 1998, Queretaro, Mexico: activation of an undocumented fault in the northern edge of central Trans-Mexican Volcanic Belt. *Tectonophysics*, 361, 3, 229-238.

Zúñiga F.R., Reyners M., Villamor P., 2005, Temporal variations of the earthquake data in the catalogue of seismicity of New Zealand, *Bull. New Zeal. Soc. Earthquake Eng.,* 38, 87-107.

Zúñiga F.R., Ortuño M., Figueroa-Soto A., 2012, Incorporation Of Paleoseismological Data in the Calculation of the Seismic Hazard: An Example in Central Mexico. Proceedings of the 3rd INQUA-IGCP 567 International Workshop on Earthquake Geology, Palaeoseismology and Archaeoseismology, Morelia México.

Zúñiga F.R., Suárez G., Figueroa A., Mendoza A., 2016, A first order seismotectonc regionalization of Mexico for seismic hazard and risk estimation, *J. Seismol.,* in review.

Geofísica Internacional (2017) 56-1: 103-116

Original paper

Frecuency-wavenumber analysis of strong ground motion in Mexico City

Marcela Baena-Rivera, L. Eduardo Pérez-Rocha and Francisco J. Sánchez-Sesma

Received: May 20, 2016; accepted: November 09, 2016; published on line: January 01, 2017

DOI: 10.19155/geofint.2017.056.1.8

Resumen

Se presentan los resultados del análisis de las densidades espectrales de potencia en el dominio frecuencia-número de onda (f-$\mathbf{k}$) de los movimientos sísmicos registrados por la Red Acelerométrica de la Ciudad de México (MCAN, por sus siglas en inglés). En este trabajo se analizaron las series de tiempo de un evento sísmico registrado por la MCAN. Se acepta que cada registro es una realización de un campo aleatorio homogéneo cuya representación espectral revela las diversas ondas que se propagan en el medio. Se hizo una descomposición cinemática que separa las ondas según sus desplazamientos en las direcciones longitudinal y transversal, las cuales se asocian con las componentes horizontales de las ondas de Rayleigh y de Love, respectivamente. El análisis se aplicó a diferentes ventanas de tiempo de las señales para identificar las ondas generadas localmente que se propagan hacia diversas direcciones como resultado de su interacción con la geología superficial. Para cada componente longitudinal y transversal se estimó la densidad espectral de potencia en el dominio f-$\mathbf{k}$, la cual aporta las amplitudes, velocidades y direcciones de propagación de las ondas más significativas. Estos valores en función de la frecuencia constituyen los espectros cinemáticos del campo ondulatorio. Los resultados permiten establecer escenarios coherentes del campo de ondas en el valle de México identificando las ondas superficiales generadas localmente.

Palabras clave: Frecuencia-número de onda (f-$\mathbf{k}$), propagación de ondas, ondas superficiales, espectros cinemáticos.

M. Baena-Rivera
F. J. Sánchez-Sesma
Instituto de Ingeniería
Universidad Nacional Autónoma de México
Ciudad Universitaria
Delegación Coyoacán 04510
CDMX, México
*Corresponding author: mbaenar@gmail.com

L. Eduardo Pérez-Rocha
Instituto de Investigaciones Eléctricas
Cuernavaca 64490
Morelos, México

Abstract

An analysis of frequency-wavenumber (f-$\mathbf{k}$) spectral power densities of strong ground motion recorded by the Mexico City Accelerometric Network (MCAN) is presented. Time series of a seismic event recorded by the MCAN are analysed. Each recorded motion is assumed to be the insight of a homogeneous random field whose spectral representation reveals an assortment of propagating waves. A kinematic decomposition that separates the waves in longitudinal and transversal displacements was made. These motions are associated to Rayleigh and Love waves, respectively. The analysis on different time windows of the MCAN signals to identify back-propagating waves locally generated as a result of their interactions with shallow geological features was applied. For each component, we estimate the f-$\mathbf{k}$ spectral power density, which provide the amplitudes, velocities and directions of propagation of the most significant waves. These values, as functions of frequency, constitute the kinematic spectra of the wave field. Results obtained using this method allow to establish coherent scenarios of the wave field in Mexico City Valley that imply pointing out locally generated surface waves.

Key words: Frequency-wavenumber (f-$\mathbf{k}$), wave propagation, surface waves, kinematic spectra.

Introduction

Analysis of seismic data from an array of sensors has been very useful to study wave propagation, particularly, to discriminate between natural earthquakes and underground nuclear explosions. With this purpose, in the 1960s and 1970s, the use of large aperture seismic arrays, generally designed for optimal detection of regional and teleseismic events, was widely spread. An example was, the LASA (Large Aperture Seismic Array) located in Montana (USA), an array of 525 short-period seismometers covering a radius of 100 km by groups of 25 sensors concentrically arranged. In each group, the sensors were equally distributed in an area of 3.5 km radius (Green *et al.*, 1965). Another large aperture arrangement was NORSAR, located north of Norway. With a similar configuration, NORSAR consisted of 132 short-period seismometers and covered a radius of 50 km. The sensors of these two arrangements recorded only the vertical component of the movement. Over the years, the use of arrays of seismic sensors of a single component has been very helpful in the first arrival detection and in the identification of apparent velocities and directions of the fields of incident waves. Ringdal and Husebye (1982) made a detailed review of these experiences. Since the first experiences, diverse theories have been proposed aimed to characterize the motion in terms of power density estimators in the f-$\mathbf{k}$ domain.

In general, it has been assumed that the motion, recorded by an array, is a stationary random process with zero mean and standard deviation σ. When the motion is coherent, the variance of the process is a good approximation estimator of the power spectral density (Yaglom, 1962). However, the resolution of this conventional approximation estimator is rapidly lost when the coherence of records decreases. As a result, high resolution approximations estimators have received more attention. One of them is the maximum likelihood filter (Capon *et al.*, 1967; Capon, 1969; Kværna and Doornbos, 1986), especially recommended for irregularly distributed arrays.

In the analysis of tele seismic data, it is common to classify the wave field's components in terms of their apparent velocities (Aki and Richards, 1980). In many cases, the particle motion analysis, as the one proposed by Jurkevics (1988), can be used as a complement in the recognition of wave's type. Mykkeltveit *et al.* (1983) note that this procedure allows to distinguish prominent phases in seismograms. The f-$\mathbf{k}$ analysis applied to seismic data is also known as Multichannel Analysis of Surface Waves method (MASW; see Park *et al.*, 2007).

The accelerograms of the Michoacán Earthquake of September 19, 1985 (Ms 8.1) recorded by some stations within the Mexico City Valley showed, among many other aspects, the coherence between records (Campillo *et al.* 1989) and allowed to identify the presence of conspicuous waves of long and short period. This fact served to calibrate a regional crustal model. After this earthquake, the MCAN was deployed. The ensuing strong-motion recorded in Mexico City, clearly show large amplifications beyond the level predicted using simple one-dimensional (1D) shear models (Sánchez-Sesma *et al.*, 1988; Kawase and Aki, 1989). This strongly suggests significant lateral effects of three-dimensional (3D) nature. The spatial variability and polarization of observed ground motion have been interpreted as 3D effects (Pérez-Rocha *et al.* 1991; Sánchez-Sesma *et al.*, 1993).

Currently, the MCAN has over 70 three-axial surface accelerometers irregularly distributed in the city; the area covered is of approximately 600 km^2. More than 170 intense and moderate events, mainly from the coast, have been recorded by this network.

In this work, seismic records of motion caused by a well recorded earthquake in Mexico City Valley (March 20, 2012), were analysed. The results reveal the propagation of wave components across the Valley in both longitudinal and transversal motions. The characteristics of these components allow identifying the interaction of incoming waves with the geological structure of the Mexico City Valley.

In order to estimate the power spectra of the kinematic wave components in the f-$\mathbf{k}$ domain, a wave decomposition was performed, implementing a maximum likelihood filter, based on the Helmholtz theorem and the Capon method (1969). A spectral representation that displays amplitudes, directions and propagation velocities of waves with longitudinal and transversal polarization allows interpreting the behaviour of waves trapped in a sedimentary environment.

Power spectral density of the kinematic components of a wavefield

Fourier analysis in time domain is an usual tool in seismology and it is the keystone of many developments in mathematical-physics. Its extension to space-time configurations in

which one or various coordinates are dealt with analytically, shows the great resolving power of Fourier analysis. This is the case when it is used in regular arrays. In many instances it comes out that arrays in which data is avilable, are not regular and even an approximate description is desirable.

An analysis of the kinematic components of a vector wavefield is presented, starting from the continuous description of a vector field in the space-time frame and using the results within the frame of approximate spectral estimation based on the maximum likelihood theory of Capon (1969).

Power spectral density

The displacement field $u(\mathbf{x};\ \omega)$ due to the propagation of a harmonic plane wave is given by:

$$u(\mathbf{x};\ \omega)= u_0 e^{-i\mathbf{a}\cdot\mathbf{x}} e^{i\omega t}=u_0 e^{-ia_x x} e^{-ia_y y} e^{i\omega t}, \quad (1)$$

where $u_0=u_0(\omega)$ is the spectrum of the signal with information of its waveform. Here $\mathbf{a} = (a_x,\ a_y)^T = (\omega\ /\ c)\mathbf{n}$ is the wavenumber vector with components, $a_x = \omega n_x\ /\ c$ and $a_y = \omega n_y\ /\ c$; ω is the angular frequency, and c the wave propagation velocity. The wave direction is given by the vector $\mathbf{n} = (n_x,\ n_y)^T$. Finally, $\mathbf{x} = (x,\ y)^T$ is the position vector.

After the spatial Fourier transform, the field in wavenumber domain is:

$$u(\mathbf{k};\ \omega)=\iint u(\mathbf{x};\ \omega) e^{ik_x x} e^{ik_y y} dxdy, \quad (2)$$

$$u(\mathbf{k};\ \omega)= u_0 \delta\,(k_x - a_x)\ \delta\,(k_y - a_y), \quad (3)$$

where $\delta\,(\cdot)$ is the Dirac's Delta function:

$$\delta(k-a)= \begin{cases} 1\ if\ k = a \\ 0\ if\ k \neq a \end{cases} \quad (4)$$

Therefore, the spectrum in the wavenumber domain given by eq. (2) is theoretically zero for the coordinates indicated by the vector $\mathbf{k} = (k_x,\ k_y)^T$ that differs from $\mathbf{a} = (a_x,\ a_y)^T$. This represents a prominent peak in the spectrum and leads to determine the direction and velocity of propagation of a plane wave.

The velocity c and the azimuthal direction of propagation θ are obtained with the following equations:

$$c = \frac{\omega}{\sqrt{a_x{}^2 + a_y{}^2}}, \quad (5)$$

$$\theta = \arctan\,(a_x / a_y). \quad (6)$$

It is clear that the azimuth is measured with respect to North-South (NS) direction. Capon (1969) designed a high resolution filter to estimate the f-$\mathbf{k}$ power spectral density $|u(\mathbf{k};\ \omega)|^2$ when the field is only known in M sensors distributed in the x-y space. This estimation allows the undistorted passage of any monochromatic plane wave that propagates with wavenumber vector $\mathbf{a}$:

$$|u(\mathbf{k};\ \omega)|^2= \left[\sum_{j=1}^{M} \sum_{l=1}^{M} g_{jl}(\omega) \mathrm{e}^{i\mathbf{k}\cdot(x_j - x_l)} \right]^{-1}, \quad (7)$$

where $g_{jl}(\omega)$ is the jl element of the matrix $G=F^{-1}$ and F is the spectral correlation matrix; each element jl of F is given by $f_{jl}(\omega)=u_j(\mathbf{x};\ \omega)\ u_l{}^*(\mathbf{x};\ \omega)$ (here * denotes complex conjugate).

Kinematic decomposition

Assume that P waves (with longitudinal polarization of particle motion) and S waves (with transversal polarization of particle motion) propagate in a medium. According to the kinematic decomposition of Helmholtz, if Φ and $\mathbf{\Psi}$ are the displacement potentials for P and S waves, respectively, with $\nabla\cdot\mathbf{\Psi} = 0$, then the total displacements field is written as:

$$\mathbf{u}=\nabla\Phi + \nabla\times\mathbf{\Psi}. \quad (8)$$

By definition $\mathbf{u}^P=\nabla\Phi$ and $\mathbf{u}^S=\nabla\times\mathbf{\Psi}$. Then, it can be written

$$\mathbf{u} = \mathbf{u}^P + \mathbf{u}^S. \quad (9)$$

The total horizontal displacements in the plane $x - y$, admit the next representation:

$$\begin{aligned} u_x &= \frac{\partial\Phi}{\partial \mathrm{x}} + \frac{\partial\mathbf{\Psi}}{\partial \mathrm{y}} \\ u_y &= \frac{\partial\Phi}{\partial \mathrm{y}} - \frac{\partial\mathbf{\Psi}}{\partial \mathrm{x}} \end{aligned} \quad (10)$$

since $\mathbf{\Psi} = (0,\ 0,\ \Psi)$. If the potentials Φ and Ψ are harmonic and represented by:

$$\Phi = \Phi_0 e^{i\omega t - ik_x x - ik_y y}, \quad (11)$$

$$\Psi = \Psi_0 e^{i\omega t - ik_x x - ik_y y}, \quad (12)$$

Then, the components of the displacements field in the x and y directions acquire the forms:

$$u_x = -i(\Phi k_x + \Psi k_y), \quad (13)$$

$$u_y = -i(\Phi k_y - \Psi k_x), \qquad (14)$$

If $\mathbf{l}=(k_y, -k_x)^T$, the total field $u(\mathbf{k}; \omega)$ can be written as:

$$u(\mathbf{k}; \omega) = -i[\Phi(\mathbf{k}; \omega)\mathbf{k} + \Psi(\mathbf{k}; \omega)\mathbf{l}], \qquad (15)$$

where $\mathbf{k} \cdot \mathbf{l} = 0$.

In this result, the propagation vectors associated with P and S waves are recognized parallel and perpendicular to the vector $\mathbf{k}$, respectively. Moreover, the displacement field produced by P waves is the component of the total field in the direction of the vector $\mathbf{k}$, whereas the field produced by S waves is the component of the total field in the direction of the vector $\mathbf{l}$:

$$\mathbf{u}^P(\mathbf{k}; \omega) = [\mathbf{u}(\mathbf{k}; \omega) \cdot \mathbf{n}]\mathbf{n}, \qquad (16)$$

$$\mathbf{u}^S(\mathbf{k}; \omega) = [\mathbf{u}(\mathbf{k}; \omega) \cdot \mathbf{m}]\mathbf{m}, \qquad (17)$$

The unit vectors $\mathbf{n}$ and $\mathbf{m}$ indicate the directions of propagation of the wavenumbers $\mathbf{k}$ and $\mathbf{l}$, respectively, and are given by,

$$\mathbf{n} = \begin{bmatrix} n_x \\ n_y \end{bmatrix} = \begin{bmatrix} k_x/|\mathbf{k}| \\ k_y/|\mathbf{k}| \end{bmatrix} \qquad (18)$$

$$\mathbf{m} = \begin{bmatrix} m_x \\ m_y \end{bmatrix} = \begin{bmatrix} k_y/|\mathbf{k}| \\ -k_x/|\mathbf{k}| \end{bmatrix} \qquad (19)$$

where $|\mathbf{k}| = \sqrt{k_x^2 + k_y^2}$. This kinematic decomposition is developed for the plane x - y, therefore the longitudinal component of Rayleigh waves is analogous to P waves in the above development. In the same way, the transversal component of Love waves is regarded as S waves.

Numerical example on a 2D space

The kinematic decomposition is validated in a 2D setting by simulating the propagation of two plane waves. Thus, two plane P and SV waves are considered with propagation velocities of 2.6 and 1.5 km/s, respectively. The respective azimuths are 60 and -20 degrees. Both waveforms are Ricker wavelets with characteristic frequency of 1 Hz.

The array used in this example is shown in Figure 1. It is composed by a random distribution of 30 stations in a square of 4 km x 4 km. The purpose of applying the f-$\mathbf{k}$ spectral analysis in a random array with few stations is to check the strength of the kinematic decomposition formulation to describe the total field in longitudinal and transversal components.

Figure 2 displays the k_x - k_y diagrams of the longitudinal and transversal displacements, associated with the frequency of 1 Hz. The component distinctions emerge from the application of the separation vector described in eqs. (16) and (17).

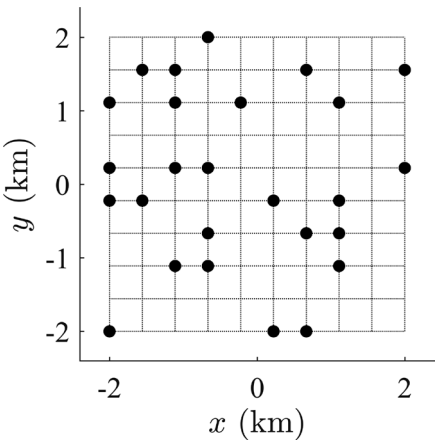

Figure 1. Spatial array of 30 stations randomly distributed in a square of 4 km x 4 km.

In each diagram, energy concentrations can be observed, associated with the incidence or emission of coherent waves observed in a large number of station arrays detected by this analysis. Using the wavenumbers (k_x, k_y) in which each peak is located, the wave propagation speed c, and direction, θ, can be determined by applying eqs. (5) and (6). The direction corresponds to the azimuth, which is measured from NS direction or in this particular case from axis. Therefore, $k_x = (c/\omega)\sin\theta$ and $k_y = (c/\omega)\cos\theta$

Figure 2 clearly depicts a longitudinal wave located in k_x / ω = 0.32 km^{-1} and k_y / ω = 0.2 km^{-1}, which represent a wave traveling with c = 2.63 km/s and θ = 58 degrees. A transversal wave is also observed in k_x / ω = -0.22 km^{-1} and k_y / ω = 0.62 km^{-1}, which corresponds to a wave with c = 1.53 km/s and θ = -19 degrees. The description of these two waves from f-$\mathbf{k}$ analysis exactly matches the initial parameters of the incident waves.

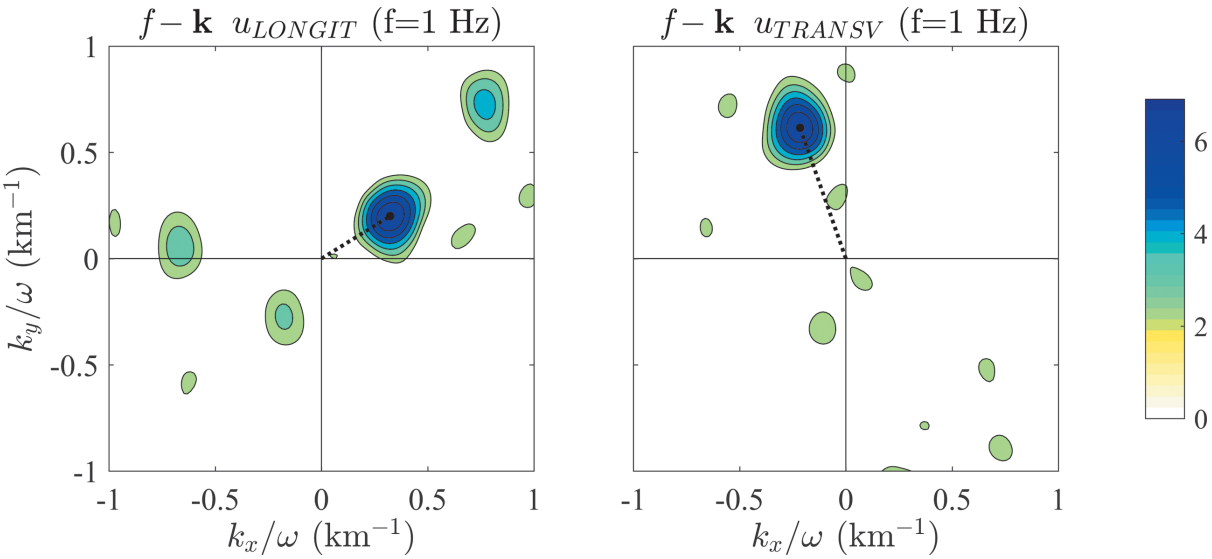

Figure 2. $k_x - k_y$ diagrams of components longitudinal (u_{LONGIT}) and transversal (u_{TRANSV}) components, at left and right, respectively, associated to the frequency of 1 Hz for two P and SV plane waves propagating in a 2D space and crossing the array depicted in Figure 1. The black doted lines indicate the vector of the principal peak for each diagram.

Numerical example on a 3D alluvial valley

In order to calibrate this kinematic decomposition, the surface field of an elastic 3D alluvial valley on an elastic half-space under the incidence of plane waves (P, SV, SH and Rayleigh) is separated in terms of longitudinal and transversal spectral motion. The reference results were computed with IBEM for the model presented by Sánchez-Sesma and Luzón (1995) for the scattering and diffraction of elastic waves by soft elastic inclusion models of alluvial deposits in an elastic half-space.

This is a closed irregular *croissant*-type alluvial valley (V) over a half-space (HS), depicted in Figure 3. The valley is 0.25 km depth, and is 2 km of longitude in its longest side. The free surface of both the valley and the half-space are assumed flat. The shear wave speeds are β_V = 1 km/s and β_{HS} = 2 km/s; the Poisson ratios are υ_V = 0.35, υ_{HS} = 0.25, and the mass densities satisfy $\rho_V = 0.8\rho_{HS}$. A quality factor of 100 was assumed for both P and S waves inside the valley. The half-space has no internal attenuation.

The array has 20 x 20 stations equally spaced (Δx = 0.0526 km) within a square. It is located inside the *croissant* valley on free surface as depicted in Figure 3 (b). Note that the right side of the array cross the valley's edge. The side's length of this square array is L = 1 km.

Both dimensional parameters: L in the studied direction, and Δx, control the confidence limits of the wavenumbers in the f-$\mathbf{k}$ analysis. In an arbitrary array, the minimum wavenumber that should be analysed is: $k_{min} = \Delta k/2\pi = 1/L$, and the maximum wavenumber, or Nyquist (Nq) wavenumber, that should be studied is $k_{max} = k_{Nq}/2\pi = 1/2\Delta x$. In this particular case, these two dimensional parameters are: k_{min} = 1 cycles/km, and k_{max} = 9.5 cycles/km.

We consider the incidence of a SV wave with θ = -10 degrees, and a Rayleigh wave with θ = 90 degrees, both of them with propagation velocity of 0.5 km/s. For the incoming waves Ricker wavelets with characteristic period equal to 0.33 Hz, was assumed. Synthetic seismograms are depicted in Figure 4.

The f-$\mathbf{k}$ analysis in four time windows of 10 s with an overlap of 2 s: 0 – 10 s, 8 – 18 s, 16 – 26 s, and 24 – 34 s (see Figure 4) was applied, in order to follow waves both incident or emitted by the edges of the valley, and identify their type, velocities and directions of propagation.

The windows' length depends on the desired level of detail in the analysis. Generally, the records' total duration can be used, but waves with large amplitudes overwhelm coherent waves with low amplitudes in the coda and thus prevent their detection. The window's resolution depends on the signal frequency, the likely apparent velocity and the array's spatial

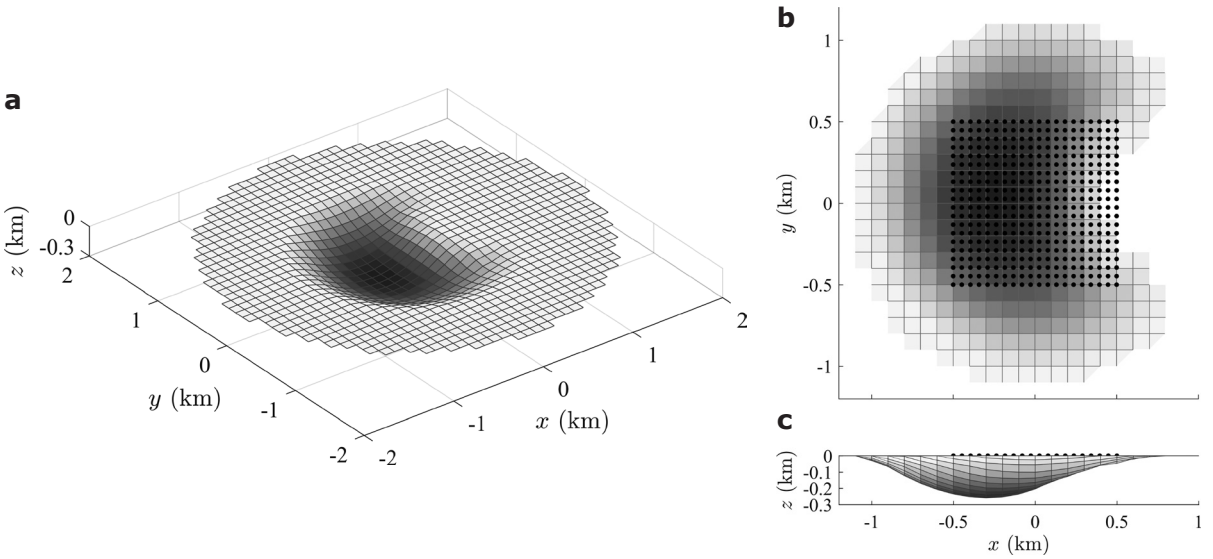

Figure 3. Synthetic model of a *croissant*-type alluvial valley. (a) Depict the 3D topography of the interface; (b) *croissant* plan view, where the location of the array is indicated with black dots, which is composed of a distribution of 20x20 equally spaced stations, and (c) valley's lateral view.

dimension. It is recommended that the time window contains at least three wavelengths to allow that the propagating waveform is contained in the selected window, so that their spectrum amplitude and phase are well retrieved.

For each time window we construct kinematic spectra of the amplitudes, velocities and directions of propagation for the longitudinal, transversal and vertical displacements of the wave field. These spectra are constructed from the wavenumbers (k_x, k_y) of the peaks detected in the k_x - k_y diagrams for each frequency using eqs. (5) and (6) to compute c and θ, respectively.

The vertical component is used jointly with the longitudinal one to corroborate the possible presence of Rayleigh waves. The propagation velocities and directions of these waves must be equal in both the longitudinal and vertical components, and in the amplitudes, vertical component must be slightly larger, at least for a prevailing fundamental mode.

At the kinematic spectra for the time window 0 – 10 s depicted in Figure 5 (a), using both the longitudinal and vertical components, a prominent Rayleigh wave i can be seen s observed, with frequency between 0.3 and 0.4 Hz, c = 0.4 km/s approximately and θ = 90 degrees. From the transversal component, a S

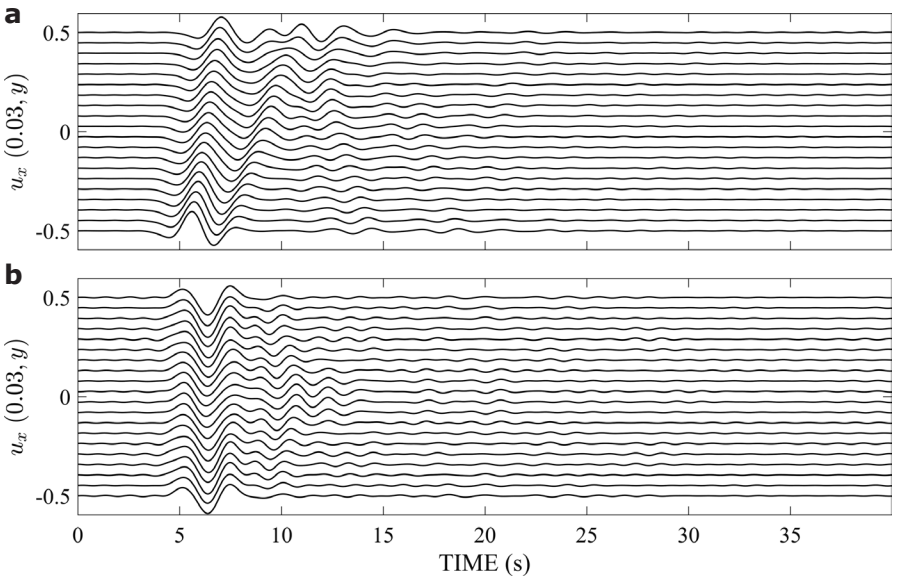

Figure 4. Displacements at stations located at x = 0.03 km of the synthetic model shown in Figure 3 subjected to the incidence of two plane waves: (a) a SV with θ = -10 degrees, and (b) a Rayleigh wave with θ = 90 degrees.

wave of f = 0.35 Hz, c = 0.5 km/s and θ = -20 degrees can be seen. In the same time span, another S wave with f = 0.3 Hz, c = 0.5 km/s and θ = 135 degrees, almost opposite to the previous one, can also be seen .

Figure 5 (b) correspond to time window between 8 and 18 s. It reveals a principal S wave f = 0.35 Hz, c = 0.4 km/s, and θ = -10 degrees. No prominent waves in the longitudinal component can be seen in this time window.

The results depicted in Figure 5 (c) and (d) correspond to time windows 16 – 26 s and 24 – 34 s, respectively, and reveal very interesting patterns of interference of the refracted waves inside the basin and, in some cases, significant emission of waves is observed.

From Figure 5 (c), that covers time window 16 – 26 s, we can see the propagation of initial waves with f = 0.5 Hz in the three components. In the longitudinal component it travels with c = 0.3 km/s, and θ = 45 degrees. In the transversal component, it revels three S waves with c = 0.3 km/s, in a range of directions of approximately 5, 65 and 130 degrees.

From Figure 5 (d), corresponding to time window 24 – 34 s, we can see in the longitudinal component: the propagation of a wave with a range of frequencies between 0.7 and 0.77 Hz, with c = 0.3 km/s, and θ = -145 degrees, i.e., it is traveling backward. With the same frequencies and velocity but with smaller amplitudes there are two waves propagating with θ = 17 and 57 degrees, almost opposite to the first one.

There is also a wave with f = 0.4 Hz, with c = 0.35 km/s, and θ = 40 degrees. In the transversal component, the propagation of three waves is spotted for an interval of frequencies between 0.7 and 0.77 Hz, with velocities in the interval of 0.27 and 0.32 km/s, and directions of -30, 11 and 125 degrees. Moreover, one can infer the propagation of a transversal cylindrical wave with f = 0.5 Hz, velocity around 0.3 km/s, coming from N135E, i.e., traveling backward.

We attribute the changes in the propagation directions and the presence of several peaks in the power spectra as an evidence of the scattering and diffraction of the incident wave field by the basin's edge.

Figure 6 shows the k_x - k_y diagrams associated to only one frequency for each of the four time windows analyzed. The various panels presented give support to the kinematic spectra depicted in Figure 5.

Analysis of seismic data recorded by MCAN

The important site effects that occur at Mexico City subsoil due to earthquakes, especially the long duration and the increased amplitudes on seismograms recorded in free surface inside de City, lead to the search of ways to improve the understanding on the mechanisms that control these phenomena.

In this study, we apply a time-space spectral analysis to obtain in the f-$\mathbf{k}$ domain, spectral power densities of the strong ground motion recorded by the MCAN. This method will allow us to figure out the behaviour of the incident and emitted wave fields within the Valley.

Figure 7 shows the distribution of the MCAN as well as the Geotechnical Zonation location. Two parameters control the confidence limits of the wavenumbers in the f-$\mathbf{k}$ analysis. They are: the array length in the studied direction, L = 30 km for both sides, and the average separation between stations, Δx = 3.33 km which comes from the maximum instrument density located in the central area of the network. Therefore, taking into account these two values, the minimum wavenumber that should be analysed is $k_{min} = \Delta k/2\pi$ = 0.033 cycles/km, and he maximum wavenumber, or Nyquist (Nq) wavenumber, that should be studied is k_{max} = 0.15 cycles/km.

Previous studies (Campillo *et al*., 1989, and Sánchez-Sesma *et al*., 1993) identified, in the vertical component of the displacements recorded inside Mexico City Valley, crustal surface waves coming from the Mexican subduction zone. Campillo *et al*. (1989) identified two prominent surface waves with characteristic periods of 0.1 Hz and 0.33 Hz in the records produced by the September 19, 1985, Michoacán earthquake (Mw 8.1) and proposed a cortical model that allowed them to postulate that the long-period waveform of 0.1 Hz corresponds to the fundamental mode of Rayleigh surface wave, and is preceded by a short-period waveform of 0.33 Hz which is associated with the propagation of higher modes of Lg surface waves. Sanchez-Sesma *et al*. (1993) detected also these two particular waves in the MCAN's records of the April 25, 1989, earthquake (Mw 6.9) by applying the f-$\mathbf{k}$ analysis.

In this study, a more recent event (with characteristics similar to the ones mentioned

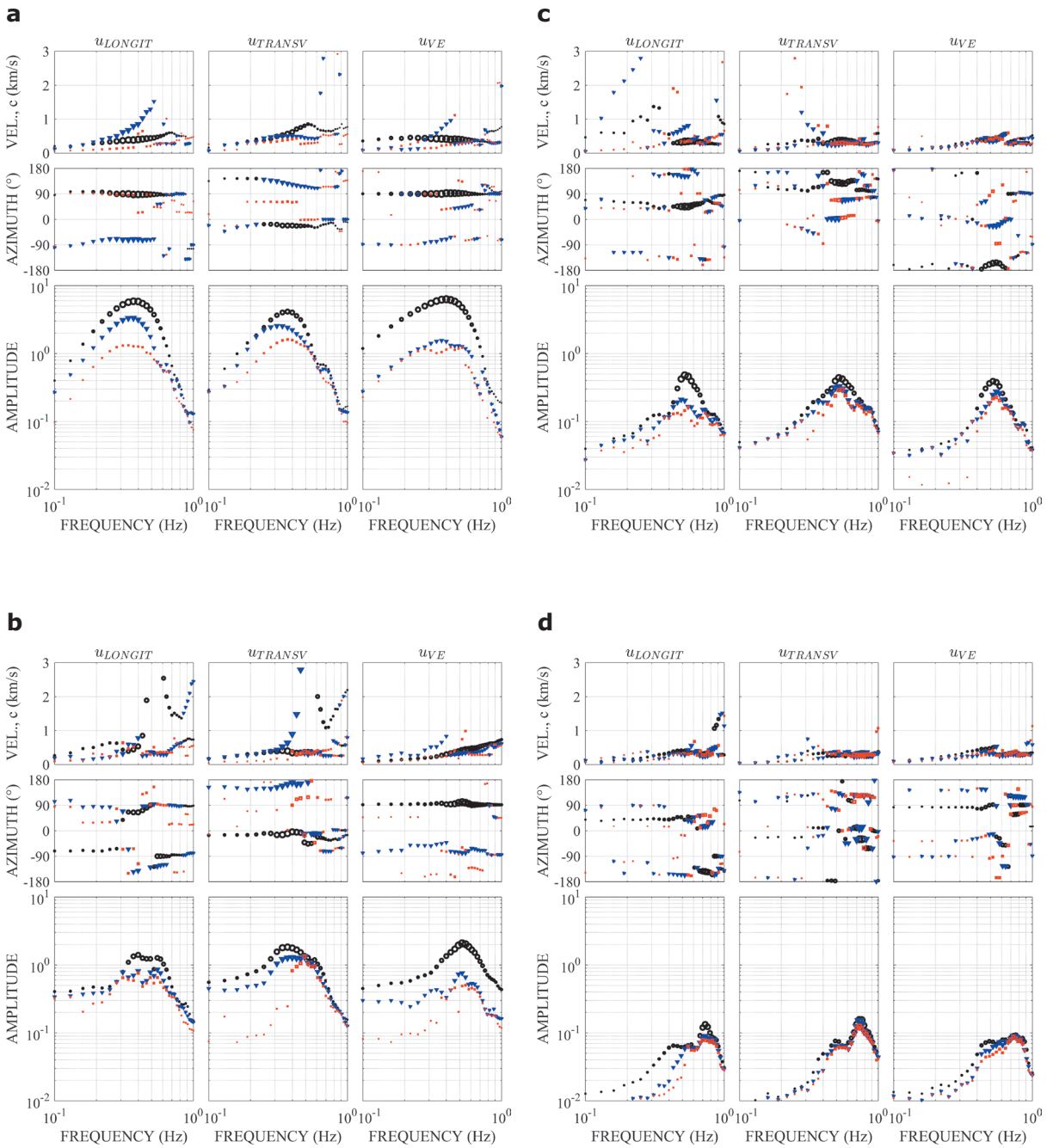

Figure 5. Kinematic spectra of longitudinal (u_{LONGIT}), transversal (u_{TRANSV}), and vertical (u_{VE}) displacements of the 3D synthetic model depicted in Figure 3, corresponding to the time windows (a) 0 – 10 s, (b) 8 – 18 s, (c) 16 – 26 s, and (d) 24 – 34 s. The propagations velocities are at the top, the azimuths are at the middle and the amplitudes are at the bottom. The markers' types indicate the relevance of the peaks detected in the $k_x - k_y$ diagrams; thus, higher amplitudes are indicated with black circles, followed by blue triangles and then by red squares. The markers' sizes depend on the amplitude of each frequency normalized with respect to the maximum amplitude for all frequencies.

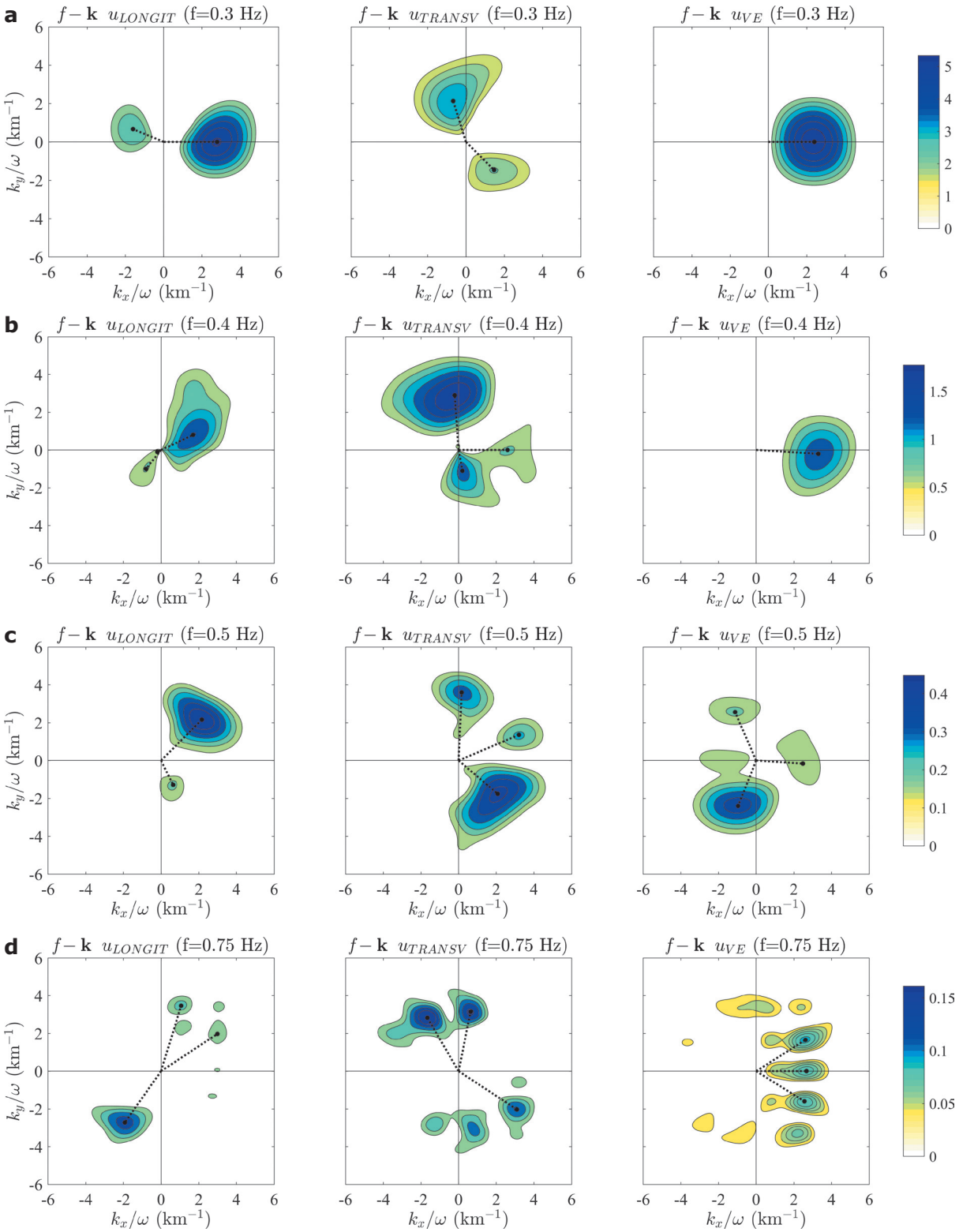

Figure 6. Diagrams in the $k_x - k_y$ space for the four studied time windows (a-d). Each one is associated to the spectra shown in Figure 3. The diagrams correspond to a single frequency. For each case, the window limits and the associated frequency are: (a) 0 – 10 s for f = 0.35 Hz, (b) 8 – 18 s for f = 0.35 Hz, (c) 16 – 26 s for f = 0.5 Hz and (d) 24 – 34 s for f = 0.75 Hz. In each row, longitudinal (u_{LONGIT}), transversal (u_{TRANSV}) and vertical (u_{VE}) displacement amplitudes are at the left, center, and right, respectively. The black doted lines indicate the vector of the principal peaks for each diagram.

above) was selected to be analysed, i.e., large magnitude with its epicenter in the Mexican subduction zone, and with important site effects when arriving to Mexico City Valley. The event is the March 20, 2012, earthquake (Mw 7.4) recorded at 60 MCAN stations.

The displacements in six MCAN arbitrary sites due to this event after the double integration of the accelerograms, appear in Figure 8. In the vertical displacement of the set of records, it is also possible to observe two conspicuous incidences: Rayleigh (f = 0.1 Hz) and Lg (f = 0.33 Hz) surface waves between 80 and 130 s.

A successive f-$\mathbf{k}$ analysis of time windows can determine the wave field behaviour of the records at late times, which are very likely the result of multi-pathing inside the Valley, i.e., the product of waves interaction with the edges of the basin. This interpretation should be subjected to closer scrutiny considering more realistic cortical models and the correlation with surficial geological structures.

In this sense, the displacement spectral densities and the kinematic decomposition in longitudinal and transversal components, for four time windows: (a) 80 – 130 s, (b) 120 – 170 s, (c) 160 – 210 s, and (d) 200 – 250 s were estimated. The last three time windows correspond to the early coda of the earthquakes.

Figure 9 displays the kinematic velocity spectra, direction of propagation and Fourier amplitudes for the four time windows in the frequency band between 0.06 and 0.6 Hz. These spectra were constructed with the three maximum peaks of the diagrams for each frequency. This representation allows identifying the spectral characteristics of the k_x - k_y wave field components.

Figure 9 (a) shows three representative peaks in all components at frequencies equal to 0.11, 0.15 and 0.33 Hz. The first peak with relevant amplitudes can be observed in an interval of frequencies between 0.1 and 0.13 Hz which propagates in direction around -10.3 degrees, with velocity equal to 2.9 km/s. This peak appears in the longitudinal and vertical direction, which strongly suggests that it is the fundamental mode of Rayleigh waves. Another representative peak occurs at 0.33 Hz in the transversal component, which propagates at -13 degrees with a velocity of 3.6 km/s. We associate this wave with Lg surface waves. The direction of propagation of these two waves is very close to the epicentral direction N10W. This fact suggests that they are incident waves coming from the source. The inferred type of wave and velocities matches with the ones identified by Campillo *et al*. (1989). The speed and direction of propagation of these two wave episodes are directly seen on seismograms. Therefore, we consider it as a validation of the method that can track

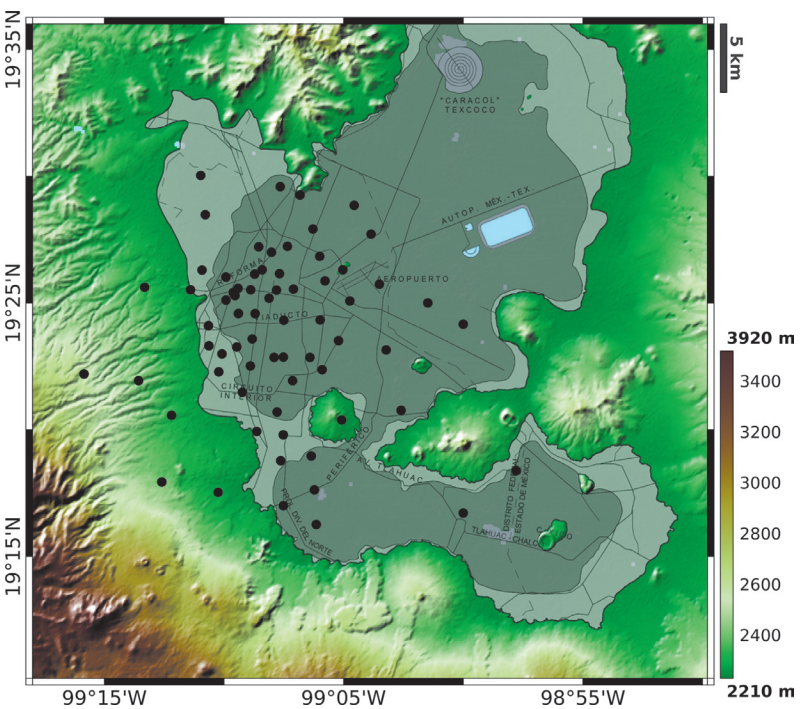

Figure 7. Elevation map of Mexico City Valley and Geotechnical Zonation. The black line inside the basin delineates the edges of the lacustrine deposits. Within these edges the Lake Zone is shaded in solid dark grey, and the Transition Zone is represented by solid light grey. Outside these edges, the Hill Zone begins in green (above 2,300 m.a.s.l.). The black dots indicate the locations of Mexico City Accelerometric Network (MCAN).

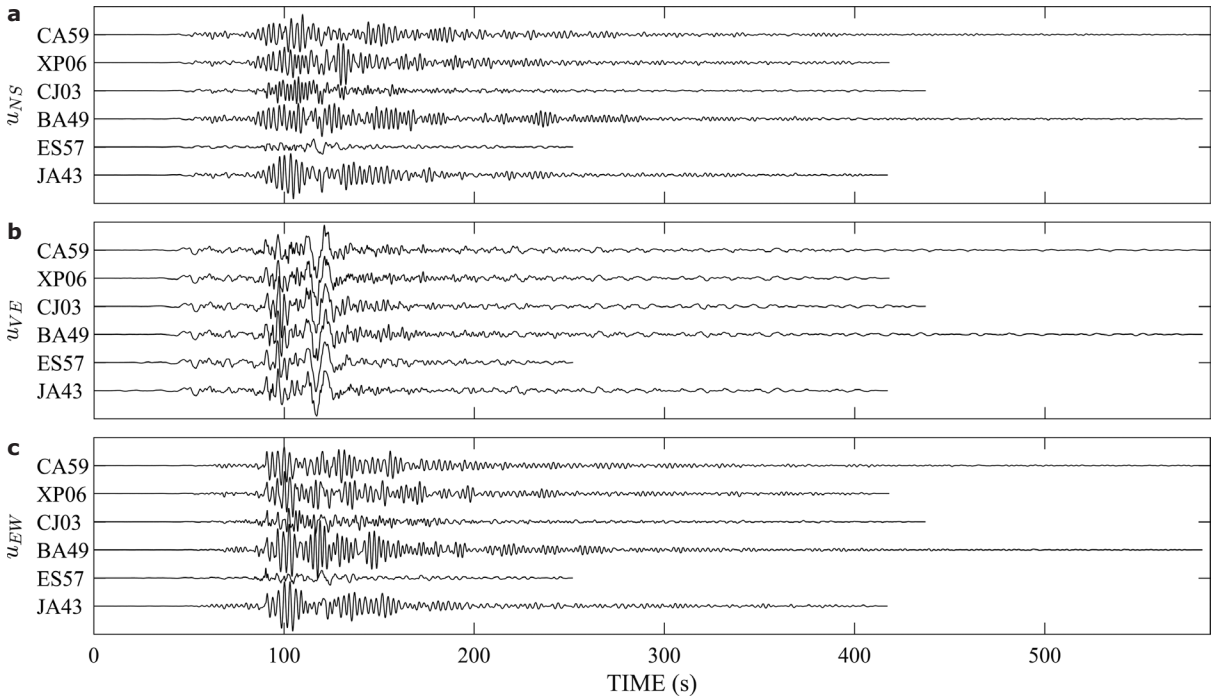

Figure 8. Displacements of the March 20, 2012, earthquake after the double integration of the accelerograms observed in six MCAN arbitrary stations. (a) North-South component (u_{NS}), (b) Vertical component (u_{VE}), and (c) East-West component (u_{EW}). The stations' names are indicated on the left of each trace. The u_VE traces are scaled by a factor of 5.

waves crossing the Valley and are not clearly detected on seismograms. Another identified waves episode in the transversal component corresponds to the f = 0.15 Hz, with c = 2.8 km/s, and θ = -18 degrees.

Figure 9 (b), (c) and (d) which correspond to the early coda of the seismograms show the kinematic spectra of the longitudinal, transversal, and vertical components. It can be seen, in the interval of frequencies between 0.2 to 0.5 Hz, comparable amplitudes in the three kinematic components with significant changes in directions and velocities of propagation. As in the synthetic model case of a *croissant*-type alluvial valley, we attribute this behavior of the wave field to an evidence of the diffraction of the incident field due to its interaction with the edges of the basin, and in this real case, also to the multipath that waves take from the epicenter to the Mexico Valley. Moreover, for these frequencies our results suggest that the field is composed by surface waves higher modes, Rg and Lg, in agreement with Campillo *et al.* (1989).

The phase velocities obtained from the analysis of the MCAN data, in the range of frequencies between 0.1 to 0.5 Hz are consistent with those obtained from the dispersion curves of the accepted theoretical crustal models for central Mexico (see Gaite *et al.* 2012). A discontinuity in the experimental results about f = 0.2 Hz, both in phase velocities and propagation directions, suggests a possible conversion of surface wave to higher Rg and Lg modes, probably generated on the south edge of the Transmexican Volcanic Belt. Apparently, the cortical paths from this geological structure towards the Valley of Mexico, is very efficient for the propagation of these mode shapes. This follows from the conspicuous amplitudes of the power spectrum of these forms of propagation and could be related with the regional amplification identified by Ordaz and Singh (1992).

The resolution of the power density estimators decreases rapidly for frequencies larger than about 0.5 Hz. This is a consequence of the decrease of the signal-to-noise ratio mainly because the minimum distance between MCAN sensors is around 3 km and wavelengths are less than 6 km, because waves propagate typically with horizontal velocities less than 3 km/s.

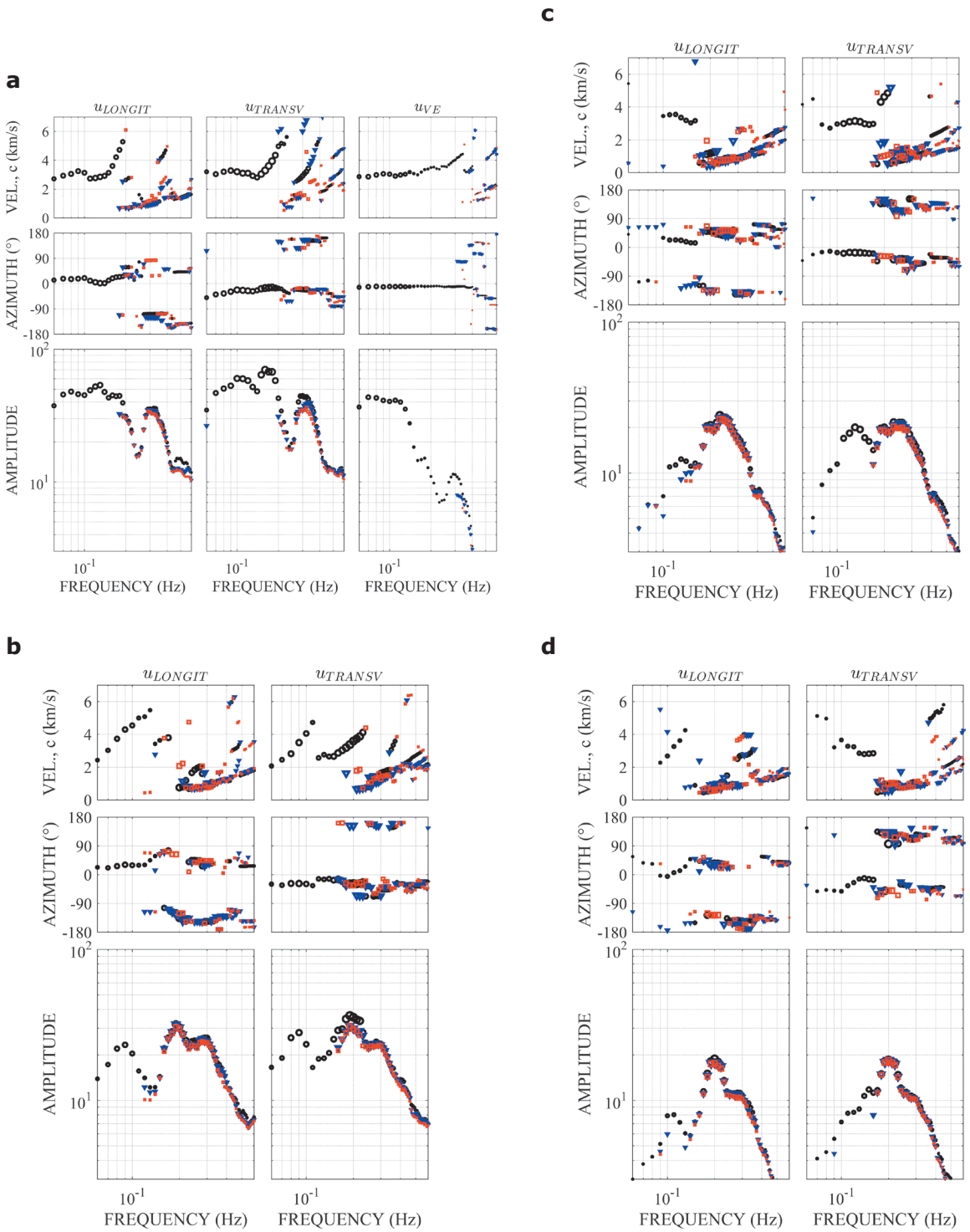

Figure 9. Kinematic spectra of longitudinal (u_{LONGIT}), transversal (u_{TRANSV}), and vertical (u_{VE}) displacements observed in the March 20, 2012, earthquake (see Figure 8), corresponding to the time windows (a) 80 – 130 s, (b) 120 – 170 s, (c) 160 – 210 s, and (d) 200 – 250 s. Because of the low amplitudes of the vertical components, the only one depicted is in case (a). The propagations velocities are at the top, the azimuths are at the middle and the amplitudes are at the bottom. The markers' types indicate the relevance of the peaks detected in the $k_x - k_y$ diagrams; thus, higher amplitudes are indicated with black circles, followed by blue triangles and then by red squares. The markers' sizes depend on the amplitude of each frequency normalized with respect to the maximum amplitude for all frequencies.

Conclusions

The importance of estimating the f-$\mathbf{k}$ power spectral densities within the analysis of wave propagation from data of an array of sensors has been discussed. Higher resolution filters based on Capon's (1969) maximum likelihood estimators, were applied. We have also proposed a kinematic decomposition of the wave field in longitudinal and transversal components, which permits to observe the directions, velocities, and polarizations of the surface displacement field.

For validation, the kinematical decomposition was implemented for two synthetic models, in 2D and 3D configurations, respectively. The results were successful because the parameters of the incident wave field like wave type, velocity and direction of propagation were well identified. The 3D model was a *croissant*-type alluvial valley, in which the influence of basin geometry was identified in surface motion.

For the March 20, 2012, earthquake recorded by the MCAN, the analysis and the kinematic decomposition in longitudinal and transversal components permitted to detect the propagation of waves in different time windows. In early times of seismograms, the incident wave field is recognized, while for late times, the analysis made possible to follow the variety of waves with frequencies between 0.2 and 0.5 Hz that are propagating across the Valley. They may be the result of the interactions of the incident wave field with the edges of the basin. The analysis of early times also reveals locally generated surface waves. They are somehow shadowed by incident waves, but their distinct azimuths may allow their detection. These facts may clarify the retrieved surface waves from correlations of strong ground motion for pairs of observers inside the Valley.

Acknowledgements

Thanks are given to A. Arciniega-Ceballos for her suggestions and detailed review of the manuscript, and to M. A. Contreras-Zazueta for computing the frequency response for the array within the *croissant*-type alluvial valley. The help of E. Plata and G. Sánchez and their team of Unidad de Servicios de Información (USI) of Instituto de Ingeniería UNAM was crucial to locate useful references. This work was partially supported by AXA Research Fund, and by Dirección General de Asuntos del Personal Académico (DGAPA) of UNAM, under Grant Number IN104712.

References

Aki K., Richards P.G., 1980, Quantitative Seismology: Theory and Methods. Ed. W.H. Freeman, San Francisco, 948 pp.

Campillo M., Gariel J.C., Aki K., Sánchez-Sesma F.J., 1989, Destructive strong ground motion in Mexico City: Source, path and site effects during the great 1985 Michoacán earthquake. *Bull. Seism. Soc. Am., 79, 1718-1735*.

Capon J., Greenfield R.J., Kolker R.J., 1967, Multidimensional maximum-likelihood processing of a large aperture seismic array. *Proc. IEEE, 55, 192-211*.

Capon J., 1969, High resolution frequency-wavenumber spectrum analysis. *Proc. IEEE, 57, 1408-1418*.

Gaite B., Iglesias A., Villaseñor A., Herraiz M., Pacheco J.F., 2012, Crustal structure of Mexico and surrounding regions from seismic ambient noise tomography. *Geophys. J. Int., 188, 1413-1424.*

Green P.E.Jr., Frosch R.A., Romney C.F., 1965, Principles of an experimental large aperture seismic array (LASA). *Proc. IEEE, 53, 1821-1833*.

Jurkevics A., 1988, Polarization analysis of three-component array data. *Bull. Seism. Soc. Am., 78, 1725-1743.*

Kawase H., Aki K., 1989, A study on the response of a soft basin for incident S, P, and Rayleigh waves with special reference to the long duration observed in Mexico City. *Bull. Seism. Soc. Am., 79, 1361-1382.*

Kværna T., Doornbos D.J., 1986, An integrated approach to slowness analysis with arrays and three-component stations, in NORSAR Sci., Rept., Semiannual Technical Summary, No. 2-85/86, Kjeller, Norway, 1 October 1985-31 March 1986.

Mykkeltveit S., Åstebøl K., Doornbos D., Husebye E., 1983, Seismic array configuration optimization. *Bull. Seism. Soc. Am., 73, 173-186.*

Ordaz M., Singh S.K., 1992, Source spectra and spectral attenuation of seismic waves from Mexican earthquakes and evidence of amplification in the hill zone of Mexico City. *Bull. Seism. Soc. Am., 82, 24-43.*

Park C.B., Miller R.D., Xia J., Ivanov J., 2007, Multichannel analysis of surface waves (MASW)-active and passive methods. *The Leading Edge, 1-6.*

Pérez-Rocha L.E., Sánchez-Sesma F.J., Reinoso E., 1991, Three-dimensional site effects in Mexico City: evidence from accelerometric network observations and theoretical results, in 4th International Conference on Seismic Zonation, Stanford, California, 26-29 August. *Earthquake Engineering Research Institute, 2, 327-334.*

Ringdal F., Husebye E.S., 1982, Application of arrays in the detection, location and identification of seismic events. *Bull. Seism. Soc. Am., 72, S201-S224*.

Sánchez-Sesma F.J., Chávez-Pérez S., Suarez M., Bravo M.A., Pérez-Rocha L.E., 1988, On the seismic response of the Valley of Mexico. *Earthquake Spectra, 4, 569-589*.

Sánchez-Sesma F.J., Pérez-Rocha L.E., Reinoso E., 1993, Ground motion in Mexico City during the April 25, 1989 Guerrero Earthquake. *Tectonophysics, 218, 127-140*.

Sánchez-Sesma F.J., Luzón F., 1995, Seismic response of three-dimensional alluvial valleys for incident P, S, and Rayleigh waves. *Bull. Seism. Soc. Am*., 85, 269-284.

Yaglom A.M., 1962, An introduction to the Theory of Stationary Random Functions. Englewood Cliffs, N. J. Prentice Hall.

Geofísica Internacional (2017) 56-1: 117-135

Original paper

High-Resolution Early Earthquake Damage Assessment System for Mexico City Based on a Single-Station

Mario Ordaz*, Eduardo Reinoso, Miguel A. Jaimes, Leonardo Alcántara and Citlali Pérez

Received: April 04, 2016; accepted: December 09, 2016; published on line: January 01, 2017
DOI: 10.19155/geofint.2017.056.1.9

Resumen

Se presenta un sistema de evaluación temprana de daños de alta resolución desarrollado para la Ciudad de México basado en cálculos en tiempo real de intensidades espectrales sísmicas en un sitio de referencia. Para obtener las intensidades en todo el Valle de México, se usan relaciones espectrales de respuesta pre-calculadas en sitios blandos. Se utilizan las estimaciones de las intensidades sísmicas (aceleración máxima del suelo, velocidad máxima del suelo y ordenadas espectrales para determinados periodos estructurales), junto con las relaciones de intensidad-daño de edificios, de víctimas y de la red de distribución de agua potable para obtener la distribución espacial del daño esperado en toda la ciudad. El proceso dura aproximadamente 10 minutos sin intervención humana. Dado que el tiempo disponible para realizar todos los cálculos es corto, se construyó una base de datos representativa de edificios y población que concentra toda la información en una malla cuadrada de 400 × 400 m. Los resultados se envían a un Centro de Emergencia y a los tomadores de decisiones para activar planes de emergencia previamente establecidos y proporcionar información antes de que los planes de emergencia estén en pleno funcionamiento.

Palabras clave: Sistema de evaluación temprana de daño sísmico, Ciudad de México, relaciones de intensidad-daño, peligro sísmico, riesgo sísmico

Abstract

A high-resolution early earthquake damage assessment system is presented for Mexico City based on real-time computations of seismic spectral intensities at a reference site. To obtain intensities for the entire Mexico Valley, pre-calculated response spectral ratios at soft sites are used. The estimates of seismic intensities (peak ground acceleration, peak ground velocity and spectral ordinates for selected structural periods), together with intensity-damage relations for buildings, fatalities and water supply network were used to obtain the spatial distribution of expected damage throughout the city. The process takes approximately 10 minutes with no human intervention. Since the available time to carry out all the computations is short, we have built a representative building and population database that concentrates all the information in a square mesh of 400 × 400 m. Results are sent to an Emergency Center and to decision makers to trigger previously set emergency plans and to provide information before emergency plans are in full operation.

Key words: Early earthquake damage assessment system, Mexico City, intensity-damage relations, seismic hazard, seismic risk.

M. Ordaz*
E. Reinoso
M. A. Jaimes
L. Alcántara
C. Pérez
Instituto de Ingeniería
Universidad Nacional Autónoma de México
Ciudad Universitaria
Delegación Coyoacán 04510
CDMX, México
*Corresponding author: MOrdazS@iingen.unam.mx

Introduction

On September 19, 1985, a magnitude 8.1 earthquake occurred near the Pacific coast of Mexico on the Michoacán Gap of the Mexican subduction zone. Severe damage occurred in Mexico City, at a distance of 300 km to the rupture area, caused mainly by the dynamic amplification of the lakebed deposits. The government did not know the full extent of the damage until many hours later because the communication systems were severely disrupted. A total of 7,400 buildings were affected, including 265 collapsed and 775 severely damaged (Meli, 1986). The number of deaths was estimated between 10,000 and 15,000 (Astiz *et al*., 1987). Mexico City's primary water system failed leaving almost 3.5 million people without water (Ayala and O'Rourke, 1989; O'Rourke and Ayala, 1993). The power supply was interrupted in vast areas. The damage caused by the earthquake was much larger than anyone could have expected, and the weakness and lack of proper management of the emergency by the government was revealed.

Technological advances in seismic instrumentation, digital communication and computer technologies enable the implementation of real-time early warning and rapid damage assessment systems. An earthquake early warning system can provide a rapid notification (time, location and magnitude) from a few to tens of seconds before the arrival of strong ground shaking. This information can help to minimize loss of lives and property (Kanamori *et al*., 1997). In some cases, managers or authorities in charge of strategic facilities may receive this information even before the ground shaking begins, allowing timely emergency shutdowns or other opportune protection measures for systems susceptible to damage, such as power stations, transport and computer centers and telephone systems (Erdik *et al*., 2003; Erdik, 2006). Erdik and Fahjan (2006) provide a review of early warning systems in countries such as Japan, Mexico, United States, Taiwan, Italy, Rumania, Turkey and Greece.

Systems for rapid damage assessment can provide real-time estimates of the distribution of ground shaking intensities, building damage and impacts on the population. This information is useful to activate previously set emergency management scenarios and to efficiently execute search and rescue activities. For instance, the EPEDAT system (Early Post-Earthquake Damage Assessment Tool) was developed to estimate building and lifeline damage in Southern California (Eguchi *et al*., 1994; 1997). In Japan, the Tokyo Gas Company developed the SIGNAL system (Seismic Information Gathering and Network Alert), to estimate damage of a natural gas network based on extensive earthquake monitoring and geographic information systems (Yamasaki *et al*., 1994). Currently, there are several systems capable of computing damage and casualties in several regions of the world. Erdik *et al*. (2010) summarizes the work done over the last decades regarding the development of recent approaches and the setting up of new applications for earthquake rapid response systems. What is common to most of these systems is that they require a large number of seismic stations deployed over the epicentral region for a quick detection of the earthquake, a reasonably accurate estimation of the potential damage and a continuous communication between the seismic stations and the central processing station.

In this work, the early earthquake damage assessment system developed for Mexico City, based on a single station, which has been working since 2005 is presented. This system estimates losses (fatalities and building and water supply network damage) immediately after an earthquake is recorded, without human intervention. The system records accelerations (two horizontal components) at the base station and computes their response spectra. Pre-calculated response spectral ratios are then used to compute response spectra at thousands of predefined sites throughout the city. Fatalities, as well as building and water supply network damages are estimated using intensity-fatality and intensity-damage relations derived for six classes of buildings representative of Mexico City's stock, and one relation for the water supply network. This information, along with the geographic distribution of the buildings, the population and the water supply network, allows the computation of expected losses after about two minutes. These estimates are finally sent to government officials, to a web page and to the Emergency Management Center, to provide the information for an opportune decision (http://aplicaciones.iingen.unam.mx/webSAPS/).

Description of early earthquake damage assessment system

Figure 1 presents a general scheme of the early earthquake damage assessment system in Mexico City, which involves mainly two processes: (Process A) pertaining to seismic data acquisition and processing; and (Process B) dealing with the storage, delivery and publication of the generated information.

Process A includes the following tasks:

1. Acquisition, detection and recording of real-time acceleration data;

2. Computation of peak ground acceleration, peak ground velocity and response spectra at the reference station;

3. Computation of peak ground acceleration, peak ground velocity and response spectra at other sites throughout the city;

4. Estimation of damage in buildings and the water supply network, as well as fatalities;

5. Transferring of the generated maps and tables to a server for Process B.

Tasks of Process B are related to the automatic publication of the generated information. A detailed description of Process B is out of the scope of this study, which focuses on the seismological aspect.

Real-time seismic data recording

The real-time seismic data acquisition is based at the reference station CU (Ciudad Universitaria), where strong ground motions of more than 30 events have been recorded since 1964. Since the early nineties, this station has also a broadband seismometer. It is located at a hill zone site over basaltic lava flows, and it has become the reference site to study the dynamic amplification at the lakebed zone of Mexico City (Singh *et al*., 1988a,b; Ordaz *et al*., 1989; Montalvo-Arrieta *et al*., 2002).

CU station operates a parallel redundant system of two accelerometers, each one connected by optic fiber cable to a separate computer, where seismic data are processed independently. The optic fiber cables pass through their own conduit but the pipeline is the same in certain sections. Therefore, if the pipelines were damaged by an earthquake, it could generate damage to the optic fiber cable and cut communication. In this study, we assumed that during a large earthquake (e.g., a similar or worse event than that of September 19, 1985) the CU station will no suffer severe

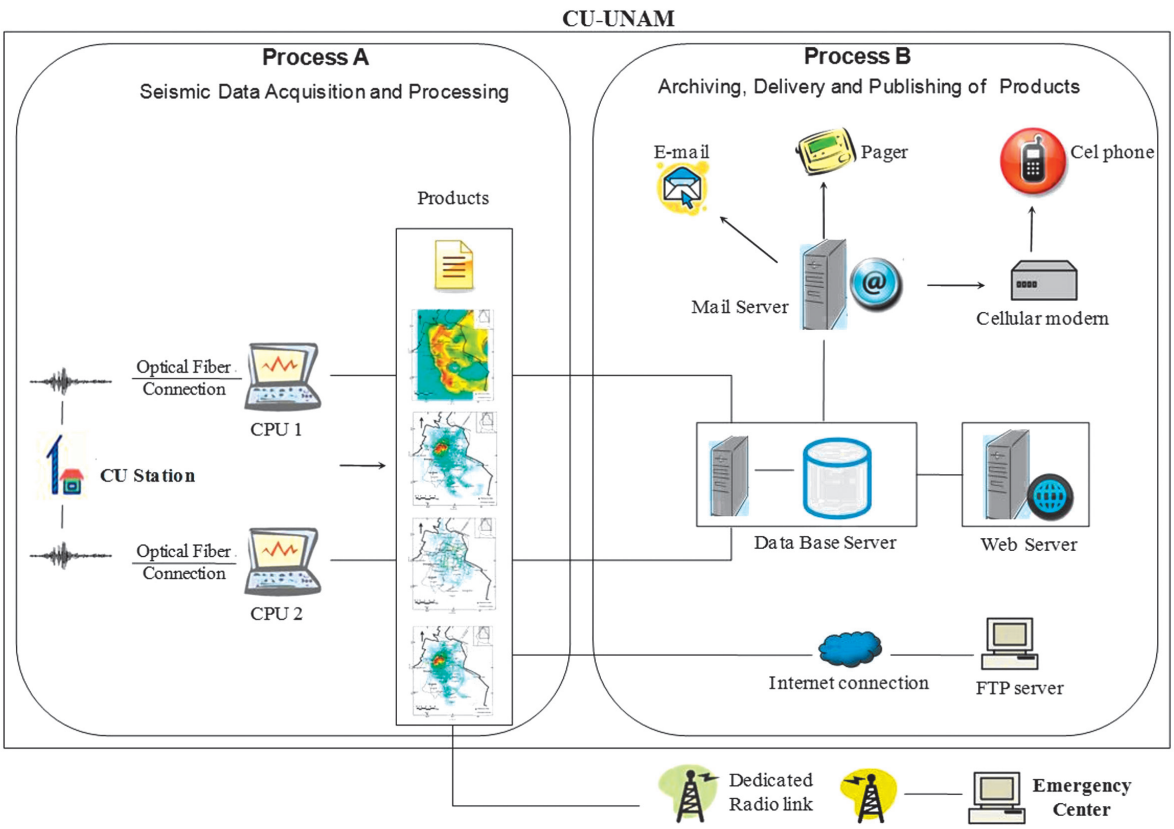

Figure 1. Scheme of the early earthquake damage assessment system in Mexico City.

damage. For instance, during the 1985 seismic event, no damage was reported at the CU station and surrounding structures (e.g., Meli, 1986; O'Rourke and Ayala, 1993), since it is not located at the lakebed zone, the shaking does not reach levels to damage the station and the conduit. Additionally, it is important to note that CU station is approximately 100 m away from the Seismic Processing Centre of the Institute of Engineering of the National Autonomous University of Mexico (II-UNAM). Therefore, it was not considered necessary to use two different routes to reach the optic fiber to the Seismic Processing Centre. Other options could be used to improve the real-time seismic data acquisition. For instance, adding more stations for true redundancy and improving the real-time seismic data acquisition (e.g., stations *Tacubaya, TACY* or *Secretaría de Comunicaciones y Transportes, SCT*). Another option is to implement a radio transmission system between CU station and the II-UNAM Seismic Processing Centre.

It should be noted that each accelerometer has an external deep cycle battery of 70 Ampere-hour, which can keep operating the system during 10 to 12 days without power supply. In addition, these batteries are recharged by a dual power supply system. A first energy-supply system is based on an array of solar panels with a design that requires only 3 h of solar insolation to maintain the battery charged. The second energy-supply system operates with a single-phase supply of 127 volts. Although the time life of the batteries is estimated to be about 3 years, new batteries are installed every 12 to 18 months.

Data acquisition, detection and recording are carried out using the SEISLOG system (Havskov, 2006), which was configured to generate events in SEISAN format based on a STA/LTA (Short Time Average/Long Time Average) trigger algorithm. As it was mentioned before, each accelerometer is connected to a different computer, where seismic data are processed independently. Therefore, in case of a large event the system retrieves the seismic data from the first computer (CPU 1). If for any reason the seismic data were not generated in this computer, then the system would proceed to use the information from the second computer (CPU 2).

Evaluation of strong ground motion AT the reference station

The seismic signal at CU station is continuously recorded and evaluated to determine when a seismic event has occurred or not. The system then computes, for two horizontal components, peak ground acceleration, peak ground velocity and spectral accelerations for selected structural periods.

Results by Iglesias *et al*. (2007) suggest that the minimum peak ground acceleration (PGA) at CU for an earthquake to be considered a relevant event should be about 2 cm/s^2, since this intensity would occur about twice per year, and in view of the amplification at the lakebed zone, it would be felt by most people. However, we observed that some seismic events with no relevant magnitude (Mw<5.9) could trigger the system based on a single measure. Therefore, we have considered a second criterion where the mean horizontal spectral acceleration at T=1 s must be 1.5 times larger than the mean horizontal PGA to prevent that these earthquakes could be triggered. Consequently, we have proposed that a warning must be issued when the following two criteria are fulfilled: (1) the mean horizontal PGA equals or exceeds 2 cm/s^2; and (2) the spectral ratio between the mean horizontal spectral acceleration at T=1 sec and its corresponding mean horizontal PGA is larger than 1.5.

Table 1 shows some representative earthquakes used to check these two conditions. Note that the two criteria implicitly take into account that the rapid damage assessment system will be triggered with earthquakes with magnitude approximately larger than Mw=5.9 (events with symbol √).

Estimation of ground motion intensities at Soft Soil

Once the ground motion at the reference station is evaluated and fulfills the above described criteria, the next step is the calculation of ground motion intensities at other sites in the city. As it was mentioned previously, it is assumed that the strong ground motion at CU is a measure of the seismic input motion that excites the soft soil of Mexico City.

Estimation of seismic intensities (PGA, PGV and spectral responses) for other sites throughout the city is performed using response spectral ratios (RSR) (Rosenblueth and Arciniega, 1992; Reyes, 1999) pre-computed for a grid of 6400 points, approximately 400 m apart. The mean response spectrum measured at CU station is multiplied by the RSR at each of these points in order to obtain an estimation of the local response spectrum. Also, PGV measured at CU is multiplied by a pre-computed amplification factor at each point in order to obtain the local PGV value.

Table 1. Representative earthquakes recorded at CU used to test the two triggering conditions for damage assessment.

			PGA (cm/s^2)			Sa (T=1 s) (cm/s^2)			Sa(T=1 s)/ PGA			Triggered
No	Date	Magnitude	NS	EW	Mean	NS	EW	Mean	NS	EW	Mean	
1	06/07/1964	6.7	18.29	15.73	17.01	22.70	40.27	31.49	1.24	2.56	1.85	√
2	12/07/1974	3.5	48.97	31.44	40.21	3.67	2.08	2.87	0.07	0.07	0.07	×
3	07/06/1976	6.3	13.45	6.66	10.06	20.30	25.50	22.90	1.51	3.83	2.28	√
4	14/03/1979	7.0	17.01	17.02	17.02	38.77	19.11	28.94	2.28	1.12	1.70	√
5	24/10/1980	7.0	25.27	23.46	24.37	50.30	27.52	38.91	1.99	1.17	1.60	√
6	19/09/1985	8.1	26.80	32.54	29.67	69.90	91.71	80.81	2.61	2.82	2.72	√
7	21/09/1985	7.6	14.75	12.99	13.87	37.81	4.64	21.23	2.56	0.36	1.53	√
8	25/04/1989	6.9	13.40	10.53	11.97	29.80	20.30	25.05	2.22	1.93	2.09	√
9	31/05/1990	5.9	5.07	3.21	4.14	8.20	10.62	9.41	1.62	3.31	2.27	√
10	30/10/1992	4.7	13.40	15.79	14.60	18.30	24.46	21.38	1.37	1.55	1.47	×
11	10/12/1994	6.3	5.39	5.48	5.44	7.99	11.70	9.84	1.48	2.13	1.81	√
12	14/09/1995	7.3	12.42	7.65	10.04	24.00	28.64	26.32	1.93	3.74	2.62	√
13	15/06/1999	7.0	11.40	11.85	11.63	29.00	15.77	22.38	2.54	1.33	1.93	√
14	30/09/1999	7.6	7.66	7.80	7.73	26.58	24.31	25.44	3.47	3.12	3.29	√
15	21/07/2000	5.9	13.09	12.48	12.79	8.38	11.12	9.75	0.64	0.89	0.76	×
16	14/08/2005	5.8	1.09	1.08	1.09	3.10	2.74	2.92	2.85	2.54	2.69	×
17	16/10/2005	3.5	2.16	5.04	3.60	3.10	2.74	2.92	1.44	0.54	0.81	×
18	26/05/2005	4.6	0.46	0.49	0.48	0.54	0.21	0.37	1.16	0.42	0.78	×

RSR for the grid of points are determined -off line- in two steps. First, for all instrumented sites in the city (about 120, located mainly in the lakebed zone; see Figure 2), empirical spectral ratios and PGV ratios are obtained by averaging the computed ratios, for each accelerometric station with respect to CU station and for all the earthquakes that have been recorded simultaneously at each station and at CU. In a second step, RSR are determined for arbitrary sites (those that pertain to the 6400-point grid) through interpolation (Pérez-Rocha, 1999; Pérez-Rocha *et al*., 2009). The interpolation procedure is as follows: 1) each RSR at an instrumented site is normalized with respect to its dominant period (Reinoso and Lermo, 1991); 2) the normalized RSR of the instrumented sites are used in a two-dimensional Bayesian interpolation scheme to obtain the normalized RSR at an arbitrary site (the Bayesian prior amplification values at an arbitrary site are those associated to 1D SH-wave propagation analysis); and 3) the interpolated normalized RSR is renormalized with respect to its dominant period. In this study, we considered that RSR for lakebed sites are relatively constant regardless of the magnitude, epicentral distance and azimuth of subduction and normal faulting earthquakes (Reinoso and Ordaz 1999). For other occasional rare large earthquakes within the Trans-Mexican Volcanic Belt (e.g., the Acambay earthquake of 1912 M~7.0), we also assumed that RSR for lakebed sites with respect to CU for shallow, crustal earthquakes at regional distances may be similar to those estimated for shallow, coastal earthquakes (e.g., Singh *et al*. 2011). At least for Mexico City, it is well known that the clay has behaved almost linearly for most of the sites so far, and that the observed nonlinear behavior, if any, is very small (Reinoso and Ordaz, 1999).

As mentioned, in order to reduce the computing time of the real-time calculation, we pre-calculate the RSR for a grid of points.

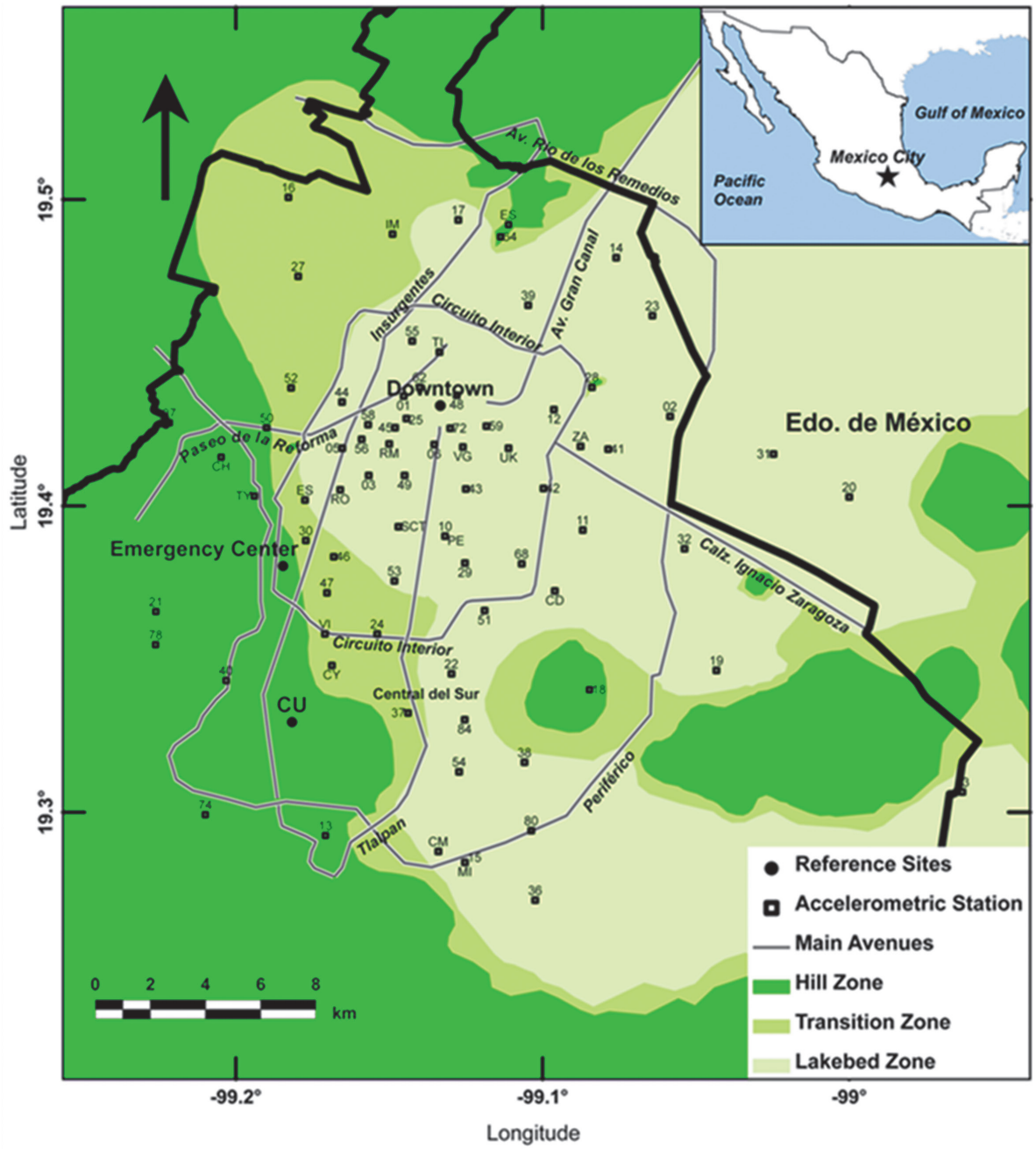

Figure 2. Mexico City: accelerometric stations, geotechnical zones and some reference sites.

Real-Time estimation of damage and fatalities

Construction of the exposure database

We use three sets of exposure databases: buildings, water supply network, and population. The area of study is presented in Figure 3, including zones where heavy damage has been reported during past seismic events, such as the 1957 (M = 7.5; Orozco and Reinoso, 2007), 1979 (M = 7.6) and 1985 (M = 8.1) events.

Building database

We obtained from the Mexico City government a database of all buildings. A total area of 830 million square meters of the city is covered, with a total built area of approximately 313 million square meters. For each property, the data base contains structural information such as year of construction, number of stories, construction area, occupancy and a qualification of the maintenance. According to our experience, we divided the total 1,023,508 buildings into

six classes, depending on their corresponding number of stories. Characteristics of these six classes, along with some related statistics, are shown in Table 2.

Table 2. Building characteristics divided into six classes.

Class	Number of stories	Total number of buildings	Participation of the total lot
1	1-2	724,612	40.58%
2	3-5	282,380	42.28%
3	6-10	13,230	10.39%
4	11-15	1,674	3.16%
5	16-20	422	1.55%
6	>20	190	0.04%

We assumed structural systems for the six classes based on their dynamic response and on construction characteristics at Mexico City, namely: a) building classes 1 and 2 are buildings of confined masonry walls with reinforced concrete slabs commonly used for housing; b) buildings class 3 are reinforced concrete frame buildings with masonry infill walls; c) building classes 4 and 5 are reinforced concrete frame buildings with concrete shear walls and d) buildings class 6 are steel frame buildings with concrete shear walls. From an analysis of the database information, it was also concluded that the building classes could also be grouped considering the year of construction, as those built after 1987 (building classes 1, 2, 5 and 6) and those built between 1959 and 1976 (building classes 3 and 4).

A key parameter to estimate the seismic response of a building is its dominant period, T. In order to estimate the period of vibration, we used an empirical expression inferred from acceleration records obtained during earthquakes in instrumented buildings in Mexico City, in terms of the number of stories, N, as $T=0.08\times N^{1.26}$ (Mosquera, 2007).

With this information, we created a database in a geographical information system (GIS), including our own corrections from either full or sidewalk inspections.

Since the available time to carry out the computation is short, the studied area was divided into 6400 cells, each one of 400 × 400 m, where only 4250 of 6400 cells contain available information representative of the building and population database of the city (Figure 3). For the purpose of this work, at each cell we obtained spatially aggregated information of built-up area per square meter and maximum number of occupants of the six considered building classes. Table 3 shows additional characteristics of the six building classes, including their assigned fundamental period. Table 3 also shows parameters related to expected fatalities caused directly by the buildings damage (F_H, F_T, and F_F) and parameters that define the vulnerability of the structures (K and α) whose details will be shown later. Figure 4 shows the distribution of the built-up area of buildings with number of stories between 6 and 10. It can be noted that these buildings are located at zones where severe damages were reported during past earthquakes (Figure 3). Although results were obtained for all classes of buildings, in what follows only results for these buildings will be shown.

Water supply network

From Mexico City government a description of the Mexico City's main water supply network was obtained, having more than 600 km length with a flow of about 35 m^3/sec of water for 8.5 million inhabitants. The database of water supply network created in a GIS has a wide variety of diameters, mainly 20" (140.20 km, 23.2%), 32" (22.78 km, 3.8%), 36" (81.79 km, 13.5%), 48" (323.4 km, 53.6%) and 72" (25.36 km, 4.2%). The materials of the pipelines are made of asbestos cement, concrete, cast iron and steel. The location of pipelines by material is unknown. As it will be seen later, pipeline damage in soft soil of Mexico City is only related to the ground motion parameter PGV^2/PGA (Pineda and Ordaz, 2007). Figure 5 shows the distribution of Mexico City's water network.

Population Database

In order to assess the social impact related to earthquake life losses caused by building damage, we estimated information related to the maximum number of occupants in the buildings. Statistics of percentage of population by time of the day, day of week and occupancy type are available in the literature (Coburn *et al* 1992). However, we used approximate occupation density by building occupancy (Reinoso and Jaimes, 2015). Building occupants were inferred by multiplying the approximate occupation density by the construction area contained into the database for each building. From a total of 1,023,508 buildings in Mexico City, approximately 12.67 million of maximum occupants were obtained. The percentages corresponding with the number of stories into six classes above mentioned are 43.46% (1 to 2), 40.32% (3 to 5), 10.86% (6 to 10),

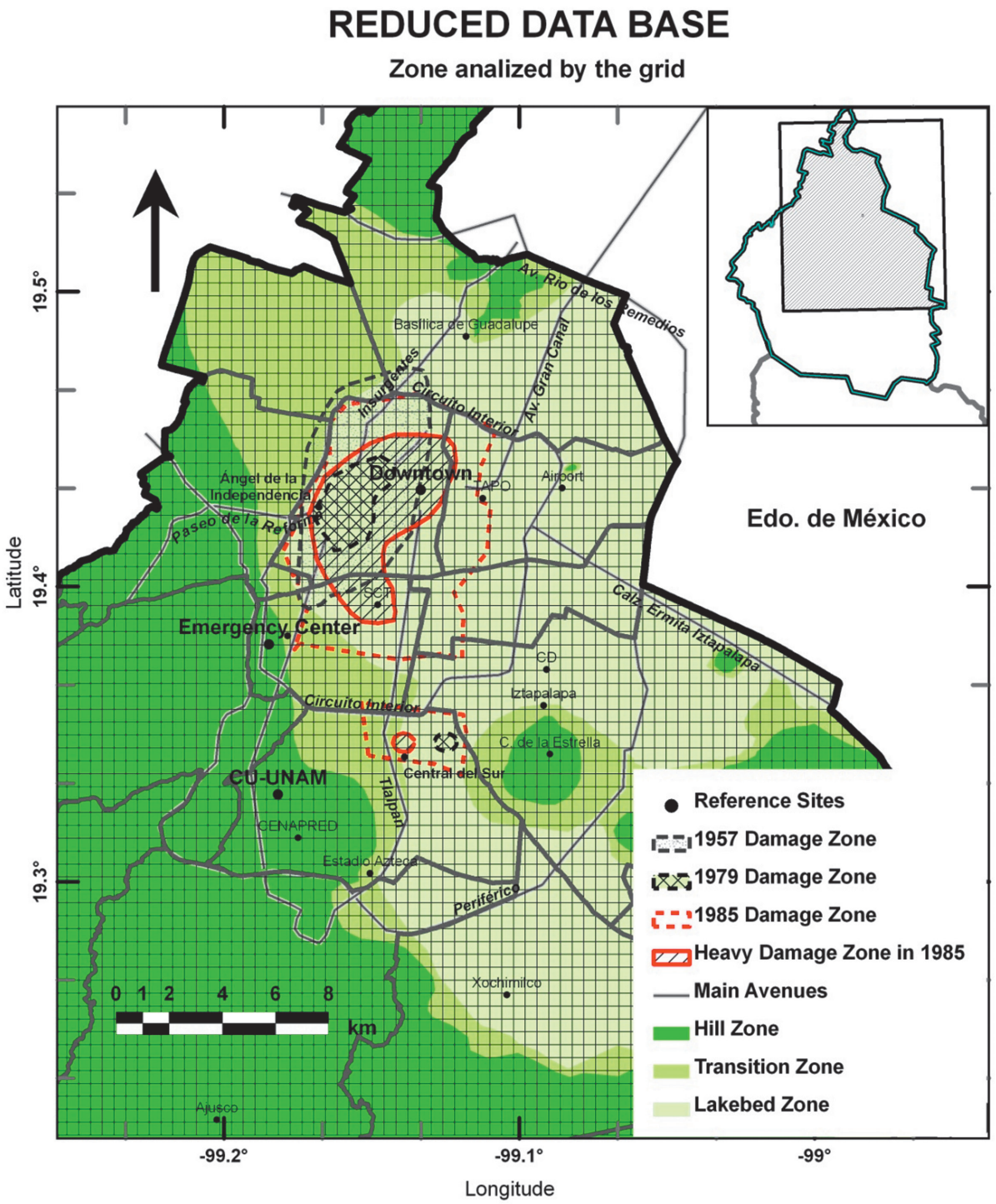

Figure 3. Area of study for the early earthquake damage assessment system in Mexico City.

3% (11 to 15), 1.41% (16 to 20) and 0.95% (>20). Finally, as it was previously mentioned, we obtained spatially aggregated information of the maximum number of occupants, O_{ij}, for the structural class i and for the cell j. Figure 6 illustrates the distribution of population in buildings with 6 to 10 stories.

As it has been observed during earthquakes, the time of the earthquake occurrence determines where the person is more likely to be trapped. Therefore, it will be a different scenario if the earthquake occurs during the day, when people are located out-doors, in public buildings and offices, or during the night, when almost everyone is at their homes. Table

Table 3. Building characteristics (structural class, year of construction and structural period), parameters to estimate fatalities depending on the hour of the day (F_H), parameters that define the vulnerability of the structures (K and a) and parameters related to expected fatalities (F_T and F_F).

				FH	Eq. (1)					
Class	Structural system	Year of construction	T	Day (%)	Commuting (%)	Nigh (%)	Ki	αi	FT (%)	FF (%)
1	Confined masonry	>1987	0.1	55	49	71	1.0	1.60	34	44
2	Confined masonry	>1987	0.3	59	48	56	0.93	1.60	58	46
3	Reinforced concrete frames	1959 < year < 1976	0.8	58	52	57	1.62	1.60	43	35
4	Reinforced concrete frames with concrete shear walls	1959 < year < 1976	1.6	68	50	47	0.95	1.60	55	42
5	Reinforced concrete frames with concrete shear walls	> 1987	2.6	72	51	38	0.74	1.63	55	42
6	Steel frames with concrete shear walls	> 1987	3.5	73	50	36	1.3	1.60	42	55

3 presents average occupant ratios at different hours of the day (F_H, in this work) based on the survey origin-destination (Coburn *et al*. 1992; INEGI, 2010). The time intervals based on the survey are: 1) daytime is considered to be from 9:00 a.m. to 2:00 p.m. and from 4:00 p.m. to 6:00 p.m., 2) nighttime between 8:00 p.m. and 7:00 a.m., and 3) commuting time from 7:00 a.m. to 9:00 a.m., from 2:00 p.m. to 4:00 p.m. and from 6:00 p.m. to 8:00 p.m. With the mentioned ratios, we estimated the distribution of 7.31, 6.18 and 7.86 millions of persons at the buildings during the day, commuting and night, respectively.

Seismic damage anda fatalities

Building Damage Assessment

For the case of buildings, seismic intensity is expressed in terms of spectral acceleration at the fundamental period of vibration of the building. The mean damage ratio D_{ij}, defined as the ratio of the expected repair cost to the replacement cost of the structure, for a group of class structures i, located in the cell j, is computed a

$$D_{ij} = K_i S_{ij}^{\alpha_i} \quad (1)$$

In Eq. (1), S_{ij} is the spectral acceleration measured at the period assigned to class i. K_i and α_i are parameters that define the vulnerability of structures of class i based on a combination of construction material, construction type, number of stories and year of construction (Ordaz *et al*., 1994). In this study, the parameters K_i and α_i were determined by:

1. Comparing vulnerability functions ended up in a proprietary software (RS-Mex©, also known as the UNAM model, Ordaz *et al*., 2000) used by the insurance industry to compute and manage their catastrophic risk. Recently, this software has been used by national governments and institutions to study scenarios of losses and affected people (R-FONDEN for Mexico and CAPRA for Latin America), and

2. Carrying out empirical analysis of damage due to past earthquakes at Mexico City, but mainly due to the 1985 earthquake.

These damage functions, together with the seismic intensities, allow us the calculation of damage for each class of building at each cell. Table 3 presents the values of K_i and α_i.

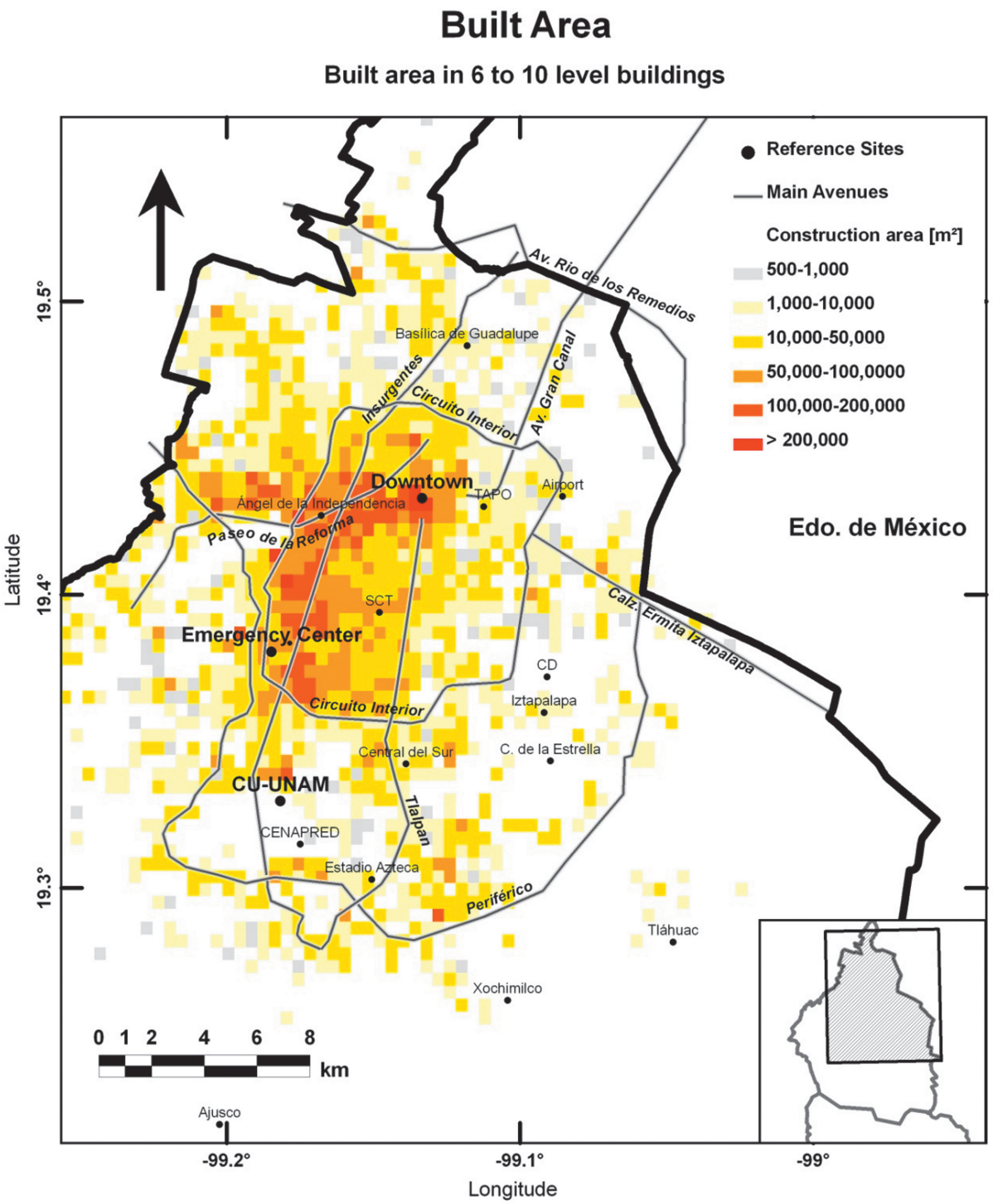

Figure 4. Example of distribution of building database by cell for the rapid damage assessment system in Mexico for buildings having between 6 and 10 stories.

Figure 7 shows the six damage functions used in this work. If we accept that, within a cell, the replacement cost of structures of a given class is constant, then D_{ij} can be interpreted as the fraction of the total area covered by structures of class i in cell j that was damaged.

To compute the damage, we translated the damage ratio given by Eq. (1) into loss by multiplying it by the total area A_{ij} covered by structures of class i at cell j. The result is an equivalent damaged area with a reconstruction value proportional to the value of the economic losses produced by the earthquake,

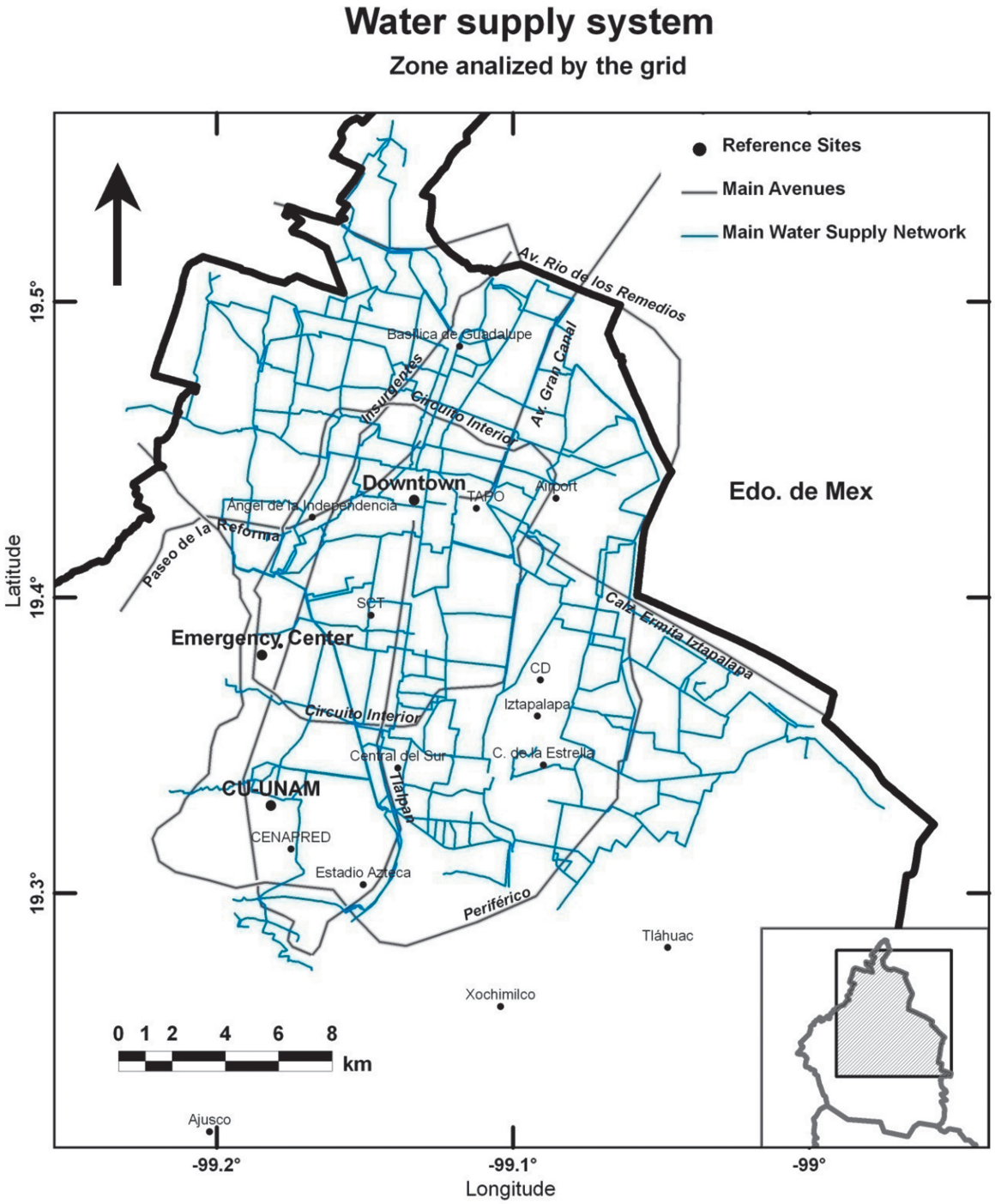

Figure 5. Distribution of Mexico City's water network.

$$P_{Bij} = K_i S_{ij}^{\alpha_i} A_{ij} \qquad (2)$$

Notice that P_{Bij} has units of area. Assuming that the reconstruction cost per unit area is independent of structural class, the expected loss at cell j for all the structural classes P_{Bj} can be obtained with a simple addition:

$$P_{Bj} = \sum_i P_{Bij} \qquad (3)$$

Once the total losses are calculated for all cells the geographical distribution of the damage can be generated.

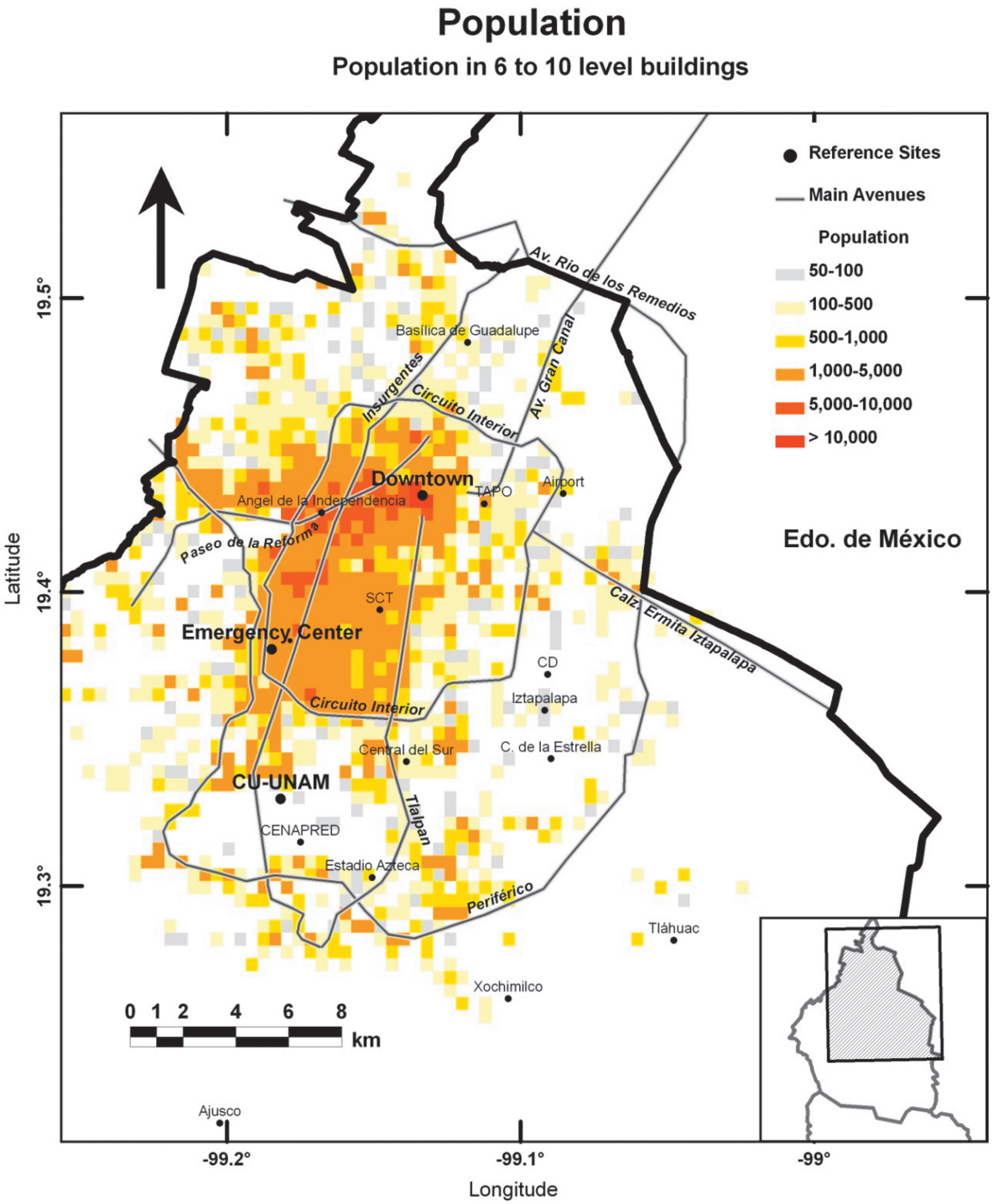

Figure 6. Distribution of maximum potential occupants in buildings having between 6 and 10 stories.

Damage assessment for Mexico City's water network

The damage to the water system was quantified in terms of the number of pipe repairs per unit length of pipeline. Pineda and Ordaz (2007) analyzed the behavior in the Mexico City's primary water network due to the 1985 earthquake and proposed an intensity-damage relation in terms of PGV^2/PGA, where PGV and PGA are the peak ground velocity and acceleration, respectively, yielding a relationship between the pipeline damage rate D_{pi} (number of repairs per kilometer) and PGV^2/PGA given by

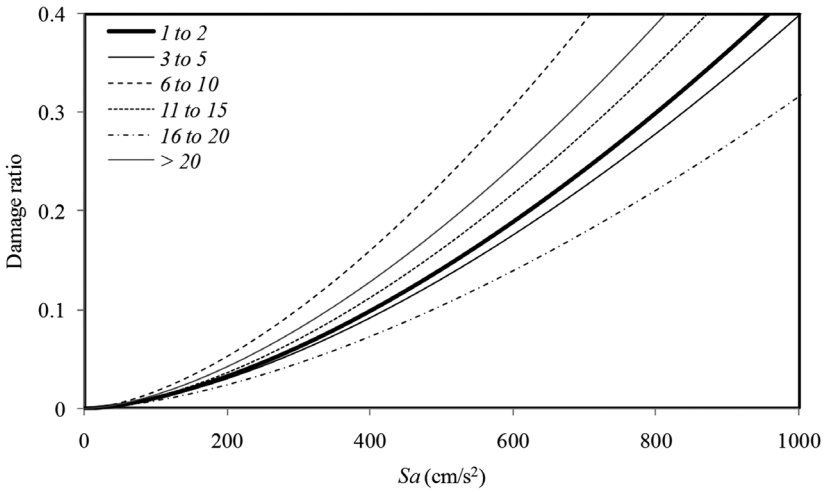

Figure 7. Example of building intensity-damage relations for the rapid damage assessment system in Mexico City.

$$D_{pi} = \begin{cases} 0 & if \quad PGV^2/PGA < 1.8\ cm \\ 0.122 & if \quad 1.8 \le PGV^2/PGA < 8.72\ cm \\ 0.032\dfrac{PGV^2}{PGA} - 0.157 & if \quad PGV^2/PGA \ge 8.72\ cm \end{cases} \tag{4}$$

This pipeline damage function, together with the seismic intensity (measured in terms of PGV^2/PGA) obtained at midline for each segmented pipeline; allowed to compute the geographical distribution of the damage of water supply network.

Fatality assessment

There are models that relate the fatalities from earthquakes to factors such as buildings with severe damage or collapse, and the occupancy at the time of earthquake (e.g. Coburn *et al*., 1992; Murakami, 1992; Reinoso *et al*. 2005). A method proposed by Reinoso *et al*. (Reinoso and Jaimes, 2015) was used to obtain fatality ratios associated directly with structural damage for the six building classes and the occupancy at the time of an earthquake. The mean fatality ratio, R_{Fij}, for a structure of class *i* located at cell *j*, is obtained as

$$R_{Fij} = F_H \cdot F_T \cdot F_F \cdot F_{SFij} \tag{5}$$

where, as it was mentioned earlier, F_H is the occupants ratio in the structure class *i* at the time of the earthquake occurrence and the maximum occupancy; F_T is the ratio of trapped people which depends on the structural type and the occupants at the time of an earthquake; F_F is the ratio of trapped people and those who would die if not rescued (this value depend on the structural type, number of stories, and the emergency management of the city); and F_{SFij} is a structural damage factor related to the expected damage (Eq. 1) for a group of class structures *i*, located in the cell *j*. As it will be explained later, F_{SFij} is proposed to relate the affected people on the building with D_{ij}.

F_T depends on the preparedness, education and building size, among others; it is well known that some people manage to evacuate the building before it collapses or present severe damage. On the other hand, most collapsed buildings leave spaces and gaps where people may escape the ruins by themselves or eventually are rescued. Ratios of trapped people with respect to number of occupants at the time of the earthquake were used. This means that only a fraction of the people, F_T, who are in the building will be trapped in the ruins. Table 3 shows the values of F_T resulting from a comprehensive empirical analysis of a database obtained for the 1985 earthquake (Reinoso an Jaimes, 2015).

F_F depends on type of contents, age and health of occupants, structural type and type of collapse, occupancy and number of stories, rescue teams efficiency, weather conditions, fires, and intensities of aftershocks among others. Published data on fatalities rates is limited. Coburn *et al*. (1992) summarized approximate casualty rates for masonry and reinforced concrete structures based on worldwide data. Table 3 shows the values of F_F used in this work.

F_{SFij} depends on the damage of every building. We assume that large expected damage is correlated with large probabilities of caused victims. This may not be true especially for modern ductile buildings, where the expected damage can be very large but they

do not collapse. F_{SFij} is expressed through a lognormal probability distribution of the mean damage ratio D_{ij} as

$$F_{SFij}(D) = \Phi\left[\frac{1}{\beta_c}\ln\frac{D_{ij}}{x_m}\right] \quad (6)$$

where Φ is the cumulative standard normal distribution, x_m is the median of the damage of the building required to produce damage to the people in the building, β_c is the log-standard deviation, and D_{ij} is the damage given by Eq. 1 in percentage. Values of x_m and β_c of 17 and 0.3, respectively, were obtained from a comprehensive empirical analysis of the database of earthquakes in Mexico, mainly the 1985 earthquake. Figure 8 shows an example of intensity-fatality relations during day for the six structural classes.

The expected fatalities during an earthquake and their spatial distribution throughout the city for the structural class *i* and for the cell *j* is,

$$P_{Fij} = R_{Fij}O_{ij} \quad (7)$$

where O_{ij} is the maximum number of occupants for a group of class structures *i*, located in the cell *j* and R_{Fij} is the mean fatality ratio given by Eq. 5.

The expected fatality in the cell *j* for all the structural classes, P_{Fj}, is obtained as,

$$P_{Fj} = \sum_i P_{Fij} \quad (8)$$

Similarly, once the total fatalities are calculated for all cells, the geographical distribution of the fatalities can be generated to estimate losses.

Illustrative examples

In what follows, the results for two examples will be shown: 1) the Michoacán, September 19, 1985, earthquake and 2) the April 25, 1989 earthquake.

We use strong ground motion records of the September 19, 1985 earthquake (M = 8.1) recorded at CU station as a hypothetical event to trigger the rapid damage assessment system. Figure 9 presents the spatial distribution throughout the city considering the September 19, 1985 event: spectral intensity for structural period of T=2 sec (Figure 9a), building damages applying Eq. (3) (Figure 9b), damages for the Mexico City's primary water network (Figure 9c) and fatalities applying Eq. (8) (Figure 9d). Note that damage distribution matches the zones where heavy damages have been reported during past earthquakes (Figure 2).

The second case study is the April 25, 1989 earthquake (M = 6.9). This earthquake was very well recorded by all stations of the Guerrero and Mexico City networks. Also, this earthquake has been the strongest earthquake felt in Mexico City after the 1985 one. Figure 10 presents the same maps as those shown in Figure 9 for the 1989 earthquake. Note that neither damages to buildings nor fatalities are predicted.

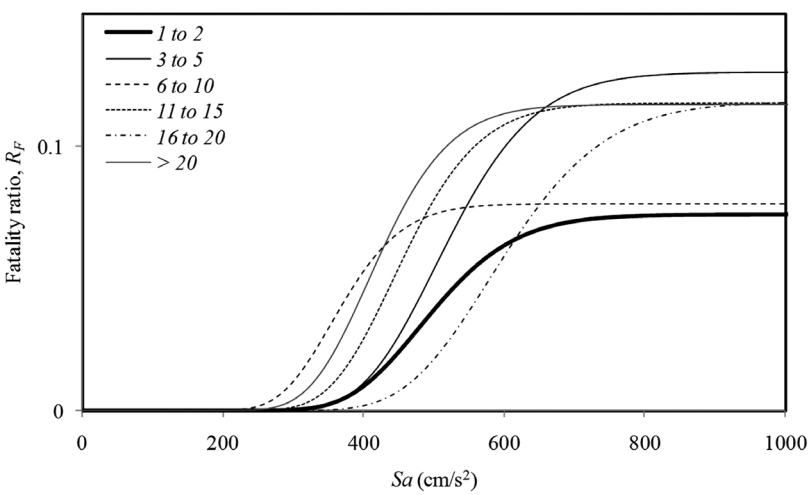

Figure 8. Example of intensity-fatality relations considering the number of stories and that the earthquake occurs during the day for the rapid damage assessment system in Mexico City.

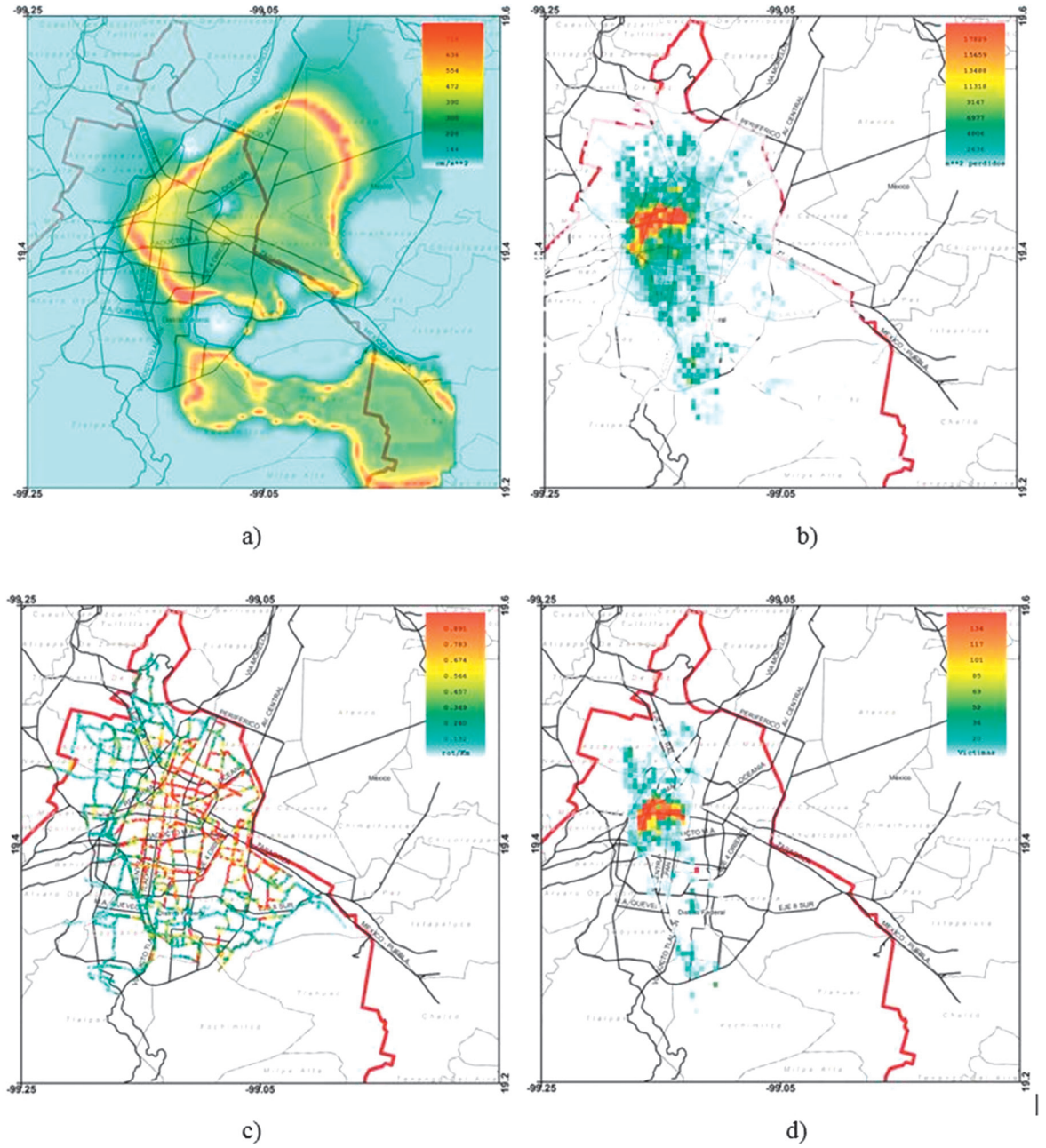

Figure 9. Spatial distribution throughout the city considering the September 19, 1985 event: a) spectral intensity for structural period of T=2 s, b) building damage, c) damage of the Mexico City's primary water system and d) fatalities.

Notification system structure

After a major disaster, many types of data must be displayed as an aid to make decisions. Therefore, an automated reporting system is fundamental to obtain timely information for an effective response.

In order to carry out these automated processes, a custom application SAPS (*Sistema Automático de Publicación de Shakemaps*, Automatic System for Publishing Shakemaps) was developed to allow the rapid delivery of information by different communication mediums. The system is written under the Visual Studio (.NET) environment and the SQLServer is used as the database management system for storing and retrieving the information. Web Services are also employed for communication in the internal network, and to offer data access management and delivery of notifications in a simple and secure way. The application allows the following activities:

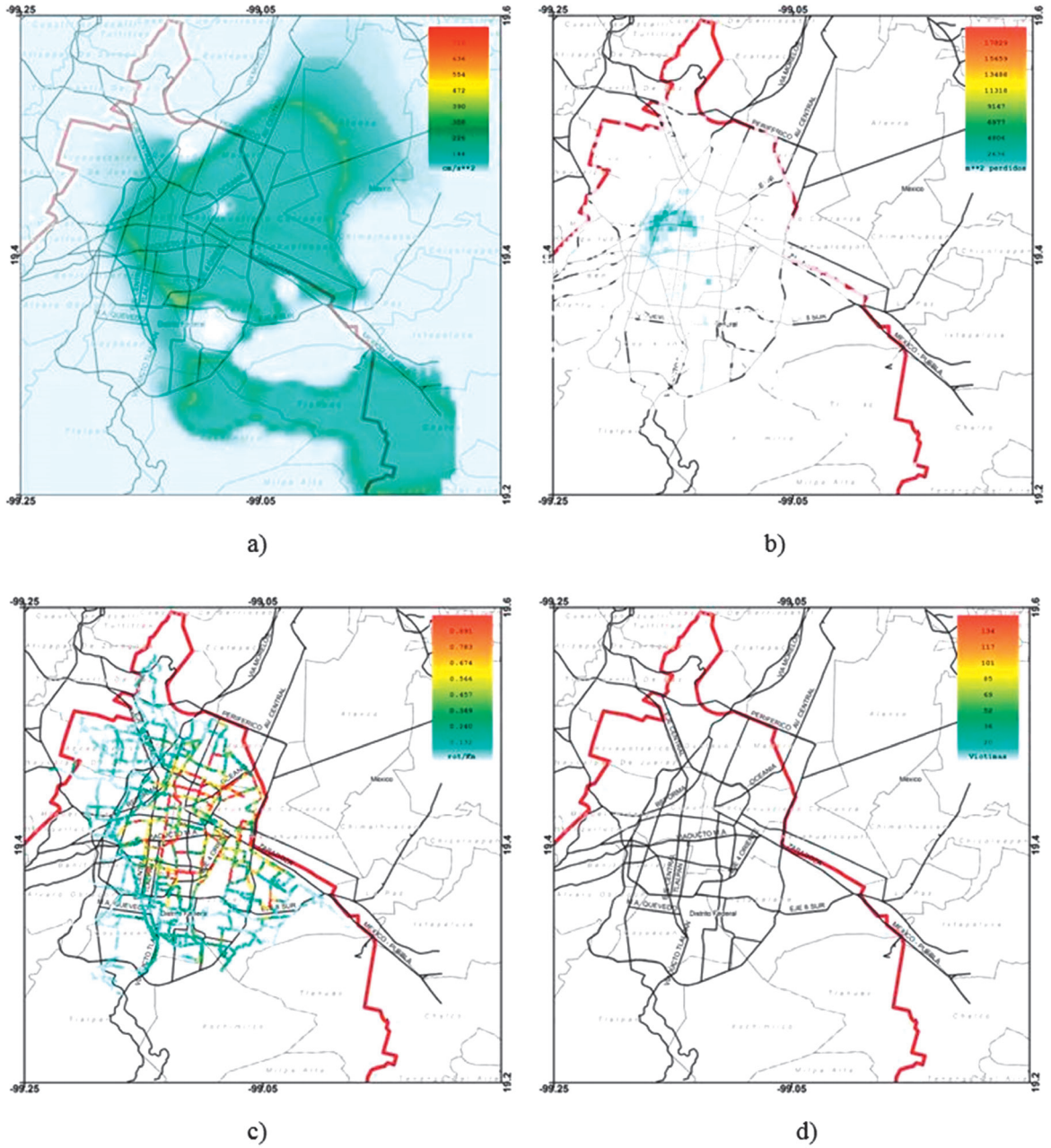

Figure 10. Spatial distribution throughout the city considering the April 25, 1989 event: a) Spectral intensity for structural period of T=2 s, b) building damage, c) damage of the Mexico City's primary water system and d) fatalities .

- Creation and consulting of a historic database of shaking related products
- Information related to the last published event
- Recovery of an event to be published in case of an error
- Storing maps and kmz google files
- Management of e-mail distribution lists and notifications
- Management of the web site
- System monitoring and alerts
- Management of errors

In Figure 1, the notification system structure transmits products to the Emergency Center and to decision makers by the following ways:

- Short text messages to cell phones and pagers
- Different types of e-mail messages and attached maps, according to previously set configurations
- FTP servers over the Internet
- Radio communication link based on disperse spectrum radio-modems with Ethernet inter-phase and FreeWave brand, and Yagi antennas
- Via a passive Web page in which the user must seek for the information

Conclusions

A high-resolution rapid damage assessment system for Mexico City was presented to estimate real-time loss due to an earthquake and to improve emergency response based on a single accelerometric station. Fatalities and damage to buildings and the water supply system throughout the city in 10 to 15 minutes after an earthquake were estimated (depending on the standard PC computer speed), using real-time recorded (PGA) and computed (PGV and spectral ordinates for selected structural periods) seismic intensities at the reference station, pre-calculated response spectral ratios at soft sites, intensities-damage and intensities-fatalities relations, along with the geographic distribution of constructions, population, and water supply system. Since the available time to carry out the computation is short, building and population database in populated areas, with a square mesh of 400 × 400 m, were elaborated. The system runs automatically on two computers with no human intervention. This information is sent to an Emergency Center so that decision makers can prioritize response and recovery efforts to focus on those areas most impacted by the earthquake during the initial period of the emergency (i.e., the first 1-3 hours). In addition, damage estimates can be used to set previously designed emergency plans which may include possibly required resources.

The development of the system could be applied to other regions and could be useful for variety of potential users. Any organization with a need to know damage impacts immediately after moderate and large earthquakes can benefit from this real-time earthquake damage assessment system. This technology which makes up rapid loss estimation could, however, be applied in a number of planning and response environments. This earthquake rapid damage assessment system could be adjusted to improve the emergency response of governments, lifeline maintenance teams and large corporations with geographically distributed facilities and assets.

Acknowledgments

The authors would like to thank to the Secretaría de Protección Civil of the Gobierno del Distrito Federal and to the Secretaría de Gobernación of the Federal Government of México for the financial support to build the entire system. We are very grateful to anonymous reviewers whose comments and suggestions considerably improved our original article. We also would like to acknowledge the generous participation of Ana Laura Ruiz, Rosario Delgado, Héctor Sandoval and David García-Soto for the system's monitoring.

References

Astiz L., Kanamori H., Eissler H., 1987, Source characteristics of earthquakes in the Michoacán seismic gap in Mexico, *Bulletin of the Seismological Society of America,* 77, 4, 1326 - 1346.

Ayala O., O'Rourke M., 1989, Effects of the 1985 Michoacán earthquake on water systems and other buried lifelines in Mexico, *Technical Report NCEER-89-0009*, Multidisciplinary Center for Earthquake Engineering Research, New York.

Coburn A., Spence R., Pomonis A., 1992, Factors determining human casualty levels in earthquakes: mortality prediction in building collapse, *Proceedings of the 10th World Conference on Earthquake Engineering*, Madrid, Spain, 5989-5994.

Eguchi R., Goltz J., Seligson H., Heaton T., 1994, Real-time earthquake hazard assessment in California: the early post-earthquake damage assessment tool and the Caltech-USGS broadcast of earthquake, *Proc. Of the 5th U.S. National Conference on Earthquake Engineering*, II, 55-63.

Eguchi R., Goltz J., Seligson H., Flores P., Blais N., Heaton T., Bortugno E., 1997, Real-time loss estimation as an emergency: the early post-earthquake damage assessment tool

(EPEDAT), *Earthquake Spectra,* 13, 4, 815-832.

Erdik M., Fahjan Y., Ozel O., Alcik H., Mert A., Gul M., 2003, Instanbul earthquake rapid response and the early warning system, *Bulletin of Earthquake Engineering,* 1, 157-163.

Erdik M., 2006, Urban earthquake rapid response and early warning systems, *First European Conference on Earthquake Engineering and Seismology*, Geneva, Switzerland.

Erdik M., Fahjan Y., 2006, Early warning and rapid damage assessment, *Assessing and Managing Earthquake Risk, Geotechnical, Geological, and Earthquake Engineering,* 2, 323-338.

Erdik M., Sesetyan K., Demircioglu B., Hancilar U., Zulfika C., 2010, Rapid earthquake loss assessment after damaging earthquakes, *Earthquake Engineering in Europe, Geotechnical, Geological, and Earthquake Engineering,* 17, 523-547.

Havskov J., 2006, A seismic data acquisition system for Windows9X/NT/2000/XP, *Department of Earth Science, University of Bergen, Noruega*, http://www.geo.uib.no/seismo/software/software.html.

Iglesias A., Singh S.K., Ordaz M., Santoyo M.A., Pacheco J., 2007, The seismic alert system for Mexico City: an evaluation of its performance and a strategy for its improvement, *Bulletin of the Seismological Society of America* 97, 5, 1718-1729.

INEGI, 2010, Population and Housing Census 2010, http://www.inegi.org.mx/sistemas/mexicocifras/

Kanamori H., Hauksson E., Heaton T., 1997, Real-time seismology and earthquake hazard mitigation, *Nature,* 390, 461-464.

Meli R., 1986, Evaluación de los efectos de los sismos de 1985 en los edificios de la ciudad de México (3 volúmenes y 7 anexos), *Informe Interno DE/EST-V2/1*, Instituto de Ingeniería, UNAM (in Spanish).

Montalvo-Arrieta J., Sánchez-Sesma F., Reinoso E., 2002, A Virtual reference site for the valley of Mexico, *Bulletin of the Seismological Society of America,* 92, 5, 1847-1854.

Mosquera J., 2007, Validación de un modelo continuo simplificado y estudio paramétrico de edificios instrumentados en la ciudad de México y California sujetos a sismos, *Master's thesis*, UNAM, México (in Spanish).

Murakami H.O., 1992, A simulation model to estimate human loss for occupants of collapsed buildings in an earthquake, *Proceedings of the 10th World Conference on Earthquake Engineering*, Madrid, Spain, 5969-5974.

Ordaz M., Reinoso E., Singh S.K., Vera E., Jara J.M., 1989, Espectros de respuesta en diversos sitios del Valle ante temblores postulados en la brecha de Guerrero, *Memorias del VIII Congreso Nacional de Ingeniería Sísmica and VII Congreso Nacional de Ingeniería Estructural, Acapulco*, México, A187-A198 (in Spanish).

Ordaz M., Meli R., Montoya-Dulche C., Sánchez L., Pérez-Rocha L.E., 1994, Bases de datos para la estimación de riesgo en la Ciudad de México, *Cuadernos de Investigación*, CENAPRED, México (in Spanish).

Ordaz M., Miranda E., Reinoso E., Pérez-Rocha LE., 2000, Seismic loss estimation for Mexico City, *XII Congreso mundial de Ingeniería Sísmica*, CD.

O'Rourke M., Ayala G., 1993, Pipeline Damage to Wave Propagation, *Journal of Geotechnical Engineering, ASCE* 119, 9.

Orozco V., Reinoso E., 2007, Revisión a 50 años de los daños ocasionados en la ciudad de Mexico por el sismo del 28 de julio de 1957 con ayuda de investigaciones recientes y sistemas de información geográfica, *Revista de Ingeniería Sísmica*, 76, 61-87 (in Spanish)

Perez-Rocha L.E., 1999, Respuesta sísmica estructural: efectos de sitio e interacción suelo-estructura, *Ph. D. Thesis*, Faculty of Engineering, UNAM (in Spanish).

Perez-Rocha L.E., Ordaz M., Reinoso E., 2009, Interpolación espacial de las amplificaciones dinámicas del terreno en el valle de México, *Revista de Ingeniería Sísmica,* 80, 85-112 (in Spanish).

Pineda O., Ordaz M., 2007, A new seismic intensity parameter to estimate damage in buried pipelines due to Seismic Wave Propagation, *Journal of Earthquake Engineering,* 11, 5, 773-786.

Reinoso E., Jaimes M.A., 2015, Estimation of life vulnerability inside buildings during earthquakes, *Informe final del proyecto*

Sistema de cuantificación de pérdidas, control de recursos y análisis de riesgo para el FONDEN para la Secretaría de Hacienda y Crédito Público y Fonden, México (in Spanish).

Reinoso E., Lermo J., 1991, Periodos del suelo del valle de México medidos en sismos y con vibración ambiental, *Proc. IX National Conference on Earthquake Engineering*, Mexico 2.149-2.156 (in Spanish).

Reinoso E., Ordaz M., 1999, Spectral ratios for Mexico City from free field recordings, *Earthquake Spectra* 15, 2, 273-295.

Reinoso E., Zeballo A., Hernández O., Moore F., Chávez G., Hernández J.J., Arredondo R., Jürg J., 2005, Estudio de la vulnerabilidad sísmica de Managua, *Informe final del proyecto Reducción de la vulnerabilidad ante desastres naturales*, Sistema Nacional para la Prevención, Mitigación y Atención de Desastres, Nicaragua (in Spanish).

Rosenblueth E., Arciniega A., 1992, Response spectral ratios, *Earthquake Engineering and Structural Dynamics* ,21, 483-492.

Reyes C., 1999, El estado límite de servicio en el diseño sísmico de edificios, *Phd Thesis*, UNAM, México (in Spanish).

Singh S.K, Lermo J., Domínguez T., Ordaz M., Espinosa J.M., Mena E., Quaas R., 1988a, A study of amplification of seismic waves in the valley of Mexico with respect to a hill zone site (CU), *Earthquake Spectra,* 4, 653-674.

Singh S.K, Mena E., Castro R., 1988b, Some aspects of source characteristics of 19 September 1985 Michoacan earthquake and ground motion amplification in and near Mexico City from the strong motion data, *Bulletin of the Seismological Society of America,* 78, 451-477.

Singh S.K, Iglesias A., Ordaz M., Pérez-Campos X., Quintanar L., 2011, Estimation of ground motion in Mexico City from a repeat of the M~7.0 Acambay earthquake of 1912, *Bulletin of the Seismological Society of America* 101, 5, 2015-2028.

Yamazaki F., Katayama T., Yoshikawa Y., 1994, On-line damage assessment of city gas networks based on dense earthquake monitoring, *Proceedings of 5th U.S. National Conference on Earthquake Engineering*, 4, 829-837.